Vector Boson Scattering and Electroweak Production of Two Like-Charge W Bosons and Two Jets at the Current and Future ATLAS Detector

Dissertation

zur Erlangung des akademischen Grades
Doctor rerum naturalium
(Dr. rer. nat.)

vorgelegt der Fakultät Mathematik und Naturwissenschaften
der Technischen Universität Dresden

von

M.Sc. Ulrike Schnoor
geboren am 22.4.1988 in Stuttgart

Datum der Einreichung: 27. November 2014
Tag der mündlichen Prüfung: 30. Januar 2015

1. Gutachter: Prof. Dr. Michael Kobel
2. Gutachter: Prof. Dr. Sabine Lammers

Abstract

The scattering of electroweak gauge bosons is closely connected to the electroweak gauge symmetry and its spontaneous breaking through the Brout-Englert-Higgs mechanism. Since it contains triple and quartic gauge boson vertices, the measurement of this scattering process allows to probe the self-interactions of weak bosons. The contribution of the Higgs boson to the weak boson scattering amplitude ensures unitarity of the scattering matrix. Therefore, the scattering of massive electroweak gauge bosons is sensitive to deviations from the Standard Model prescription of the electroweak interaction and of the properties of the Higgs boson.

At the Large Hadron Collider (LHC), the scattering of massive electroweak gauge bosons is accessible through the measurement of purely electroweak production of two jets and two gauge bosons. No such process has been observed before. Being the channel with the least amount of background from QCD-mediated production of the same final state, the most promising channel for the first measurement of a process containing massive electroweak gauge boson scattering is the one with two like-charge W bosons and two jets in the final state. This thesis presents the first measurement of electroweak production of two jets and two identically charged W bosons, which yields the first observation of a process with contributions from quartic gauge interactions of massive electroweak gauge bosons.

An overview of the most important issues in Monte Carlo simulation of vector boson scattering processes with current Monte Carlo generators is given in this work. The measurement of the final state of two jets and two leptonically decaying same-charge W bosons is conducted based on proton-proton collision data with a center-of-mass energy of $\sqrt{s} = 8\,\text{TeV}$, taken in 2012 with the ATLAS experiment at the LHC. The cross section of electroweak production of two jets and two like-charge W bosons is measured with a significance of 3.6 standard deviations to be $\sigma^{\text{fiducial}}_{W^\pm W^\pm jj-\text{EW}} = 1.3 \pm 0.4(\text{stat.}) \pm 0.2(\text{syst.})\,\text{fb}$ in a fiducial phase space region selected to enhance the contribution from WW scattering. The measurement is compatible with the Standard Model prediction of $\sigma^{\text{fiducial}}_{W^\pm W^\pm jj-\text{EW}} = 0.95 \pm 0.06\,\text{fb}$. Based on this measurement, limits on anomalous quartic gauge couplings are derived. The effect of anomalous quartic gauge couplings is simulated within the framework of an effective chiral Lagrangian unitarized with the K-matrix method. The limits for the anomalous coupling parameters α_4 and α_5 are found to be $-0.14 < \alpha_4 < 0.16$ and $-0.23 < \alpha_5 < 0.24$ at 95 % confidence level.

Furthermore, the prospects for the measurement of the electroweak production of two same-charge W bosons and two jets within the Standard Model and with additional doubly charged resonances after the upgrade of the ATLAS detector and the LHC are investigated. For a high-luminosity LHC with a center-of-mass energy of $\sqrt{s} = 14\,\text{TeV}$, the significance of the measurement with an integrated luminosity of $3000\,\text{fb}^{-1}$ is estimated to be 18.7 standard deviations. It can be improved by 30 % by extending the inner tracking detector of the ATLAS experiment up to an absolute pseudorapidity of $|\eta| = 4.0$.

Kurzzusammenfassung

Der Prozess der elektroschwachen Eichbosonenstreuung ist eng verbunden mit der elektroschwachen Eichsymmetrie und ihrer spontanen Brechung durch den Brout-Englert-Higgs-Mechanismus. Da die Eichbosonenstreuung sowohl Dreier-Eichboson-Vertizes als auch Vierer-Eichboson-Vertizes enthält, ermöglicht dieser Prozess die Untersuchung der Selbstwechselwirkung der massiven elektroschwachen Eichbosonen. Der ebenfalls in der Streuamplitude enthaltene Austausch von Higgs-Bosonen sorgt für die Einhaltung der Unitarität der Streumatrix des Prozesses der Eichbosonenstreuung. Daher gibt dieser Prozess Aufschluss über mögliche Abweichungen der Natur von der im Standard-Modell beschriebenen elektroschwachen Wechselwirkung und den Eigenschaften des Higgs-Bosons.

Die Streuung schwacher Eichbosonen kann am Large Hadron Collider (LHC) durch die Messung von rein elektroschwacher Produktion von zwei Jets und zwei massiven elektroschwachen Eichbosonen gemessen werden. Ein solcher Prozess ist noch nie beobachtet worden. Da der Untergrund aus QCD-enthaltender Produktion des gleichen Endzustandes im Kanal mit zwei gleich-geladenen W-Bosonen am geringsten ist, ist dies der am besten geeignete Endzustand für die erste Messung eines Prozesses, der die Streuung massiver elektroschwacher Vektorbosonenstreuung enthält. Die vorliegende Arbeit beschreibt die erste Messung der elektroschwachen Produktion von zwei Jets und zwei gleich geladenen W-Bosonen, die zur ersten Beobachtung eines Prozesses führt, zu dem die Viererwechselwirkung massiver elektroschwacher Eichbosonen beiträgt.

Die Arbeit enthält einen Überblick der wichtigsten Aspekte der Monte-Carlo-Simulation von Eichbosonenstreuung. Die Messung wird im Endzustand zweier leptonisch zerfallender, gleich geladener W-Bosonen durchgeführt und basiert auf Protonenkollisionen, die im Jahr 2012 bei einer Schwerpunktsenergie von $\sqrt{s} = 8\,\text{TeV}$ vom ATLAS-Experiment am LHC aufgenommen worden sind. Der Wirkungsquerschnitt für die elektroschwache Produktion von zwei Jets und zwei gleichgeladenen W-Bosonen wird mit einer Signifikanz von 3.6 Standardabweichungen in Höhe von $\sigma^{\text{fiducial}}_{W^\pm W^\pm jj-\text{EW}} = 1.3 \pm 0.4(\text{stat.}) \pm 0.2(\text{syst.})\,\text{fb}$ in einem mit Eichbosonstreuung angereicherten Phasenraumvolumen gemessen. Ausschlussgrenzen auf anomale quartische Eichbosonkopplungen werden im Rahmen einer effektiven elektroschwachen Feldtheorie aus dieser Messung abgeleitet. Der Beitrag der anomalen Kopplungen wird dabei mit der K-Matrix-Methode unitarisiert. Für die beiden anomalen Kopplungsparameter α_4 und α_5 ergeben sich die Ausschlussgrenzen $-0.14 < \alpha_4 < 0.16$ und $-0.23 < \alpha_5 < 0.24$ mit einem Konfidenzniveau von $95\,\%$.

Des weiteren werden in der vorliegenden Arbeit die Aussichten für die Messung von zwei gleich geladenen Eichbosonen und zwei Jets nach dem Standard-Modell sowie mit zusätzlichen, zweifach geladenen Resonanzen nach der Aufrüstung des ATLAS-Detektors und des LHC untersucht. Mit dem Hoch-Luminositäts-LHC mit einer Schwerpunktsenergie von $\sqrt{s} = 14\,\text{TeV}$ wird die Signifikanz der Messung im Fall des Standard-Modell-Prozesses bei einer integrierten Luminosität von $3000\,\text{fb}^{-1}$ auf 18.7 Standardabweichungen steigen. Die Signifikanz kann durch Verlängerung des Spurdetektors von ATLAS bis zu einer Pseudorapidität von $|\eta| = 4.0$ um $30\,\%$ verbessert werden.

Contents

Acknowledgements xi

Notations and conventions xiii

Utilized software xv

Legal Declaration xvii

1 Introduction 1

2 Vector Boson Scattering and the Standard Model 3

2.1 The Standard Model of particle physics . . . 3

2.1.1 Construction of the Standard Model: Symmetries . . . 4

2.1.2 Electroweak theory . . . 4

2.1.3 Electroweak symmetry breaking: The Higgs mechanism . . . 7

2.1.4 Quantum Chromodynamics . . . 8

2.1.5 Particle content of the Standard Model . . . 8

2.1.6 Predictions based on the Standard Model . . . 9

2.1.7 Outlook to physics beyond the Standard Model . . . 10

2.2 Electroweak gauge boson scattering in the Standard Model . . . 12

2.2.1 Definition of vector boson scattering . . . 12

2.2.2 Electroweak gauge boson scattering as scattering of Goldstone Bosons . . . 13

2.2.3 Scattering of electroweak gauge bosons and the Higgs boson . . . 15

2.2.4 Unitarity bound on the Higgs mass . . . 15

2.3 Electroweak gauge boson scattering beyond the Standard Model . . . 17

2.3.1 Parametrizing the unknown: Effective field theories . . . 17

2.3.2 The electroweak chiral Lagrangian . . . 18

2.3.3 Anomalous couplings in the electroweak chiral Lagrangian . . . 19

2.3.4 Resonances in the electroweak chiral Lagrangian . . . 19

2.3.5 Effective field theory with linear symmetry breaking . . . 20

2.3.6 Unitarity . . . 21

2.3.7 Experimental constraints on electroweak quartic gauge interactions 22

3 Monte Carlo generation and electroweak gauge boson scattering 23

3.1 Monte Carlo Simulation 23

3.1.1 Monte Carlo integration method 24

3.1.2 Perturbative QCD and the factorization theorem 25

3.1.3 Matrix-Element integration and event generation 27

3.1.4 Evolution of the final state 27

3.1.5 Commonly used Monte Carlo generators 30

3.1.6 Detector simulation 30

3.1.7 From "Truth" to "Reconstruction": Levels in the full simulation chain 32

3.2 Monte Carlo simulation for electroweak gauge boson scattering 33

3.2.1 Defining purely electroweak vs. QCD-mediated production of two electroweak bosons and two partons 33

3.2.2 Generator settings for VVjj-EW generation 36

3.2.3 Interference between purely electroweak and QCD-mediated di-boson plus di-jet production 39

3.2.4 Various channels of gauge boson flavors 40

3.2.5 Definition of generation phase space for vector boson scattering 41

3.2.6 Higher order corrections in Monte Carlo simulation for vector boson scattering 42

3.2.7 Monte Carlo Generators for vector boson scattering 43

3.3 Scattering of two same-charge W bosons 44

3.3.1 Comparison of $W^{\pm}W^{\pm}jj$-EW and $W^{\pm}W^{\pm}jj$-QCD 44

3.3.2 VBS topology in $W^{\pm}W^{\pm}jj$ 48

3.3.3 Resonant and non-resonant contributions to the final state $\ell^{\pm}\nu\ell^{\pm}\nu jj$ 49

3.3.4 Interference of electroweak and QCD-mediated production 50

3.3.5 Higgs mass dependence 50

3.3.6 Generator validation 51

3.4 Simulating new physics in Vector Boson Scattering 58

3.4.1 Modelling new physics via effective field theories 58

3.4.2 MC generation with effective field theory content 58

4 The ATLAS detector at the LHC 63

4.1 The Large Hadron Collider 63

4.2 The ATLAS Detector at the LHC: Functionality and layout 64

4.2.1 A Toroidal LHC ApparatuS: Overview 64

4.2.2 Inner Detector 65

4.2.3 Calorimeters 69

4.2.4 Muon Spectrometer 73

4.2.5 Forward detectors . . . 77
4.2.6 Magnets in the ATLAS detector . . . 77
4.2.7 Trigger and data acquisition . . . 78
4.2.8 ATLAS data storage and computing . . . 79
4.3 Reconstruction and calibration . . . 80
4.3.1 Jets . . . 80
4.3.2 Electrons . . . 81
4.3.3 Muons . . . 82
4.3.4 Missing transverse energy . . . 82
4.4 Data taking operation and luminosity . . . 83

5 Measurement of $W^{\pm}W^{\pm}jj$ production with the ATLAS detector 85
5.1 Selection of $W^{\pm}W^{\pm}jj$ events . . . 86
5.1.1 Object selection and corrections . . . 86
5.1.2 Baseline selection of events . . . 90
5.1.3 Signal selection . . . 90
5.1.4 Fiducial phase space . . . 93
5.2 Background estimates . . . 95
5.2.1 Background with additional prompt leptons . . . 96
5.2.2 Charge mis-identified background . . . 101
5.2.3 Background with mis-identified leptons . . . 102
5.2.4 Double parton scattering background . . . 105
5.2.5 Background from a W boson in association with a converted photon . . . 105
5.2.6 Expected event yields . . . 106
5.3 Systematic uncertainties . . . 107
5.3.1 Theoretical predictions for diboson processes . . . 107
5.3.2 Theory uncertainties . . . 107
5.3.3 Experimental uncertainties . . . 110
5.4 Measurement of the fiducial cross section . . . 113
5.4.1 Kinematics of the signal . . . 115
5.5 Anomalous quartic gauge couplings in $W^{\pm}W^{\pm}jj$-EW . . . 117
5.5.1 Cross sections and acceptance in the $\alpha_4,\ \alpha_5$-plane . . . 117
5.5.2 Fiducial cross sections of anomalous couplings samples . . . 118
5.5.3 Efficiency in the $\alpha_4,\ \alpha_5$-plane . . . 120
5.5.4 Systematic uncertainties of aQGC samples . . . 120
5.5.5 Measurement of anomalous couplings . . . 124
5.5.6 Interpretation of aQGC in light of new resonances . . . 125

6 Towards higher energy: $W^{\pm}W^{\pm}$ scattering after the LHC and ATLAS upgrades **127**
6.1 $W^{\pm}W^{\pm}$ scattering at a higher energy Large Hadron Collider . . . 127
6.2 The upgraded LHC and ATLAS detector . . . 128
6.2.1 Plans for the LHC . . . 128
6.2.2 Extension of the Inner Detector . . . 129
6.2.3 Performance assumptions for the ATLAS detector at 14 TeV . . . 129
6.3 Analysis of $W^{\pm}W^{\pm}jj$-EW at 14 TeV . . . 130
6.3.1 Generation of signal and background processes . . . 130
6.3.2 Application of the performance assumptions . . . 132
6.3.3 Event selection criteria . . . 134
6.3.4 Statistical analysis of the expected discovery significance . . . 135
6.4 Significance of SM signal measurement with the nominal ATLAS detector . . . 136
6.5 Effect of the extension of the tracking detector on the SM signal measurement . . . 137
6.5.1 Re-optimization of cuts . . . 137
6.5.2 Event yields and cut efficiencies with an extended tracker . . . 138
6.5.3 Effect of the extended tracker on the additional lepton veto . . . 142
6.5.4 Significance as a function of $|\eta|_{\text{tracker}}$ extension . . . 143
6.6 Resonances in $W^{\pm}W^{\pm}jj$-EW: Prospects at 14 TeV . . . 143
6.6.1 Resonance model . . . 143
6.6.2 Selection and kinematics of resonances . . . 143
6.6.3 Nominal tracker vs. extended tracker . . . 145
6.6.4 Luminosity and coupling dependent discovery significance . . . 146
6.7 Outlook . . . 147
6.7.1 Vector boson scattering in other diboson channels . . . 148
6.7.2 VBS at future accelerators . . . 148

7 Summary and conclusions **149**

A Steering files for MC simulation of vector boson scattering processes **155**
A.1 $W^{\pm}W^{\pm}jj$-EW generation input . . . 156
A.2 $W^{\pm}Zjj$-EW generation input . . . 158

B Kinematics in the VBS signal region **161**

C Anomalous quartic gauge couplings in vector boson scattering **165**
C.1 Comparison of anomalous couplings in WZ and $W^{\pm}W^{\pm}$ scattering . . . 165
C.2 Anomalous couplings samples used in $W^{\pm}W^{\pm}jj$-EW . . . 166
C.3 Kinematics of $W^{\pm}W^{\pm}jj$-EW events with anomalous couplings . . . 167

D Monte Carlo samples used for the analysis of $W^{\pm}W^{\pm}jj$ at 8 TeV **171**

E Kinematic distributions of resonances at 14 TeV 175

Bibliography 179

List of Figures 197

List of Tables 201

Acknowledgements

Many people have supported me in the last four years leading up to the completion of this thesis. First, I would like to thank my advisor, Michael Kobel, for the continued trust that the project of measuring vector boson scattering at the LHC was possible, albeit highly doubted by many people in the community. Thank you for your support and encouragement throughout my PhD time.

The same goes for my fellow PhD students in the VBS Dresden group: Philipp Anger, Christian Gumpert, and Felix Socher. We did VBS before it was cool! Thanks for all of the never-ending discussions and helpful technical advice, and the friendship. My thanks includes the rest of the VBS Dresden group and my office mates in Dresden: Carsten Bittrich, Constanze Hasterok, Alexander Melzer, Daniel Reichelt, Franziska Speiser, Peter Steinbach, Stefanie Todt, and Anja Vest. Thank you to Sabine Lammers for bringing in her ideas and experience, and for being the second reviewer of this thesis.

The rest of the Dresden ATLAS group and the occasional exchange with members of the phenomenology group has contributed to create a good working environment. Thank you for that, in particular to Felix Friedrich, Wolfgang Mader, Marco Pruna, Tania Robens, Frank Siegert, and Dominik Stöckinger. It was a pleasure and a great experience to work with the "Netzwerk Teilchenwelt" crew on sharing the knowledge with people outside the physics community. Many thanks also to Tatjana Sereda, Kristin Walter and all of the administrative team.

Financial support by the Graduiertenkolleg "Mass, Spectrum, Symmetry" and the Graduate Academy of the TU Dresden is gratefully acknowledged. I am very happy to have been a part of the Graduiertenkolleg, which has provided many excellent opportunities for acquiring knowledge about the broad field of particle physics and for exchanging ideas with other students.

In a large experiment such as ATLAS, it is never a short list of people who have contributed to one analysis. For good collaboration in the same-sign WW group I would like to thank Simone Pagan Griso, Jianbei Liu, Lulu Liu, Marc-Andre Pleier, Jake Searcy, Alexander Sood, and Junjie Zhu.

Special thanks goes out to my collaborators in the upgrade studies, Jessica Metcalfe and Nika Valencic, as well as Chris Pollard. To them and all other people I have encountered through the Muon Offline Monitoring, DAST team, in the ATLAS control room or other occasions, who have shared insight in the workings of ATLAS, physics or computing, thank you for that.

I am particularly grateful to the Whizards, especially Wolfgang Kilian, Jürgen Reuter, Sebastian Schmidt, and Marco Sekulla, for their replies to experimentalist's questions, bug reports, feature requests, and for the collaborative spirit.

Many people have contributed to the necessary balance on the other side of PhD work. My CERN friends, especially Priscilla, Duc, Jörn, Oscar, and Pieter, have helped making my stay in Geneva such a great experience. Special thanks to the Higgs boson and the LHC for the timely discovery in the eventful year of 2012.

I am grateful to all of "Die Physiker" in Dresden for the friendship since the first semester, and for joining me in the process of becoming a physicist. Although they are now scattered around the world, I would like to thank Sarah, Falk, Andreas, Kathrin, Markus, Uwe, and Stefan. Many other friends from Dresden and Michigan have crossed my path and shared the journey. I cannot list you here, but thanks for being there!

Special thanks goes to Axel, for his support and continuous encouragement, particularly in the phase of writing up. To Luitgard, my twin, contemporaneous thesis writer, and strong friend, I am grateful for all shared and imparted experiences. My greatest thanks goes to my family, Luitgard, Ekkehard, Friedrich, and my parents, for being supportive, always eager to learn about the unbeknown world of elementary particles, and generally never boring.

Notations and conventions

List of abbreviations

ATLAS A Toroidal LHC Apparatus

aTGC Anomalous Triple Gauge Coupling

aQGC Anomalous Quartic Gauge Coupling

BSM Beyond the Standard Model

C.L. Confidence Level

Diboson production used for: Production of two electroweak gauge bosons

Dijet production used for: Production of two jets

EFT Effective Field Theory

EW Electroweak

EWChL Electroweak chiral Lagrangian

EWSB Electroweak Symmetry Breaking

ID Inner Detector

(Electron/Muon) ID Electron/Muon identification

LEP Large Electron-Positron collider

LHC Large Hadron Collider

leading lepton/jet lepton/jet with largest transverse momentum in an event

lepton commonly used for: charged lepton

LO Leading Order

MC Monte Carlo [simulation]

MS Muon Spectrometer

NLO Next-to-Leading Order

PDF Parton Distribution Function

p.d.f. Probability density function

pQCD Perturbative Quantum Chromodynamics

QCD Quantum Chromodynamics

SF Scale factor

SM Standard Model

subleading lepton/jet lepton/jet with the second largest transverse momentum in an event

V Boson W or Z boson

VBS Vector Boson Scattering

$W^{\pm}W^{\pm}jj$-EW Electroweak production of $W^{\pm}W^{\pm}jj$; cf. Section 3.2.1

$W^{\pm}W^{\pm}jj$-QCD QCD-mediated production of $W^{\pm}W^{\pm}jj$; cf. Section 3.2.1

Conventions

Unit system Throughout this thesis, natural units are used with the speed of light and the reduced Planck constant set to $c = \hbar = 1$. In this system, masses and momenta obtain units of energy usually given in MeV, GeV, or other multiples of eV.

Notation for particles Terms for particles are commonly used also for anti-particles, especially in the experimental context. "Quarks" also denotes anti-quarks, "electrons" also denotes positrons, "neutrinos" also denotes anti-neutrinos, etc. The term "lepton" is used meaning charged leptons only. Jets and partons are usually abbreviated with j.

Angular distance measures Measures of angular distances of two objects i, k in the detector coordinate system are defined as follows: The distance in the pseudorapidity-azimuth plane is defined in Section 4.2.1 as $\Delta R(i,k) = \sqrt{\Delta\phi(i,k)^2 + \Delta\eta(i,k)^2}$. For the azimuthal angle ϕ, the distance is defined as $\Delta\phi = \phi(i) - \phi(k)$ within the interval $[-\pi, \pi]$. The pseudorapidity distance is the difference in pseudorapidity $\Delta\eta(i,k) = \eta(i) - \eta(k)$.

Utilized software

A range of open source software has been employed in the scope of this work. Monte Carlo tools used for the simulation of physical processes are listed in Section 3.2.7. Software frameworks utilized for data analysis include ROOT [1], RIVET [2], and SFRAME [3]. In addition, GNUPLOT [4] has been used for data presentation, LaTeX [5] for typesetting, and EMACS [6] for general purpose editorial tasks.

Legal Declaration

Hiermit versichere ich, dass ich die vorliegende Arbeit ohne unzulässige Hilfe Dritter und ohne Benutzung anderer als der angegebenen Hilfsmittel angefertigt habe; die aus fremden Quellen direkt oder indirekt übernommenen Gedanken sind als solche kenntlich gemacht. Die Arbeit wurde bisher weder im Inland noch im Ausland in gleicher oder ähnlicher Form einer anderen Prüfungsbehörde vorgelegt.

Diese Arbeit wurde am Institut für Kern- und Teilchenphysik der Technischen Universität Dresden unter wissenschaftlicher Betreuung von Prof. Dr. Michael Kobel angefertigt.

Es haben keine früheren erfolglosen Promotionsverfahren stattgefunden.

Ich erkenne die Promotionsordnung der Fakultät Mathematik und Naturwissenschaften an der Technischen Universität Dresden vom 23.02.2011 mit den vom Fakultätsrat am 15.06.2011 und 18.06.2014 beschlossenen Änderungen an.

Dresden, den 27.11.2014

Ulrike Schnoor

CHAPTER 1

Introduction

One of the most prominent tasks of the experiments at the Large Hadron Collider (LHC) is the study of the mechanism of electroweak symmetry breaking. While this field of research has been pursued since the 1960s, the discovery of a bosonic resonance compatible with the Higgs boson of the Standard Model in 2012 [7, 8] has stimulated the investigation of the exact nature of the symmetry breaking. A crucial process giving access to the mechanism of electroweak symmetry breaking is the scattering of two weak gauge bosons, measured in the purely electroweak production of two weak gauge bosons and two jets.

The process of electroweak gauge boson scattering is tied to two hardly explored aspects of the Standard Model, i.e. our current understanding of the interactions of elementary particles: The self-couplings of electroweak bosons described by the gauge theory of the electroweak interaction as well as the symmetry breaking of the electroweak gauge symmetry established through the Brout-Englert-Higgs mechanism [9, 10].

The electroweak gauge theory of the Standard Model [11] describes the electroweak gauge bosons as vector fields introduced to conserve local gauge invariance. The electroweak gauge bosons self-interact via triple and quartic gauge boson vertices. While triple gauge couplings [12–14] as well as quartic gauge couplings involving photons [15, 16] have been studied already at LEP, the quartic coupling of four massive electroweak gauge bosons is unconstrained by data from colliders prior to the LHC. The cross section of electroweak gauge boson scattering contains contributions from both triple and quartic gauge boson interactions. Therefore, the observation of weak gauge boson scattering is the first opportunity to gain information on quartic gauge couplings of massive weak bosons and to compare to the Standard Model prediction.

Furthermore, the scattering of two weak bosons is closely linked to the mechanism of electroweak symmetry breaking. In the Standard Model, the electroweak symmetry is spontaneously broken by introducing a scalar field generating four degrees of freedom of which one is the Higgs boson and the other three constitute the longitudinal modes of the weak bosons W^+, W^-, and Z^0. Hence, the scattering of massive electroweak bosons directly probes the symmetry breaking sector. The Higgs boson

itself also plays a role in the scattering of weak bosons: Its contribution leads to a regularization of the scattering amplitude which, without the Higgs boson, would violate unitarity at LHC energies [17, 18]. Consequently, properties of the Higgs boson deviating from the Standard Model can be visible in vector boson scattering as well.

Hence, the scattering of electroweak gauge bosons addresses some of the unresolved aspects of the current understanding of elementary particles and their interactions as described by the Standard Model. New physics that would be directly detectable only at higher energy than accessible by the LHC can be visible indirectly through its low-energy effects. Modeling these effects with an effective field theory allows to probe anomalous quartic gauge couplings in the process of electroweak gauge boson scattering.

The first observation of a vector boson scattering process via the measurement of the electroweak production of two same-charge W bosons and two jets is described in this thesis. Since the scattering of electroweak bosons is not separable in a gauge invariant manner from other ways of producing two gauge bosons and two jets via electroweak vertices, the measurable process is the purely electroweak production of two gauge bosons and two jets. Other combinations of di-bosons have been previously investigated as potential candidates for a measurement at the LHC [19, 20], but the scattering of two same-charge W bosons has the advantage of a suppressed background from QCD-mediated production of two same-charge W bosons and two jets. The measurement of electroweak production of two same-charge W bosons and two jets is conducted based on proton-proton collision data with a center-of-mass energy of $\sqrt{s} = 8$ TeV taken in 2012 with the ATLAS detector. In addition to the extraction of the cross section, limits on anomalous quartic gauge couplings are derived from the measurement.

As the LHC is entering the next run of data taking at an increased center-of-mass energy of $\sqrt{s} = 13$ to 14 TeV and will continue to take data in the next decade and beyond, this thesis explores the possibility to measure electroweak gauge boson scattering and possible new resonances in the final state of two same-charge W bosons and two jets with an upgraded ATLAS detector at an upgraded LHC.

This work outlines the preparation and implementation of the first measurement of a process containing vector boson scattering. The theoretical basis of the Standard Model and the process of vector boson scattering within the Standard Model and beyond are introduced in Chapter 2. Chapter 3 describes the simulation of physics processes containing the scattering of two weak gauge bosons by means of Monte Carlo simulation. Generator settings for the production of two electroweak gauge bosons and two jets are validated and applied to the case of anomalous quartic gauge couplings in the final state of two same-charge W bosons and two jets. The layout and operation of the ATLAS detector as the experimental setting used for the measurement are summarized in Chapter 4. Chapter 5 presents the first observation of electroweak production of two same-charge W bosons and two jets, as well as limits on anomalous quartic gauge couplings derived from this measurement. The prospects for observation of this process assuming the Standard Model or scenarios with additional resonances are investigated in Chapter 6.

CHAPTER 2

Vector Boson Scattering and the Standard Model

To prepare the necessary theoretical tools for studying vector boson scattering, this chapter introduces the Standard Model of particle physics (Section 2.1). Its construction principles, based on symmetry groups and a Lagrangian density, as well as its empirically determined particle content are described.

In the second part of this chapter (Section 2.2), the scattering of electroweak gauge bosons is explained within the framework of the Standard Model. Additionally, the possibilities for new physics processes influencing electroweak gauge boson interactions are explored in Section 2.3 following the formulation of an effective field theory of physics beyond the Standard Model in the electroweak sector.

2.1 The Standard Model of particle physics

The Standard Model of Particle Physics (SM) is a quantum field theory (QFT) describing the interactions of the smallest building blocks of the universe that are accessible to current particle physics experiments. As a QFT it describes systems in the relativistic and the microscopic limit. Particles are introduced as quantized fields acting according to a Lagrangian density formulation. The Lagrangians governing the interactions of the fields are required to obey a set of local gauge symmetries.

The development of QFT started in the late 1920s with the formulation of Dirac's equation and continued with the foundation of the ingredients of the SM: Quantum Electrodynamics, electroweak theory and electroweak symmetry breaking, and Quantum Chromodynamics. Today, the Standard Model is largely accepted as it provides precise predictions for data at the current and precursory high-energy experiments, such as the LHC, Tevatron, and LEP.

The discovery of a boson consistent with the SM Higgs boson at the LHC Run-1 [7, 8] has provided some insight into the nature of the electroweak symmetry breaking mechanism. The origin and properties of this mechanism remain to be thoroughly studied in the next years and at future colliders. Even though most of the current data is well described by the SM, there are a few limitations of this

theory. These are briefly discussed in Section 2.1.7.

The presentation of the physics of the SM in this chapter is by no means complete and can only touch the most important concepts. In-depth coverage of SM physics can be found for instance in [21–23].

2.1.1 Construction of the Standard Model: Symmetries

The construction of the SM Lagrangian is based on a set of symmetries postulated from first principle. Like any QFT, the SM Lagrangian obeys a set of global symmetries: translation in time and space, rotation, and inertial frame invariance, which are connected by Noether's theorem [24] to the conservation of energy, momentum, and angular momentum. In addition, the SM Lagrangian is a non-Abelian gauge theory with the $\mathrm{SU}(3)_C \otimes \mathrm{SU}(2)_L \otimes \mathrm{U}(1)_Y$ symmetry group. Invariance with respect to this group leads to conservation of color charge, weak isospin, and weak hypercharge.

Furthermore, the SM Lagrangian is required to be renormalizable. This means that infinities arising through loops in the perturbative expansion can be treated by reparametrization of physical properties in a way that leads to finite observables. The regularization introduces an arbitrary energy scale, the *renormalization scale*.

The most general renormalizable Lagrangian obeying above-mentioned symmetries is the SM Lagrangian. It consists of the following components:

$$\mathcal{L}_{\mathrm{SM}} = \mathcal{L}_{\mathrm{EW}} + \mathcal{L}_{\mathrm{QCD}} + \mathcal{L}_{\mathrm{Higgs}} + \mathcal{L}_{\mathrm{Yukawa}}, \tag{2.1}$$

i.e. terms for the unified electroweak interaction, Quantum Chromodynamics (QCD), and electroweak symmetry breaking with the Higgs potential as well as the coupling of the fermions to the Higgs field via Yukawa coupling. In the following, these Langrangian terms are discussed, along with their associated fields, symmetries and the conserved properties.

2.1.2 Electroweak theory

The electroweak theory comprises the description of electromagnetic and weak interactions, combined in one gauge theory.

Quantum Electrodynamics

Electromagnetic interactions are described by the QFT of Quantum Electrodynamics (QED), which has been completed by Feynman and Schwinger by the year 1949 [25–28]. QED is based on the Lagrangian

$$\mathcal{L}_{\mathrm{QED}} = \bar{\psi}\left(i\gamma^{\mu}\partial_{\mu} - m\right)\psi + e\bar{\psi}\gamma^{\mu}QA_{\mu}\psi - \frac{1}{4}F_{\mu\nu}F^{\mu\nu} \tag{2.2}$$

with the field strength tensor

$$F_{\mu\nu} = \partial_{\mu}A_{\nu} - \partial_{\mu}A_{\nu} \tag{2.3}$$

describing the interactions of the Dirac fields ψ and their adjoint fields $\bar{\psi} \equiv \psi^\dagger\gamma^0$ associated with particles with mass m and electric charge Q. Furthermore, a gauge field A_μ is introduced which corresponds to the electromagnetic gauge boson, the photon. The QED Lagrangian is constructed from the Dirac equation by introducing the massless gauge field A_μ to ensure local gauge invariance under $U(1)_Q$ transformation. γ^μ are the Dirac matrices and e is the electromagnetic coupling constant, defined as $e = \sqrt{4\pi\alpha}$ based on the fine-structure constant α. Einstein's sum rule of implicitly summing over upper and lower indices is used throughout this chapter.

Weak theory

The weak interaction, also denoted as Quantum Flavor Dynamics (QFD), is based on the Fermi theory [29]. The underlying gauge symmetry is that of the $SU(2)_I$ symmetry group whose associated charge is the weak isospin I. Left- and right-handed spinors are separated by applying the projection operators $P_L = \frac{1}{2}(1-\gamma_5)$ and $P_R = \frac{1}{2}(1+\gamma_5)$ on the fermion fields: $\psi_L = P_L\psi$ and $\psi_R = P_R\psi$. Due to maximal parity violation , the weak interaction couples only to left-handed fermions. According to the present-day version of the Fermi theory, the Lagrangian of weak interactions can be written as [30]

$$\mathcal{L}_w = \frac{G_F}{2} J_\mu(x) J^\mu(x) \tag{2.4}$$

with the Fermi constant G_F and a current $J_\mu(x) = J_\mu^{(l)}(x) + J_\mu^{(h)}(x)$ comprising of the sum of the leptonic current

$$J_\mu^{(l)} = 2\bar{e}_L(x)\gamma_\mu\nu_{e,L}(x) + 2\bar{\mu}_L(x)\gamma_\mu\nu_{\mu,L}(x) + 2\bar{\tau}_L(x)\gamma_\mu\nu_{\tau,L}(x)$$

and the hadronic current

$$J_\mu^{(h)} = 2\bar{u}_L(x)\gamma_\mu d_L(x) + 2\bar{c}_L(x)\gamma_\mu s_L(x) + 2\bar{t}_L(x)\gamma_\mu b_L(x).$$

While describing well the low-energy weak interactions, this theory is non-renormalizable and features a divergent high-energy behavior.[1] Introducing intermediate gauge bosons cures the high-energy behavior of the theory. However, it stays non-renormalizable due to the non-vanishing masses of the W^-, W^+, and Z^0 bosons. This issue is solved by the mixing of QED and weak theory to the electroweak theory.

Electroweak theory

The electroweak theory was developed by Glashow, Salam, and Weinberg from 1961 to 1969 [11, 31, 32]. In this theory, the electromagnetic and weak interactions are combined by embedding the symmetry groups $SU(2)_I$ and $U(1)_Q$ into the new group $SU(2)_L \otimes U(1)_Y$ according to the newly introduced weak hypercharge $Y = 2(Q - I_3)$. The currents of the weak interaction couple only to left-handed

[1] It can be understood as an effective theory, cf. Section 2.3.

fermions (hence the subscript L), which are grouped into $SU(2)$ doublets with the third component of the weak isospin $I_3 = \pm\frac{1}{2}$. Right-handed fermions form $SU(2)$ singlets with the third component of weak isospin $I_3 = 0$. The electroweak Lagrangian takes the form

$$\mathcal{L}_{EW} = \sum_{f_l, f_R} \bar{\psi}_f i\gamma^\mu D_\mu \psi_f - \frac{1}{4} B_{\mu\nu} B^{\mu\nu} - \frac{1}{4} W_{\mu\nu} W^{\mu\nu} \tag{2.5}$$

with the covariant derivative

$$D_\mu = \partial_\mu + i g_Y \frac{1}{2} \hat{Y} B_\mu + i g_w \frac{1}{2} \tau_a W_{a\mu} \tag{2.6}$$

where $\hat{Y}$ is the weak hypercharge operator, τ_a are the three generators of the $SU(2)_L$ group, and $B_{\mu\nu}$ and $W_{\mu\nu}$ are the field strength tensors based on the gauge fields of the $U(1)_Y$ group B_μ and the gauge fields $W_{i\mu}$ ($i = 1, 2, 3$) of the $SU(2)_L$ symmetry group. This form of the covariant derivative ensures invariance under local gauge transformations of the $SU(2)_L \otimes U(1)_Y$ group. The coupling constants are related according to

$$g_Y \cos\theta_w = g_w \sin\theta_w = e \tag{2.7}$$

with the weak mixing angle θ_w and the electromagnetic coupling constant e. The gauge bosons $W_{1\mu}$ and $W_{2\mu}$ are combined linearly to the mass eigenstates

$$W_\mu^\pm = \frac{1}{\sqrt{2}} \left(W_{1\mu} \mp i W_{2\mu} \right) \tag{2.8}$$

while B_μ and $W_{3\mu}$ mix according to the weak mixing angle as

$$A_\mu = B_\mu \cos\theta_w + W_{3\mu} \sin\theta_w \tag{2.9}$$

$$Z_\mu = -B_\mu \sin\theta_w + W_{3\mu} \cos\theta_w. \tag{2.10}$$

Here, A_μ is the photon field, describing the massless photon particle, and Z_μ is the Z boson field, describing the massive Z boson. The mass eigenstates of the fermions, for instance the electron $e = e_L + e_R$, do not respect the $SU(2)_L \otimes U(1)_Y$ symmetry as terms of the form $m\bar{\psi}\psi$ are not $SU(2)_L$ invariant. The symmetry breaking is introduced as a spontaneous symmetry breaking via the Higgs mechanism, which retains renormalizability of the theory as well as gauge invariance.

2.1.3 Electroweak symmetry breaking: The Higgs mechanism

The breaking of the $SU(2)_L \otimes U(1)_Y$ symmetry is realized by the Higgs mechanism as proposed by Brout, Englert, and Higgs in the 1960s [9, 10].[2] A complex $SU(2)_L$ doublet Φ with non-vanishing vaccuum expectation value $v = <0|\Phi|0>$ is introduced as

$$\Phi = \begin{pmatrix} \phi^+ \\ \phi^0 \end{pmatrix} = \begin{pmatrix} (\phi_1 + i\phi_2)/\sqrt{2} \\ \phi_3 + i\phi_4)/\sqrt{2} \end{pmatrix} \tag{2.11}$$

by adding the Lagrangian [21, sec. 15.2]

$$\mathcal{L}_{\text{Higgs}} = (D_\mu \Phi)^\dagger (D^\mu \Phi) - V(\Phi) \tag{2.12}$$

with the covariant derivative from (2.6) to the electroweak Lagrangian (2.5). The Lagrangian $\mathcal{L}_{\text{Higgs}}$ comprises the kinetic term of the Higgs field, governing its interactions with the electroweak gauge bosons, as well as the Higgs potential. The kinetic term gives rise to the masses of W and Z bosons according to $m_W = \frac{1}{2} v g_w$ and $\frac{m_Z}{m_W} = \cos\theta_w$. The potential is of the form [21, sec. 14.9]

$$V(\Phi) = -\mu^2 \Phi^\dagger \Phi + \lambda (\Phi^\dagger \Phi)^2 \text{ with } \mu^2, \lambda > 0. \tag{2.13}$$

As the minimum of the potential is identified with the vacuum expectation value, it follows $\mu^2 = \lambda v^2$. The remaining parameters v and λ need to be determined from experiment. The local gauge symmetry is broken spontaneously by assigning the ground state

$$\Phi_0 = \frac{1}{\sqrt{2}} \begin{pmatrix} 0 \\ v \end{pmatrix}. \tag{2.14}$$

This breaks the $SU(2)_L \otimes U(1)_Y$ symmetry into $U(1)_Q$. Of the four degrees of freedom of the gauge field (2.11), three are absorbed by the $W^\pm$ and Z bosons. The fourth generates the Higgs boson with mass $m_H = \sqrt{2\lambda} v$.

The masses of fermions are generated through the interactions with the Higgs field by introducing a Lagrangian term of the form [21, sec. 15.4]

$$\mathcal{L}_{\text{Yukawa}} = -G_1 \bar{L} \Phi R + G_2 \bar{L} \Phi_c R + \text{ hermitian conjugate} \tag{2.15}$$

where the doublet $\Phi_c = -i\tau_2 \Phi^*$ is introduced in order to account for masses of up-type quarks, L denotes the doublets of left-handed fermions, and R the singlets of right-handed fermions. G_1 and G_2 contain the Yukawa couplings g_f of the fermions to the Higgs field according to the fermion masses, as $m_f = \frac{1}{\sqrt{2}} g_f v$.

[2] At least four additional physicists, Anderson, Hagen, Kibble, and Guralnik, are equally associated with the proposal of this theory. However, it is common to refer to the particle only by the name of Higgs, since he was the first to describe the existence of an excitation of the field.

The described mechanism is the minimal model of electroweak symmetry breaking through the Higgs mechanism, and explains the introduction of masses of the gauge bosons and fermions.

2.1.4 Quantum Chromodynamics

The strong interactions of quarks are described by the theory Quantum Chromodynamics (QCD) developed in the 1970s [33, 34]. It is a non-Abelian gauge symmetry with the symmetry group $SU(3)_c$ associated with the strong color charge. The QCD Lagrangian is of the form

$$\mathcal{L}_{\mathrm{QCD}} = \sum_f i\bar{q}_f \gamma^\mu D_\mu q_f - \frac{1}{4} G^i_{\mu\nu} G^{i\ \mu\nu} \tag{2.16}$$

where the covariant derivative is

$$D_\mu = \partial_\mu + \frac{i}{2} g_s \lambda_i G^i_\mu, \tag{2.17}$$

containing the quark fields q_f in triplets of the color charge, the strong coupling constant $g_s = \sqrt{4\pi\alpha_s}$, the eight generators λ_i of the $SU(3)_c$ group, and the field strength tensors $G_{\mu\nu}$ associated with the eight boson fields $G_{a\mu}$. The gauge bosons of the strong interaction are the massless gluons which carry color and anti-color.

Important features of QCD are asymptotic freedom and confinement. Their influence on perturbative QCD and dynamics of partons in high-energy interactions are discussed in Section 3.1.2.

2.1.5 Particle content of the Standard Model

A summary of the empirically determined particle content of the SM is given in the following tables:

	1st generation		2nd generation		3rd generation	
	e^-	ν_e	μ^-	ν_μ	τ^-	ν_τ
el. charge Q	-1	0	-1	0	-1	0
3rd component of weak isospin I_3						
– left-handed ($SU(2)$ doublets)	$-1/2$	$+1/2$	$-1/2$	$+1/2$	$-1/2$	$+1/2$
– right-handed ($SU(2)$ singlets)	0	–	0	–	0	–
color charge	–	–	–	–	–	–

Table 2.1: Overview of leptons of the SM and corresponding values of the charges. For each of these leptons, an anti-lepton with conjugated charge and parity and the same mass exists.

	1st generation		2nd generation		3rd generation	
	u	d	c	s	t	b
electric charge Q	$+2/3$	$-1/3$	$+2/3$	$-1/3$	$+2/3$	$-1/3$
3rd component of weak isospin I_3						
– left-handed ($SU(2)$ doublets)	$+1/2$	$-1/2$	$+1/2$	$-1/2$	$+1/2$	$-1/2$
– right-handed ($SU(2)$ singlets)	0	0	0	0	0	0
color charge	r,g,b	r,g,b	r,g,b	r,g,b	r,g,b	r,g,b

Table 2.2: Overview of quarks of the SM and corresponding values of the charges. For each quark, an anti-quark with conjugated charge and parity and the same mass exists.

	electroweak: SU(2)$_L$⊗U(1)$_Y$			strong: SU(3)$_C$
	γ	$W^\pm$	Z^0	g
electric charge Q	0	±1	0	0
3rd component of weak isospin I_3	0	±1	0	0
color charge	-	-	-	8 color-anticolor combinations

Table 2.3: Gauge bosons of the SM ordered by the corresponding gauge group.

2.1.6 Predictions based on the Standard Model

Scattering theory and Feynman calculus

The SM is a successful theory which allows to predict interactions between elementary particles. In order to probe its predictions, experimentally observable decays or scattering processes should be compared to their cross sections, calculated based on the SM. The calculation of a cross section is based on the matrix-element or amplitude $\mathcal{M}$ for the process and the phase space in which it proceeds.

To calculate the amplitude, each contributing diagram is evaluated according to the perturbative approach of so-called Feynman rules, which can be obtained from the terms of the given Lagrangian. They contain prescriptions for the calculation of propagators of the fields and their interaction vertices. Then, the integral of the sum of all diagrams is evaluated over the desired phase space PS. This gives an entity proportional to the cross section as

$$\sigma \sim \int_{PS} |\mathcal{M}|^2 \mathrm{d}\Phi. \tag{2.18}$$

The proportionality factor is taken from scattering theory and can be found in many textbooks [22, 23]. It is useful to express the amplitude as a function of Lorentz invariant variables. For a $2 \to 2$

process, amplitudes are often expressed in terms of the Mandelstam variables, defined for a process $AB \to CD$ with four-momenta p_i ($i = A, B, C, D$) as

$$s = (p_A + p_B)^2 \tag{2.19}$$

$$t = (p_A - p_C)^2 \tag{2.20}$$

$$u = (p_A - p_D)^2. \tag{2.21}$$

2.1.7 Outlook to physics beyond the Standard Model

Despite its success in describing physics in the currently experimentally accessible energy range, there are limitations to the SM that motivate ideas for new physics. The following issues [35], [22, ch. 12] are still unsolved and might be answered at the LHC or other experiments:

- Dark matter is postulated to exist in order to explain galactic rotation velocities and other discrepancies between gravitational mass and visible mass, found in large-scale gravitational effects. Candidate particles for dark matter are assumed to be heavy, weakly interacting, neutral and stable particles. Theories providing such a particle include supersymmetry (SUSY) [36] as well as the Peccei-Quinn mechanism [37]. However, no candidate for a dark matter particle has yet been confirmed.

- No renormalizable QFT for gravity exists. It is therefore unclear if a theory of gravitation can be incorporated into the framework of an extended SM.

- A set of issues are raised by the fact that large energy scale differences exist in the SM, resulting in the need of fine-tuned cancellations of loop contributions. This is known as the hierarchy problem. Proposed solutions to the hierarchy problem include technicolor [38, 39] and extra dimensions [40].

- From the abundance of matter over anti-matter it is concluded that the CP symmetry is violated. However, the observed CP violation from the weak interaction is not sufficient to yield the degree of violation necessary to explain the asymmetry between matter and anti-matter.

- A first insight to the nature of the mechanism of electroweak symmetry breaking has been achieved by the discovery of a Higgs-like boson at the LHC. However, more investigation is necessary to measure its properties and to clarify whether electroweak symmetry breaking is realized in the minimal SM way, or differently. Other ansaetze include strong electroweak symmetry breaking where the Higgs is a bound state of a strongly coupled gauge theory, as well as the “Little Higgs” model in which the Higgs boson is the Goldstone boson of a higher, broken symmetry [41].

- The pursuit of a Grand Unified Theory (GUT), consisting of a larger symmetry group containing the SM, is based on the idea that all forces of the SM are embedded in one original force. SUSY

models provide such a unification of the weak, strong, and electromagnetic interactions at large energy. Many searches for SUSY are on-going at the LHC [42].

2.2 Electroweak gauge boson scattering in the Standard Model

The scattering of two electroweak gauge bosons directly probes the nature of the electroweak symmetry breaking mechanism. It is therefore one of the key processes of the LHC's physics program. With the discovery of a Higgs-like boson at the ATLAS and CMS detectors in 2012 [7, 8], a new era of investigation of the EWSB mechanism has begun. This chapter will set the basis for the description of electroweak gauge boson scattering in the SM.

The terms **electroweak gauge boson scattering** and **vector boson scattering** are used synonymously throughout this thesis as in the literature [43, 44], and are abbreviated by the acronym **VBS** or by the short form VV scattering, where $V = W, Z, \gamma$. The term "vector bosons" includes also gluons and a range of non-fundamental mesons with non-zero integer spin. It is used exclusively for fundamental electroweak vector bosons, i.e. W, Z and photons in this work. While the scattering of massive vector bosons (W, Z) is the only one sensitive to the mechanism of EWSB because of the generation of their longitudinal modes through the Higgs mechanism, in many cases scattering processes involving photons are also counted toward VBS. This is in part due to the inability to fully separate Z and γ contributions experimentally. Furthermore, scattering processes involving photons are not sensitive to new physics in the EWSB sector, and as such provide a good control of the SM dynamics of quartic gauge interactions.

The observation that unitarity is violated in $V_L V_L \to V_L V_L$ processes with a heavy Higgs boson has been published as early as 1973 by Dicus and Mathur [45]. The term Vector Boson Scattering for such processes has been used at least since Veltman in 1979 [46]. Scattering of electroweak gauge bosons has been a process of interest for hadron collider physics since the first proposal by Chanowitz and Gaillard [47] to use the measurement of this process to distinguish between strong EWSB and a light Higgs sector. Like-charge $W^{\pm}W^{\pm}$ scattering in particular has been studied early on by Chanowitz and Golden, who concluded that its signal is "unlikely to be observable [at a 15-TeV-LHC]" [48]. Further studies by Barger, Han, and others have investigated experimental prospects by studying kinematic properties of $VVjj$ signals at then prospective colliders like the LHC [49, 50]. The study of vector boson fusion to Higgs processes with the Higgs decaying to vector bosons provided complimentary insight into the properties of VBS, leading to the development of jet tagging for VBS and VBF processes [51, 52]. In this context, the signal was often produced with an effective W approximation [53, 54]. Early MC based studies of prospects for the measurement of WW scattering at the LHC were performed [19, 20, 55] to prepare experimental efforts for this measurement. Experimentally, a signal dominated by VBS has not been observed before the measurement of $W^{\pm}W^{\pm}jj$-EW presented in this thesis and published by the ATLAS collaboration [56].

2.2.1 Definition of vector boson scattering

As described in Chapter 2.1.3, the Higgs mechanism of spontaneous symmetry breaking of the local gauge invariance with respect to the symmetry group $SU(2) \otimes U(1)$ produces three Goldstone modes

and a Higgs boson which can be observed through its decay products. The three Goldstone modes correspond to the longitudinal, massive modes of the weak gauge bosons. In the scattering of two vector bosons, the interaction of their longitudinal degrees of freedom therefore corresponds to the interaction of these Goldstone modes. Complementary to the direct measurement of the properties of the Higgs boson, this channel provides information on the properties of the other three degrees of freedom of the Higgs field. Thus, studying the gauge interactions of the weak bosons is essential for the understanding of EWSB within or beyond the SM. Triple gauge interactions can be probed experimentally in the production of two electroweak gauge bosons [57] and in vector boson fusion (VBF) to W or Z bosons [58]. The quartic gauge interaction is accessible through VV scattering or production of three electroweak bosons.

Vector boson scattering in the SM is defined according to the Feynman diagrams shown in Figures 2.1, 2.2a, and 2.2b.

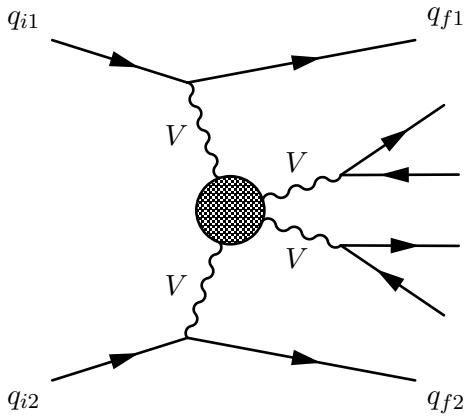

Figure 2.1: Feynman diagram of electroweak vector boson scattering. The grey circle stands for any connected diagram with the given external lines at leading order, i.e. the diagrams shown in Figures 2.2a and 2.2b.

The scattering process is described with Feynman diagrams containing

- quartic gauge boson vertex
- triple gauge boson vertices in the s, t, and u channels
- and Higgs exchange.

Depending on the charge of the initial and final state vector bosons, not all of these diagrams are allowed in all channels. In the case of $W^{\pm}W^{\pm}$ scattering, no s-channel gauge boson or Higgs exchange is allowed.

2.2.2 Electroweak gauge boson scattering as scattering of Goldstone Bosons

The scattering of vector bosons in their longitudinal polarization state can be calculated employing the Goldstone Boson Equivalence theorem (GBET) [18, 23]. It is based on the fact that in the high-energy limit, the dynamics of longitudinally polarized electroweak gauge bosons are governed by

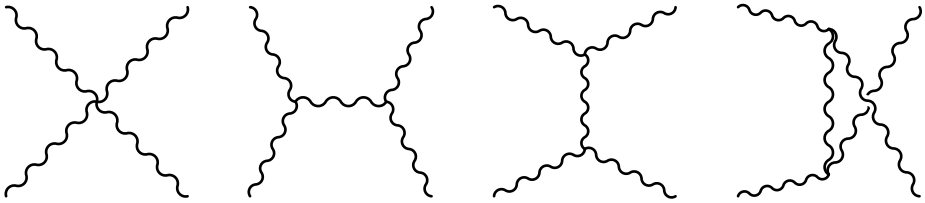

(a) Contributions from electroweak gauge boson interactions.

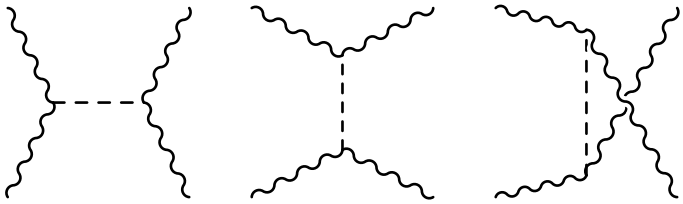

(b) Higgs exchange contributions.

Figure 2.2: $VV \to VV$ diagrams included in vector boson scattering at tree-level. Dashes indicate Higgs propagation.

the Goldstone boson originating from the Higgs mechanism. This allows to associate the amplitude of scattering of the massive electroweak vector bosons' longitudinal modes V_L to the scattering amplitude of the would-be Goldstone scalars [59]

$$\mathcal{M}(W_L W_L \to W_L W_L) = \mathcal{M}(ww \to ww) \tag{2.22}$$

$$\mathcal{M}(W_L Z_L \to W_L Z_L) = \mathcal{M}(wz \to wz) \tag{2.23}$$

$$\mathcal{M}(W_L W_L \to Z_L Z_L) = \mathcal{M}(ww \to zz) \tag{2.24}$$

$$\mathcal{M}(Z_L Z_L \to Z_L Z_L) = \mathcal{M}(zz \to zz) \tag{2.25}$$

if the external W bosons are treated as real longitudinally polarized gauge bosons.
As the polarization vector

$$\epsilon_L^\mu = \frac{1}{m_V}\left(|\vec{p}|, \frac{\vec{p}}{|\vec{p}|}E\right) = \frac{p^\mu}{m_V} + \mathcal{O}(\frac{m_V}{E}) \tag{2.26}$$

grows with momentum p, longitudinally polarized gauge bosons yield the dominant contribution to the $VV \to VV$ cross section at high energy [60].

Using the GBET to calculate the amplitude for $W_L^+ W_L^+ \to W_L^+ W_L^+$, the relevant diagrams of Figures 2.2a and 2.2b with Goldstone bosons as the external lines yield the amplitude [50]

$$\mathcal{M}(w^+ w^+ \to w^+ w^+) = -\frac{g_w^2 m_H^2}{4m_W^2}\left[\frac{t}{t - m_H^2} + \frac{u}{u - m_H^2}\right]. \tag{2.27}$$

Here, $s, |t|, |u|, m_H^2 \gg m_W^2$ such that γ, Z exchange are neglected. This has been shown to be equiv-

alent to the exact calculation with external W bosons instead of Goldstone bosons in the limit of $s \gg m_W^2, m_H^2$ [50].

2.2.3 Scattering of electroweak gauge bosons and the Higgs boson

The amplitude of WW scattering shall be inspected further. Using unitary gauge, which means setting the Goldstone bosons to zero, in the high energy limit the amplitude for the scattering of two longitudinally polarized gauge bosons $W^\pm W^\mp \to W^\pm W^\mp$ without Higgs contributions (Figure 2.2a) takes the form [59, 60]

$$\mathcal{M}^{gauge} = -\frac{g_w^2}{4m_W^2}u + \mathcal{O}\left(\left[\frac{E}{m_W}\right]^0\right). \tag{2.28}$$

This E^2 behavior remains after cancellation of $\sim E^4$ terms between the quartic and triple gauge interaction diagrams in Figure 2.2a [50]. The remaining amplitude rises with energy and therefore violates unitarity at the unitarity bound. The amplitude of the Higgs exchange contributions (Figure 2.2b) is given by

$$\mathcal{M}^{\text{Higgs}} = -\frac{g_w^2}{4m_W^2}\left[\frac{(s-m_W^2)^2}{s-m_H^2} + \frac{(t-m_W^2)^2}{t-m_H^2}\right]. \tag{2.29}$$

In the high-energy limit, where $s, t, u \gg m_W^2, m_H^2$, this reduces to:

$$\mathcal{M}^{\text{Higgs}} = \frac{g_w^2}{4m_W^2}u. \tag{2.30}$$

Thus, the terms rising with energy cancel and leave a constant term which is not violating unitarity. This only holds if the Higgs boson behaves as described in the SM with SM Higgs couplings to the gauge bosons and if $\rho \equiv \frac{m_W^2}{m_Z^2\cos^2(\theta_w)} = 1$ is valid for the ρ parameter [60]. Without the SM-Higgs boson, unitarity of the S-matrix would be violated in all VBS channels through the high-energy behavior of the scattering of longitudinally polarized vector bosons. This is illustrated by Figure 2.3.

2.2.4 Unitarity bound on the Higgs mass

From the considerations on the violation of unitarity in the absence of a light Higgs boson follows a limit on the Higgs boson mass. If the mass of the Higgs boson is not $m_H \ll \sqrt{s}$, Equation (2.30) is not valid and the divergent terms in (2.28) are not canceled. This results in a theoretical constraint on the Higgs boson mass deduced from the unitarity limit. Using the unitarity bound for the partial wave a_ℓ (cf. 2.45)

$$|\text{Re } a_\ell| \leq \frac{1}{2} \tag{2.31}$$

applied to the zeroth partial wave of $W_L^+W_L^- \to Z_LZ_L$ scattering yields the constraint [59]

$$m_H^2 < \frac{4\sqrt{2}\pi}{G_F} \approx (1.2\,\text{TeV})^2. \tag{2.32}$$

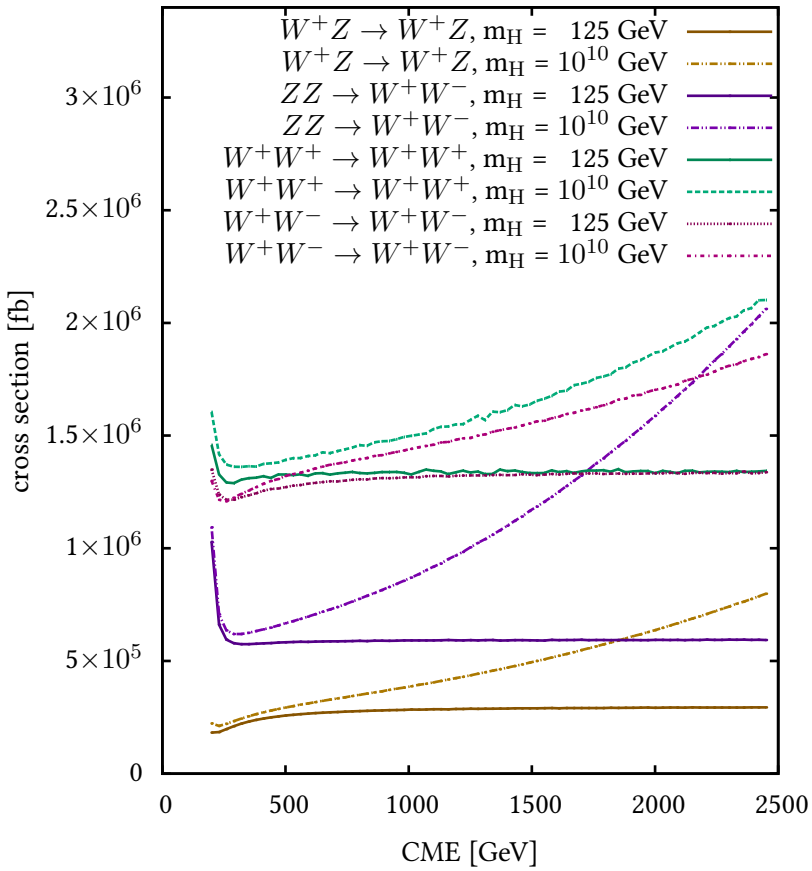

Figure 2.3: Center-of-mass energy dependence of scattering cross sections of Vector Boson Scattering processes in the various channels with a SM-Higgs of mass m_H = 125 GeV and with a heavy Higgs of mass $m_H = 10^{10}$ GeV, respectively. The heavy Higgs fails to unitarize the VBS processes.

The SM Higgs mass therefore needs to be below this threshold, otherwise another mechanism providing unitarization would have to be present. After the discovery of a Higgs-like boson with $m_H \simeq$ 126 GeV which respects this constraint, no urgent need for an alternative mechanism is present.

2.3 Electroweak gauge boson scattering beyond the Standard Model

In the light of the discovery of a Higgs boson consistent with the SM Higgs boson at the LHC [7, 8], the next step is the thorough investigation of the EWSB sector. As argued above, the process of VV scattering is a suitable channel for this investigation complimentary to direct Higgs measurements and searches for new particles. A variety of models in which the observed Higgs boson is not a SM Higgs boson are still consistent with data.

One class of models are those in which the Higgs is a composite particle of some strong dynamics in the EWSB sector. This can consist of a strongly interacting fourth family [61], a technicolor dynamic where the Higgs boson is an isosinglet scalar generated by a walking technicolor mechanism [62, 63], or a pseudo-Nambu-Goldstone generation of the Higgs boson [64].

Another ansatz consists of theories in which the observed state is embedded in an extended Higgs sector. The extensions of the Higgs sector can be described for instance in the form of an additional singlet [65], or as a Two Higgs Doublet Model (2HDM) [66], which includes the Minimal Supersymmetric Standard Model (MSSM).

Any of these models imply deviations of the properties of the Higgs boson, for instance in its couplings to other particles, and new physical states arising at higher energy.

Since an arbitrary number of new models is possible, it becomes clear that a check of each model's implication on VBS processes and the comparison to data, a "top-down" approach, is quite elaborate. Alternatively, a "bottom-up" approach can be chosen, by devising a model-independent appearance of new physics. Comparing data with this generic model is practical if a translation of specific models to the generic theory is known. A way of introducing new physics in the electroweak sector in the form of an effective field theory is demonstrated in this section. It remains model independent except for the effects of a necessary unitarization procedure.

2.3.1 Parametrizing the unknown: Effective field theories

An effective field theory (EFT), models the effects of new physical degrees of freedom present at energy scales much higher than the currently experimentally accessible range. At low energy, they appear as modifications of the interactions of known particles with respect to the interactions that the SM specifies. In this framework, the SM is a low-energy effective theory. The effective field theory contains additional operators with higher energy dimension suppressed by the scale of new physics Λ added to the SM Lagrangian [67] as

$$\mathcal{L}_{\mathrm{EFT}} = \mathcal{L}_{\mathrm{SM}} + \sum_{d>4} \sum_{i} \frac{c_i^{(d)}}{\Lambda^{d-4}} \mathcal{O}_i^{(d)}. \tag{2.33}$$

Here, $c_i^{(d)}$ are the coefficients of the new operators $\mathcal{O}_i^{(d)}$. The operators with dimension $d > 4$ should obey the symmetries of the SM. In principle, the EFT composed as (2.33) has the following properties:

Any new physics can be effectively modeled by a certain set of additional operators, which also fixes their coefficient to certain values, as long as the new physics scale is above the kinematic range. Operators with higher dimensions are more strongly suppressed by Λ^{d-4}. Therefore, the Lagrangian (2.33) is usually truncated at a fixed dimension. The SM is the low-energy theory of this EFT, i.e. if $\Lambda \to \infty$, the SM is reproduced. [67]

2.3.2 The electroweak chiral Lagrangian

A commonly used EFT for the electroweak sector is the electroweak chiral Lagrangian (EWChL). It is introduced in analogy to chiral perturbation theory, a common approach for low-energy calculations in QCD [68]. Chiral perturbation theory (χPT) is a widely-used tool for the calculation of low-energy strong interactions between partons outside the range of asymptotic freedom that can therefore not be calculated perturbatively by an expansion in α_s. To this effect, χPT is based on the chiral flavor symmetry of QCD, i.e. the symmetry between massless quarks of the same chirality but different flavor under isospin rotations. This symmetry is explicitly broken by the masses of quark condensates or mesons. The resulting pseudo-Goldstone bosons of the symmetry breaking are the pions. A Lagrangian for the interaction of mesons can be formulated, with additional operators at fixed order of derivatives, such as the Gasser-Leutwyler Lagrangian [69] with 10 operators and 10 coefficents. Fixed by the full QCD theory, the values of these coefficients represent a distinct pattern characteristic for QCD [70].

In analogy, an effective Lagrangian is devised for the electroweak sector to model the mechanism of breaking the electroweak $SU(2)_L \otimes U(1)_Y$ symmetry to $U(1)_Q$ and a remaining symmetry in the scalar sector, the custodial symmetry $SU(2)_C$. In this case, the effective Lagrangian is constructed with a non-linear representation of the $SU(2)_L \otimes (U1)_Y$ symmetry and contains a mechanism to spontaneously break it. This has been initially developed by Longhitano, Appelquist and Bernard [71, 72]. By adding higher-order operators and their coefficients as in the case of QCD, it should be possible to probe the underlying full theory through the experimentally determined values of these coefficients, the low-energy couplings [70].

The symmetry breaking is realized by introducing a field $\Sigma(x)$, which is a unitary matrix transforming under local $SU(2)_L$ transformations $U(x)$ and $U(1)_Y$ transformations $V(x)$ as

$$\Sigma(x) \to U(x)\Sigma(x)V^\dagger(x).$$

It can be parametrized as [73, 74]

$$\Sigma(x) = \exp\left(\frac{-i}{v}\sum_{a=1}^{3} w^a \tau^a\right) \tag{2.34}$$

with the Goldstone bosons $w^a (a = 1, 2, 3)$ generated by the spontaneous breaking of the electroweak

symmetry. The effective Lagrangian

$$\mathcal{L}_{\mathrm{EWChL}} = \mathcal{L}_{2(W)} + \mathcal{L}_3 + \mathcal{L}_k + \mathcal{L}_\Sigma \tag{2.35}$$

is written in terms of the Σ matrix consisting of Lagrangian terms for the weak boson masses $\mathcal{L}_{2(W)}$, the fermion masses $\mathcal{L}_3$, the kinetic terms of the electromagnetic and weak interactions $\mathcal{L}_k$ and a symmetry breaking term $\mathcal{L}_\Sigma$ [71, 74].

2.3.3 Anomalous couplings in the electroweak chiral Lagrangian

Calculating the one-loop correction terms for the EWChL yields several terms which obey the custodial isospin symmetry $SU(2)_C$ as well as CP invariance. Of those, the following two operators $\mathcal{L}_i$ with couplings α_i influence quartic gauge boson couplings only [74, Sec. 2.3.2]

$$\mathcal{L}_4 = \alpha_4(\mathrm{tr}[\mathbf{V}_\mu \mathbf{V}_\nu])^2, \tag{2.36}$$

$$\mathcal{L}_5 = \alpha_5(\mathrm{tr}[\mathbf{V}_\mu \mathbf{V}^\mu])^2 \tag{2.37}$$

with the definition $\mathbf{V}_\mu = \Sigma(D_\mu\Sigma)^\dagger$. These terms introduce anomalous quartic couplings (aQGC) of the electroweak gauge bosons and can be probed in VBS processes.

2.3.4 Resonances in the electroweak chiral Lagrangian

The EWChL can also be extended by explicitly adding new degrees of freedom at lowest order. They appear as resonances of different spin-isospin configuration: scalar fields σ and ϕ, a vector field ρ as well as tensor fields $\mathbf{f}$ and $\mathbf{t}$ can be added to the Lagrangian by a kinetic term and their couplings to W/Z bosons [73].

The types of resonances, their partial widths for decays into vector bosons, and their conversion into α_4 and α_5 contributions are listed in Table 2.4.

resonance	spin J	isospin I	Γ/Γ_0	$\Delta\alpha_4$ / α	$\Delta\alpha_5$ / α
ϕ	0	2	1	$1/4$	$-1/12$
σ	0	0	6	0	$1/12$
t	2	2	$1/30$	$-5/8$	$35/8$
ρ	1	1	$4/3\ v^2/M^2$	$3/4$	$-3/4$
f	2	0	$1/5$	$5/2$	$-5/8$

Table 2.4: Resonances in VBS and their properties. The remaining factors are $\Gamma_0 = g^2/64\pi \cdot M^3/v^2$ and $\alpha = 16\pi\Gamma/M \times v^4/M^4$ [73].

The conversion between resonances and anomalous couplings are determined from integrating out the resonances [73]. In many of the currently experimentally accessible cases, these conversions have been found to be valid only up to a point where the contribution from non-SM terms is very small [75].

For $W^{\pm}W^{\pm}$ scattering, the relevant resonances are the t resonance (tensor quintet) as well as the ϕ resonance (scalar quintet), since both of them can be doubly electrically charged. Translated to complete new physics theories, t resonances correspond to extended composite Higgs models, while ϕ-type resonances appear in the Littlest Higgs model [44].

2.3.5 Effective field theory with linear symmetry breaking

The EWChL ansatz is especially suitable if the symmetry breaking dynamics are strongly interacting. After the discovery of a SM-like Higgs boson candidate, the inclusion of a SM Higgs resonance and symmetry breaking through the Higgs mechanism is the choice at hand.

Alternatively to the EWChL approach with its non-linear symmetry breaking, it is also possible to construct an effective Lagrangian with linear realization of the $SU(2)_L \otimes U(1)_Y$ gauge symmetry [67, 76].

Considering only genuine quartic gauge vertices, the operators added in the frame of (2.33) are at least of dimension 8. Operators with lower dimension contribute also to triple gauge couplings and are thus more strongly constrained by processes sensitive to triple gauge interactions. The two independent dimension 8 operators without derivatives of the gauge fields are [76]

$$\begin{aligned} \mathcal{O}_{S,0} &= [(D_\mu \Phi)^\dagger D_\nu \Phi] \times [(D^\mu \Phi)^\dagger D^\nu \Phi] \\ \text{and} \quad \mathcal{O}_{S,1} &= [(D_\mu \Phi)^\dagger D^\mu \Phi] \times [(D_\nu \Phi)^\dagger D^\nu \Phi]. \end{aligned} \tag{2.38}$$

combined with the couplings to the Lagrangian terms

$$\begin{aligned} \mathcal{L}_{S,0} &= \frac{f_{S,0}}{\Lambda^4} \mathcal{O}_{S,0} \\ \text{and} \quad \mathcal{L}_{S,1} &= \frac{f_{S,1}}{\Lambda^4} \mathcal{O}_{S,1}. \end{aligned} \tag{2.39}$$

with the covariant derivative (2.6) and the Higgs field Φ.

A conversion between aQGC operator couplings (2.36) and those of the linear symmetry breaking approach (2.39) is only possible in a vertex-specific manner. For $W^{\pm}W^{\pm}jj$ production, the conversion is given for the normalized parameters $\tilde{f}_{S,i} = f_{S.i}\,\mathrm{TeV}^4/\Lambda^4$ by [67, 77].

$$\alpha_4 = k\tilde{f}_{S,0} \tag{2.40}$$

$$\text{and} \quad \alpha_5 = \frac{1}{2}k(\tilde{f}_{S,1} - \tilde{f}_{S,0}) \tag{2.41}$$

where

$$k = v^4/(8\,\mathrm{TeV}^4) \approx 1/2176. \tag{2.42}$$

In addition to the operators $\mathcal{O}_{S,0}$ and $\mathcal{O}_{S,1}$ which only contain derivatives of the Higgs doublet, eight operators $\mathcal{O}_{M,i}$ containing two electroweak field strength tensors and two covariant derivatives

of the Higgs doublet exist, as well as eight operators $\mathcal{O}_{T,i}$ containing four field strength tensors [67].

2.3.6 Unitarity

The addition of new operators to the effective Lagrangian generally can lead to unitarity violation in the scattering process, i.e. the unitarity of the S-matrix, and therefore conservation of probability, is violated. This occurs when the cancellation described in 2.2.3 breaks down as additional terms are added which can grow as $\mathcal{O}(s)$, $\mathcal{O}(s^2)$, and beyond. In an effective theory, if the center-of-mass energy rises to a value close to the scale of new physics, contributions from higher-order operators are not sufficiently suppressed.

In order to restore unitarity and to obtain physical results from an effective theory, a unitarization procedure has to be applied. Such a procedure cancels the high-energy divergence of the scattering amplitude, providing a modified amplitude compliant with a unitary S-matrix, such that the cross section stays below the cross section of the scattering process at the unitarity bound.

The unitarity condition is expressed in terms of the optical theorem derived from energy conservation in the scattering [44]

$$\sigma_{\text{tot}} = \frac{4\pi}{k}\text{Im}A(k, \theta = 0). \tag{2.43}$$

It relates the total cross-section σ_{tot} to the imaginary part of the forward scattering amplitude $A(k, 0)$ with momentum k. The unitarity bound can be determined from the optical theorem using a partial wave expansion of the scattering amplitude in terms of Legendre polynomials P_ℓ [59]

$$A(k, \theta) = \frac{1}{k}\sum_\ell (2\ell + 1)a_\ell P_\ell(\cos\theta). \tag{2.44}$$

Then, each partial wave cross section is bounded by a unitarity condition which can be expressed by the Argand-circle condition for elastic scattering

$$|a_\ell(s) - i/2| = 1/2 \tag{2.45}$$

for the partial amplitudes a_ℓ.

Various unitarization procedures enforcing this condition are known in the literature and used for phenomenological and experimental studies: The most important procedures, k-matrix unitarization [78] and form factors [79], are described in Section 3.4.2.

If the unitarity bound depends on the unitarization procedure, and the unitarization procedure has an influence on the total and differential cross sections of the process, it essentially becomes a part of the model.

2.3.7 Experimental constraints on electroweak quartic gauge interactions

No process containing massive electroweak vector boson scattering at tree level has been measured prior to the measurement described in Chapter 5 and published in [56]. Hence, this measurement leads to the first derived limits on anomalous quartic gauge couplings parameters involving only massive bosons. However, experimental constraints on electroweak quartic gauge interactions involving photons have existed since LEP times. The genuine quartic gauge couplings a_0^W and a_C^W for $WW\gamma\gamma$ vertices and a_0^Z and a_C^Z for $ZZ\gamma\gamma$ vertices are defined as introduced by [80] as the coefficients in the following Lagrangian terms

$$
\begin{aligned}
L_6^0 &= \frac{e^2}{8}\frac{a_0^W}{\Lambda^2}F_{\mu\nu}F^{\mu\nu}W^{+\alpha}W_\alpha^- - \frac{e^2}{16\cos^2\Theta_W}\frac{a_0^Z}{\Lambda^2}F_{\mu\nu}F^{\mu\nu}Z^\alpha Z_\alpha \\
L_6^C &= \frac{-e^2}{16}\frac{a_C^W}{\Lambda^2}F_{\mu\alpha}F^{\mu\beta}(W^{+\alpha}W_\beta^- + W^{-\alpha}W_\beta^-) - \frac{e^2}{16\cos^2\Theta_W}\frac{a_C^Z}{\Lambda^2}F_{\mu\alpha}F^{\mu\beta}Z^\alpha Z_\beta,
\end{aligned}
\tag{2.46}
$$

with the energy cutoff Λ corresponding to the scale of new physics. These terms obey the custodial symmetry as well as the charge-conjugation and parity symmetries. Various channels are available to set limits on these couplings, mainly divided in triple gauge boson production channels, such as $WW\gamma$, and VBS channels such as $\gamma\gamma \to WW$ or $WW \to \gamma\gamma$. Neutral couplings of $ZZ\gamma\gamma$ are forbidden in the SM. Limits on the a_0^W, a_C^W, a_0^Z, and a_C^Z parameters have been set in the measurements listed in Table 2.5.

Experiment	Channel	Limits on	published
L3	$WW\gamma$, $\nu\bar{\nu}\gamma\gamma$	a_0^W, a_C^W, a_0^Z, a_C^Z	2002[15]
OPAL	$\nu\bar{\nu}\gamma\gamma$, $q\bar{q}\gamma\gamma$	a_0^W, a_C^W, a_0^Z, a_C^Z	2004 [16]
D0	$\gamma\gamma \to WW$	a_0^W, a_C^W	2013 [81]
CMS	WW$\to \gamma\gamma$	a_0^W, a_C^W	2013 [82]
CMS	WWγ, WZγ	a_0^W, a_C^W	2014 [83]

Table 2.5: Experimental constraints on quartic gauge couplings involving photons. The channels in which the anomalous couplings have been set are listed for each experiment, as well as the exclusion limits at 95 % confidence level.

Limit setting on anomalous quartic gauge couplings of massive electroweak gauge bosons from the measurement of electroweak production of $W^\pm Zjj$ is ongoing work in ATLAS [84, 85].

CHAPTER 3

Monte Carlo generation and electroweak gauge boson scattering

The adequate simulation of processes occuring in proton-proton interactions is crucial for research at the LHC. Computer simulation is an essential tool for the understanding of expected background processes as well as a signal which is to be extracted, whether it is a signal of new physics or the measurement of a property predicted by the SM. In this respect, Monte Carlo methods play a role from the generation of matrix-element events to the simulation of particle interactions with the detector material and to the statistical analysis of an extracted signal.

As an introduction, Section 3.1 explains the MC method in general and the necessary steps for simulation of high-energy physics processes. Section 3.2 will go into the details of MC simulation for VBS processes. Comprehensive information on Monte Carlo simulation in high-energy physics can be found in references [86–89]. , which have also been consulted for the summary presented in this chapter.

3.1 Monte Carlo Simulation

Physics processes occurring at the LHC and at other high-energy experiments comprises a multitude of particle interactions at different energy scales. A full physics simulation thus takes into account [89]:

- the matrix-element of the hard scattering process,
- a parton shower algorithm to include higher-order effects of QCD and QED,
- non-perturbative QCD processes leading to the allocation of particles for the hard scattering as well as the formation of final state particles,
- an underlying event prescription modelling secondary scattering interactions, and

- the detector response to the produced particles.

Due to the high dimensionality of the integrals that have to be evaluated, Monte Carlo (MC) techniques are widely used for the numerical integration of the cross sections of high-energy particle processes. The combination of the above-mentioned steps produces a sample of events that can be directly compared to data produced at the LHC. Throughout this thesis and in the literature, these samples are called Monte Carlo samples and abbreviated MC samples, keeping in mind that they are the result of several subsequent steps of MC simulation.

3.1.1 Monte Carlo integration method

MC methods are widely-used techniques for sampling of random variables from a given probability density function in order to numerically integrate highly dimensional mathematical expressions.

The integration is based on a pseudo-random number generator which provides uniformly distributed, statistically independent random numbers in the interval [0,1). The uniformly distributed random numbers are transformed into random numbers sampled according to a probability density function (*p.d.f.*). Then, according to the Law of Large Numbers, the sum [86]

$$\frac{1}{n}\sum_{i=1}^{n} h(X_i) \;\text{ with } (X_i, ..., X_n) \text{ sampled from the p.d.f. } f(x)$$

converges to the integral of interest,

$$\int_{\mathrm{PS}} h(x) f(x)\,\mathrm{d}x, \text{with probability density function } f(x).$$

The transformation of a set of random numbers drawn from a uniform distribution can be carried out by inverting the cumulative p.d.f. If that is impossible or too difficult, an acceptance-rejection method can be used [86]. Several algorithms are available for this, yielding differing levels of quality and speed. Another option are *Markov Chain Monte Carlos* which are based on highly efficient algorithms generating random numbers with a short-distance correlation [86].

MC in high-energy physics The MC method is particularly suited for the application to processes in high-energy physics because of the large number of dimensions of phase space (space-time, spin, and flavor of n final state particles). A MC integration for high-energy physics events makes use of the possibility to factorize the full process into sub-processes occurring at different energy scales, which is described in Section 3.1.2. Markov chain type simulations are particularly useful for parton showers, taking advantage of their property of short-distance correlation but absence of long-distance dependence.

The simulation of processes involving elementary particles is based on the mechanisms of the SM (or extensions thereof) as described in chapter 2.

3.1.2 Perturbative QCD and the factorization theorem

For particle collisions at a hadron collider, a major issue for theoretical predictions is the treatment of quarks and gluons, which is realized through the formalism of QCD. The calculations are based on Feynman diagrams using a perturbative approach:

In case of QCD, the solution of the renormalization group equations (RGE) yields a negative β-function, indicating that the theory is *asymptotically free.* This means that above a certain threshold (called Λ_{QCD}, the strong coupling constant α_s is a running coupling decreasing logarithmically as a function of the renormalization scale μ_R. Therefore, as Figure 3.1 shows, the coupling becomes small in hard interactions, which can thus be calculated perturbatively. This is called the *parton model* of QCD, allowing the treatment of quarks and gluons as free particles despite their *confinement* at low energies. [90]

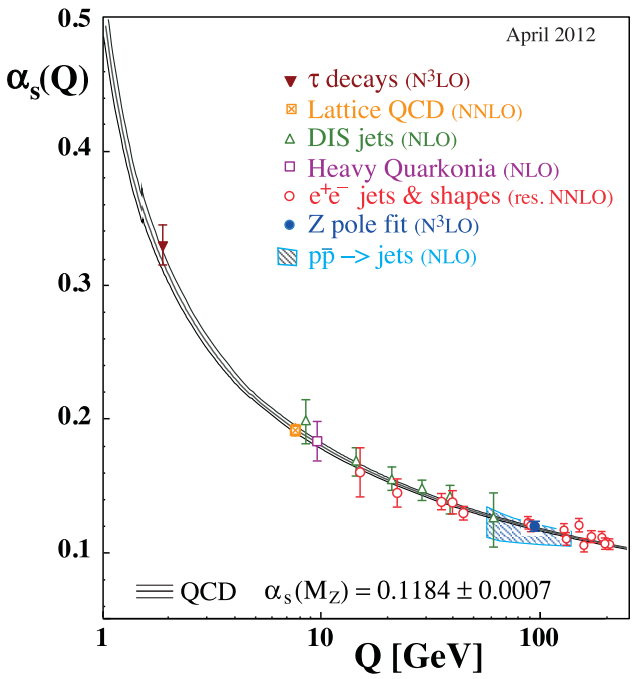

Figure 3.1: Running of the strong coupling α_s. From Particle Data Group review on QCD [91].

Thanks to asymptotic freedom, infrared safe observables can be calculated perturbatively. Non-infrared-safe observables can be split into an infrared-safe part (hard interaction, short distance) and a soft (long-distance) part which is not infrared safe but can be deduced from universally measurable quantities.

Subprocesses occurring at different energy scales in a hadronic collision can be separated according to the *factorization theorem* [92]. It states that a scattering process $ab \to n$ at a hadron collider with

initial hadronic particles $a,\ b$ and final state particles n can be written as:

$$\sigma_{ab\to n} = \sum_{a,b} \int_0^1 \mathrm{d}x_a \mathrm{d}x_b \int f_a^{h_1}(x_a, \mu_F) f_b^{h_2}(x_b, \mu_F)\ \mathrm{d}\hat{\sigma}_{ab\to n}(\mu_F, \mu_R). \tag{3.1}$$

As illustrated in Figure 3.2, this allows for the factorization of the total cross section $\sigma_{ab\to n}$ into

- the non-perturbative part, obtained by evaluating the *parton distribution functions (PDFs)* $f_i^h(x_i, \mu_F)$ of the initial parton i with respect to the original hadron h at a given momentum fraction x and the *factorization scale* μ_F,
- and the *partonic* cross section $\hat{\sigma}_{ab\to n}(\mu_F, \mu_R)$, calculated perturbatively by considering the process $ab \to n$ with free partons in the initial state.

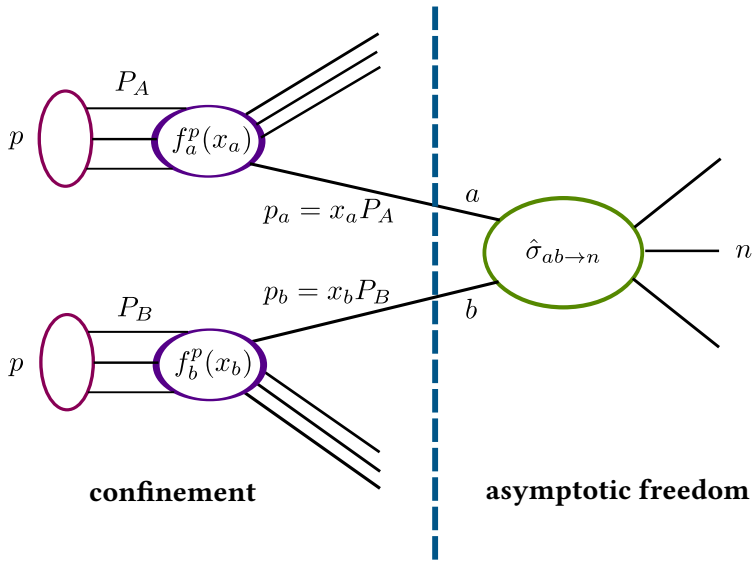

Figure 3.2: Illustration of the factorization theorem (equation 3.1). The total cross section of the process can be factorized in a long-distance part, where confinement governs the partonic interactions, and a short-distance part with asymptotically free partons.

Thus, the cross section can be factorized into an integral over the final-state phase space Φ_n, as

$$\sigma_{ab\to n} = \sum_{a,b} \int_0^1 \mathrm{d}x_a \mathrm{d}x_b \int \mathrm{d}\Phi_n\ f_a^{h_1}(x_a, \mu_F) f_b^{h_2}(x_b, \mu_F) \times \frac{1}{2\hat{s}} |\mathcal{M}_{ab\to n}|^2(\Phi_n; \mu_F, \mu_R). \tag{3.2}$$

The integrand consists of the matrix element $|\mathcal{M}_{ab\to n}|^2$, which is usually a sum over multiple Feynman diagrams, weighted by the PDFs. Thus, the factorization theorem allows for the calculation of the cross section of the hadronic process while introducing a dependence on an arbitrary scale, the factorization scale μ_F. The non-perturbative part of the calculation usually features a set of parameters tunable with data.

In order to calculate the full cross section, knowledge about the PDFs of partons of type a and b in the initial hadrons has to be available. In the above equation, $f_i^h(x_i, \mu_F)\,\mathrm{d}x_i$ indicates the probability to find a parton of type i with momentum fraction x_i in a hadron h probed at the energy scale μ_F. PDFs are provided by several theoretical collaborations based on data from previous and current experiments and extrapolated to the appropriate energy using the DGLAP evolution equations [93–95].

3.1.3 Matrix-Element integration and event generation

The matrix-element integration is performed by sampling the phase space and calculating the differential cross sections $\mathrm{d}\sigma$ at a large number of sampling points. Then, the sum of these differential cross sections yields the total cross section σ of the partonic process.

At tree-level, the matrix elements are calculated based on the computation of the relevant Feynman diagrams or using the underlying field theory. Singularities in physical distributions need to be removed via kinematic cuts. Formation of hadrons and jets is not included in the matrix-element integration. Equivalence between partons and jets is assumed [88].

For event generation, the above generated sampling points are considered as events with the weight $\mathrm{d}\sigma$. In order to provide a physical sample of events, they have to be un-weighted in order to yield a sample of events with unity weights. Un-weighting of events is performed with an acceptance-rejection method.

3.1.4 Evolution of the final state

Final states of the hard scattering, generated from the matrix-element, consist of stable, non-observable partons and stable leptons regardless of flavor. The matrix-element is determined at fixed order, neglecting higher-order corrections, which can have sizable effects on particle kinematics. It is therefore necessary to evolve the matrix-element events, incorporating contributions from higher orders, formation of hadrons, decays of unstable particles and underlying event. Figure 3.3 illustrates the components of a simulated event, which are described in the following.

Parton shower

Final states of parton-level events miss any contributions exceeding the fixed order to which the matrix element is calculated. In order to account for effects of higher order QCD corrections and hadronization, these events can be interfaced to a parton showering and hadronization algorithm.

Parton showers exploit the observation that in certain kinematic regions, the dominant effects of additional emissions can be described in a trivial, recursive way. In a Markov chain process, the components of the hard subprocess are evolved by adding successive branchings of one parton into two other partons, in the limit of soft parton or collinear gluon splitting.

An evolution variable t is chosen with a starting value T. For a splitting of parton i, the next value

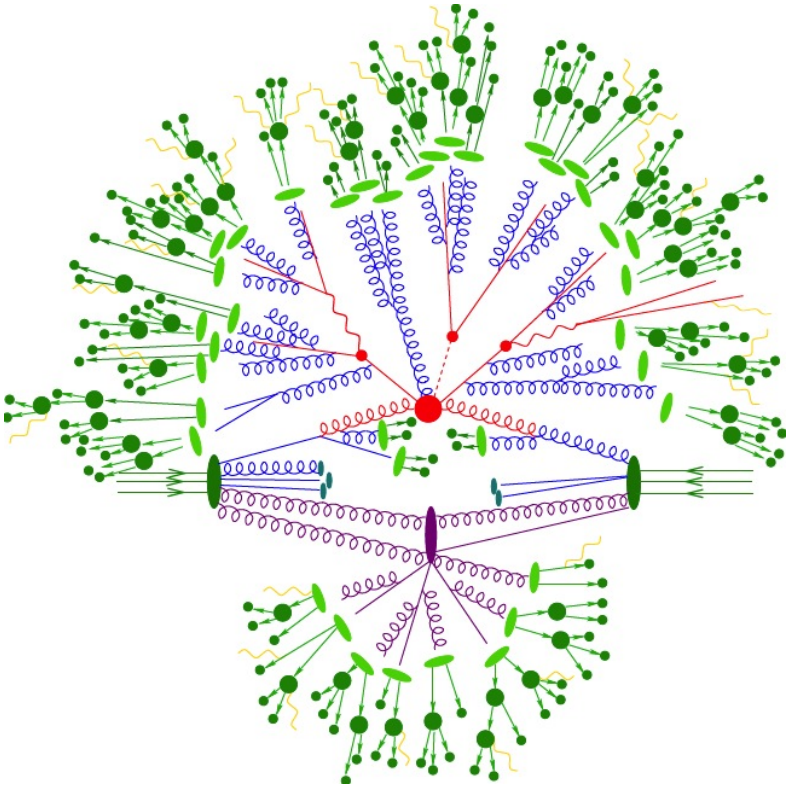

Figure 3.3: Monte Carlo simulated event as produced by the SHERPA generator: This includes the hard interaction (shown in red), parton shower emissions (blue), and hadronized partons (green). Hadron decays are shown in dark green, and QED radiation in yellow. The underlying event is depicted as additional interactions in purple. From [96].

of t is determined by solving the equation [88]

$$\Delta_i(T, t_0) = \mathcal{R}\Delta_i(t, t_0) \tag{3.3}$$

for the new scale t. Here, $\Delta_i(q_1, q_2)$ denotes the *Sudakov form factor*[97], which describes the probability for a parton of flavor i not to split during the evolution from scale q_1 to scale q_2. $\mathcal{R}$ is a random number sampled from a uniform distribution in [0,1] and t_0 is the infrared cutoff scale (typically, $t_0 \approx 1\,\text{GeV}$). The equation can be solved e.g. with a rejection method [88].

In case that the new scale $t < t_0$, the splitting of parton i is terminated. Otherwise, the splitting of parton $i \to j + k$ is continued by solving equation 3.3 with a new random number for the flavors j and k at the new initial scale [98].

The evolution variable can be chosen in various ways, most commonly as either a time-like or a space-like variable. Finally, the initial parton is replaced by a shower of partons travelling in similar direction. A set of parameters on which the algorithm depends can be tuned to data. The total cross section is not influenced by the parton shower algorithm [89].

Matching Matrix-Element and Parton Shower

In many final states, the tree-level matrix-element combined with a parton shower still does not describe data with the required accuracy. If available, the NLO QCD corrections to a given process should therefore be included. However, for many processes of interest at the LHC, the NLO calculation is very

involved and has not been carried out yet. In these cases, it can be advantageous to include additional real QCD radiation. Although adding only the real emissions neglects the virtual emissions of the full NLO calculation, it improves the agreement with data in many cases.

Combining a tree-level process that went through a parton shower algorithm with the same process including one additional emission poses a new challenge: There is an overlap between events with a real emission from the matrix-element and events with a parton shower emission with the same kinematics. It is therefore crucial to consistently remove this overlap, e.g. through the correction of the matrix element, or the method of truncated showers (e.g. the CKKW method [99]).

Hadronization

The resulting partons after the parton shower are then combined to color neutral composite states, forming hadrons. As hadronization occurs at scales in the non-perturbative regime, no calculation from first principles exists. Hadronization is therefore modelled based on generic properties of QCD. Several different models exist, which prescribe the combination of partons into hadrons: The main methods used in current generators are the *string model*, based on linear confinement of partons, and the *cluster model*, based on the preconfinement of parton showers.

Hadron and τ decays

Some of the resulting hadrons after hadronization, as well as all τ leptons produced in the hard scattering or the parton shower, are unstable and cannot be measured in the detector. As far as available, hadron decay modelling is based on hadronic measurements and closely connected to the hadronization model. For τ decays, a better description of data is reached by including spin effects.

QED radiation

Electromagnetic radiation can occur from the initial and the final state of an event. It can be modelled similarly as the QCD parton shower with electric charge substituting the color charge. Another method is based on the YFS formalism [100], which is based on a multipole evolution and used primarily for objects radiating only electromagnetically.

Underlying event

In addition to the scattering of the two partons which contribute to the main collision, a range of interaction activity is taking place which is described by the *underlying event* or *soft QCD*. It is modelled in terms of additional interactions between partons of the colliding protons. Understanding the underlying event is interesting in its own right (e.g. see [101]), but also for the prediction of background contributions to other processes (cf. Section 5.2.4).

Jets in hadronic events

Jets in the final state of a simulated event arise from several sources: Initial state radiation, emission from the partons of the hard process, as well as the underlying event. Jets are not fundamental objects defined by the SM. They have to be defined using a *jet algorithm*, which prescribes how to form jets from outgoing partons (at the matrix-element level), from hadrons (after parton shower and hadronization), or from energy deposits in the calorimeter (at reconstruction level and in collision data). For consistency between theory and experiment, any jet clustering algorithm is required to be infrared and collinear safe. Section 4.3.1 describes jet reconstruction as used in ATLAS and in this work.

3.1.5 Commonly used Monte Carlo generators

A variety of generators provide MC simulation in the high-energy physics context, not all of which can be mentioned here. Multi-purpose event generators such as SHERPA [102], PYTHIA6/8 [103, 104], and HERWIG++ [105] combine the capability to calculate exact or factorized generic matrix-elements combined with parton showering and, if applicable, matching the parton-showered events to the matrix-element. They also take care of QED radiation, hadronization, decays of hadrons and τ leptons, and an underlying event structure.

Partonic multi-purpose generators such as MADGRAPH [106] and WHIZARD [107, 108] generate matrix elements and usually provide an interface to a parton shower from an external generator, e.g. PYTHIA8. Specialized codes for particular tasks in the final state evolution exist as well, which can be employed instead of the multi-purpose generator for this task: For instance, TAUOLA++ ([109]) provides an implementation of the decay of τ leptons in the final state. PHOTOS ([110]) is a tool for calculating QED radiative corrections.

A variety of codes which provide NLO matrix-element calculations for specific processes exist as well. Generators such as VBFNLO [111] and POWHEGBOX [112] can be interfaced to a parton shower algorithm and the matrix elements are corrected for matching between matrix-elements and parton shower emission contributions.

3.1.6 Detector simulation

Based on event samples containing process-specific proton-proton collision events, the ATLAS simulation chain has the task to mimic the passage of final state particles through the detector, including all interactions and subsequent decays. Finally, these events should be stored in the same format as the collision data measured by the ATLAS detector.

Figure 3.4 shows the simulation chain implemented in ATLAS.

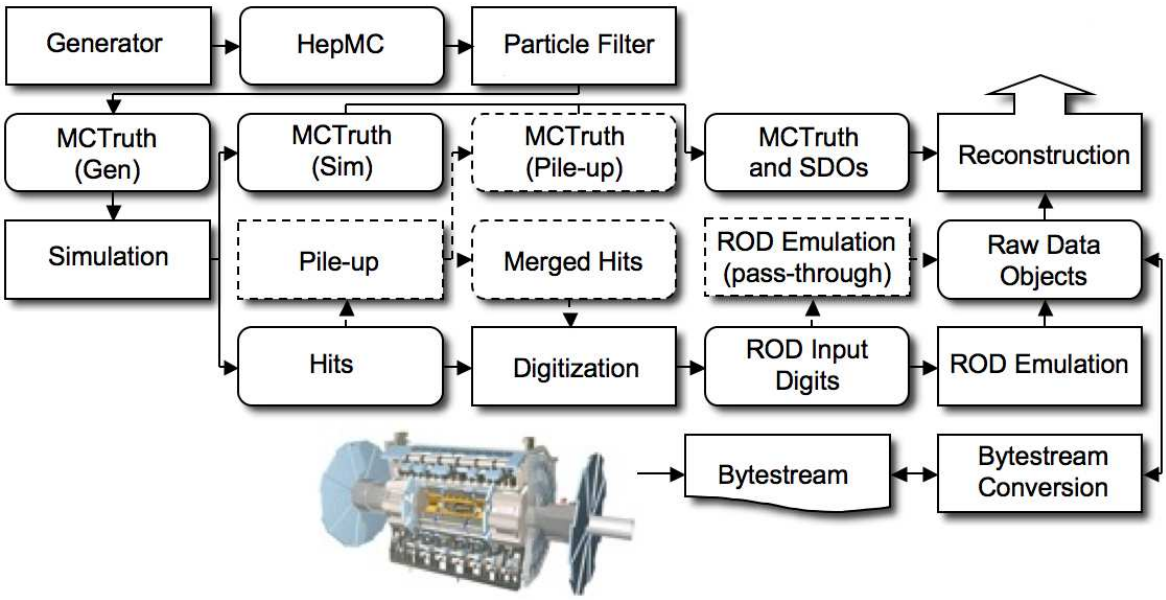

Figure 3.4: Computing chain for ATLAS simulation and data taking. Round-cornered boxes indicate persistent data objects, while algorithms and applications are placed in square-cornered boxes. Algorithms framed by dashed lines are optional. From [113].

Events in HepMC format [114] are generated using a MC generator and, if applicable, passed through a filter selecting events according to a kinematic requirement. Generator level ("MC truth") information of these events is passed to the detector simulation, resulting in simulated energy deposition signals and their coordinates in the detector, which are stored in "Hits" files. Again, in the simulation stage, information of tracks and particle decays in the detector, e.g. photon conversion, are retained in the "MC truth" record. Maps from the detector hits to generator-level particles in the MC-truth record are stored in SDOs (Simulated Data Objects).

In the digitization step, the energy deposits stored as "Hits" are converted into digital signals identical to the signals delivered by the detector read-out drivers (RDOs). Simultaneously, minimum bias events are overlayed in order to mimic *pile-up* contributions from additional interactions in the same or a previous bunch-crossing.

Finally, the resulting events are passed to the reconstruction. They have the same structure and content as data events from the ATLAS detector, which are passed to storage in a bytestream format to be converted into the Raw Data Objects format. [113]

In this way, the ATLAS simulation chain is run successively, storing the output of each step, which simplifies validation and optimizes usage of resources. The most CPU-expensive step is the simulation step, which takes several minutes per event.

3.1.7 From "Truth" to "Reconstruction": Levels in the full simulation chain

The various steps necessary for a full simulation of ATLAS data have been described in the previous sections. To summarize and to define widely-used terms, Figure 3.5 shows the different levels of MC simulations available in MC samples for a typical HEP experiment like ATLAS.

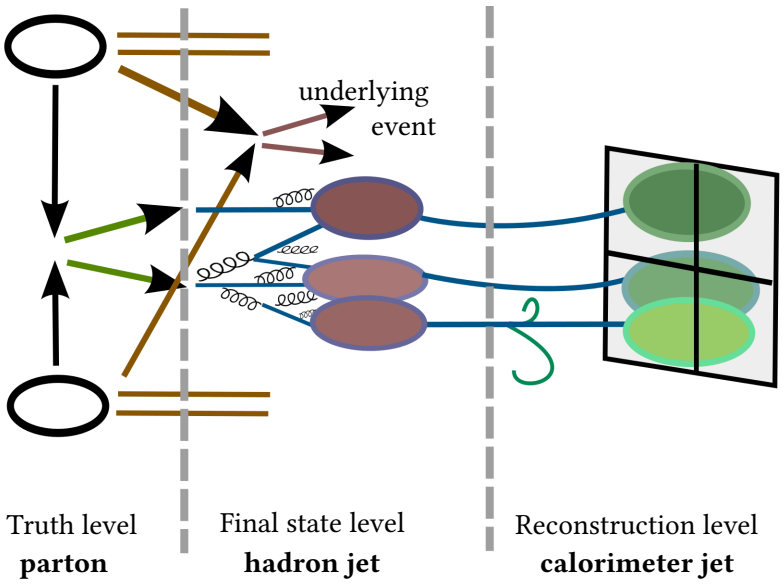

Figure 3.5: Levels in a MC simulation of a high-energy collision event.

Events on **"truth level"** or "parton level" contain particles as described by the matrix element calculations without QED radiation, parton shower and hadronization. Therefore, the final state of a collision event contains un-decayed leptons and partons. **"Final state level"** events contain information on stable particles remaining after hadronization. They can be directly originating in the hard subprocess, or modified by the parton shower and hadronization algorithm. Underlying event objects are included. On **"Reconstrunction level"**, the event information contains objects as reconstructed by algorithms run on fully detector simulated events. Material effects, magnetic fields, decays, and the detector response are simulated. Additional interactions such as pile-up are included.

3.2 Monte Carlo simulation for electroweak gauge boson scattering

In this section, the principles of MC generation for LHC processes as explained in section 3.1 are applied to the specific process of electroweak gauge boson scattering. A classification of the Feynman diagrams considered for the signal and main background processes in the definition used throughout this work will be given, as well as studies of the VBS specific phase space, important generator settings, and other studies relevant to VBS. Major generators used for VBS at leading-order (LO) and next-to-leading-order (NLO), as well as for the SM and BSM cases, will be presented.

3.2.1 Defining purely electroweak vs. QCD-mediated production of two electroweak bosons and two partons

The scattering of electroweak gauge bosons, as defined in Figures 2.2a and 2.2b, now has to be set in the context of a proton-proton collision with initial spectator quarks radiating off the electroweak bosons, which then scatter and subsequently decay into fermions that can be measured in the detector.

This shows that there are multiple processes with the identical final state, some of which cannot be separated from the VBS diagrams in a gauge invariant way. In this section, the classification is first given in the final state of $VVjj$, i.e. ignoring the fermionic decay of the vector bosons. The resulting difference to the full fermionic final state consists of non-resonant contributions which are discussed below.

The production of two electroweak gauge bosons and two partons in the final state, $VVjj$, at tree-level can be categorized in the following way:

VBS: The electroweak-only contribution to VVjj with scattering of electroweak gauge bosons. This component consists of all tree-level diagrams with actual scattering of the two electroweak bosons. The scattering occurs via triple or quartic gauge vertices, or the exchange of a Higgs boson. The VBS component includes only vertices mediated by the electroweak interaction. Figure 3.6(a) shows all possible $VVjj$-EW-VBS diagrams.

Non-VBS EW: Irreducible electroweak-only VVjj diagrams without scattering. This component consists of all VVjj production diagrams which contain electroweak vertices only, but the bosons do not scatter. This sub-process cannot be separated in a gauge invariant manner from the VBS component. It is therefore included in the signal and cannot be kinematically distinguished from VBS. Figure 3.6(b) shows examples for non-VBS $VVjj$-EW diagrams.

The entirety of the purely electroweak VBS and non-VBS diagrams is called **electroweak VVjj** or **VVjj-EW**. Additionally, processes with the same final state exist, which can be separated gauge invariantly from the VBS component and are therefore considered as background. As a consequence for the experiment, kinematic selection cuts can be used to suppress the contribution from the following processes:

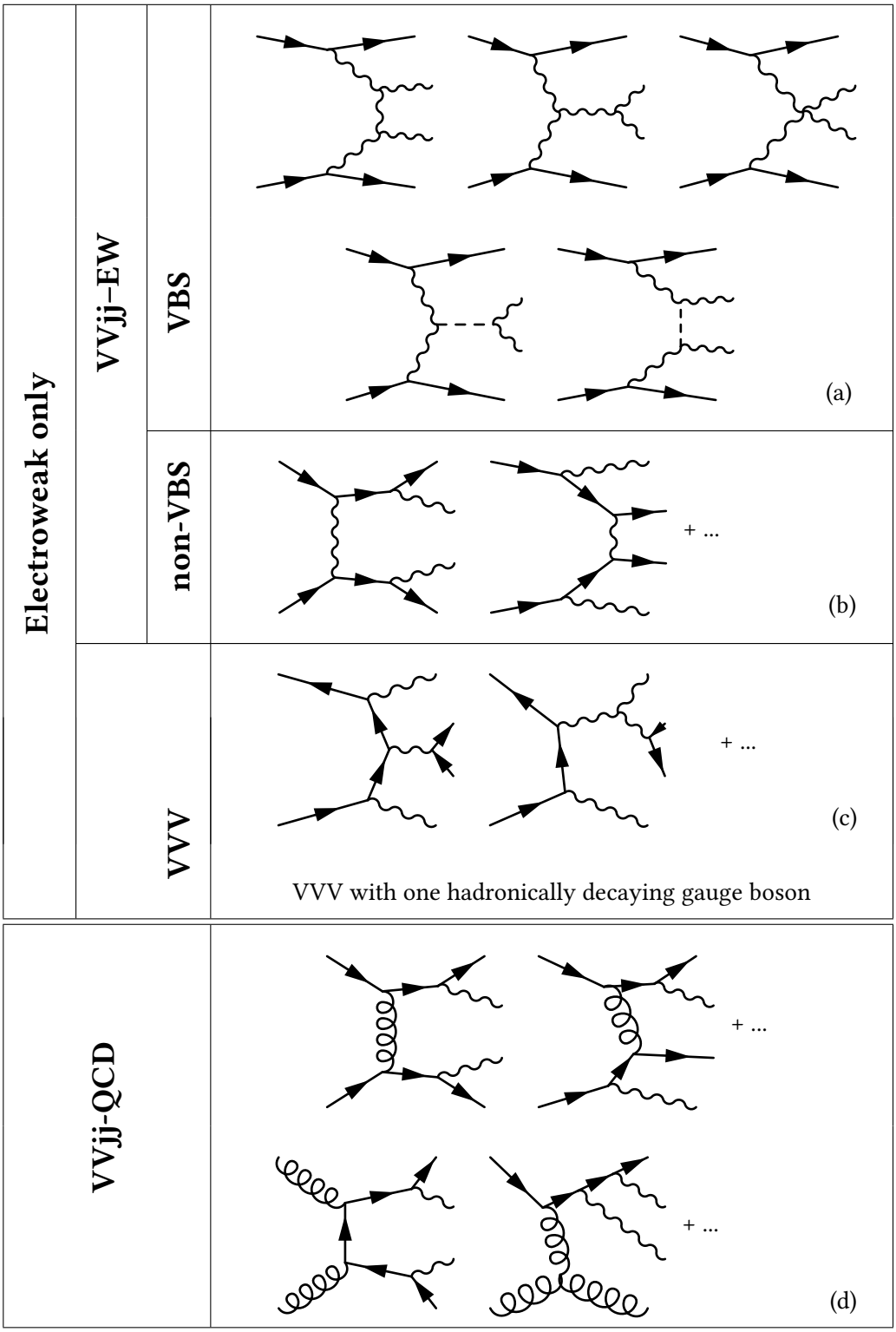

Figure 3.6: Categorization of Feynman diagrams with $VVjj$ final state at leading-order.

Tri-Boson or VVV background Tri-boson production via various possible channels, when one of the bosons is decaying hadronically yielding a $VVjj$ final state. This background is purely electroweak, but gauge invariantly separable nevertheless, due to the hadronic decay. The resonant decay of a W or Z boson in two partons can be suppressed by applying a requirement on the invariant mass of the partons. Examples for the tri-boson $VVjj$ production are shown in Figure 3.6(c).

VVjj-QCD The $VVjj$ final state can also be produced via at least one vertex with strong interaction. This background is gauge invariantly separable from the VBS component. Its kinematic properties also differ from the $VVjj$-EW production process. Depending on the possible parton combinations for the VV flavors, this contribution can be smaller or much larger than the $VVjj$-EW component. Example Feynman diagrams for the $VVjj$-QCD process are shown in Figure 3.6(d).

Production of the fermionic final state: Non-resonant contributions

In addition to the processes described above, the purely electroweak production of the $\ell^{\pm}\nu\ell^{\pm}\nu jj$ final state also contains contributions from non-resonant diagrams. These are diagrams which result in the same fermionic final state, but contains the electroweak bosons only in t-channels. Although there is no resonant W or Z production in these diagrams, they are not gauge invariantly separable from the VBS diagrams. Example Feynman diagrams are shown in Figure 3.7.

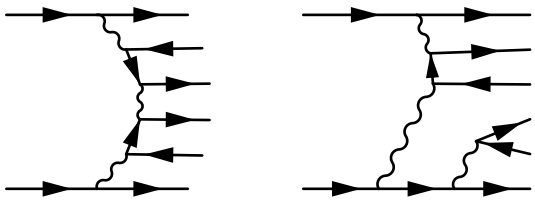

Figure 3.7: Example diagrams for non-resonant contributions to the fully fermionic final state

Further studies on the issue of non-resonant contributions to the $\ell^{\pm}\nu\ell^{\pm}\nu jj$ final state in particular are described in Section 3.3.3.

Processes involving heavy quarks

The categorization described above can be applied without regard to the parton flavor. Processes involving *top* quarks are of interest in their own right, and are therefore often provided in dedicated separate event samples. Experimentally, a distinction between light quark jets, originating from quarks of the flavors u, d, s, c, and heavy quark jets, originating from b quarks, can be made to a certain extent by using b-tagging algorithms. $VVjj$ production with one or two heavy flavor jets in the initial and final state is gauge invariantly separable from the $VVjj$ process of the same electroweak order with light jets only.

3.2.2 Generator settings for VVjj-EW generation

This section describes the settings for MC simulation of electroweak production of two gauge bosons and two jets. Two example steering files implementing these settings for the processes of $W^{\pm}W^{\pm}jj$-EW and $W^{\pm}Zjj$-EW for the `Whizard` generator are given in Appendix A.

Selection of EW diagrams only Several approaches ensure selection of the $VVjj$-EW process in the ME generation:

- Setting the strong coupling constant to $\alpha_s = 0$, such that all diagrams not from $VVjj$-EW vanish. This ensures that all $VVjj$-EW processes are included. No equivalent definition for $VVjj$-QCD exists. This approach is employed by the `Whizard` generator.
- Setting the order of QCD and electroweak interactions in the leading-order matrix elements to $\mathcal{O}$(EW) = 6 for the generation of $VVjj$-EW. Similarly, $VVjj$-QCD can be generated by setting $\mathcal{O}$(EW) = 4 or $\mathcal{O}$(QCD) = 2. This approach can be used in the generators `Sherpa` and `MadGraph`.
- For the case of MC generators with built-in libraries for certain processes, the possibility to generate $VVjj$-EW or $VVjj$-QCD depends on the available processes.

Electroweak coupling scheme The parameters of the electroweak theory, the Fermi constant G_F, the mass of the W boson M_W, the mass of the Z boson M_Z, the fine structure constant α, and the sine of the weak mixing angle $\sin\theta_W$, have been experimentally determined at high to very high precision (see Table 3.1)

Constant		in $\alpha(Q^2)$ scheme	in G_F scheme
Electromagnetic coupling			
– at $Q^2 = 0$	$\alpha(0)$	1/137.03599074(44)	$\approx$ 1/132.2
– at $Q^2 = M_Z^2$	$\alpha(M_Z^2)$	128.944 $\pm$ 0.014 [115]	
Fermi constant	G_F	1.1663787(6)$\cdot 10^{-5}$ GeV^{-2}	1.1663787(6)$\cdot 10^{-5}$ GeV^{-2}
Sine-squared of weak mixing angle	$\sin^2\theta_W$	0.23126(5)	$1 - \frac{M_W^2}{M_Z^2} \approx 0.2226$
Mass of W boson	m_W	80.385(15) GeV	80.385(15) GeV
Mass of Z boson	m_Z	91.1876(21) GeV	91.1876(21) GeV

Table 3.1: Values of the parameters of the electroweak theory, from [116].

In the calculation of VBS processes, these parameters have to be set consistently in order to ensure gauge invariance and the restoration of unitarity in VBS through cancellation of VBS- and Higgs diagrams (cf. Section 2.2.3). Therefore, the electroweak coupling scheme should be chosen in such a way that tree-level relationships between the parameters are valid. For consistent comparison with data, it is required to reproduce kinematical properties, usually ensured by using physical boson masses.

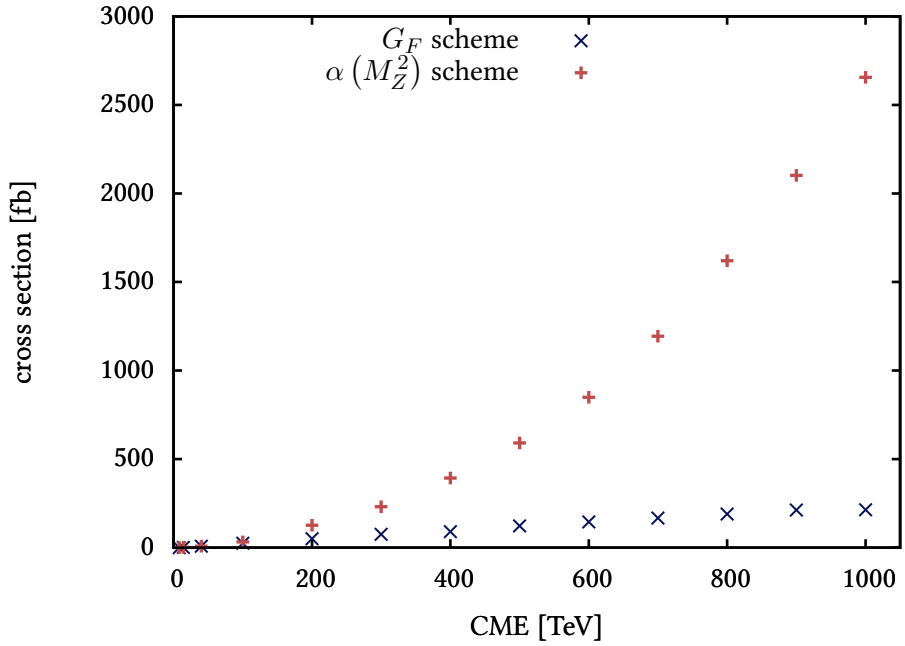

Figure 3.8: Dependence of cross section on the center-of-mass energy (CME) for the $W^{\pm}W^{\pm}jj$-EW process generated at NLO using VBFNLO [111] in the VBS phase space (p. 95). While the slightly larger phase space leads to a small cross section rise in the case of the G_F scheme (blue), the cross section increases rapidly when the $\alpha(M_Z)$ scheme is used (red).

Therefore, the most common choice of electroweak scheme respecting these requirements, is the so-called G_F (or G_μ) scheme, in which the electromagnetic coupling constant α and the weak mixing angle θ_W are determined from experimentally measured values of the vector boson masses M_W, M_Z, and the Fermi constant G_F. The vector boson masses are related to the weak mixing angle according to

$$\sin^2\theta_W = 1 - \frac{M_W^2}{M_Z^2}.$$

Thus, the electromagnetic coupling constant α can be derived using

$$\alpha = M_Z^2 \cos^2\theta_W \sin^2\theta_W \frac{\sqrt{2}\,G_F}{\pi} \approx 1/132.2.$$

If, instead, all parameters are set to their experimentally measured values, a common choice for α is to use its value at the Z-mass scale, $\alpha(M_Z^2) = 1/128.944$, for the electroweak coupling. This is often called the $\alpha(M_Z^2)$ scheme. Another approach uses the measured value for α at the $Q^2 = 0$ scale, $\alpha(0) \approx 1/137$, called the $\alpha(0)$ scheme [117, Sec. 2.1]. Figure 3.8 shows the increase of the $W^{\pm}W^{\pm}jj$-EW cross section when the G_F scheme is not used.

Moreover, the G_F scheme has been found to minimize EW higher-order corrections, e.g. for the process of W boson production [117]. If not noted otherwise, the G_F scheme is used for $VVjj$-EW production throughout this work.

Particle masses and widths Particle masses of the electroweak gauge bosons, Higgs boson, charged leptons and quarks have to be set for the generation. In most applications, the values collected by the Particle Data Group [116] can be used. Light quark, electron and muon masses can be set to zero, while the τ mass should be set to its physical value in order for the decay to be correctly modelled.

After the 2012 discovery, the Higgs mass is commonly set to $m_H = 125$ or 126 GeV. Correspondingly, the width of the Higgs boson is set to $\Gamma_H = 4.07$ MeV, determined according to the SM for $m_H = 125$ GeV [118].

Parton distribution functions A variety of parton distribution functions exists. Each choice introduces an experimental uncertainty which can be evaluated according to the prescription in Section 5.3.2.

Factorization and renormalization scales As introduced in Section 3.1.2, two unphysical scales need to be defined in the MC production: the factorization and renormalization scales. The choice of factorization and renormalization scales is highly process dependent and is aimed at finding a scale which has small impact on crucial differential cross sections as well as on the total cross section, in order for the measurement to have a scale uncertainty as small as possible. In general, a scale close to a characteristic energy scale of the event should be chosen. Several different ansätze exist: The scales can be set to fixed values or, as a *dynamic scale*, determined for each event from its kinematic properties according to a chosen prescription. In the case of VBS, natural choices for the scales can be chosen as

- the invariant mass of the VV system, $M(VV)$, as determined from the bosons' decay products
- the momentum transfer of the exchanged gauge boson,
- a combination of the kinematic properties of jets j_i and weak gauge bosons V_i, such as ([119])

$$\mu_{R,F} = \frac{1}{2}\left(\sum_{i=1,2} p_{\mathrm{T}}(j_i) + \sqrt{M^2(V_i) + p_{\mathrm{T}}^2(V_i)}\right) \tag{3.4}$$

  or ([120])

$$\mu_{R,F} = \frac{1}{2}\left(\sum_{i=1,2} p_{\mathrm{T}}(j_i) \exp|y(j_i) - y_{12}| + \sqrt{p_{\mathrm{T}}^2(V_i) + M^2(V_i)}\right) \tag{3.5}$$

  with $y_{1,2} = (y(j_1) + y(j_2))/2$, where $y(j_i)$ denotes the rapidity of jet i and $p_{\mathrm{T}}(j_i)$ its transverse momentum. The invariant mass of the weak boson k is $M(V_k)$ and its transverse momentum is $p_{\mathrm{T}}(V_k)$.

The latter choice of scale (3.5) has been recently shown to lead to a k-factor less dependent on the invariant mass M_{jj} and on the rapidity difference $\Delta y(jj)$ of the tagging jets [120]. The scale uncer-

tainties for the $W^{\pm}W^{\pm}jj$-EW production are evaluated in Section 5.3.2, where Equation 3.4 is used for the central value.

In the case of using an effective field theory with anomalous couplings (see Section 2.3.3), the choice of scale needs to be adapted to the conditions of the anomalous couplings. In the case of anomalous triple gauge couplings, a fixed scale can lead to unphysical results when using an effective theory. This behavior has been shown to be cured by using a dynamic scale [121]. For the anomalous quartic gauge couplings in the $W^{\pm}W^{\pm}jj$-EW channel considered in this work, a scale dependence study was conducted, see section 5.5.4.

3.2.3 Interference between purely electroweak and QCD-mediated di-boson plus di-jet production

Interference can occur between diagrams from the purely electroweak $VVjj$ production and diagrams from QCD-mediated $VVjj$ production with the same initial and final states. The phase space integral over the full matrix element of $VVjj$ production, $\mathcal{M}_{\mathrm{EWQCD}}$, contains the sum of the matrix elements of $VVjj$-EW ($\mathcal{M}_{\mathrm{EW}}$) and $VVjj$-QCD ($\mathcal{M}_{\mathrm{QCD}}$), including interference terms $\mathcal{M}_{\mathrm{INT}}$,

$$\begin{aligned}\int \mathrm{d}\Phi|\mathcal{M}_{\mathrm{EWQCD}}|^2 &= \int \mathrm{d}\Phi|\mathcal{M}_{\mathrm{EW}} + \mathcal{M}_{\mathrm{QCD}}|^2 \\ &= \int \mathrm{d}\Phi \left[\mathrm{Re}^2(\mathcal{M}_{\mathrm{EW}}) + \mathrm{Im}^2\,\mathcal{M}_{\mathrm{EW}} + \mathrm{Re}^2(\mathcal{M}_{\mathrm{QCD}}) + \mathrm{Im}^2\,\mathcal{M}_{\mathrm{QCD}}\right] \\ &+ \int \mathrm{d}\Phi \left[2(\mathrm{Re}(\mathcal{M}_{\mathrm{EW}})\,\mathrm{Re}(\mathcal{M}_{\mathrm{QCD}}) + \mathrm{Im}(\mathcal{M}_{\mathrm{EW}})\,\mathrm{Im}(\mathcal{M}_{\mathrm{QCD}}))\right] \\ &= \int \mathrm{d}\Phi \left[|\mathcal{M}_{\mathrm{EW}}|^2 + |\mathcal{M}_{\mathrm{QCD}}|^2 + |\mathcal{M}_{\mathrm{INT}}|^2\right]. \end{aligned} \tag{3.6}$$

As the total cross section $\sigma_{\mathrm{EWQCD}} \sim \int \mathrm{d}\Phi|\mathcal{M}_{\mathrm{EWQCD}}|^2$, these terms can be identified as

$$\sigma_{\mathrm{EWQCD}} = \sigma_{\mathrm{EW}} + \sigma_{\mathrm{QCD}} + \sigma_{\mathrm{INT}}, \tag{3.7}$$

where the interference term

$$\sigma_{\mathrm{INT}} \sim \int \mathrm{d}\Phi \left[\mathrm{Re}(\mathcal{M}_{\mathrm{EW}})\,\mathrm{Re}(\mathcal{M}_{\mathrm{QCD}}) + \mathrm{Im}(\mathcal{M}_{\mathrm{EW}})\,\mathrm{Im}(\mathcal{M}_{\mathrm{QCD}})\right] \tag{3.8}$$

contains the phase space integral over products of the electroweak and the QCD-mediated $VVjj$ production matrix elements. Since the major contributions of $\mathcal{M}_{\mathrm{EW}}$ and $\mathcal{M}_{\mathrm{QCD}}$ are expected to occur in different regions of phase space, interference is generally expected to be small compared to the total cross section σ_{EWQCD}.

The size of σ_{INT} depends on the diboson flavors and the phase space definition. It is expected to be small especially in channels which contain gluons in the initial states of $VVjj$-QCD production. In $W^{\pm}W^{\pm}jj$-QCD production, no diagrams with gluons in the initial state are possible. Therefore,

interference is relatively large in $W^{\pm}W^{\pm}jj$ production (see Section 3.3.4) compared to other channels.

Table 3.2 shows how the interference contribution differs between the different channels of flavor combinations of the electroweak bosons. The largest share of the interference with respect to the total cross section is present in the $W^{\pm}W^{\pm}jj$ channel, where $\sigma_{\mathrm{INT}}/\sigma_{\mathrm{EWQCD}} = 7\,\%$. In the $W^{\pm}W^{\mp}jj$ and $W^{\pm}Zjj$ production channels, the interference contributes less than 1 % to the total cross section σ_{EWQCD}, while it contributes $\sigma_{\mathrm{INT}}/\sigma_{\mathrm{EWQCD}} \approx 2\,\%$ in $ZZjj$.

However, interference contributions are not negligible with respect to the electroweak production mechanism in this rather loose VBS-like phase space with $M_{qq} > 150\,\mathrm{GeV}$ (Table 3.2): Compared to the purely electroweak production cross sections, the interference amounts to 15 % for $W^{\pm}W^{\pm}jj$, 5 % for $W^{\pm}W^{\mp}jj$, 15 % for $W^{\pm}Zjj$, and 21 % for $ZZjj$. Stricter selection of a VBS topology can reduce this contribution as the contribution of VVjj-QCD decreases (cf. Sec. 3.3.4).

3.2.4 Various channels of gauge boson flavors

The general settings for $VVjj$ production can be applied to any configuration of gauge boson flavors with leptonic decay. Possible processes and their cross sections at 8 TeV center-of-mass energy, as well as the interference contribution between $\sigma(VVjj{-}\mathrm{EW})$ and $\sigma(VVjj{-}\mathrm{QCD})$ are listed in Table 3.2.

Final state	σ(EW) [fb]	σ(QCD) [fb]	σ(EWQCD) [fb]	σ(INT) [fb]	$\frac{\sigma(VVjj-\mathrm{EW})}{\sigma(VVjj-\mathrm{QCD})}$
$W^{\pm}W^{\pm}jj$	83.4 ± 0.2	84.7 ± 0.2	180.4 ± 0.4	12.3 ± 0.5	0.98 ± 0.005
$W^{\pm}W^{\mp}jj$	394.4 ± 0.9	6572.0 ± 6.1	6985.0 ± 6.5	18.6 ± 8.9	$0.06 \pm 2 \times 10^{-4}$
$W^{\pm}Zjj$	124.0 ± 0.4	2183.0 ± 2.2	2325.0 ± 2.3	18.0 ± 3.1	$0.06 \pm 2 \times 10^{-4}$
$ZZjj$	31.0 ± 0.1	327.5 ± 0.3	365.3 ± 0.4	6.8 ± 0.5	$0.01 \pm 4 \times 10^{-4}$

Table 3.2: Cross sections determined with the MadGraph generator for electroweak and QCD-mediated production of $VVjj$ final states of different VV combinations at a center-of-mass energy of $\sqrt{s} = 8\,\mathrm{TeV}$ generated with a $M_{jj} > 150\,\mathrm{GeV}$ cut. The cross sections are given for the full $VVjj$ final state not taking into account the decay modes of the bosons. Heavy flavor contributions (b quarks in the initial and final states) are not included.

The $W^{\pm}W^{\pm}jj$ channel has the highest ratio of the purely electroweak to QCD-mediated production. Interference contributes significantly to the full process. The $W^{\pm}W^{\pm}jj$ channel is different to the other channels in that no diagrams with gluons in the initial state exist for the QCD-mediated production. This is the reason for both the relatively low $VVjj$-QCD cross section and also the comparatively large interference. Owing to its good $\sigma(VVjj\text{-EW})/\sigma(VVjj\text{-QCD})$ ratio, this channel is the first one to be observed significantly at the ATLAS and CMS experiments ([56, 122]).

The $W^{\pm}W^{\mp}jj$ final state cross sections in Table 3.2 do not include b-quarks in the initial state, thus $t\bar{t}$ pair production and single-*top* production with associated W bosons is not included. The large background from $t\bar{t}$ is the main reason that $W^{\pm}W^{\mp}jj$-EW has not been measured at the LHC.

The $W^{\pm}Zjj$ final state features a similarly small $\sigma(VVjj\text{-EW})/\sigma(VVjj\text{-QCD})$ ratio. In this case, heavy flavors contribute both to the electroweak as well as to the QCD-mediated production channels. The $W^{\pm}Zjj$-EW process has not been significantly observed at the LHC, but its measurement and

limits on anomalous couplings are in preparation at ATLAS in the fully leptonic channel [123].

Electroweak production of $ZZjj$ has a very low cross section and its $\sigma(VVjj\text{-EW})/\sigma(VVjj\text{-QCD})$ ratio is smaller than that of the other channels. Therefore, despite its low background at the LHC, no measurement of $ZZjj$-EW exists up to now.

3.2.5 Definition of generation phase space for vector boson scattering

Topology of VBS events

The topology of VBS events determines the definition of the generation phase space for $VVjj$ production samples. Figure 3.9 shows a topological sketch of a typical VBS-like event. It contains two highly energetic jets, the so-called *tagging jets*, and the decay products of the gauge bosons. This sketch depicts production of two W bosons which decay leptonically, resulting in two charged leptons and missing transverse momentum $E_{\mathrm{T}}^{\mathrm{miss}}$.

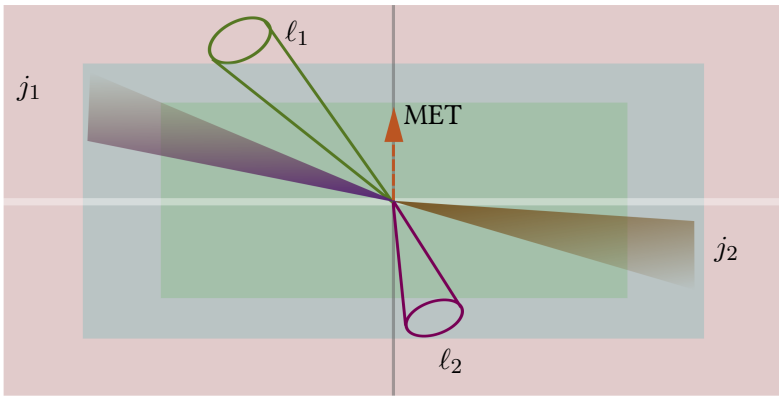

Figure 3.9: Topology of a typical vector boson scattering event with two W bosons in the final state. The tagging jets j_1 and j_2 are produced at large $|\eta|$ and large difference in η. The charged leptons from the decay of the W bosons can be found more centrally in the detector. The neutrinos are invisible but their combined transverse momentum can be determined as missing transverse energy in the event.

The decay products of the bosons tend to be central, while the jets are largely separated in pseudorapidity. Due to the lack of color flow in the central region in purely electroweak $VVjj$ production, little hadronic activity is expected in the region between the tagging jets. Thus, kinematic cuts aimed at tagging the VBS process include cuts on the invariant mass of tagging jets, their distance in pseudorapidity, as well as requiring the leptonic decay products of the gauge bosons to be found at smaller pseudorapidity than the tagging jets. Kinematic distributions illustrating the VBS topology for the $W^{\pm}W^{\pm}jj$ channel are shown in Section 3.3.1.

When defining the generation phase space for $VVjj$-EW events, this topology needs to be taken into account. Singularities in the matrix element should be excluded by omitting the corresponding phase space region. At the same time, the generation phase space is required to be sufficiently inclusive to contain all signal contributions as well as contributions possibly migrating into the signal region during the parton shower or during the full simulation stage.

Tagging jets separation

The tagging jets tend to be produced rather forward in the detector and with large momentum (cf. Figure 3.12a and 3.12b). Thus, their invariant mass and pseudorapidity difference are two crucial variables for tagging a VBS process.

For matrix-element event generation, the jets are defined as partons required to have a certain momentum and $\Delta R(jj)$ distance in order to omit singularities. Taking advantage of the tagging jet properties, it is also possible to apply a cut on M_{jj} during the generation. However, this cut needs to be inclusive enough to provide for migration effects from parton shower (cf. Page 55).

Dilepton kinematics

Divergences of the matrix element are unphysical and need to be rejected by removing the corresponding phase space from the generation phase space. To this effect, cuts on the transverse momenta of leptons and jets are applied at parton level. Also, divergences in dilepton observables such as the invariant mass of two opposite-charge leptons need to be removed. In the context of VBS channels, the final states of $W^{\pm}W^{\mp}jj$, $ZZjj$, and $WZjj$ are affected. Divergencies occur e.g. in diagrams such as depicted in Figure 3.10, where a photon decays into two opposite-charge leptons. A cut on the invariant mass of the two leptons, $M_{\ell\ell}$, should hence be applied.

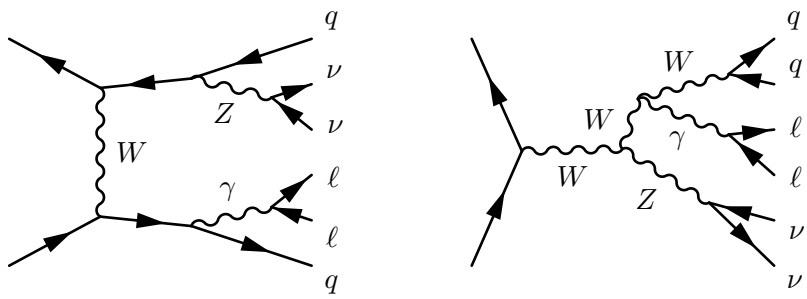

Figure 3.10: Feynman diagrams included in electroweak $\ell^+\ell^-\nu\nu jj$ production which lead to a divergence in the low dilepton mass spectrum. Similar diagrams occur in the $\ell\ell\ell\nu jj$ final state.

In addition to physical divergences, it is necessary to optimize the cuts and the number of sampling points in order to avoid integrator difficulties with large logarithmic terms in the neighborhood of such divergences [124].

3.2.6 Higher order corrections in Monte Carlo simulation for vector boson scattering

All previous considerations on MC generation for VBS processes can be extended to include higher order corrections in the matrix-element calculation of the VBS process, both from QCD and from electroweak interactions. Calculations at NLO in QCD are available for $W^{\pm}W^{\pm}jj$-QCD production [125] and for $W^{\pm}W^{\pm}jj$-EW production [120, 126, 127]. The NLO corrections have an effect of up to $\sim 10\,\%$ with respect to the LO result [127].

In terms of MC programs, QCD corrections at NLO are implemented for several channels of $VVjj$-EW and $VVjj$-QCD in the generators VBFNLO [111] and PowhegBox [112] (cf. Section 3.2.7). Special care has to be taken to match the resulting NLO matrix element to the parton shower (cf. Section 3.1.4).

Electroweak higher order corrections have not been calculated in any channel of diboson production associated with dijets so far. Some calculations exist in diboson production without associated jets [128, 129], and efforts to extend this to $VVjj$ production are under way [130]. Calculations using a logarithmic high-energy approximation as well as the equivalent vector-boson approximation for VBS at an electron-positron collider predict an effect of $-10\,\%$ to $-50\,\%$ with respect to the leading-order cross section [131].

3.2.7 Monte Carlo Generators for vector boson scattering

Various generators are available for the simulation of $VVjj$-EW processes. General-purpose event generators like Sherpa [102] and Whizard [107], capable of generating $2 \rightarrow 6$ particle matrix-elements, allow to automatically simulate $VVjj$ processes. Other generators contain dedicated implementations of these processes, such as Pythia8 [103, 104], VBFNLO [111], and PowhegBox [112]. The following paragraph introduces the most relevant generators used for MC generation of VBS processes in this work.

Whizard

Whizard [132] is a general-purpose leading-order event generator applicable to physics processes at the LHC and at all other high-energy particle physics experiments, in particular the future ILC. Its matrix-element generator O'Mega automatically produces matrix-element code for the desired process with up to eight final state particles. The integration over phase space is carried out by the VAMP [133] algorithm. Based on the integration, partonic events can be generated, and a parton shower algorithm can be applied using external tools (e.g. Pythia8) or a built-in analytic parton shower [134].

Whizard is particularly interesting for VBS as it provides an implementation of additional resonances and anomalous gauge couplings with K-matrix unitarization as described in chapter 3.4 [73].

VBFNLO and PowhegBox

Several vector boson scattering and fusion channels are implemented in the VBFNLO and PowhegBox programs. The implemented matrix-elements are computed at NLO in QCD and can be integrated over the desired phase space to determine the respective cross sections.

VBFNLO can generate events based on the leading-order processes. PowhegBox is an implementation of the POWHEG method [135] allowing to apply a parton shower to NLO events and taking care of the matrix-element to parton shower matching.

Sherpa

The general-purpose MC generator `Sherpa` provides leading-order matrix-element integration and event generation for general processes at high-energy colliders. It provides two built-in matrix-element generators for the matrix-element generation, as well as a phase space integrator to compute cross sections and generate unweighted events. Furthermore, modules for parton showering, multi-parton interactions, and the matching of parton shower and matrix-element are available. The latter allows for the generation of a matrix-element of the leading-order process with an additional multiplicity of real emissions, which are matched consistently to the matrix-element based on the CKKW method [99]. In general, this approach improves the description of data [136]. In VBS it is intended for the more accurate description of the hadronic activity between the tagging jets.

Pythia

In the scope of this work, the event generator `Pythia8` is used primarily for its parton shower algorithm applied to parton-level events produced by other generators. However, it is also possible to generate VBS processes within `Pythia` [20]. In that case, the $pp \to \ell\ell\nu\nu$ process is factorized in the emission of W bosons, their scattering, and their consequent decay into leptons. To this effect, the effective W boson approximation (EWA) [53] is used. At current experiments and with currently available MC tools, the EWA approach is less favored, as it does not reproduce the results of the full integration [73].

3.3 Scattering of two same-charge W bosons

As concluded in the previous section, the $W^{\pm}W^{\pm}jj$ final state is particularly suited for the first measurement of a $VVjj$-EW process, as its ratio of electroweak to QCD-mediated $VVjj$ production is the highest of all channels (cf. Table 3.2). Several aspects relevant to MC simulation of the $W^{\pm}W^{\pm}jj$ channel have been studied in the scope of this work and are described in this section.

3.3.1 Comparison of $W^{\pm}W^{\pm}jj$-EW and $W^{\pm}W^{\pm}jj$-QCD

Vector boson scattering is a subprocess of electroweak $VVjj$ production which is not separable in a gauge invariant way (see Section 3.2.1). A VBS-like phase space in $W^{\pm}W^{\pm}jj$ includes cuts which enhance the contribution from $W^{\pm}W^{\pm}jj$-EW while suppressing the QCD-mediated component. Optimal cuts can be identified from kinematic distributions such as those shown in this section.

Figures 3.11a to 3.16b show kinematic distributions of the $W^{\pm}W^{\pm}jj$-EW and $W^{\pm}W^{\pm}jj$-QCD processes in a rather loose phase space, corresponding to the extended fiducial volume of the $W^{\pm}W^{\pm}jj$ measurement defined on Page 95.

The two hardest, i.e. the jets with highest transverse momentum in the event, passing the selection are considered as tagging jets used to tag the VBS process. In the case of electroweak $VVjj$ production,

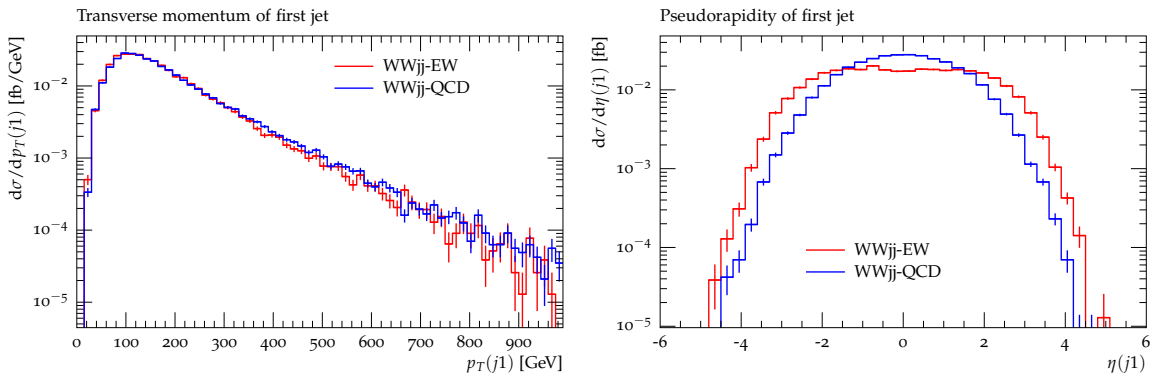

(a) Transverse momentum $p_{\mathrm{T}}(j1)$ of the jet with largest p_{T} in the event.

(b) Pseudorapidity $\eta(j1)$ of the jet with largest p_{T} in the event.

Figure 3.11: Kinematic distributions of the $pp \to W^{\pm}W^{\pm}jj$ channel comparing the electroweak and QCD-mediated production mechanisms. The red and the blue histograms show the contributions of $W^{\pm}W^{\pm}jj$-EW and $W^{\pm}W^{\pm}jj$-QCD, respectively. Statistical uncertainties from MC generation are indicated by error bars. Both histograms are normalized to the same cross section.

the tagging jets are found at larger values of pseudorapidity than in the case of $W^{\pm}W^{\pm}jj$-QCD (see Figure 3.11a). Their transverse momentum p_{T} is slightly smaller than the p_{T} of the two hardest jet in $W^{\pm}W^{\pm}jj$-QCD production (see Figure 3.11b). This indicates that the highest p_{T} might not be the best criterion for the selection of the tagging jets. However, experimentally, a high p_{T} is required in order to avoid contamination from pile-up jets.

The dijet properties, however, are very good indicators for tagging the VBS process: The rapidity separation (figure 3.12a) as well as the invariant mass of the tagging jets (figure 3.12b) tend to larger values for the $W^{\pm}W^{\pm}jj$-EW process than in the $W^{\pm}W^{\pm}jj$-QCD process.

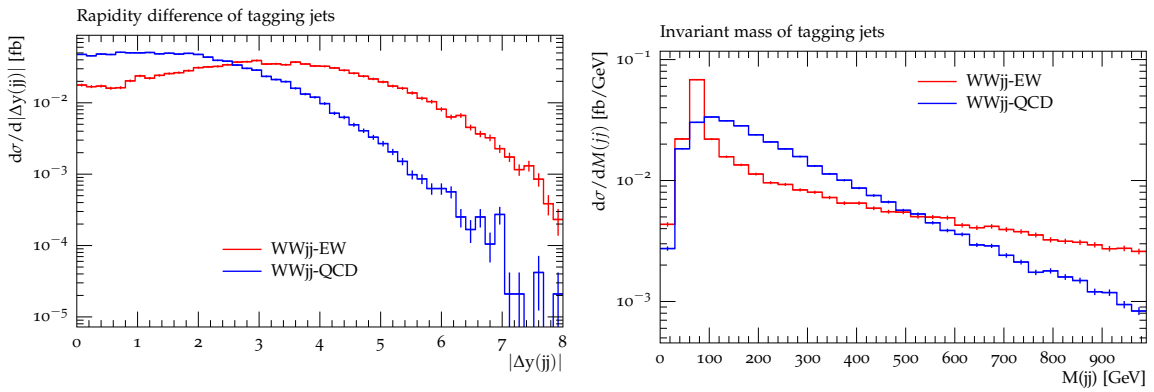

(a) Separation of rapidity $|\Delta y(jj)|$ of the tagging jets.

(b) Invariant mass of the tagging jets, M_{jj}.

Figure 3.12: Kinematic distributions of the $pp \to W^{\pm}W^{\pm}jj$ channel comparing the electroweak and QCD-mediated production mechanisms. The red and the blue histograms show the contributions of $W^{\pm}W^{\pm}jj$-EW and $W^{\pm}W^{\pm}jj$-QCD, respectively. Statistical uncertainties from MC generation are indicated by error bars. Both histograms are normalized to the same cross section.

Comparing the η coordinate of the tagging jet with the largest $|\eta|$ (Figure 3.13a) to the η coordinate of the tagging jet with the smaller $|\eta|$ (Figure 3.13b), one of the jets tends to be produced rather centrally, while the other one moves in forward direction. This is valid for both $W^{\pm}W^{\pm}jj$-EW and $W^{\pm}W^{\pm}jj$-QCD events. However, in the electroweak production, the absolute pseudorapidity of both jets is larger than in $W^{\pm}W^{\pm}jj$-QCD. The jet with higher $|\eta|$ is produced much more forward in $W^{\pm}W^{\pm}jj$-EW events.

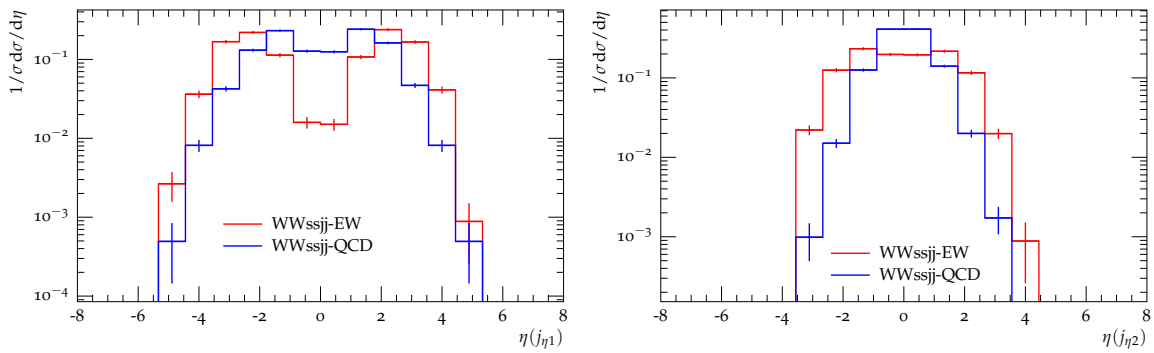

(a) Pseudorapidity of the tagging jet with largest pseudorapidity

(b) Pseudorapidity of the tagging jet with second largest pseudorapidity

Figure 3.13: Kinematic distributions of tagging jets in the $pp \to W^{\pm}W^{\pm}jj$ channel comparing the electroweak and QCD-mediated production mechanisms. The red and the blue histograms show the contributions of $W^{\pm}W^{\pm}jj$-EW and $W^{\pm}W^{\pm}jj$-QCD, respectively. Loose VBS like cuts (3.11), including $M_{jj} > 150$ GeV, are applied. Both histograms are normalized to the same cross section. Statistical uncertainties from MC generation are indicated by error bars.

Another measure for the tagging jet separation is the product of their η coordinates (Figure 3.14). This variable is widely used in VBS studies to separate from $VVjj$-QCD background [55]. As Figure 3.14 shows, the pseudorapidity product is rather symmetric for $VVjj$-QCD, while there is a strong preference for the tagging jets to lie on opposite hemispheres, i.e. $\eta(j_1) \times \eta(j_2) < 0$, for $VVjj$-EW.

The W bosons tend to scatter at small pseudorapidities in the collision. Thus, their visible decay products, the charged leptons, are found at smaller values of pseudorapidity than the leptons in $W^{\pm}W^{\pm}jj$-QCD events (Figure 3.15a). The neutrinos from the W decay can only be partially observed as missing momentum in the transverse plane. The $E_{\mathrm{T}}^{\mathrm{miss}}$distribution from $W^{\pm}W^{\pm}jj$-EW events (Figure 3.15b) tends to slightly larger values than the one from $W^{\pm}W^{\pm}jj$-QCD events.

The transverse momenta of leptons from $W^{\pm}W^{\pm}jj$-EW events are slightly larger than those of leptons from $W^{\pm}W^{\pm}jj$-QCD production (fig. 3.16a), while the dilepton invariant mass $M_{\ell\ell}$ is smaller in the case of $W^{\pm}W^{\pm}jj$-EW (fig. 3.16b), indicating that both W bosons decay in the center of the detector.

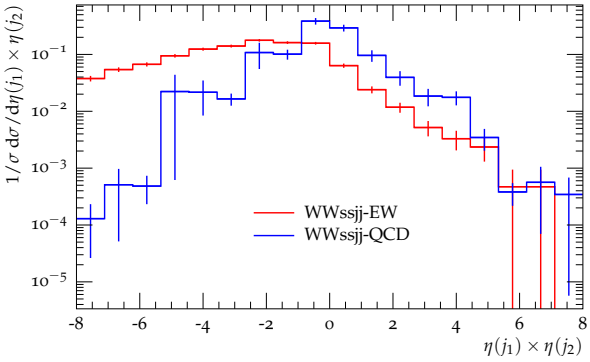

Figure 3.14: Product of pseudorapidity coordinates of the two tagging jets in the $pp \to W^{\pm}W^{\pm}jj$ channel comparing the electroweak and QCD-mediated production mechanisms. The red and the blue histograms show the contributions of $W^{\pm}W^{\pm}jj$-EW and $W^{\pm}W^{\pm}jj$-QCD, respectively. Loose VBS like cuts (3.11), including $M_{jj} > 150$ GeV, are applied. Both histograms are normalized to the same cross section. Statistical uncertainties from MC generation are indicated by error bars.

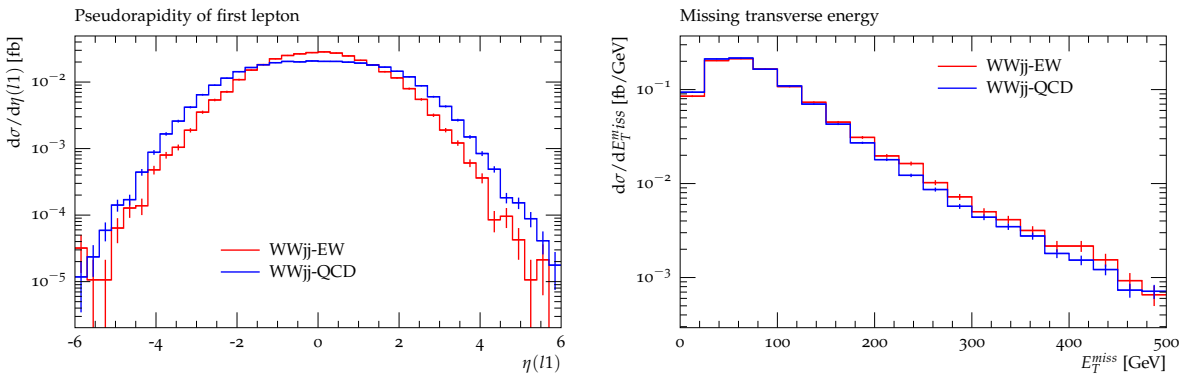

(a) Pseudorapidity of the first lepton $\eta(\ell 1)$

(b) Missing transverse momentum, $E_{\mathrm{T}}^{\mathrm{miss}}$

Figure 3.15: Kinematic distributions of leptonic decay products of the W bosons in the $pp \to W^{\pm}W^{\pm}jj$ channel comparing the electroweak and QCD-mediated production mechanisms. The red and the blue histograms show the contributions of $W^{\pm}W^{\pm}jj$-EW and $W^{\pm}W^{\pm}jj$-QCD, respectively. Statistical uncertainties from MC generation are indicated by error bars. Both histograms are normalized to the same cross section.

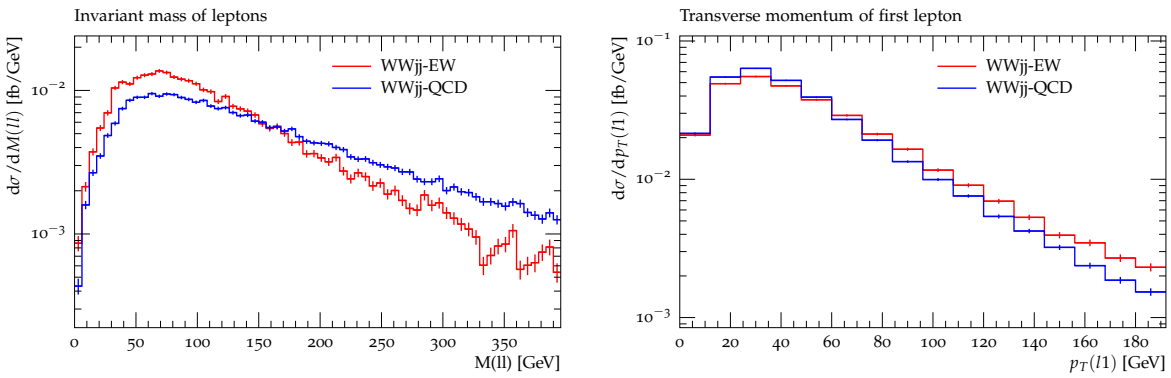

(a) Invariant mass of the two leptons $M_{\ell\ell}$

(b) Transverse momentum of the first lepton

Figure 3.16: Kinematic distributions of leptonic decay products of the W bosons in the $pp \to W^{\pm}W^{\pm}jj$ channel comparing the electroweak and QCD-mediated production mechanisms. The red and the blue histograms show the contributions of $W^{\pm}W^{\pm}jj$-EW and $W^{\pm}W^{\pm}jj$-QCD, respectively. Statistical uncertainties from MC generation are indicated by error bars. Both histograms are normalized to the same cross section.

3.3.2 VBS topology in $W^{\pm}W^{\pm}jj$

Taking into account the observations from the comparison between $W^{\pm}W^{\pm}jj$-EW and $W^{\pm}W^{\pm}jj$-QCD as well as the considerations for generation of VBS in general (Section 3.2.2), the phase space and parameters for the conducted generator studies are defined as follows.

The process is set up as $pp \to \ell^{\pm}\ell^{\pm}\nu\nu jj$ with $\alpha_s = 0$ for the electroweak production. All quark flavors are allowed in the initial and final states. No diagrams with gluons exist.

The full sample phase space is constrained by the following cuts:

$$\begin{aligned} &\text{Leptons}: \; p_{\mathrm{T}} > 8\,\mathrm{GeV}, |\eta| < 5; \\ &\text{Jets}: \; p_{\mathrm{T}} > 15\,\mathrm{GeV}, |\eta| < 5; \\ &\text{and } \Delta R(jj) > 0.4. \end{aligned} \tag{3.9}$$

In the VBS-like phase space, events are selected according to

$$\begin{aligned} &\text{Jets}: \; p_{\mathrm{T}} > 30\,\mathrm{GeV}, |\eta| < 4.9; \\ &\text{Leptons}: \; p_{\mathrm{T}} > 25\,\mathrm{GeV}, |\eta| < 2.5; \\ &E_{\mathrm{T}}^{\mathrm{miss}} > 40\,\mathrm{GeV}; \\ &M_{jj} > 500\,\mathrm{GeV}, \text{and } |\eta(jj)| > 2.4. \end{aligned} \tag{3.10}$$

The factorization and renormalization scales are set to the same value of $\mu_R = \mu_R = 2m_W$. The PDF set CTEQ6L1, a general purpose PDF based on leading-order cross section fits and NLO α_s [137], is used.

3.3.3 Resonant and non-resonant contributions to the final state $\ell^\pm\nu\ell^\pm\nu jj$

In addition to the production of two jets with two leptonically decaying resonant W bosons, the final state of $\ell^\pm\nu\ell^\pm\nu jj$ includes contributions from non-resonant production of leptons and neutrinos, for instance as in fig. 3.7. As the non-resonant contributions are not gauge invariantly separable from the $VVjj$-EW diagrams, they need to be included in the MC generation. In most generators, it is also possible to generate the process with resonant production of two W bosons separately.

Using `Whizard`, the two cases are compared in the following. In the *restricted* case, the process is specified as purely electroweak $pp \to jjW^\pm W^\pm \to jj\ell^\pm\ell^\pm\nu\nu$. The *inclusive* process contains all diagrams contributing to purely electroweak $pp \to jj\ell^\pm\ell^\pm\nu\nu$. The cross sections of the full samples are compared in Table 3.3. Selection cuts are applied according to (3.9) and (3.10).

	Inclusive diagrams: $pp \to jj\ell^\pm\ell^\pm\nu\nu$ (EW)	Restricted diagrams: $pp \to jjW^\pm W^\pm \to jj\ell^\pm\ell^\pm\nu\nu$ (EW)
Full sample	7.20 fb	8.19 fb
VBS cuts	0.25 fb	0.53 fb

Table 3.3: Comparison of inclusive and restricted cross sections

The cross section of the restricted process is higher than the one of the inclusive process owing to missing negative terms which lead to higher momenta of jets and leptons. This is illustrated in fig. 3.17a and 3.17b. Higher lepton and jet momenta also lead to a larger acceptance to the VBS region (Table 3.3).

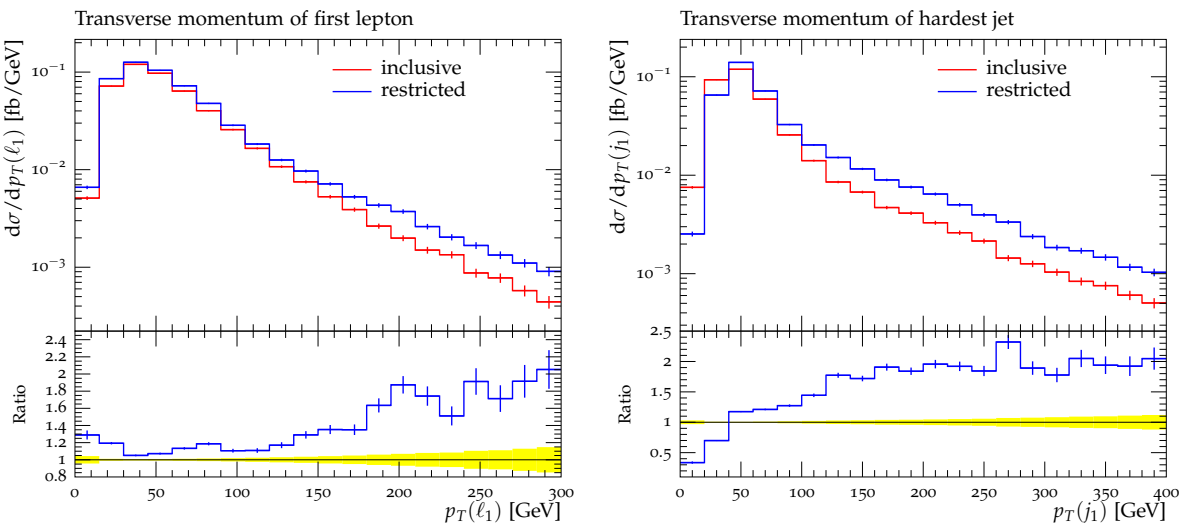

(a) Transverse momentum of hardest lepton

(b) Transverse momentum of hardest jet

Figure 3.17: Differential cross sections distributed according to the transverse momentum of the hardest lepton (left) and hardest jet (right) comparing the inclusive production process $pp \to jj\ell^\pm\ell^\pm\nu\nu$ to the resonant diboson pair production ($pp \to jjW^\pm W^\pm \to jj\ell^\pm\ell^\pm\nu\nu$).

The contribution in the Breit-Wigner peak region at the W boson mass is larger for the restricted production of resonant $W^{\pm}W^{\pm}jj$ (fig. 3.18a). Restricting the generation to resonant W bosons also has an influence on event properties used to tag the VBS topology, such as the pseudorapidity difference of the tagging jets as illustrated in Figure 3.18b.

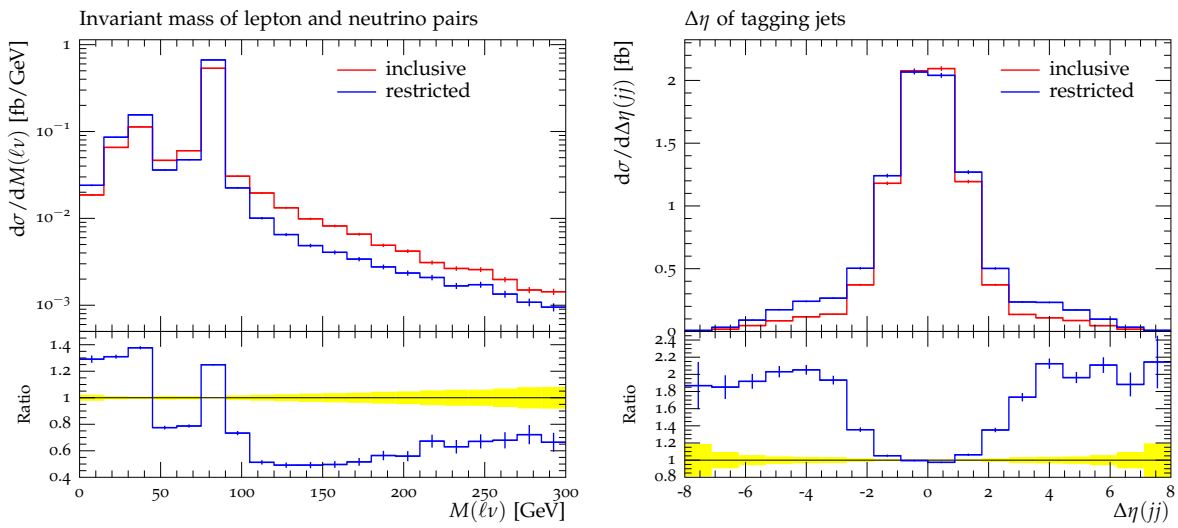

(a) Invariant mass of lepton and neutrino pairs (b) Pseudorapidity difference of the two hardest jets.

Figure 3.18: Differential cross sections comparing the inclusive production process $pp \to jj\ell^{\pm}\ell^{\pm}\nu\nu$ to the resonant diboson pair production ($pp \to jjW^{\pm}W^{\pm} \to jj\ell^{\pm}\ell^{\pm}\nu\nu$).

3.3.4 Interference of electroweak and QCD-mediated production

As described in Section 3.2.3, the interference between the $VVjj$-EW and $VVjj$-QCD channels is most relevant for the $W^{\pm}W^{\pm}jj$ process. Reasons are the lack of diagrams with gluons in the initial state at leading-order as well as the fact that only left-chiral quarks contribute to both $VVjj$-EW and $VVjj$-QCD [120].

It has been shown in [120] and [138] that the contribution of the interference decreases with respect to the $VVjj$ contribution when stricter VBS phase space cuts are applied, such as a cut on M_{jj}.

3.3.5 Higgs mass dependence

In an inclusive phase space with no strict VBS cuts applied, the $VVjj$-EW cross section shows a dependence on the mass of the Higgs boson. Diagrams with a s-channel Higgs exchange exist in the case of triple vector-boson production, which contributes to the $VVjj$-EW process. One example diagram with resonant Higgs-strahlung, where the Higgs decays to a W boson pair, is depicted in Figure 3.19a.

The inclusive cross section of $VVjj$-EW production thus depends on the mass and width of the Higgs boson. This is illustrated in Figure 3.19b. The contribution from diagrams with resonant Higgs-exchange can be suppressed with a phase space cut on the invariant mass of the tagging jets M_{jj},

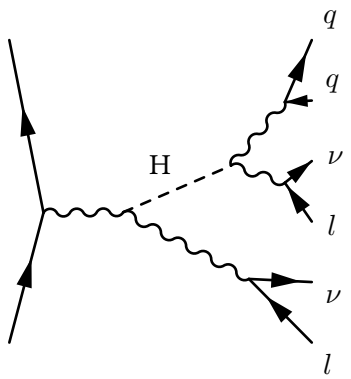

(a) Production of a Higgs boson associated with a W boson, where the Higgs decays into a WW pair. If one of the W bosons from the Higgs decays hadronically, and the other one leptonically, this yields a $W^{\pm}W^{\pm}jj$ final state.

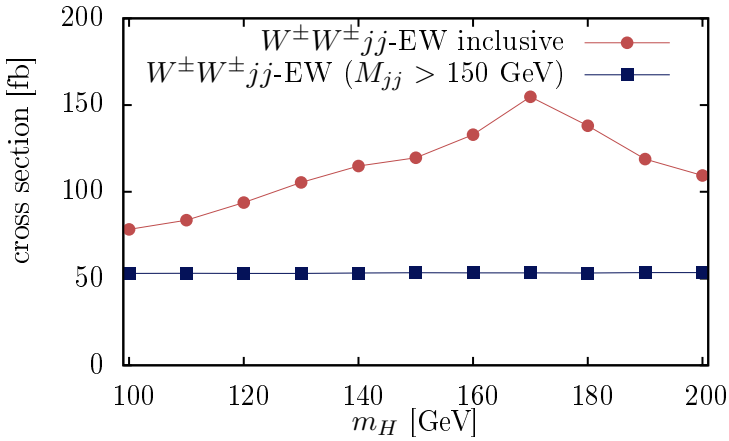

(b) Dependence of the $VVjj$-EW production cross-section on the mass and corresponding width of the SM Higgs boson. The red curve shows the cross section for inclusive $VVjj$-EW production, while a cut $M_{qq} > 150$ GeV is applied for the blue curve.

Figure 3.19: Higgs mass dependence of electroweak production of $W^{\pm}W^{\pm}jj$.

as resonant Higgs-strahlung only occurs in the VVV production. Figure 3.19b compares the cross sections of inclusive $VVjj$-EW production to those of $VVjj$-EW production with a $M_{qq} > 150$ GeV cut applied on the outgoing quarks. Values of the Higgs mass m_H are varied and the correct width $\Gamma_H(m_H)$ is chosen according to the SM (provided by [118]).

As the $H \to WW$ channel opens around the value of $2m_W$, the cross section of the inclusive production rises. In the case of an $M_{qq} > 150$ GeV cut applied on the matrix-element, the dependence on the Higgs mass is completely removed.

3.3.6 Generator validation

In the scope of this study, an extensive generator validation was performed with the aim of validating the Sherpa and Whizard generators for the measurement of the $W^{\pm}W^{\pm}jj$ final state. With the same parameters and VBS compatible settings, the two generators should yield the same results. Potential differences and pitfalls for the generation of $W^{\pm}W^{\pm}jj$-EW production with Whizard and Sherpa are explored in the following. The specific settings are generator-code dependent; the general ideas however can be applied to any used program.

Phase space setup

When using a general-purpose MC generator, the automatically generated matrix-element code contains all possible diagrams for the given process. However, it is still necessary to take care that the integration phase space is correctly set up for the case of VBS processes. This is particularly important

since $VVjj$ production contributes in a broad range of regions in a high-dimensional phase space. With six fermions in the final state and various intermediate resonances, the settings for phase space and integration need to be optimized carefully, such that no contributions are neglected in the integration. Special care has to be taken if potentially off-shell intermediate particles are present. In the case of $VVjj$-EW, diagrams with off-shell W bosons contribute to the full process. Therefore, the phase space sampling setup has to take special care of regions with off-shell vector bosons. Furthermore, the sampling density of points in the phase space needs to be sufficiently high such that no contributions are missed or insufficiently sampled.

With the Whizard generator, taking into account non-resonant regions in the phase space is ensured with the option `?phs_keep_nonresonant = true` (cf. Appendix A). Table 3.4 compares the total cross sections generated with a dense phase space sampling allowing off-shell resonances (inclusive phase space) to those generated ignoring those phase space regions. In the same table, cross sections for the inclusive phase space with a coarser sampling are given.

	Inclusive diagrams		
`?phs_keep_nonresonant`	`true`	`false`	`true`
sampling	dense	dense	coarse
iterations	15×200000	15×200000	10×100000
Full sample	7.20 fb	5.29 fb	5.85 fb
VBS cuts	0.25 fb	0.85 fb	0.71 fb

Table 3.4: Comparison of integrated cross sections with different phase space setup. The number of grid sampling points in the phase space is given. All diagrams of the process $pp \to jj\ell^{\pm}\ell^{\pm}\nu\nu$ (EW) are taken into account. MC-statistical errors are below 3 %.

In the case of dense phase space sampling, 2×10^5 calls to the matrix element function are issued in each of 15 iterations (in Whizard: `{iterations= 15:200000, 15:200000}`). However, in the example with coarse sampling of the phase space, the number of calls is reduced to 1×10^5 and the number of iterations is reduced to 10 (in Whizard: `{iterations= 10:100000, 10:100000}`). Events are selected according to (3.9) and (3.10).

Cross sections in the full sample phase space are smaller than in the case of non-optimal phase space setups. Furthermore, the coarser sampling or the neglect of non-resonant contributions in the phase space leads to enhanced differential cross sections in some kinematic regions particularly sensitive to VBS. This leads to higher cross sections after VBS selection.

The invariant mass distribution of all possible lepton-neutrino pairs (Figure 3.20a) differs between the case of inclusive phase space and the cases of constrained phase space or reduced sampling density both in the low and in the high mass regions. While the coarse sampling misses part of the contributions below the W mass, the phase space neglecting non-resonant contributions misses all but the Breit-Wigner shape of the W boson. In the high-mass region, both cases show an enhanced cross section compared to the nominal case of inclusive, finely sampled phase space integration. The

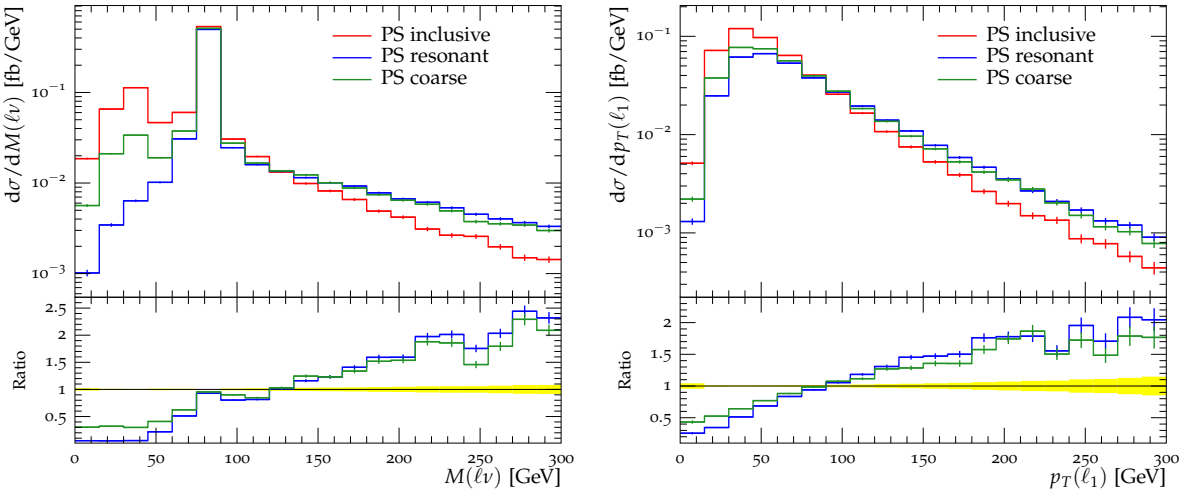

(a) Invariant mass of lepton and neutrino pairs

(b) Transverse momentum of hardest lepton

Figure 3.20: Differential cross sections comparing the electroweak production of $pp \to jj\ell^\pm\ell^\pm\nu\nu$ with an inclusive phase space (PS inclusive) to the same process integrated over a phase space ignoring non-resonant contributions.

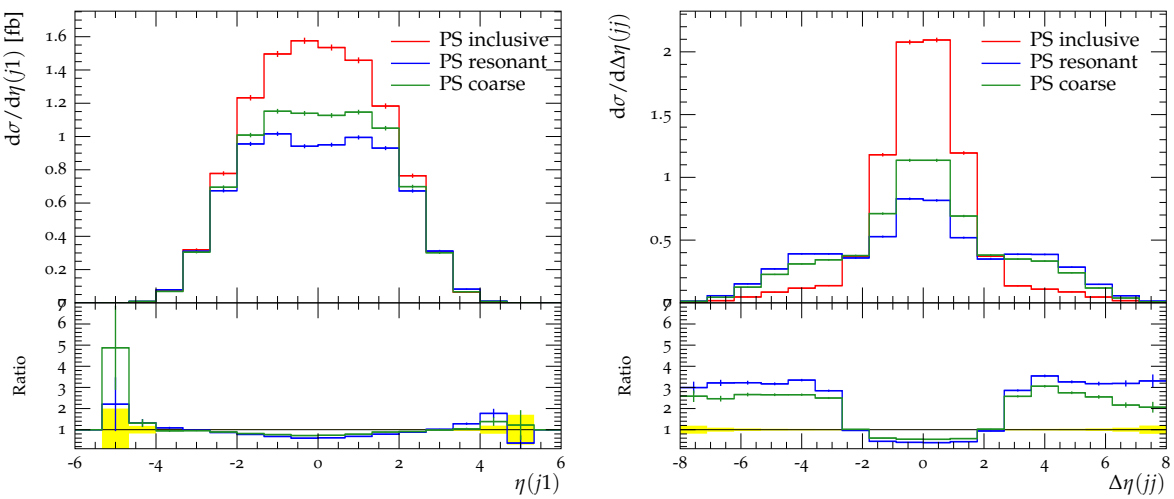

(a) Pseudorapidity of hardest jet

(b) Pseudorapidity difference of the two hardest jets

Figure 3.21: Differential cross sections comparing the electroweak production of $pp \to jj\ell^\pm\ell^\pm\nu\nu$ generated in an inclusive phase space (PS inclusive) to the same process integrated over a phase space ignoring non-resonant contributions.

transverse momentum of the first lepton is modeled to be too large in both non-optimal phase spaces (Figure 3.20b).

The pseudorapidity of the hardest jet contains a central contribution which is partly missed by the two non-optimal phase space setups (Figure 3.21a). In the pseudorapidity difference distribution (Figure 3.21b) this appears as an enhancement at large $\Delta\eta(jj)$ which mimicks VBS-like topology.

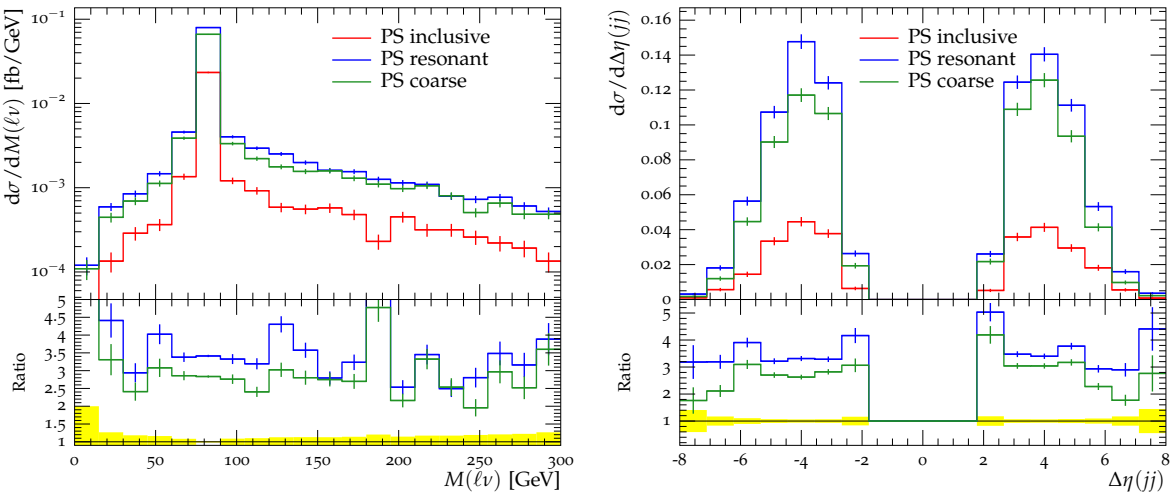

(a) Invariant mass of lepton and neutrino pairs (b) Pseudorapidity difference of the two hardest jets

Figure 3.22: Differential cross sections comparing the electroweak production of $pp \to jj\ell^\pm\ell^\pm\nu\nu$ generated in an inclusive phase space (PS inclusive) to the same process integrated over a phase space ignoring non-resonant contributions. The distributions are shown after the application of kinematic cuts for VBS selection (eq. 3.10).

After the application of VBS kinematic cuts (3.10), the shapes of the distributions assimilate. Figures 3.22a and 3.22b show the $M(\ell\nu)$ and the $\Delta\eta(jj)$ distributions after VBS cuts. Their ratios are essentially flat, which means that the shape difference is reduced after VBS cuts. It is thus crucial to examine and optimize the phase space setup according to the desired precision in the relevant phase space volume.

Similarities can be observed to the restricted process to resonant WW production (cf. Section 3.3.3). However, in the case of restricting the process to $pp \to jjW^\pm W^\pm \to jj\ell^\pm\ell^\pm\nu\nu$, the diagrams are ignored in the matrix-element calculation, while the constrained phase space comes into play during the integration.

Restricting the generation phase space

A large dijet invariant mass is the dominant feature of the tagging jets in VBS-like events. In addition, contributions from VVV diagrams (cf. Section 3.2.1) are suppressed by applying a kinematic cut on M_{jj} on reconstruction level. Therefore, it can be useful to apply such a cut on the matrix element generation in order to save CPU time for the integration and event generation.

However, if a parton shower is applied, the effect of a low M_{jj} cut, e.g. $M_{jj} > 150\,\text{GeV}$, can be visible beyond this value of M_{jj} after parton shower and on reconstruction level. When applying a M_{jj} selection on parton level, it is therefore necessary to check the impact of this cut after parton shower.

The effect of a cut on the matrix-element level M_{jj} on the dijet kinematics at reconstruction level has been checked for the case of $W^{\pm}W^{\pm}jj$-EW production. Figure 3.23 shows the invariant mass of the two highest p_{T} jets in two $W^{\pm}W^{\pm}jj$-EW samples, one generated with `Whizard` with a cut on $M_{jj} > 150\,\text{GeV}$, and one generated with `Sherpa` with no such criterion.

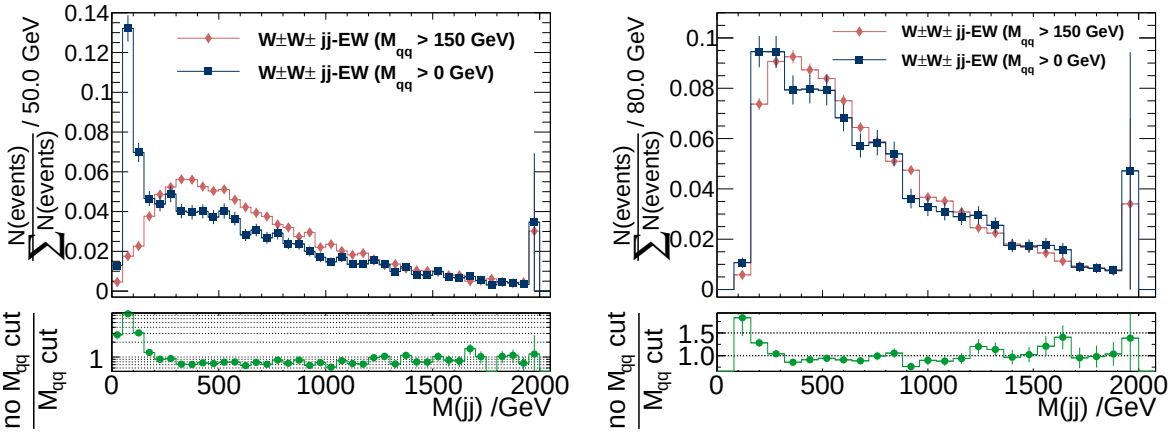

(a) Before $M_{jj} > 150\,\text{GeV}$ cut.

(b) After $M_{jj} > 150\,\text{GeV}$ cut.

Figure 3.23: Comparison of a `Whizard` sample with $M_{qq} > 150\,\text{GeV}$ cut on parton level, to a `Sherpa` sample with no M_{qq} criterion on parton level. The histogram curves are normalized to the same area. The bottom plot shows the ratio between the blue histogram, where no parton level M_{qq} cut is applied, and the red histogram, using the sample with $M_{qq} > 150\,\text{GeV}$ cut on parton level.

Figure 3.23(a) shows the invariant mass of the resulting jets after the selection of events with at least two jets and no further requirement, following the selection steps from Section 5.1.3. It shows a large discrepancy between the two samples in the low M_{jj} region, resulting from the partonic M_{qq} cut. When selecting events with $M_{jj} > 150\,\text{GeV}$ on reconstruction level, this difference is reduced. However, due to the discrepancy between matrix-element quarks and final state jets, the difference is not fully removed, as illustrated in the first bins of Figure 3.23(b).

Agreement between generators

In conclusion, phase space and integration settings need to be optimized for good modelling of VBS processes. If all settings are consistent, different generators yield consistent total and differential cross sections.

In the following, four generators capable of producing $VVjj$ final states are compared with respect to $W^{\pm}W^{\pm}jj$-EW production: The three general-purpose generators `MadGraph`, `Whizard`, and `Sherpa`, as well as the VBS specialized program `VBFNLO`. The resulting parton-level events generated at leading-order are compared in a loose VBS-like phase space according to the following selection criteria:
(3.11):

$$\begin{aligned}
&\text{Jets}: \; p_{\mathrm{T}} > 30\,\mathrm{GeV}, |\eta| < 4.9; \\
&\text{Leptons}: \; p_{\mathrm{T}} > 25\,\mathrm{GeV}, |\eta| < 2.5; \\
&E_{\mathrm{T}}^{\mathrm{miss}} > 40\,\mathrm{GeV}, \text{and } M_{jj} > 150\,\mathrm{GeV}.
\end{aligned} \tag{3.11}$$

A cut of $M_{jj} > 150\,\mathrm{GeV}$ is suitable for control regions more inclusive than a strict VBS selection, while removing the effect of VVV diagrams (cf. Section 3.2.1) which are not counted towards the VBS signal. Since `VBFNLO`'s implementation of the $W^{\pm}W^{\pm}jj$-EW process does not take VVV diagrams into account, this cut is necessary for comparability with `VBFNLO` events.

Figures 3.24a, 3.24b, 3.25a, and 3.25b illustrate the good agreement between the event samples produced with the four different generators. The histograms are scaled to the same cross section in the VBS phase space. The event samples show good agreement within statistical uncertainties in each of the observables.

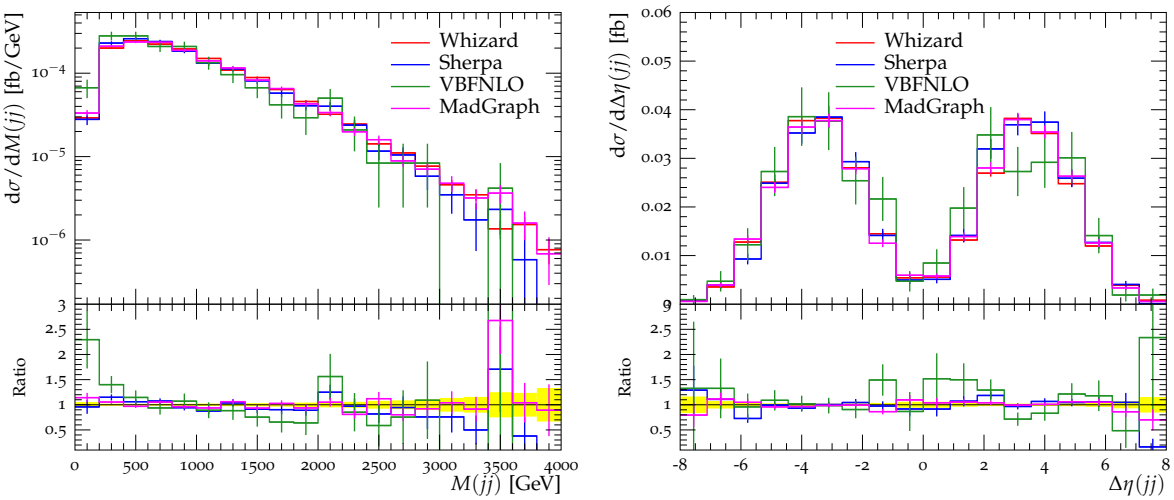

(a) Invariant mass of the two hardest jet

(b) Pseudorapidity difference of the two hardest jets

Figure 3.24: Differential cross sections comparing the electroweak production of $pp \to jj\ell^\pm\ell^\pm\nu\nu$ with different generators in a loose VBS-like phase space (3.11).

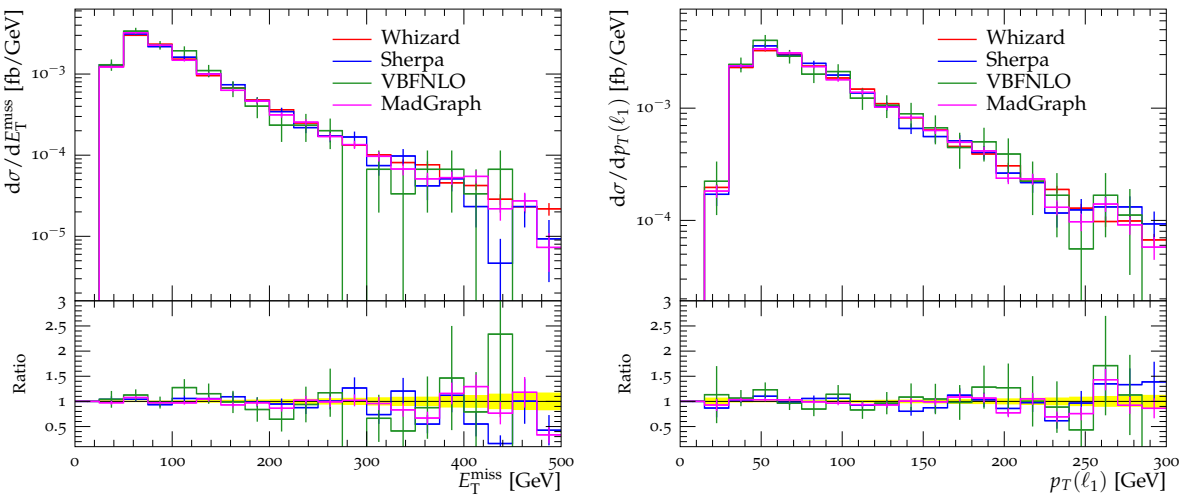

(a) Missing transverse momentum E_T^{miss}

(b) Transverse momentum of the hardest lepton

Figure 3.25: Differential cross sections comparing the electroweak production of $pp \to jj\ell^\pm\ell^\pm\nu\nu$ with different generators in a loose VBS-like phase space (3.11).

3.4 Simulating new physics in Vector Boson Scattering

The effective field theory approach for modelling the low-energy effects of new physics in VBS is detailed in Section 2.3. Methods and tools to generate events containing such new physics models are described in this section.

3.4.1 Modelling new physics via effective field theories

Anomalous quartic gauge couplings, as introduced in Section 2.3.3, model the effect of new physics at higher energies in the electroweak sector which has an influence on quartic gauge interactions. In order to measure the value of an anomalous coupling constant, it is essential to simulate events including effects of non-SM anomalous couplings in the final state to be measured. Events can be generated using an implementation of such a model in a MC generator.

Various generators provide implementations of aQGC models. Implementations of anomalous couplings α_4, α_5 from non-linear EWSB exist e.g. in `Pythia6` [104, Sec. 8.5.2], `Whizard` [73], and `Sherpa` [102, Sec. 3.2.3]. The operators from the linear EWSB approach ($f_{S,0}$, $f_{S,1}$) are implemented e.g. in the generators `VBFNLO` [139] and `MadGraph` [140].

Additional resonances can be introduced in the frame of effective field theories as described in Section 2.3.4. Implementations of this model can be exploited in searches for new physics [141]. It is available in the `Whizard` generator [73].

3.4.2 MC generation with effective field theory content

When generating events with aQGC or additional resonances, the following aspects need to be taken into account:

- Non-SM aQGCs and additional resonances enhance the amplitude in a region in phase space which is usually suppressed by the PDF. It might therefore be necessary to increase the sampling density or adjust the phase space setup.
- Due to the possible violation of unitarity in VBS with additional EFT operators, event samples need to be unitarized in order to ensure that only physically sensible events are generated.

Unitarization

As motivated in Section 2.3.6, the amplitude of a scattering process with an EFT operator needs to be unitarized by a procedure ensuring that the cross section stays below the cross section at the unitarity bound $\sigma_{scat} \leq \sigma_{UB}$. This is especially important for quartic interaction operators which violate unitarity in the LHC energy range. The most common approaches are dipole form factors and the K-matrix unitarization method.

K-Matrix unitarization The K-matrix unitarization procedure, originally proposed in [78], has been broadly employed in the context of nuclear interactions such as $\pi\pi$ scattering [142]. It is also well suited for VBS in the framework of the effective chiral Langrangian. An implementation exists in `Whizard` [73] for the unitarization of aQGC and additional resonances in VBS.

In order to fulfill elastic unitarity, the normalized eigenamplitudes $a(s)$ need to obey the optical theorem, expressed by the *Argand*-circle condition (cf. Section 2.3.6)

$$|a(s) - i/2| = 1/2. \tag{3.12}$$

Real amplitudes $a(s)$ as calculated at tree-level are projected on the Argand circle by the transformation

$$\hat{a}(s) = \frac{a(s)}{1 - ia(s)}. \tag{3.13}$$

This is the so-called K-matrix unitarization scheme illustrated in Figure 3.26.

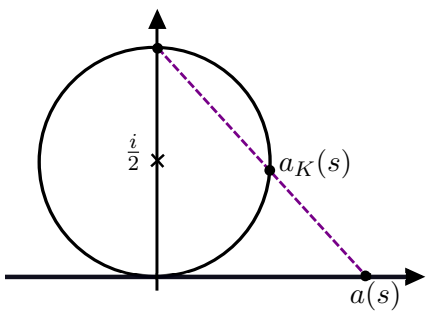

Figure 3.26: K-Matrix unitarization method: Projection of the real scattering amplitude $a(s)$ on the Argand circle yields the unitarized, complex amplitude $a_K(s)$.

Figure 3.27 illustrates the effect of the K-matrix unitarization on VBS: The SM cross section is essentially independent of $\sqrt{s}$. The non-unitarized VBS process with an anomalous coupling parameter α_4 = 0.1 a priori violates unitarity. The cross section exceeds the unitarity bound and rises infinitely with the collision energy. When K-matrix unitarization is applied, the high energy rise of the total cross section is suppressed. Physically, the K-matrix unitarization acts like an infinitely heavy and wide resonance added to the spectrum.

Multipole form factors

A different method ensuring unitarity of the scattering matrix is by multiplying the anomalous coupling with a form factor $\mathcal{F}$ (cf. e.g. [79, ch. 4.2])

$$\mathcal{F} = \frac{1}{(1 + \frac{s}{\Lambda_{FF}^2})^n}, \tag{3.14}$$

where n is a positive integer, e.g. $n \in \{2, 4\}$, Λ_{FF} is the form factor scale, and s is the Mandelstam variable calculated from the scattering of $WW \to WW$. Application of this form factor attenuates the

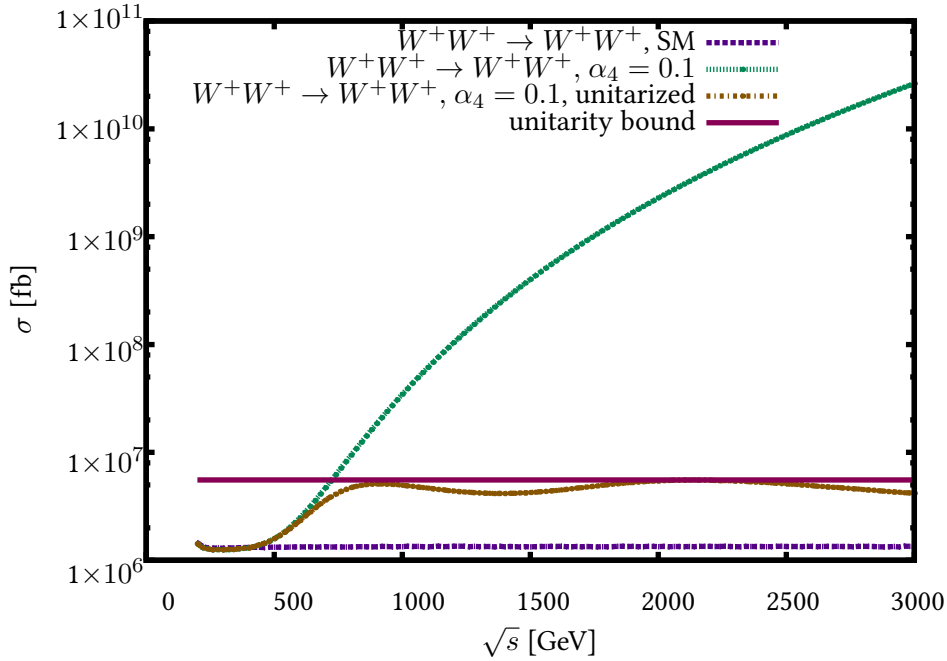

Figure 3.27: Total cross section of $W^+W^+ \to W^+W^+$ with a SM Higgs with mass $m_H = 125$ GeV. The SM cross section (violet) is compared to the cross section with $\alpha_4 = 0.1$ without unitarization (green) and with unitarization via K-matrix scheme (brown). The unitarity bound corresponds to the highest possible cross section in the unitarized case.

cross section as the energy rises above the form-factor scale Λ_{FF}. The expansion of this form factor, a series of the form $\sum_m a_m(\frac{s}{\Lambda})^m$ with arbitrary coefficients a_m, mimics the effective field theory series of operators (2.33). To this effect, the form factor can be interpreted as a resummation of higher-order operators [79, 143].

The choice of the exponent n is governed by the goal to suppress the cross section as strongly as necessary to ensure unitarity over the full investigated energy range. As the scale Λ_{FF} marks the scale above which unitarity is violated, it depends on the operators and couplings used [79, ch. 4.2]. Experimental limits on anomalous couplings with form-factor unitarization thus always depend on the exponent n and the scale Λ_{FF}.

Comparison of unitarization procedures

Both unitarization procedures, the K-matrix and form factor methods, are phenomenologically motivated and implementations of the methods in MC generators are available. For the choice of method for experimental application, their effect on VBS cross sections with anomalous quartic gauge couplings need to be considered.

Figures 3.28a and 3.28b show the cross section dependence on the anomalous quartic gauge coupling α_4 for the process $pp \to jje^+\nu_e e^+\nu_e$ with the following phase space selection: Jets are selected with $p_\mathrm{T} > 20$ GeV, $|\eta(j)| < 5$, and $\Delta R(jj) > 0.4$; leptons are selected with $p_\mathrm{T} > 10$ GeV and $|\eta(\ell)| < 5$.

A cut of $M_{jj} > 150$ GeV on the outgoing quarks is applied. The data for the form-factor unitarization are obtained by using an implementation of the $f_{S,0}$ and $f_{S,1}$ parameters introduced in section 2.3.5 and using the known conversions (2.40). The unitarization has been performed with a form factor with exponent $n = 2$ and the maximum possible form factor scale Λ_{FF}, determined with the tool [144].

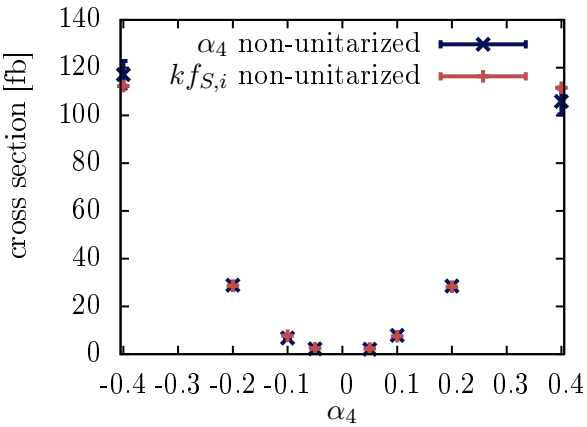

(a) Cross sections without unitarization

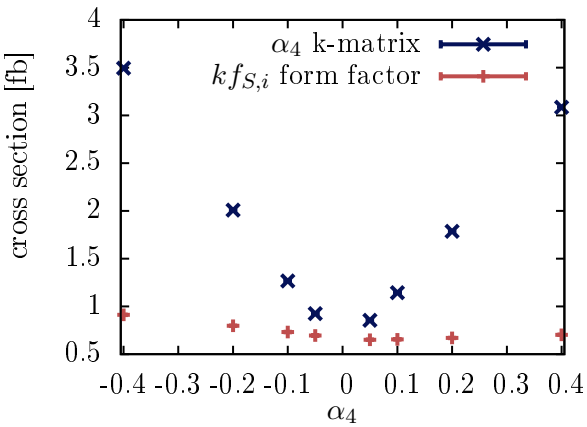

(b) Cross sections unitarized with the K-Matrix method and with form factors, respectively

Figure 3.28: Cross sections for the process $pp \to jje^+\nu_e e^+\nu_e$ in a loose VBS-like volume with $M_{jj} > 150$ GeV in dependence of α_4. The aQGC α_4 (blue) is compared to the $\tilde{f}_{S,i}$ parameters (red), where $\tilde{f}_{S,0} = \tilde{f}_{S,1}$ to satisfy Equation (2.40), and they are multiplied by $k = 1/2176$ (cf. Equation 2.42).

Both procedures yield a reduction of the cross sections by more than one order of magnitude. They modify the dependence on the coupling constant from a quadratic to a linear dependence. In both cases, the dependence becomes asymmetric in the coupling constant α_4. The reduction in case of the K-matrix is smaller compared to the reduction by form-factors. A detailed comparison of unitarization of VBS processes by the two methods described above was conducted in [145, 146].

CHAPTER 4

The ATLAS detector at the LHC

4.1 The Large Hadron Collider

The largest particle detector at a high-energy accelerator ever built, ATLAS is a multi-purpose detector located at the Large Hadron Collider (LHC) [147]. This accelerator for protons and heavy ions is located at the *Centre Européen pour la Recherche Nucléaire* (CERN) in the former Large Electron-Positron collider (LEP) [148] tunnel at the Swiss-French border close to Geneva, Switzerland. Apart from proton-proton collisions, the LHC is also used in ion-ion (Pb-Pb) or proton-ion (p-Pb) collision mode. [1] The 27-km long circular collider is located about 100 m underground, tilted by 1.4 ° for geological reasons. It consists of more than 1,600 superconducting niobium-titanium (NbTi) magnets, cooled to 1.9 K with superfluid ^{4}He.

1,232 dipole magnets with a peak field of 8.33 T are installed to bend the beams on the circlular track. The beams are focused by 392 quadrupole magnets. The LHC works as two synchrotron accelerators with beams moving in opposite direction in adjacent beam pipes in twin bore magnets, which consist of two sets of coils but share the mechanical structure and the cryogenic system. [147]

The proton beams first pass through a chain of accelerators serving as pre-accelerators. [149] As the last part of this chain, the Super-Proton-Synchrotron (SPS) injector supplies 450 GeV proton beams to the LHC ring, which are then accelerated to 4 TeV (in the year 2012), and brought to collision at the 4 intersection points. Up to 1380 bunches per beam have been circulating during Run-1 (2010-2012 data taking), with a bunch spacing of 50 ns. The peak luminosity in 2012 was 7.7×10^{33} cm^{-2}s^{-1}. [150]

There are 4 major experiments located at the LHC ring at the beam crossing points: ALICE, ATLAS, CMS, and LHCb. While ATLAS and CMS are both multi-purpose detectors designed to find a light SM Higgs boson as well as new physics in general, ALICE is optimized for hadron physics, and LHCb studies flavor physics. As this thesis uses data of the ATLAS detector, a description of its composition and functionalities follows in this chapter.

[1] As ion collision experiments are not subject of this thesis, the term LHC will be used throughout this thesis as the proton-proton mode LHC only.

4.2 The ATLAS Detector at the LHC: Functionality and layout

The construction of the ATLAS detector has been described in all detail in [151], documenting the enormous effort of designing, building, and operating a detectors suitable for providing the measured data for investigations such as presented in this work. The detector description in this chapter will cover the components most relevant to the $W^{\pm}W^{\pm}jj$ measurement in the layout of ATLAS as present in the LHC Run-1 data taking (2010-2013).

4.2.1 A Toroidal LHC ApparatuS: Overview

Situation and coordinate system The ATLAS detector is situated in a cavern of the CERN LHC tunnel located in Meyrin, Switzerland. It is built around the LHC collision point number 1.

Seen from the nominal interaction point (IP), the right-handed coordinate system used for ATLAS is defined as follows:

- The plane transverse to the beam axis is the $x - y$ plane, where the positive x-axis points from the IP to the center of the LHC ring, and the y-axis points upwards.
- The z-axis is defined by the beam axis.

Angular coordinates are defined as follows:

- The azimuthal angle ϕ is measured around the beam axis, with $\phi = 0 = 2\pi$ at the positive x-axis.
- The polar angle Θ is the angle to the beam axis. Based on the polar angle Θ, the pseudorapidity is defined as $\eta = -\log\left(\tan\frac{\Theta}{2}\right)$.
- The distance in the pseodorapidity-azimuth plane is defined as $\Delta R = \sqrt{\Delta\phi^2 + \Delta\eta^2}$.

Total view and design principles The ATLAS detector is a device for the detection of a broad range of particle types and the measurement of their kinematic properties. It features the typical structure of multiple layers of subdetectors specialized for certain types of particles, surrounding each other such that the full detector data allows to identify and measure various types of particles at high precision over close to the full spatial angle.

In each subdetector, a substructure division into so-called "barrel" and "end-cap" structures is constructed to get as close as possible to full coverage: In the barrel region, symmetrically around $\eta = 0$, subdetectors have cylindrical shape, with layers typically parallel to the beam pipe. In the end-caps, the regions at both ends of the detector, the detector components are arranged in disk-like shapes sparing a hole for the beam pipe.

The whole detector measures 44 m in length and 25 m in diameter, and is approximately cylindrically symmetric, with an eight-fold axial symmetry for all subdetectors but the tracker, dictated by the toroid magnet layout. For safety, all subdetectors are floating and are grounded individually.

Figure 4.1 shows an overview of the ATLAS detector, sliced such that each subdetector is visible.

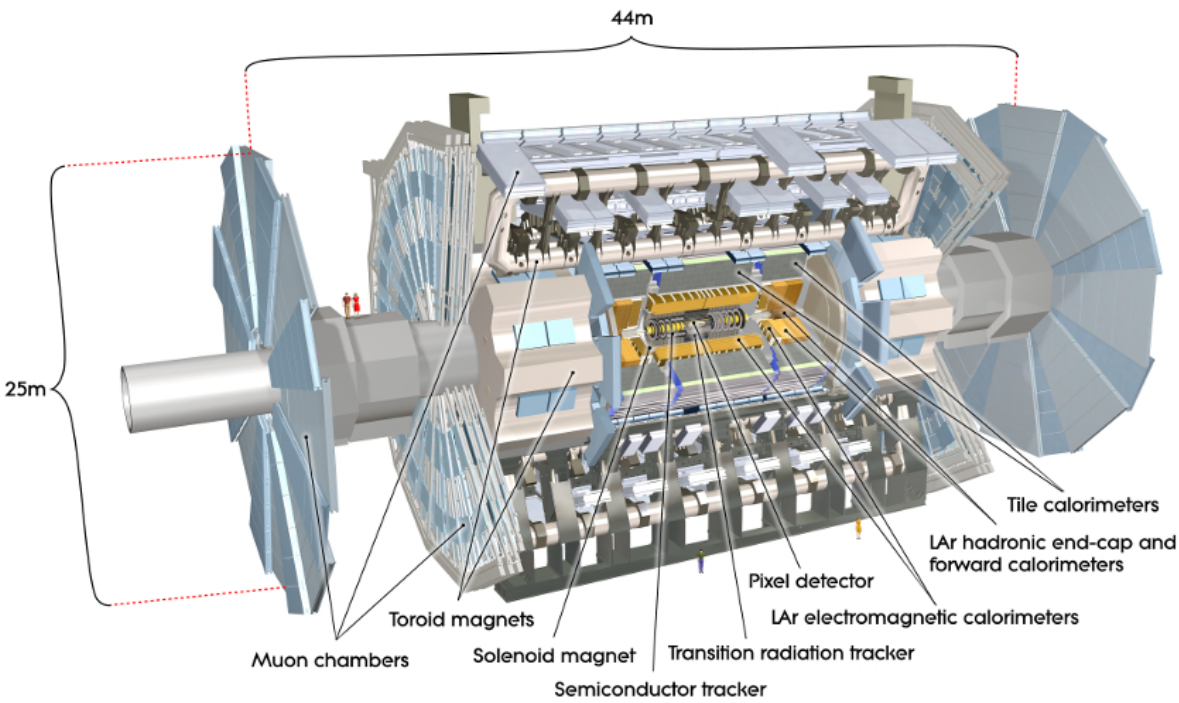

Figure 4.1: ATLAS detector overview. From [113, fig. 1.1].

The subdetectors are described in the following sections, following the detector's geometry from the parts closest to the beam pipe to the outermost layers of the Muon Spectrometer. Building on the description of functionality and layout of the detector in this section, Section 4.3 describes the reconstruction of physical objects from data taken with this detector.

4.2.2 Inner Detector

The Inner Detector (ID) is the tracking system of ATLAS. Its layout and operation parameters are driven by its design goals: measuring tracks with high momentum resolution down to low momenta of ~ 0.5 GeV, as well as reconstruction of primary and secondary vertices with high resolution, and a robust electron identification up to $|\eta| = 2.0$ within a wide range of energies. A challenge for the used technologies and materials is posed by the high-radiation environment close to the collision point, leading to type conversion of semiconductor material.

The tracking components of the ID are immersed in a 2 T magnetic field provided by the solenoid magnet (see Section 4.2.6), which leads to a curvature of charged tracks, allowing for the measurement of their charge and momentum.

The ID comprises three subdetectors: the semiconductor trackers PIXEL and SCT (silicon microstrip tracker), and the gaseous straw tubes detector TRT (transition radiation tracker). A schematic plan of the ID with measures of its subdetectors is shown in Figure 4.2.

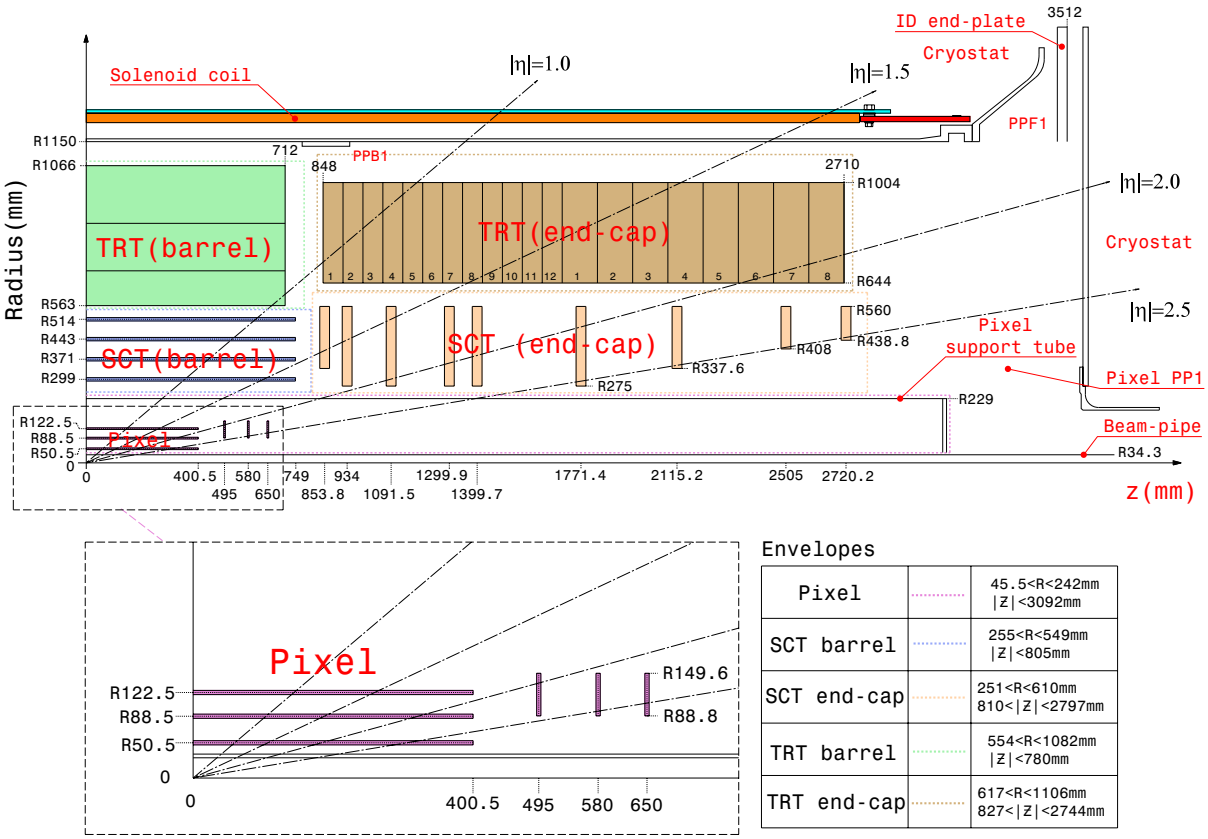

Figure 4.2: Plan view of the ATLAS Inner Detector, from [151, fig. 4.1]. Distances in mm from the interaction point are indicated in black, using prescript "R" for radial distances. The labels PP1, PPB1, and PPF1 refer to patch-panels for the service cables.

Semiconductor trackers Both the PIXEL and SCT use semiconductor detectors to register incident charged particles and photons: The sensitive volume consists of a p-n-diode depleted of mobile charges by applying an external electric field in reverse direction. A minimum ionizing particle passing the detector deposits energy in the n-type bulk material, producing pairs of electrons and holes. These charges are separated by the electric field and drift towards the nearest electrodes. Read-out chips (ASICs) on the electrodes amplify and process the signal, which is proportional to the energy of the initial particle.

PIXEL detector The subdetector with highest granularity, which is located closest to the interaction point, is the PIXEL detector, spanning up to $|\eta| = 2.5$ and radially from $R = 5.05$ cm to $R = 12.25$ cm distance from the beam axis. For the spatial measurement, it provides a radial resolution of $\sigma(R\phi) = 10$ µm, and an axial resolution of $\sigma(z) = 115$ µm [151, Tab. 4.1].

Tracking in the PIXEL is based on a semiconductor detector technology using n-type silicon wafers with n^+-implants on the side of the readout, compensating for conversion of n-type material to p-type, which is expected to occur after undergoing a radiation fluence of $F_{neq} = 2 \cdot 10^{13}\,\mathrm{cm}^{-2}$[2] [151, Sec. 4.2.1].

The PIXEL detector contains a total of 1744 silicon sensors with an external size of $19 \times 63\,\mathrm{mm}^2$ each. Each sensor holds 47232 pixels with nominal size of $50 \times 400\,\mu\mathrm{m}^2$, which is constrained by the read-out pitch. Via bump bonds, 46080 of a sensor's pixels are connected to read-out channels of the front-end electronics, amounting to a total of 80.4 $\times 10^6$ read-out channels in the whole PIXEL. One sensor along with its associated front-end electronics chip, mounted on a printed-circuit board, forms a PIXEL module. Attached to stave segments, which also contain cooling units, the PIXEL modules are arranged in three cylindrical layers parallel to the beam pipe in the barrel region, and three disks perpendicular to the beam pipe in the end-cap region, to form the PIXEL system.

Operating temperature of the PIXEL sensors is required to be -5 to $-10\,^\circ\mathrm{C}$, in order to reduce leakage currents after the detector has experienced radiation damage.

SCT detector Following its passage of the PIXEL, a particle next traverses the SCT (silicon microstrip tracker), in the range of $R = 29.9\,\mathrm{cm}$ to $R = 51.4\,\mathrm{cm}$. It uses classical p-in-n semiconductor sensor strips of 6 cm length and a pitch of 80 µm, which are bundled in sensors, each with 768 daisy-chained pairs of those strips. For better spatial resolution, the sensors are arranged in parallel pairs with a stereo angle between the strips of 40 mrad.

These sensor pairs are connected to binary signal readout chips, and glued on a baseboard providing stability and high voltage. Each module is cooled by evaporating a refrigerating fluid in a neighboring cooling pipe, such that the SCT sensors are operated at $-7\,^\circ\mathrm{C}$ in order to reduce leakage currents after radiation damage.

With 4088 modules arranged as four cylindrical layers in the barrel region and nine disk layers in each of the end-caps, the SCT provides almost 4π coverage with a total silicon surface of $63\,\mathrm{m}^2$. The SCT provides a lateral resolution of $\sigma(R\phi) = 17\,\mu\mathrm{m}$ and a resolution of $\sigma(z) = 580\,\mu\mathrm{m}$ and $\sigma(R) = 580\,\mu\mathrm{m}$ in longitudinal direction [151, Tab. 4.1]. It contains a total of 6.3$\times 10^6$ read-out channels.

PIXEL and SCT read-out According to a 40.08 MHz clock which is synchronized with the LHC bunch crossings (BC), a signal generated in the front-end electronics of a PIXEL or SCT module is stored in a buffer for $\sim 3.2\,\mu\mathrm{s}$. If a level-1 trigger signal (see Section 4.2.7) is received, the buffer content associated to this BC is transferred to a readout driver (ROD) to be passed on to the subsequent trigger chain.

Transition Radiation Tracker The outermost part of the tracking system is the TRT (transition radiation tracker), spanning from $R = 55.4\,\mathrm{cm}$ to $R = 108.2\,\mathrm{cm}$. It is responsible for charged track measurements up to $|\eta|$ = 2.0, providing typically 36 hits per track.

[2] F_{neq} denotes the neutron equivalent dose.

The TRT is based on a drift tube technology: High-energy charged particles passing the tube ionize the gas contained in the tube. The resulting electrons drift towards an anode wire located at the center of the tube, which registers a voltage proportional to the originally deposited energy. Additionally, the detector registers transition radiation photons which are produced as the particle passes layers with varying refraction indices. As the transition radiation is dependent on the particle's mass, its measurement provides means for particle identification. Thus, the TRT serves as a tracking detector as well as a transition radiation photon detector.

The TRT straw tubes have a diameter of 4 mm and are made of a polymer material coated with aluminum as cathode material. In the center of the tubes, gold-plated 31 µm tungsten wires serve as anodes, directly connected to the readout. In the barrel TRT tubes are 144 cm long and arranged in rings of layers of straws interleaved with fibres to generate transition radiation. In the end-cap regions, 37 cm long straws are interleaved with polypropylene radiator foils and organized in wheels.

The TRT only provides radial information, but no information on the z coordinate. Radially, its accuracy amounts to $\sigma(R\phi) = 130$ µm [151, Tab. 4.1]. High level of alignment and wire-tube distances are ensured using a grid of polyimide keeping the straws aligned. High requirements are also put on the purity of the Xenon-based gas mixtures. Therefore, in order to avoid contamination through leaks, the straws are surrounded by CO_2.

This CO_2 gas envelope also serves as conductor for the heat dissipated by the straws: During data taking, the ionization currents produce heat proportional to the counting rate – up to 20 mW per straw in the high-occupancy inner barrel straws. This heat is conducted off the straws via the CO_2 gas envelope to heat exchangers cooled with C_2F_{14}.

Services: Power supply, control commands, data transfer For PIXEL and SCT, the digital clock signal and control commands as well as the data transfer off the detector is transmitted via optical links. For the TRT, optical links are used for readout as well, while trigger, timing, and control (TTC) is transmitted electrically.

The PIXEL and SCT sensors as well as the TRT straws are supplied with high voltage (HV), while low voltage (LV) is necessary for the front-end electronics as well as the control electronics.

Performance of the Inner Detector The totality of the Inner Detector components is well suited to fulfill the design goals: The semiconductor trackers at small distances from the beam pipe are responsible for vertex and impact parameter measurements necessary for heavy-flavor tagging and τ identification. Momentum measurement with high resolution is ensured by the high-precision trackers at smaller radii in combination with TRT tubes providing a long measured track length with large number of hits, albeit low spatial accuracy in z-direction. At the same time, this combination yields robust pattern recognition for tracking. In addition to its tracking capacities, the TRT provides for excellent electron identification making use of transition radiation photons, combined with the information from the adjacent electromagnetic calorimeter.

4.2.3 Calorimeters

The ATLAS calorimeter system is designed to measure the amount and direction of the energy deposition of electromagnetic and hadronic showers. Its design goals are good containment of these showers as well as a high level of prevention of punch-through to the Muon Spectrometer, and an accurate measurement of the deposited energy.

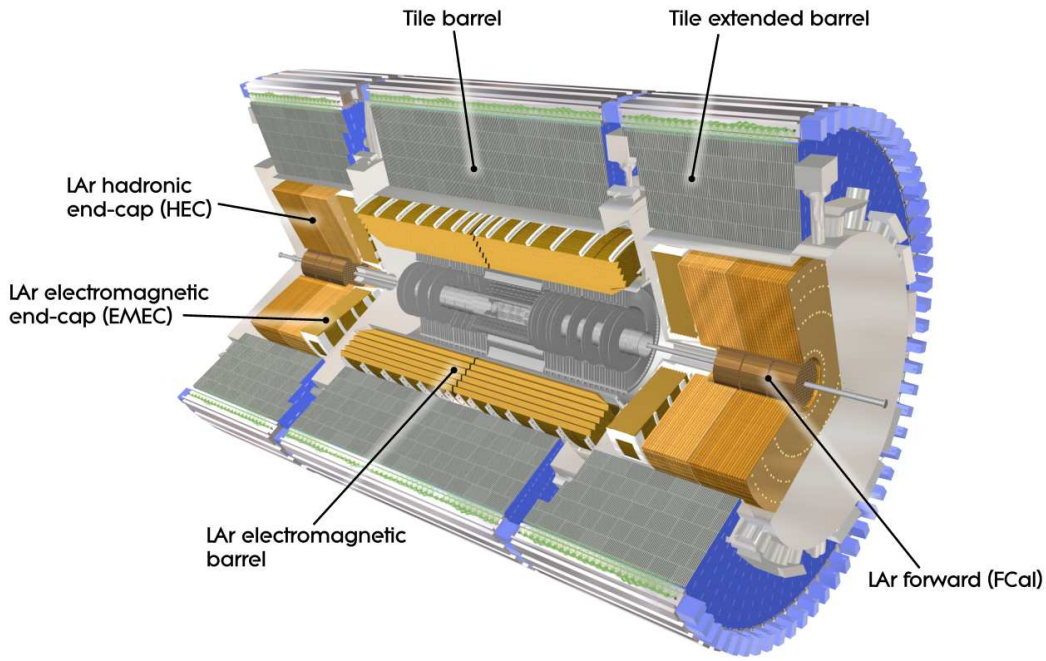

Figure 4.3: ATLAS calorimeter overview, from [151, fig. 1.3]

To achieve these goals, the calorimeter is divided in an electromagnetic (EM) calorimeter and a hadronic calorimeter. In the barrel, the electromagnetic (EM) calorimeter has a thickness of $> 22X_0$ (radiation lengths X_0) and in the endcaps $> 24X_0$.[3] Stand-alone, the hadronic calorimeter is $\sim 9.7\,\lambda$ (interaction lengths λ) in the barrel and $\sim 10\,\lambda$ in the end-caps.[4] As it is located behind the EM calorimeter which serves as active material for hadronic showers as well, the total thickness is $11\,\lambda$ at $\eta = 0$. Each shower passing the calorimeter system is sampled several times. In addition, the lateral granularity of the calorimeters is very high.

Both for electromagnetic as well as for hadronic calorimetry, ATLAS employs sampling calorimeters, which consist of alternating components of an absorber material and an active detector material. Particle showers are produced by interactions in the absorber layers, generating particles that travel into the layers of active material. There, they ionize the medium, producing secondary charged particles

[3] The radiation length is defined as the mean travel distance after which a high-energy electron reduces its energy to $1/e$ of the initial energy by emission of bremsstrahlung.

[4] The nuclear interaction length is the mean distance after which the number of particles in a hadronic jet is reduced to $1/e$ of the initial number, as particles undergo inelastic nuclear interactions with the material [152].

which drift to the adjacent high-voltage electrodes. These electrodes register the signal as a voltage pulse, which is further processes in the front-end electronics. Two types of sampling calorimeters are employed at ATLAS, categorized by their active medium: liquid argon calorimeters and scintillating tile calorimeters.

Electromagnetic Calorimeters The electromagnetic (EM) calorimeter of ATLAS uses lead as absorber and liquid argon as active medium. It consists of two half-barrels, covering the range $|\eta| < 1.475$, and two end-caps, spanning from $1.375 < |\eta| < 3.2$.

In order to provide full ϕ coverage, the kapton electrodes and the lead absorber plates have an accordion-like wave structure. By adjusting the wave amplitude and folding angles of the accordion in connection with the liquid argon gap size, the calorimeter's design provides very uniform performance.

The barrel of the EM calorimeter is divided in two half-barrels, both extending over a radius from 1.4 m to 2 m around the beam axis. An 11 mm thick liquid-argon presampler layer adjoins their inner surface, improving the energy measurement in face of energy lost by particles in the inner detector. Each of the half-barrels contains 1024 absorber plates and weighs 57 t.

Radially, the EM calorimeter barrel is structured in two or three (depending on $|\eta|$) layers with varying granularity. The second layer collects the largest fraction of the electromagnetic shower. In the central region of the detector, $|\eta| < 1.40$) which is devoted to precision physics, this is therefore the layer with the finest granularity of $\Delta\eta \times \Delta\phi = 0.025 \times 0.025$ [151, Tab. 1.3].

The liquid-argon gap size in the barrel is kept constant by varying the folding angles of the accordion waves. The read-out electrodes in the barrel modules are placed centrally in the liquid-argon gaps, providing a maximum drift time of 450 ns at a high-voltage of 2 kV. They consist of three layers of conductor, of which the outer ones provide the high voltage potential. The signal is generated via capacity coupling in the inner one, which is read out.

Each of the end-caps is divided into two coaxial wheels: the outer wheel covering $1.375 < |\eta| < 2.5$ has a granularity of $\Delta\eta \times \Delta\phi = 0.025 \times 0.1$, while the inner wheel spanning the range $2.5 < |\eta| < 3.2$ has a coarser granularity of $\Delta\eta \times \Delta\phi = 0.1 \times 0.1$ [151, Tab. 1.3]. They extend from $R = 0.33$ m to $R = 2$ m and weigh 27 t each. A presampler is installed in front of the end-caps up to $|\eta| < 1.8$.

Each wheel is segmented into eight modules, with no resulting ϕ segmentation thanks to the accordion shape of the absorbers. In the end-caps, the liquid argon gap size increases with the radius. To nevertheless provide a detector response constant in $|\eta|$, the electrodes in the center of the liquid argon gaps are provided with varying high voltage of 1 kV to 25 kV.

Hadronic Calorimeters The hadronic calorimeter consists of three parts: the tile calorimeter in the range $|\eta| < 1.7$, the liquid-argon hadronic end-cap calorimeter (HEC) ($1.5 < |\eta| < 3.2$), and the liquid-argon forward calorimeter (FCal) with coverage of $3.1 < |\eta| < 4.9$. They consist of different absorber and detector materials as described in the following paragraphs.

Tile Calorimeter Joining directly outside the EM calorimeter is the innermost component of the hadronic calorimeter. It covers the region up to $|\eta| < 1.7$ and is segmented into a central barrel and two extended barrel parts. Radially, it extends from 2.28 m to 4.25 m distance from the beam axis and is segmented in three layers in depth. The inner two layers have a granularity of $\Delta\eta \times \Delta\phi = 0.1 \times 0.1$, and the outer layer $\Delta\eta \times \Delta\phi = 0.2 \times 0.1$ [151, Tab. 1.3].

The tile calorimeter uses steel plates as absorber material and scintillating tiles as active material, which are arranged in alternating steel-scintillator modules of size $\Delta\phi \sim 0.1$. Each barrel part contains 64 of these self-supporting modules.

Wavelength-shifting fibres lead from the scintillators to the photomultiplier tubes at the rear of the module, which are connected to the front-end electronics. A total of 9852 read-out channels are provided by the Tile calorimeter. It has a radial thickness of 7.4 λ.

Liquid-argon hadronic end-cap calorimeter (HEC) In the end-caps, the hadronic calorimeter is located directly behind the EM calorimeter and shares a cryostat with the neighboring EM end-cap and FCal.

Extending over $1.5 < |\eta| < 3.2$. with an outer radius of $R = 2.03$ m, the HEC overlaps with the forward calorimeter and the tile calorimeter, to compensate the reduction of material density in the transition regions. The absorber material is copper, while liquid argon is used as active medium.

Each end-cap consists of two wheels, the front wheel and the rear wheel, both consisting of 32 wedge-shaped modules and a support structure of connecting bars at the periphery and the central bore. In the front wheels, the copper absorber plates have a thickness of 25 mm, while they are 50 mm thick in the rear wheels. As the liquid-argon gaps (active medium) are 8.5 mm in both wheels, this leads to a larger sampling fraction[5] in the front wheels of 4.4 % compared to 2.2 % in the rear wheels.

Three equidistant electrodes divide a liquid argon gap into four drift zones. Each zone has a high voltage potential of 1800 V supplied by the electrodes, which are held in place by a honeycomb sheet. The middle electrode serves as the readout electrode. The readout cell granularity of the HEC is $\Delta\eta \times \Delta\phi = 0.1 \times 0.1$ in the area below $|\eta| < 2.5$ and $\Delta\eta \times \Delta\phi = 0.2 \times 0.2$ above $|\eta| > 2.5$. A total of 5632 channels is read out.

Forward liquid-argon calorimeter Many signatures of processes connected to the exploration of electroweak physics feature forward jets, for instance the scattering of electroweak vector bosons and the process of vector-boson fusion with W, Z, or Higgs boson production. These measurements profit enormously from the FCal, which measures hadron jets in the range of $3.1 < |\eta| < 4.9$.

The FCal is designed to provide 10 interaction lengths over a relatively short range such that its distance to the IP can be large, limiting neutron albedo in the inner detector cavity.

[5] The sampling fraction f_{samp} is defined as

$$f_{samp} = \frac{E_{mip}(active)}{E_{mip}(active) + E_{mip}(absorber)}$$

where $E_{mip}(layer)$ is the energy deposited by an incident minimum-ionizing particle in the respective layer [153].

Each end-cap's Forward Calorimeter consists of three modules: the one closest to the beam pipe, the "electromagnetic layer" FCal1, uses copper as absorber material. FCal2 and FCal3, the two hadronic calorimeters, use tungsten as absorber material.

As the particle fluxes in the FCal are very high because of its position at high $|\eta|$, the liquid argon gaps are designed to have very small widths. Electrodes are inserted regularly inside a structure of the absorber material. They consist of small-diameter copper rods at the center of copper tubes, separated by plastic fibres. These electrodes are arranged parallel to the beam pipe.

The granularity varies from layer to layer (z direction) and also in $|\eta|$, being finer at the center. The FCal provides a total of 1762 readout channels and its hermetic design in connection with the surrounding calorimeters improves the uniformity of the calorimeter coverage.

Figure 4.4 shows the cumulative amount of material which the calorimeter components provide.

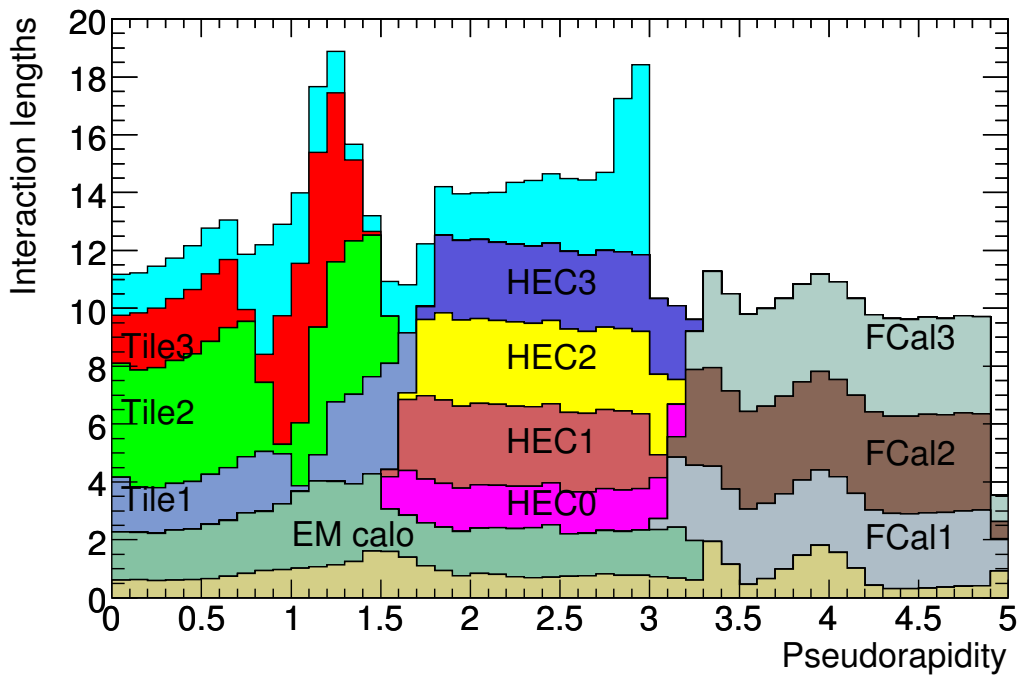

Figure 4.4: The cumulative amount of material of the various calorimeter components is shown as a function of $|\eta|$ in units of interaction lengths. The bottom part indicates the material in front of the calorimeter, while the other components are labeled according to their calorimeter part. The top area shows the total amount of material in front of the first active Muon Spectrometer layer, including support structures, cryostats, and magnets [151, fig. 5.2].

Calorimeter operation and performance The calorimeters using liquid argon as active medium (EM calorimeter, HEC, and FCal) are housed in cryostats which provide cooling to retain the liquid phase of the argon. To this effect, a 20 kW refrigerating system surrounds the calorimeters. It is operated with liquid nitrogen, whose boiling temperature at 77 K is slightly lower than that of argon

at 87 K. The nitrogen is supplied with appropriate flux and pressure such that the argon stays liquid.

The main purpose of the calorimeter readout is to provide input to the level-1 trigger in form of trigger towers of size $\Delta\eta = 0.1 \times 0.1$, and to read out the energy deposition in each calorimeter cell in case the trigger is activated for a certain collision event. To this effect, a unified readout system is used for all liquid argon calorimeters: First, the analog signal is amplified and processed in front-end electronics close to the detector, which need to be radiation hard. Subsequently, the signal is digitized and sent to off-detector digital processors. This approach ensures the low noise levels needed for a measurement range from 3 TeV down to $\sim$ 10 MeV, with a coherent noise level below 5 % and a frequency corresponding to the trigger rate of 75 kHz.

Through its large $|\eta|$ coverage and thickness, the ATLAS calorimeter system provides a good $E_{\mathrm{T}}^{\mathrm{miss}}$ measurement and a very low level of punch-through to the Muon Spectrometer.

4.2.4 Muon Spectrometer

Combined with the toroid magnet system providing the magnetic field, the outermost detector chambers of ATLAS serve as a spectrometer for all particles exiting the calorimeter system. With the exception of punch-through particles, the majority of the particles measured in this subdetector are muons. The Muon Spectrometer ranges from a radius of 4.25 m to 11 m from the beam axis. The spectrometer is designed to have excellent charge identification, high resolution of momentum measurement, and fast input to the trigger system. It covers a pseudorapidity range up to $|\eta| < 2.7$ for tracking and $|\eta| < 2.4$ for the trigger.

The magnetic field bending the muons' trajectories is generated by the toroid magnets described in Section 4.2.6. Their magnetic field is mostly orthogonal to the muons' direction.

Four sub-detectors are responsible for high-precision measurement of muon tracks as well as triggering on events with high transverse momentum muons. They are arranged in three cylindrical layers in the barrel region and three layers of planar chambers perpendicular to the beam axis in the transition and end-cap regions. Four different types of measurement and trigger chambers are in operation at ATLAS: Monitored Drift Tubes (MDT) and, at large pseudorapidities, Cathode Strip Chambers (CSC) are responsible for high-precision measurement of the track coordinates. Resistive Plate Chambers (RPC) in the barrel region and Thin Gap Chambers(TGC) in the end-caps provide input to the trigger system as well as the measurement of the track coordinate orthogonal to the MDT or CSC measurement.

Monitored Drift Tubes (MDT)

The Monitored Drift Tubes (MDT) provide high-precision tracking of muons in the barrel and end-caps regions of the Muon Spectrometer. These chambers are operated as gaseous drift chambers consisting of aluminum tubes with diameter 29.97 mm filled with an Argon/CO_2 mixture at 3 bar pressure. A muon passing the tube ionizes the gas, leading to electron-ion pairs. The electrons drift towards the tungsten-rhenium wire anode at the center of the tube, which is at a high voltage potential of 3080 V

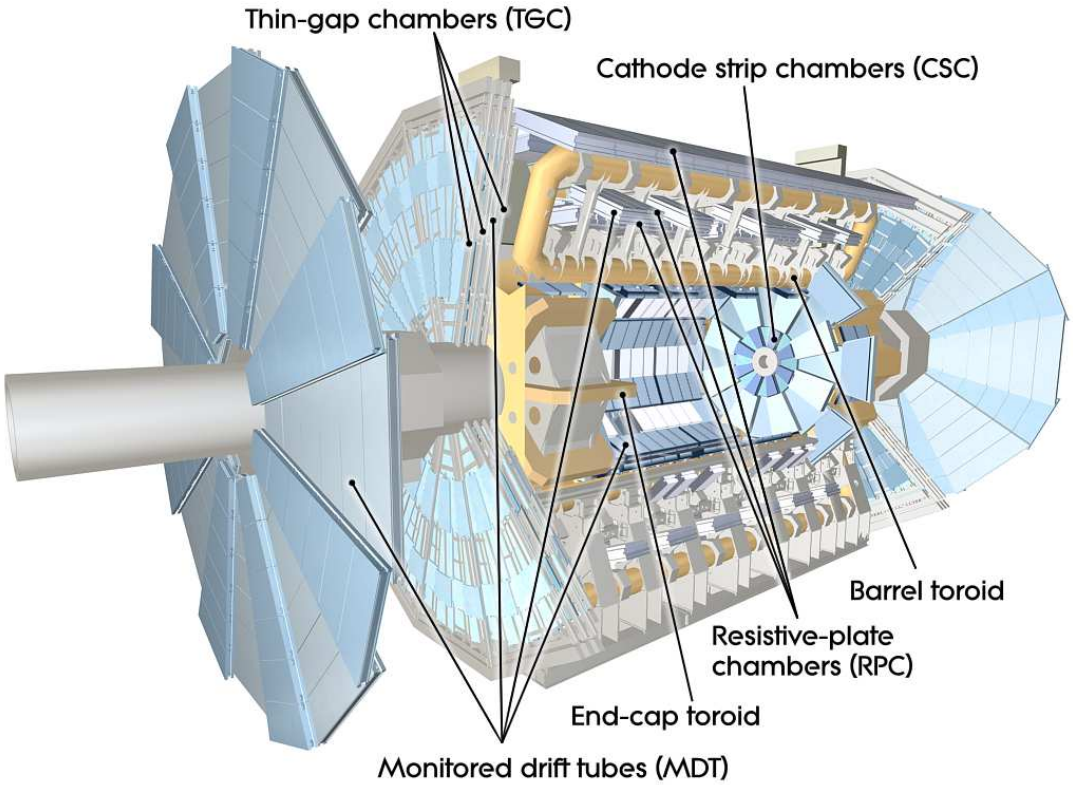

Figure 4.5: Cut-away view of the Muon Spectrometer system of ATLAS [151, fig. 1.4].

with respect to the tube and has a diameter of 50 μm. The maximum drift time is ∼700 ns [151, Tab. 6.2]. The arrival time of the signal from the point of the track closest to the wire is measured with a precision of 0.78 ns, provided by the TTC clock [151, Sec. 6.3.3]. Knowing the drift velocity, this time is converted into the spatial minimum distance of the track to the wire.

As the tubes are arranged in ϕ direction tangentially to circles around the beam axis, the MDT layers measure the z coordinates of a track. In the barrel, the tubes are arranged in rectangular chambers, while they have trapezoid shape in the end-caps.

Each MDT chamber contains two sets of multi-layers, mounted on the two sides of a support structure. The multilayers both consist of three or four layers of tubes. Both ends of a tube are closed with an end-plug keeping the wire localized and providing infrastructure for gas flow as well as high voltage supply and read-out connections.

The signal is read out via the end-plugs using one readout chip for signal processing per eight tubes. It is routed to a time-digital-converter (TDC) which measures the drift time in units of the TTC clock. Subsequently, the signal is broadcast according to the trigger to the readout drivers in the ATLAS service cavern.

Cathode Strip Chambers (CSC)

At pseudorapidities above $|\eta| > 2.0$, the first layer of the end-caps muon chambers consists of Cathode Strip Chambers (CSC), operating as multi-wire proportional chambers. This type of detector is more adapted to the high counting rates expected in that region than the drift tubes.

The CSCs are arranged in two discs per end-cap with eight chambers each, at a distance of 7 m from the interaction point.

The chambers are filled with an Argon-CO_2 mixture and contain a mesh of parallel tungsten wires operated as anodes at a potential of 1900 V. They are surrounded by two cathodes, each segmented in parallel strips. The wire-to-wire distance is 2.5 mm, which is equal to the distance between wires and cathode. One cathode's strips are arranged in parallel to the anode wires, while the other cathode's strips are perpendicular. Reading out the signals in the cathode strips allows for the measurement of the R and ϕ coordinates of the track with a precision of 40 µm in R and 5 mm in ϕ due to coarser segmentation [151, Tab. 6.1].

In contrast to the MDTs, the low drift times of < 40 ns as well as the combination of two coordinates which allows to resolve ambiguities in the presence of more than one track make the CSCs more suitable for the high particle density region. Furthermore, their small gas volume makes them less neutron sensitive.

Alignment of MDT and CSC In order to reach the target high spatial and momentum resolution, strict requirements are imposed on the alignment of the MDT and CSC components. An alignment system monitors each chamber's position relative to its neighbors, as well as deformations within the chambers. The alignment system is based on optical sensors measuring deviations from a straight plane, complemented by temperature sensors allowing to deduce information on the expansion of components. The information allows to correct the positions entered into the muon reconstruction software.

Muon trigger system

The ATLAS muon trigger chambers provide fast information on measured muon tracks as input for the trigger system. Their task is to discriminate between transverse momenta according to certain trigger thresholds and to provide the corresponding bunch crossing information, while being robust facing photon or neutron cavern background.

The trigger system works as shown schematically in Figure 4.6. It consists of three layers of trigger chambers which detect the muon track. Based on one pivotal layer, the coincidences of the first and last layer build curvature patterns of deviation from a straight line. The trigger system evaluates according to these patterns if a certain track curvature and hence a certain momentum threshold has been exceeded.

In the end-caps region, the p/p_{T} ratio is larger, such that a higher granularity is necessary. Also, particle rates are higher than in the barrel. According to these conditions, different technologies are

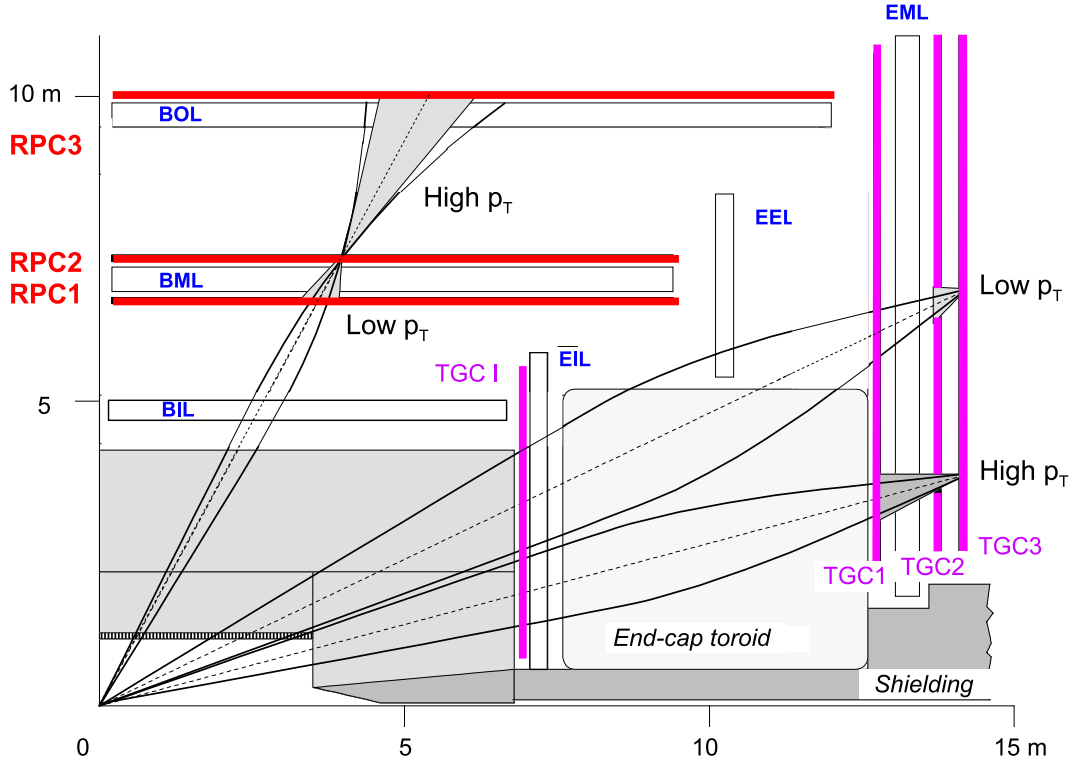

Figure 4.6: Muon trigger system [151]. The pivot layers for coincidence patterns are RPC2 for the barrel and TGC3 for the end-caps. The naming of the MDT chambers follows the general muon system naming scheme [151], where the leading "B" and "E" stand for barrel and end-caps respectively. The second letter can be "I" for inner, "M" for middle, "E" for extended, and "O" for outer layer. The third letter "L" indicates that these chambers belong to the larger ones.

used in the barrel and end-caps, which are described below.

The offline monitoring code for the RPC L1 trigger efficiencies was extended as a part of the work for this thesis [154].

Resistive Plate Chambers (RPC) Besides providing input for the muon trigger system in the barrel, which requires fast detection of tracks, the RPC sub-detector provides the measurement of the ϕ coordinate complementing the MDT coordinate measurement of z.

Three concentric cylindrical layers of RPC chambers cover the range of $|\eta| < 1.05$. The RPC detector units contain two large resistive plates of a plastic laminate material at a parallel distance of 2 mm. The gap is filled with a gas mixture at atmospheric pressure. Graphite electrodes attached to the outsides of the resistive plates provide an electric field of 4900 V/mm between the plates. An incident charged particle ionizes the gas leading to an electric discharge which in turn reduces the potential. In this way, the size and duration of the signal are limited as the potential becomes too low to maintain the discharge [152]. At an intrinsic time resolution of ≤ 1.5 ns, the RPC signals are suitable to be used by the trigger.

The signal is read out via two orthogonal sets of pick-up strips attached to the graphite electrodes. It is amplified and shaped in front-end boards located at the edges of the chambers. The two coordinates are measured with a resolution of 10 mm in z and 10 mm in ϕ [151, Tab. 6.1].

Thin Gap Chambers (TGC) The second type of trigger chambers in the muon system are thin gap chambers, covering the end-caps region between $1.05 < |\eta| < 2.7$ for the track measurement and up to $|\eta| < 2.4$ for triggering. Similarly to the CSCs, they are operated as multi-wire proportional chambers, but with a distance of 1.4 mm between the wire and the graphite cathode. A high voltage of 2900 V is applied between wires and cathodes. The gas mixture of CO_2 and n-C_5H_{12} is operated in quasi-saturated mode. This leads to a relatively low amplification with respect to the primary ionization. Combined with the high voltage, the TGCs thus provide a very good time resolution of 4 ns.

The TGCs are arranged in circular disks consisting of two rings with different granularity in ϕ, owing to the trigger requirements. Pick-up strips with a segmentation perpendicular to the direction of the wires are attached to the cathodes, separated by an insulating layer. This allows to measure the radial coordinate R with a resolution of 2-6 mm by reading out the wire anodes and the azimuth ϕ with a resolution of 3-7 mm via the radial strips [151, Tab. 6.1].

4.2.5 Forward detectors

In addition to the major subdetectors described above, the ATLAS detector possesses three smaller detector systems in the forward region. These are the LUCID detector ("Luminosity measurement using Cerenkov Integrating Detector"), which in combination with the ALFA Roman pots system ("Absolute Luminosity for ATLAS") is responsible for the luminosity measurement. Furthermore, the ZDC ("Zero-Degree Calorimeter") measures the centrality of heavy-ion collisions.

4.2.6 Magnets in the ATLAS detector

Two major magnet systems exist in ATLAS: A thin superconducting solenoid surrounding the Inner Detector, and three large superconducting toroid systems (one in the barrel, two in the end-caps) arranged with an eightfold symmetry around the calorimeters.

Solenoid magnet The solenoid magnet consists of a single layer of a NbTi superconductor coil, designed with the goal to minimize the radiation length thickness in front of the electromagnetic calorimeter. For this purpose, it is integrated in the calorimeter vessel (see Figure 4.7). The solenoid is aligned in parallel to the beam axis and generates a nearly uniform magnetic field of 2 T in axial direction. Liquid helium is used for cooling the superconductor to a temperature of 4.2 K.

Toroid magnets The eight coils of the barrel toroid magnet are housed in racetrack-shaped vacuum vessels arranged cylindrically around the calorimeter, generating an azimuthal magnetic field varying

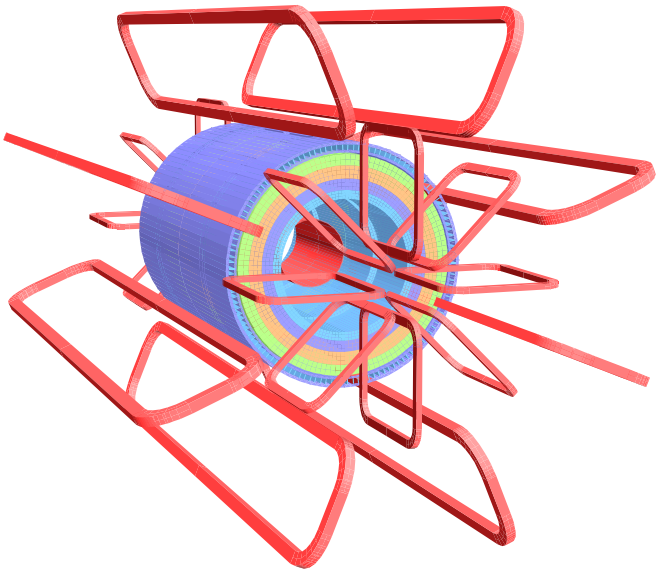

Figure 4.7: Geometric layout of the ATLAS magnets and the tile calorimeter. The eight coils of the barrel toroid magnet are shown, as well as the eight end-cap toroid coils. The solenoid magnet is located inside the tile calorimeter volume. From [151, fig. 2.1].

between 0.2 to 2.5 T. The coils consist of a Nb/Ti/Cu superconductor, operated at 4.2 K. In the end-caps, the toroid magnets are also arranged in an eight-fold symmetry consisting of eight separate toroid coils. These coils are contained in one cryostat per end-cap and rotated by 22.5° with respect to the barrel toroid coils.

Magnetic field Since the accuracy of the magnetic field measurement directly contributes to the resolution of track momentum measurements, the magnetic field in ATLAS is mapped with high precision.

In the inner detector, the field is measured so accurately that the relative bending power uncertainty does not exceed 5×10^{-4}, such that it can be neglected in comparison to the alignment uncertainty in the ID. This high level of accuracy in magnetic field measurement is achieved using a detailed map of the field contributions of all coil windings of the solenoid and by taking into account field modifications by magnetized material of e.g. the calorimeter structure. In addition, NMR and Hall probes are distributed throughout the detector to measure the magnetic field strength during operation.

The toroid field is monitored with an array of ∼1730 Hall effect sensors distributed in the Muon Spectrometer. Measurements from these points are inserted into the magnetic field model, achieving a relative accuracy of 0.2 %.

4.2.7 Trigger and data acquisition

With a bunch crossing rate of 20 MHz and an average event size of 1.5 MB, not every collision event can possibly be written to storage. The ATLAS trigger system consists of three subsequently applied selection levels identifying the bunch crossings whose associated data are to be transferred to storage. The Level-1 (L1) trigger is followed by the Level-2 (L2) trigger and the event filter. According to the trigger decisions, the data acquisition system (DAQ) stores, processes, and transfers the corresponding

detector read-out data. The DAQ system also controls and monitors the ATLAS detector performance during data taking. The hardware control and monitoring is performed by the Detector Control System (DCS).

Level 1 trigger The L1 trigger uses information from the muon trigger chambers (RPC and TGC) to search for patterns of high-p_{T} muons, as well as information from the calorimeters to search for high-p_{T} jets, electromagnetic clusters, hadronically decaying τ-leptons, and large $E_{\mathrm{T}}^{\mathrm{miss}}$ or total transverse energy. Various p_{T} thresholds can be implemented, as well as combinations of requirements. The trigger decision is made by the Central Trigger Processor (CTP) and distributed to the front-end electronics of the detector via the Trigger, Timing, and Control (TTC) system, which also handles the correct bunch crossing identification. The maximum acceptance rate of the L1 trigger is 75 kHz and the decision takes less than 2.5 µs [151, Sec. 8.2]. Events passing the L1 trigger are buffered and transmitted to the L2 trigger by the DAQ, providing regions of interest (RoI) in the event which contain possible trigger objects.

High-level trigger The L2 trigger is seeded by RoIs that have been identified by the L1 trigger. In combination with additional detector information not available at the L1 trigger stage, such as Inner Detector input, the L2 trigger refines the trigger decision. Events that are accepted by the L2 trigger are processed by event-building algorithms and transmitted to the event filter at the rate of 3.5 kHz and a latency of 40 ms [151, Sec. 8.3.5].

The event filter is based on fully built events with full detector granularity and precision, which have passed the L2 trigger. This allows a refined trigger selection according to p_{T} thresholds and better particle identification. The event filter has a 200 Hz acceptance rate and the event processing takes four seconds.

Events accepted by the full trigger chain are transferred to output nodes and subsequently to the CERN central storage.

4.2.8 ATLAS data storage and computing

Data from the ATLAS detector is stored and reprocessed in various stages, starting from the raw data as delivered by the detector. This data is calibrated and processed, reducing the information to the amount necessary, yet controllable, for the analyzer. MC simulation of events is run as described in Section 3.1 and the same reconstruction algorithms are run on simulated events as on data.

ATLAS computing model To cope with the large quantities of data produced by the detector and to facilitate the analysis by numerous analyzers at various locations, computing and storage of ATLAS data are based on two important principles: Object oriented programming and distributed computing on the grid. Simulated and measured collision events are stored in files following the object oriented

programming paradigm and a hierarchical structure of subsequently smaller event formats. A common framework called Athena provides collections of data-processing software [155].

Storage and analysis on the Grid ATLAS detector output is directly transferred to the CERN computing center, where it is stored permanently and calibration and initial processing is performed. The CERN computing facility acts as the Tier-0 in the World-wide LHC Computing Grid (WLCG) [156]. From there, the ATLAS data is distributed to thirteen Tier-1 computer centers, where copies of the raw data are kept and the data is reprocessed. The Tier-1 facilities also provide computing power for the generation of Monte Carlo simulation samples. In addition, about 160 computing centers are connected to the WLCG as Tier-2 facilities, providing resources for end-user analyses.

4.3 Reconstruction and calibration

Signals measured in the detector need to be reconstructed with algorithms adapted to the respective particle type in order to obtain candidates of objects to be used in the physics analysis. The same reconstruction algorithm is applied to the simulated detector response in MC samples.

4.3.1 Jets

Jets are showers of hadrons which are generated when a parton is produced in the event. Jets in ATLAS are reconstructed using clustering algorithms that can be run on any input consisting of four-momentum objects. Experimentally, these can be calorimeter cells, combinations of calorimeter cells, or charged tracks from the Inner Detector. The same algorithms can be applied to theoretically predicted yet non-observable objects such as partons or particles generated with a MC simulation (cf. Section 3.1.7).

Two choices of calorimeter signals can be used as input for jet reconstruction in ATLAS: Calorimeter towers or topological clusters [157]. "Calorimeter towers" consist of calorimeter cells within a fixed grid of $\Delta\eta \times \Delta\phi = 0.1 \times 0.1$. In order to compensate for noise, towers with negative signals are merged with neighboring towers within $\Delta R < 0.35$ until the energy sum is positive. "Topological clusters" are dynamically formed by clustering a seed cell with an energy greater than a certain threshold with its directly neighboring cells. If the direct neighbors have an energy above a certain smaller threshold, they are used as secondary seeds and clustered with their own direct neighbors. If no secondary seeds are found in the vincinity of a seed, all nearest neighbors with a positive energy deposit are included in the cluster. This clustering leads to an intrinsic noise suppression [157].

A jet clustering algorithm is run on this input to reconstruct jets in an event. In general, two types of jet clustering algorithms exist: Cone algorithms cluster particles according to fixed spatial distances, and sequential recombination algorithms cluster particles subsequently according to a minimized distance measure based on momentum and space. Any of these algorithms are required to be infrared and collinear safe, which means that the addition of a soft or collinear emission, for which the emis-

sion probability diverges, does not change the outcome of the algorithm. A variety of jet clustering algorithms can be applied by the ATLAS reconstruction software, chosen depending on the study and which type of QCD interactions are most relevant for the process.

Most common in ATLAS and used in the measurement of $W^{\pm}W^{\pm}jj$-EW in this work is the anti-k_{T} algorithm, a sequential recombination algorithm. For each topological cluster or calorimeter tower i, two measures of distance,

$$d_{i,j} = \min\left(p_{\mathrm{T},i}^{-2}, p_{\mathrm{T},j}^{-2}\right) \times \Delta R_{i,j}^2 / R^2$$

and

$$d_{i,B} = p_{\mathrm{T},i}^{-2}$$

are determined, where $\Delta R_{i,j}^2 = (\phi_i - \phi_j)^2 + (y_i - y_j)^2$ is the distance to any other object j in the event and $p_{\mathrm{T},i}$ denotes the transverse momentum of object i. The cone size parameter R is fixed, usually to a value from 0.4 to 1.2. For each object, the minimum of $d_{i,B}$ and $d_{i,j}$ is determined. If the minimum is $d_{i,B}$, the object i is called a jet and removed from the list of input particles. If the minimum is $d_{i,j}$, the two objects i and j are combined by adding their four-momenta. This is repeated until all initial objects have been assigned to a jet [158].

The ATLAS calorimeters' response to hadronic showers is lower than their response to electromagnetic showers, as a part of the hadronic showers' energy deposit, occurring e.g. as nuclear excitation or escaping muons and neutrinos, cannot be measured by the calorimeter. Since the ATLAS calorimeters are not correcting for this effect, they are called non-compensating. Therefore, on top of the electromagnetic scale calibration (cf. Section 4.3.2), jets have to be calibrated to the full hadronic scale, the so-called jet energy scale (JES). This calibration is based on MC simulation of QCD di-jet events, assigning weights in dependence of the transverse momentum and the pseudorapidity, which allow scaling the measurement to reproduce the truth-level particle momentum [159]. Additional corrections are applied to correct for detector effects such as inactive material, and to correct the pseudorapidity coordinate of the jet.

4.3.2 Electrons

Electron candidates are reconstructed in the following way: First, calorimeter clusters are built using a "sliding window" algorithm on energy deposits in the electromagnetic calorimeter (using topological clusters), in the area up to $|\eta| < 2.47$, excluding the transition region between barrel and endcap ($1.37 < |\eta| < 1.52$). Then, candidates for charged particle tracks in the inner detector which are seeded by these calorimeter clusters are fitted with a track hypothesis, accounting for possible energy loss through bremsstrahlung in the material. If at least one track is matched to the seed cluster according to stricter $\Delta\phi$ and $\Delta\eta$ criteria, they are combined to an electron object [160, 161].

Alternative algorithms can be seeded by the Inner Detector track, which is then matched to the cluster, or they can be based on calorimeter signals only in the forward region beyond the Inner Detector's scope [162]. The electronics calibration of the EM calorimeter is applied to the signal in the front-end

electronics cells in order to convert the signal into the corresponding energy deposit. This is corrected for inactive material and leakage outside the cluster with corrections determined from MC simulation. Finally, an in-situ calibration is determined from $Z \to ee$ events which allow for the calibration of the electromagnetic energy scale [151, 160, 163].

4.3.3 Muons

The combination of tracks in the Inner Detector and in the Muon Spectrometer allows for efficient and precise reconstruction of muons. Different strategies and algorithms exist for Muon reconstruction in ATLAS. Muons candidates consisting of a full fit of tracks in the ID and the MS are called "combined muons", while muon candidates reconstructed from a track in the MS only are called "standalone muons". An ID track combined with one segment in the MS yields a "segment tagged muon", which can occur in the case of low-p_{T} muons. "Calorimeter tagged muons" consist of an ID track and a signature of a minimum ionizing particle in the calorimeter [164].

The $W^{\pm}W^{\pm}jj$ measurement in this work uses the STACO algorithm [163, 165] which reconstructs combined muons as outlined in the following. First, segments in the Muon Spectrometer indicating hits by an incident muon are reconstructed and connected to form tracks. At the same time, inner detector tracks are reconstructed by identifying hits in the Pixel and SCT, which are linked to form track seeds in the inner layers. The track hypotheses are extended to the outer layers, adding measurements from those layers. Then, the Muon Spectrometer tracks are extrapolated and matched to tracks in the Inner Detector, accounting for multiple scattering and energy loss in the calorimeter. The quality of the track match is measured according to the track vectors and their covariance matrices. If found to match well, the two tracks are combined statistically based on the track vectors' covariance matrices.

For the calibration of the Muon system, continuous alignment monitoring is required, as described in Section 4.2.4. In addition, the conditions in the drift chambers and counters of the MDT subdetectors is monitored daily, using a dedicated stream of high-p_{T} single muon events, provided by the L2 muon trigger for calibration [166].

4.3.4 Missing transverse energy

The measurement of missing transverse momentum, defined as a transverse momentum imbalance in the x-$y-$plane in an event and denoted as $E_{\mathrm{T}}^{\mathrm{miss}}$, is the only way to infer information about neutrinos produced in an event, as they always escape the detector.

Missing transverse momentum $E_{\mathrm{T}}^{\mathrm{miss}}$ in an event is reconstructed by taking into account all energy deposits in the calorimeter and in the muon chambers, as well as tracks of low-p_{T} objects which did not continue into the calorimeter and Muon Spectrometer. All objects which are considered for the $E_{\mathrm{T}}^{\mathrm{miss}}$ reconstruction are themselves reconstructed and calibrated. Noise suppression in the calorimeters is included by using only topological clusters and by subtracting pileup during the jet calibration. For muons, the combined muon momentum is used, and the energy deposit in the calorimeter is ignored, as it is counted towards the combined momentum [167].

The transverse components in x and y of the $E_{\mathrm{T}}^{\mathrm{miss}}$ are then calculated on the basis of these objects as the negative sum of the respective x, y components $p_{\mathrm{T},x(y)}$ of the transverse momentum. The same input is used for the total transverse momentum sum of an event.

4.4 Data taking operation and luminosity

The ATLAS detector has been in operation with a center-of-mass energy of 7 TeV in 2010 and 2011, and a center-of-mass energy of 8 TeV in 2012. An integrated luminosity of 20.3 fb^{-1} of data from the 2012 run was considered in the $W^{\pm}W^{\pm}jj$-EW measurement in this work. Figure 4.8 shows the development over time of the integrated luminosity delivered by the LHC, as well as the luminosity recorded by ATLAS and flagged as good quality to be used for physics analyses.

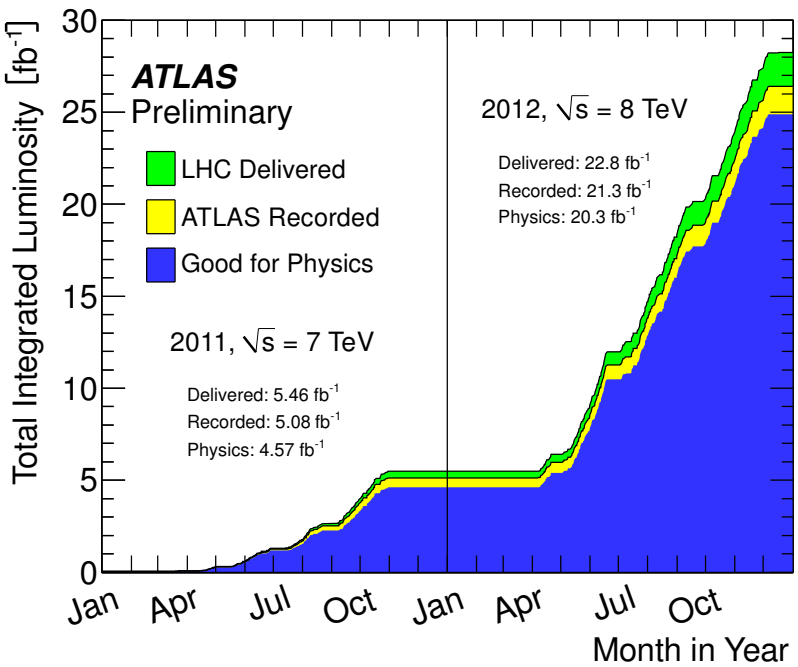

Figure 4.8: Cumulative luminosity delivered by the LHC, recorded by ATLAS, and considered in physics analyses over time in the years 2011 and 2012. The total integrated luminosity delivered at the ATLAS interaction point by the LHC is shown by the sum of the blue, yellow, and green histogram. The blue and yellow histogram show the luminosity fraction recorded by the ATLAS detector, reflecting a DAQ inefficiency as well as an inefficiency due to start-up periods in which no data can be recorded. The blue histogram indicates the integrated luminosity which is flagged as good quality and can be used for analysis [168].

Luminosity measurement The absolute luminosity is measured using *van der Meer (vdM)* scans [169]. It can be determined from the beam parameters according to

$$\mathcal{L} = \frac{n_b f_r n_1 n_2}{2\pi \Sigma_x \Sigma_y}$$

where n_b is the number of bunches colliding per revolution, f_r is the revolution frequency, and n_1, n_2 are the number of protons per bunch in each of the two beams. These parameters are determined by external LHC monitors. The horizontal and vertical convolved beam widths Σ_x and Σ_y are measured in dedicated vdM runs by varying the beam separation. These dedicated runs are used to calibrate the forward detector LUCID (see Section 4.2.5) and the Beam Conditions Monitor (BCM), which consists of four diamond sensors arranged around the interaction point. Both of these devices allow the measurement of the relative luminosity by counting events corresponding to a certain visible interaction rate σ_{vis}. With the cross section of visible interactions determined during the vdM calibration run as $\sigma_{\text{vis}} = (\mu_{\text{vis,vdM}}/\mathcal{L}_{\text{vdM}})n_b f_r$, the luminosity can be calculated according to

$$\mathcal{L} = \frac{\mu_{\text{vis}} n_b f_r}{\sigma_{\text{vis}}}.$$

The luminosity of the 2012 dataset has been determined up to an uncertainty of 2.8 % [170].

Schedule of the LHC The LHC as well as its experiments, including ATLAS, are undergoing hardware upgrades at the time of writing. Operation will restart in the beginning of 2015 at a center-of-mass energy of 13 TeV. Prospects for the measurement of electroweak gauge-boson scattering at higher energy and higher luminosity are investigated in chapter 6.

CHAPTER 5

Measurement of $W^{\pm}W^{\pm}jj$ production with the ATLAS detector

As detailed in Section 3.2.4, $W^{\pm}W^{\pm}jj$ is the most promising final state for a first measurement of a process dominated by electroweak gauge boson scattering. Consequently, an analysis of $W^{\pm}W^{\pm}jj$ events in the final state of leptonically decaying W bosons with the ATLAS detector at the LHC with $\sqrt{s} = 8$ TeV has been performed in the scope of this work. The analysis has been published by the ATLAS collaboration in [56] and is presented in this chapter. The aim of the analysis is the first measurement of the $W^{\pm}W^{\pm}jj$-EW cross section and setting limits on anomalous quartic gauge couplings in the $WWWW$ vertex.

The measurement is carried out as a counting experiment. Thus, an event sample has to be selected which contains as many as possible signal events while the background contribution must be suppressed. The event selection is carried out in three steps: In the object selection step, the reconstructed physical objects which are considered for the analysis are selected. Events are rejected or reweighted based on detector performance and overall event structure in the baseline selection step. In the event selection, signal events are identified according to kinematic properties of the selected objects.

The analysis is performed on the entire dataset of the LHC proton-proton collision run of 2012 at a center-of-mass energy of $\sqrt{s} = 8$ TeV. The total luminosity collected by the ATLAS detector amounts to 20281.4 pb^{-1}, assuming unprescaled triggers, with an uncertainty of 2.8 % determined with the method described in [171].

5.1 Selection of $W^{\pm}W^{\pm}jj$ events

5.1.1 Object selection and corrections

In the first step of the analysis, object candidates obtained by running reconstruction algorithms on the detector output are further selected according to requirements which are adapted and optimized for the analysis of the $W^{\pm}W^{\pm}jj$ final state.

W bosons from the $W^{\pm}W^{\pm}jj$-EW final state are detected through their leptonic decay products. Due to the large cross section of multijet processes at the LHC, which impedes the identification of hadronically decaying W bosons, only leptonic decays ($W \to e\nu_e, W \to \mu\nu_\mu, W \to \tau(\to e\nu_e, \mu\nu_\mu)\nu_\tau$) are considered. In the following, the term "lepton" will be used for charged leptons visible to the detector, i.e. electrons and muons, denoted by e and μ, respectively. Neutrinos, which are also decay products of the W bosons, interact too weakly and therefore cannot be detected by the ATLAS detector. An indication of neutrino production is given by the missing transverse energy variable $E_{\mathrm{T}}^{\mathrm{miss}}$ as described in 4.3.4. The outgoing quarks and gluons are observable through hadronic jets.

The following section gives an overview on the selection, requirements, and correction of these physics objects and their kinematic properties.

Electrons

Electrons [1] in the $W^{\pm}W^{\pm}jj$ analysis occur as decay products of the W bosons.

They are reconstructed and identified as electron candidates as described in 4.3.2, and simply called "electrons" from here on. In order to account for discrepancies found between simulated and measured electrons, two corrections are applied on electrons in the simulation: Their energy is scaled to match a residual η-dependent calibration obtained from $Z \to ee$ events [172] ,[173]. In addition, the electrons' energy is smeared out in order to yield the same resolution as found in data [172]. The electron energy E, pseudorapidty η, and azimuth ϕ are measured by the calorimeter. Provided a sufficient number of hits in the SCT and Pixel detectors, the η and ϕ coordinates are taken from the tracker measurement and the transverse momentum is obtained by scaling the energy by the tracker η coordinate as $p_{\mathrm{T}} = E/\cosh(\eta_{\mathrm{track}})$.

Thus defined electrons are subjected to further selection according to (ATLAS specific) measurement quality requirements as well as kinematic properties:

Electrons are not considered if a hardware problem in the relevant liquid argon calorimeter region is found. Only electrons found by the standard calorimeter cluster-based reconstruction algorithm, and possibly in addition by an ID track-based algorithm, are used in this analysis. As calorimeter clusters are matched with ID tracks for all electrons, only those with an η (as measured by the calorimeter) of $|\eta| < 2.4$ can be used, excluding the transition region between barrel and endcap calorimeter, i.e. $1.37 \leq |\eta| \leq 1.52$. For $W^{\pm}W^{\pm}jj$-EW signal electrons, this is reasonable as the W boson decay

[1] In the analysis, the term "electron" refers to electron candidate objects, reconstructed in the detector as described in 4.3.2. Their measured charge can be negative or positive, implying candidates originating from both electrons and positrons.

products are expected to occur centrally in the detector (cf. 3.2.5). Furthermore, electrons are required to pass the tight++ selection criteria [174], which implement cuts on shower shape, track quality, transition radiation, and the quality of matching the ID track to the calorimeter tower [163] (p. 75). To suppress backgrounds with soft electrons, only electrons with a transverse momentum of $p_{\mathrm{T}} > 15$ GeV are selected. Avoiding the selection of particles not originating in the primary vertex, two cuts are applied on the impact parameters of electron tracks: The longitudinal impact parameter z_0 multiplied by the polar angle component needs to fulfill $|z0 \cdot \sin(\theta)| < 0.5$ mm. The transverse impact parameter, scaled by its significance, is restricted to $\frac{d_0}{\sigma(d_0)} < 3$. Finally, electrons should be sufficiently isolated from surrounding energy deposits, which suppresses electrons originating from hadron decays in jets. This is ensured by two relative isolation criteria: The total energy deposited in topo-clusters inside a cone with radius $R = 0.3$ around an electron cluster's center is required to be less than 14 % of the electron's transverse momentum. This cut is applied after correction of the energy of the topo-clusters for leakage of energy from the electron itself [175] as well as an event-by-event ambient energy density correction, which makes this cut robust against pile-up [176]. In addition, the sum of the transverse momenta of all tracks in a cone with radius $R = 0.3$ around an electron track is not allowed to exceed 6 % of the p_{T} of the electron. The selection of electrons is summarized in Table 5.1.

Muons

Muons[2] in the $W^{\pm}W^{\pm}jj$ final state occur as decay products of the W bosons. They are reconstructed by the STACO algorithm [177] as described in 4.3.3, which combines a track in the ID with a track in the MS. They are required to fulfill the tight quality criteria for combined muons as provided by the Muon Combined Performance group within ATLAS [178].

Additionally, kinematic cuts are applied to select muons further. Their transverse momentum is required to be $p_{\mathrm{T}} > 15$ GeV and the pseudorapidity $|\eta| < 2.5$. Quality criteria on the muon tracks both in the ID and the MS are applied, requiring certain minimum numbers of hits in the subdetectors of the ID [179] to ensure good quality muons.

Furthermore, to select only muons originating in the primary vertex of the collision, the impact parameters of the combined muon track are required to be $|z0 \cdot \sin(\theta)| < 0.5$ mm for the longitudinal impact parameter and $\frac{d_0}{\sigma(d_0)} < 3$ for the transverse impact parameter of the muon w.r.t. the primary vertex. The energy deposited in calorimeter cells or tracks within cones of size $\Delta R = 0.3$ normalized by the p_{T} of the muon have to be lower than 7 % to retain isolated muons. It is ensured that the charge measured from the track curvature in the ID has the same sign as the charge measured from the MS track. All selection criteria applied on muons are summarized in Table 5.1.

Jets

Jets are reconstructed according to Section 4.3.1 using the anti-k_T jet reconstruction algorithm [180] with a jet radius parameter of $R = 0.4$ on topological calorimeter clusters [163, p. 268 ff.]. The jets

[2] Muons and anti-muons are equally considered, cf. previous footnote.

are calibrated to the EM+JES scale [159]. Calibrated jets are further selected according to kinematic properties. A transverse momentum cut $p_{\mathrm{T}} > 30\,\mathrm{GeV}$ is applied to suppress soft-QCD background events. Since the tagging jets are expected to be rather forward in the detector, jets up to $|\eta| < 4.5$ are considered in the analysis. Bad quality jets are rejected according to the BadLooseMinus criterion based on requirements on the quality of track and calorimeter entries. In order to reduce the contribution from pileup jets, those jets within ID acceptance $|\eta| < 2.4$ and with sufficient momentum ($p_{\mathrm{T}} > 50\,\mathrm{GeV}$) are required to have a Jet Vertex Fraction of $\mathrm{JVF} > 0.5$. The JVF is a measure of the contribution by tracks from a specific vertex to a given jet, and aims to reject jets with large contribution from pile-up [181].

In addition, a *b-tagging* algorithm is used to label jets originating from b-quarks in order to suppress backgrounds with t-quark decays. The algorithm of choice is the MV1-tagger [182, 183] at the 70% working point with a MV1-weight of $\mathrm{MV1} > 0.8119$. However, it can only be applied to jets up to $|\eta| < 2.5$. The selection criteria for jets are summarized in Table 5.1.

Overlap removal

In some cases, reconstruction algorithms are not mutually exclusive, i.e. a detected object can be reconstructed by multiple algorithms, yielding duplicate physics objects. A so-called overlap removal procedure is applied in order to remove these duplicates.

1. The jet reconstruction algorithm is run on topological clusters in the calorimeter, which can also be caused by electrons depositing energy in the electromagnetic calorimeter. Therefore, electrons are reconstructed by the jet algorithm and appear as reconstructed jet objects in the data record and the object selection. In order to eliminate these objects from the list of jets, any reconstructed jet closer than $\Delta R = 0.3$ to a reconstructed electron is removed from the event.

2. Muons can cause knock-on electrons while passing the detector. Therefore, if a selected muon is accompanied by a selected electron within a radius of $\Delta R = 0.1$, the electron is removed from the electrons list.

The overlap removal is only applied on the nominally selected leptons according to the criteria listed above. Possible additional leptons reconstructed in the event are not affected by the overlap removal procedure.

All selection requirements applied in the object selection step are summarized in Table 5.1.

Object selection criteria		
Electrons	**accept if**	comment
	`author: 1 or 3`	Cluster based reconstruction
	quality flag `OQ==0`, `bitmask 1446==0`	No problematic LAr cell found
	$p_{\mathrm{T}} > 15\,\mathrm{GeV}$	Transverse momentum
	$\lvert\eta\rvert < 2.47$ and not $1.37 \leq \lvert\eta\rvert \leq 1.52$	η as measured by the calorimeter
	quality: `tight++`	High quality requirements
	$\lvert z0 \cdot \sin(\theta)\rvert < 0.5\,\mathrm{mm}$	Longitudinal impact parameter
	$\frac{d_0}{\sigma(d_0)} < 3$	Transverse impact parameter scaled by its significance
	topoEtcone30 (corrected) / $p_{\mathrm{T}} < 0.14$	Relative calorimeter isolation
	ptcone30 / $p_{\mathrm{T}} < 0.06$	Relative track isolation
Muons	**accept if**	comment
	quality isCombined	Combined track in ID with track in MS [177]
	$\lvert\eta\rvert < 2.5$	Pseudorapidity
	$p_{\mathrm{T}} > 15\,\mathrm{GeV}$	Transverse momentum
	Certain number of hits in PIXEL, SCT, and TRT	Track requirements on hits in the ID [179]
	$\lvert z0 \cdot \sin(\theta)\rvert < 0.5\,\mathrm{mm}$	Longitudinal impact parameter
	$\frac{d_0}{\sigma(d_0)} < 3$	Transverse impact parameter scaled by its significance
	topoEtcone30 (corrected) / $p_{\mathrm{T}} < 0.07$	Relative calorimeter isolation
	ptcone30 / $p_{\mathrm{T}} < 0.07$	Relative track isolation
	q/p (MS) $\times$ q/p (ID) > 0	Same sign of the charge in ID and MS
Jets	**accept if**	comment
	$p_{\mathrm{T}} > 30\,\mathrm{GeV}$	Transverse momentum
	$\lvert\eta\rvert < 4.5$	Pseudorapidity
	jet cleaning	No `BadLooseMinus` jets
	JVF > 0.5	Jet Vertex Fraction for jets with $\lvert\eta\rvert < 2.4$, $p_{\mathrm{T}} < 50\,\mathrm{GeV}$
Overlap removal between nominal electrons, jets, and muons:		
Electron – jet overlap removal		
	Remove jet if $\Delta R(e, j) < 0.3$	
Muon – electron overlap removal		
	Remove electron if $\Delta R(\mu, e) < 0.1$	

Table 5.1: Summary of selection criteria for analysis objects with ATLAS specific terminology.

5.1.2 Baseline selection of events

Events are subject to several quality requirements imposed on the performance of the detector. Events passing this selection provide a baseline of events ready for the analysis.

Event corrections

Events are rejected if they are not included in a list of ATLAS runs with good overall detector performance, provided in a "Good Run List" [184]. In order to match MC events to the pileup conditions found in the dataset, the events in each MC sample are reweighted such that the sample's distribution of average number of pileup interactions $\langle\mu\rangle$ reproduces the $\langle\mu\rangle$ distribution in the used dataset. The position of the beam spot along the z-axis depends on beam conditions. Therefore, the vertex of the hard interaction in MC events is shifted along the z coordinate such that it matches the z-distribution of primary vertices in the collision dataset [185].

Detector performance

Additionally, events with selected objects concerned by faulty regions in the detector are rejected: Events with noise bursts in the liquid argon calorimeter are vetoed as well as events with corrupted tiles in the tile calorimeter. Events with missing information from a subdetector are removed using the `coreFlag` variable. If a selected jet is pointing to a hot cell in the tile calorimeter, the event is not used [186]. Furthermore, events with selected jets passing the `IsLooserBadJet` [187] algorithm are removed. The primary vertex, i.e. the vertex with the largest $\sum p_{\mathrm{T}}^2(tracks)$, is required to originate from at least three tracks.

Triggers

The High-Level Trigger information for the remaining events is retrieved to check if one of the accepted trigger chains has been activated by the event. If not, the event is rejected. Duplicate events from the `Egamma` and `Muon` data streams are removed consistently. All selection criteria counted towards the baseline selection are summarized in Table 5.2.

5.1.3 Signal selection

Further selection criteria are applied on the baseline events in order to identify the final state of $\ell^{\pm}\ell^{\pm}jj + E_{\mathrm{T}}^{\mathrm{miss}}$.

First, the trigger requirement is reinforced by matching selected electrons and muons to objects which have fired the trigger responsible for writing the event. To this effect, the transverse momenta of all muon and electron candidates are compared to the respective trigger threshold. If the trigger threshold is exceeded by the transverse momentum of the lepton by at least 1 GeV, and the ΔR distance between trigger tower and lepton candidate is smaller than $\Delta R < 0.15$ (0.1) for electrons (muons) [188], the lepton candidate is assumed to be the object to have fired the trigger. The number

Baseline event selection	
Good Run List	`data12_8TeV.periodAllYear_DetStatus-v61-pro14-02_DQDefects-00-01-00_PHYS_StandardGRL_All_Good.xml`
Pileup reweighting	Re-weight MC according to average number of pileup interactions
Vertex reweighting	Smear z position of primary vertices in MC
LAr calorimeter error	Veto event if `larError == 2`
Tile calorimeter error	Veto event if `tileError == 2`
Incomplete events	Veto event if `(coreFlags&0x40000) != 0`
Hot Tile	Veto event if it contains jets in $\eta \approx -0.15$, $\phi \approx 2.7$ (close to hot cell) during periods B1 and B2
$E_{\mathrm{T}}^{\mathrm{miss}}$cleaning	Remove events with bad quality jets
Primary vertex	At least three tracks reconstructed at primary vertex
Trigger	Accepted triggers: `EF_e24vhi_medium1`, `EF_e60_medium1`, `EF_mu24i_tight`, `EF_mu36_tight`
Lepton scale factors	Re-weight MC events according to trigger efficiency

Table 5.2: Summary of baseline event selection.

of electrons and muons to have fired a trigger has to be non-zero in order for the event to pass this validity check. Event weights are corrected according to lepton trigger scale factors in order to match the trigger efficiency in data [189, 190].

$W^{\pm}W^{\pm}jj$ selection

In this analysis, $W^{\pm}W^{\pm}jj$ events are measured in two different phase space volumes: The more inclusive volume is utilized for the measurement of the inclusive production of $W^{\pm}W^{\pm}jj$ events, i.e. the combination of $VVjj$-EW and $VVjj$-QCD production mechanisms. Since the inclusive production of $W^{\pm}W^{\pm}jj$ has not been measured previously, measuring the combined process is a necessary step for the extraction of the $W^{\pm}W^{\pm}jj$-EW cross section. Although the QCD-mediated production of $W^{\pm}W^{\pm}jj$ does not contain electroweak gauge boson scattering and a quartic gauge vertex at tree-level, it is important to probe the SM prediction of this process and its modeling by MC generators.

The following selection criteria are applied to enhance the fraction of $W^{\pm}W^{\pm}jj$ events in the sample:

Each event is required to contain exactly two selected leptons with $p_{\mathrm{T}} > 25\,\mathrm{GeV}$. In order to suppress contributions from processes with more than two leptons in the final state, an additional lepton veto is applied: Requiring exactly two leptons selected according to the criteria listed in Section 5.1.1 introduces a large number of events with three prompt leptons from WZ/γ^* where one of the leptons is not accepted by these rather tight selection cuts. In order to suppress this contribution, any event containing additional leptons selected separately from the nominal leptons according to looser identification and isolation requirements are rejected.

In contrast to the nominal electrons which are required to be of `tight++` quality and pass rather tight calorimeter and track isolation requirements, the additional electrons are only required to be of `loose++` quality. A transverse momentum down to $p_{\mathrm{T}} > 7\,\mathrm{GeV}$ is accepted. No calorimeter isolation requirement is applied on the additional electrons, and the track isolation requirement is relaxed. Additional muons can be of `loose` quality and have a transverse momentum as low as $p_{\mathrm{T}} > 6\,\mathrm{GeV}$. No calorimeter isolation and a relaxed track isolation are required for additional muons. The selection criteria for additional leptons are listed in Table 5.3.

Object selection criteria for additional leptons		
Electrons	**accept if**	comment
	`author: 1 or 3`	Cluster based reconstruction
	quality flag `OQ==0`, `bitmask 1446==0`	No problematic LAr cell found
	$p_{\mathrm{T}} > 7\,\mathrm{GeV}$	Transverse momentum
	$\lvert\eta\rvert < 2.47$ and not $1.37 \leq \lvert\eta\rvert \leq 1.52$	η as measured by the calorimeter
	quality: `loose++`	Low quality requirements
	$\lvert z0 \cdot \sin(\theta)\rvert < 0.5\,\mathrm{mm}$	Longitudinal impact parameter
	$\frac{d_0}{\sigma(d_0)} < 3$	Transverse impact parameter scaled by its significance
	topoEtcone30 (corrected) / $p_{\mathrm{T}} < \infty$	No calorimeter isolation
	ptcone30 / $p_{\mathrm{T}} < 0.13$	Looser relative track isolation
Muons	**accept if**	comment
	isCombined or segment tagged	Muon quality [177]
	$\lvert\eta\rvert < 2.5$	Pseudorapidity
	$p_{\mathrm{T}} > 6\,\mathrm{GeV}$	Transverse momentum
	Certain number of hits in PIXEL, SCT, and TRT	Track requirements on hits in the ID
	$\lvert z0 \cdot \sin(\theta)\rvert < 0.5\,\mathrm{mm}$	Longitudinal impact parameter
	$\frac{d_0}{\sigma(d_0)} < 3$	Transverse impact parameter scaled by its significance
	topoEtcone30 (corrected) / $p_{\mathrm{T}} < \infty$	No calorimeter isolation
	ptcone30 / $p_{\mathrm{T}} < 0.15$	Looser relative track isolation

Table 5.3: Selection of additional leptons ("veto leptons") which are vetoed in the event selection.

In the remaining events, each muon is required to be separated from any jet by $\Delta R > 0.3$, otherwise the event is vetoed. Events are selected if the two selected leptons are of the same electric charge and their invariant mass is $M_{\ell,\ell} > 20\,\mathrm{GeV}$. This cut is adopted in order to reject the low $M_{\ell,\ell})$ region which is prone to generator mis-modelling (cf. Page 3.2.5).

The data sample is split into three orthogonal channels according to their number of electrons and muons, respectively. These channels will be denoted by ee (two electron channel), $\mu\mu$ (two muon channel), and $e\mu$ (one electron and one muon channel). The same signal selection is applied in the three channels, except for a Z window cut which is only applied in the ee channel, where the invariant

mass of the two leptons is required to be different from the Z boson mass by at least 10 GeV.

Events are further rejected if the missing transverse momentum amounts to less than 40 GeV. Each event is required to contain at least two jets with transverse momentum $p_{\mathrm{T}} > 30$ GeV and $|\eta| < 4.5$. If at least one of the jets is b-tagged, the event is rejected. Finally, a cut on the invariant mass of the two hardest jets of $M_{jj} > 500$ GeV is applied. Selection criteria applied to select the events in the Inclusive analysis region are summarized in Table 5.4.

All selection requirements have been optimized to yield the largest signal significance [191].

$W^{\pm}W^{\pm}jj$-EW selection

For the measurement of the purely electroweak production of $W^{\pm}W^{\pm}jj$, the phase space is further restricted by applying a cut on the rapidity separation of the two hardest jets of $|\Delta y(j,j)| > 2.4$ is applied. Table 5.4 summarizes the event selection criteria.

Inclusive selection	Signal criteria	
ee	$e\mu$	$\mu\mu$
2 electrons	1 electron, 1 muon	2 muons
	Trigger matching	
	Both leptons $p_{\mathrm{T}} > 25$ GeV	
	Veto events with additional leptons	
	$\Delta R(\mu, j) > 0.3$	
	$M(\ell,\ell) > 20$ GeV	
	Both leptons same electric charge	
$\lvert M_{ee} - m_Z\rvert > 10$ GeV	–	–
	$E_{\mathrm{T}}^{\mathrm{miss}} > 40$ GeV	
	At least 2 jets with $p_{\mathrm{T}}(j) > 30$ GeV and $\lvert\eta\rvert(j) < 4.5$	
	No b-tagged jets	
	$M_{jj} > 500$ GeV	
VBS selection	$\lvert\Delta y(j,j)\rvert > 2.4$	

Table 5.4: Summary of signal event selection for the Inclusive and VBS phase spaces.

One event selected according to the $W^{\pm}W^{\pm}jj$-EW selection is shown in Figure 5.1. As a candidate for a $W^{\pm}W^{\pm}jj$-EW event, it features two very forward jets with large invariant mass M_{jj} and large rapidity separation.

5.1.4 Fiducial phase space

For the cross section measurement and theoretical calculations, two fiducial regions are defined on truth level, closely following the analysis selection. The "Inclusive phase space" is defined for the extraction of the full $W^{\pm}W^{\pm}jj$ production, while the purely electroweak production of $W^{\pm}W^{\pm}jj$ is extracted in the "VBS phase space".

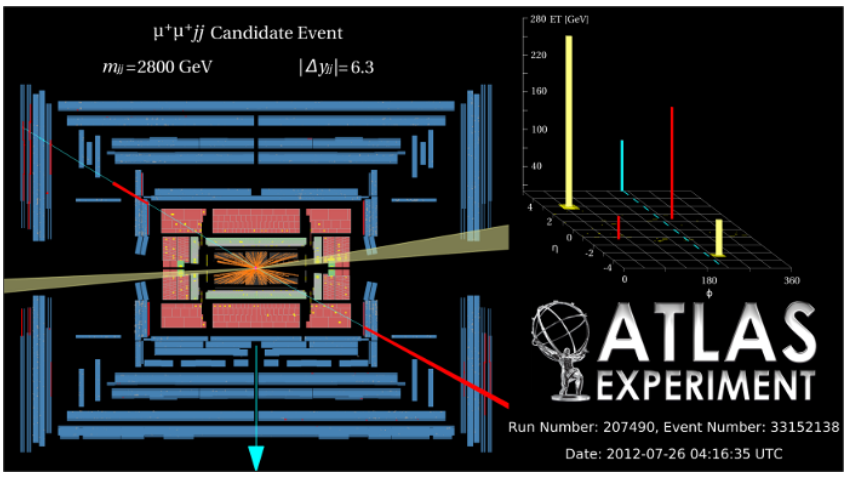

Figure 5.1: Event display of an event with two positively charged muons $\mu^+\mu^+$ in the VBS region. The invariant mass of the tagging jets is $M_{jj} = 2800$ GeV and their rapidity separation $|\Delta y(jj)| = 6.3$. Red tracks signify muon tracks. The two yellow cones are the tagging jets which are found at $\eta = 2.9$ with p_{T} = 271 GeV and at $\eta = -3.4$ with p_{T} = 54 GeV. The blue arrow points in the direction of the $E_{\mathrm{T}}^{\mathrm{miss}}$ vector [56].

Inclusive phase space

The phase space definition is based on objects selected as follows:

- Leptons are defined as "dressed" leptons by adding the four-momenta of all photons within $\Delta R = 0.1$ from the final state lepton to its four-momentum. In order to avoid photons from jet hadronization to enter the lepton definition, the selection of the highest p_{T} lepton is based on the leptons before adding photon momenta.
- Jets are clustered by using a jet reconstruction algorithm on all final state objects except for muons and neutrinos, and removing jets found within a distance of $\Delta R = 0.05$ of an electron.
- Events with selected leptons originating from τ decays are removed.

The Inclusive phase space region is then defined by requiring

- two leptons with $p_{\mathrm{T}} > 25$ GeV, $|\eta| > 2.5$, $M_{\ell\ell} > 20$ GeV, $\Delta R(\ell\ell) > 0.3$ and same electric charge,
- missing transverse momentum $E_{\mathrm{T}}^{\mathrm{miss}} > 40$ GeV,
- at least two jets reconstructed with the anti-kt algorithm with jet parameter $R = 0.4$ and with $p_{\mathrm{T}} > 30$ GeV, $|\eta| < 4.5$,
- $\Delta R(\ell, j) > 0.3$ for any pair of selected jets and leptons, and
- $M_{jj} > 500$ GeV for the two jets with largest p_{T}.

VBS phase space

In addition to the Inclusive phase space selections, the VBS fiducial region is defined by selecting events with

- rapidity difference $|\Delta y(jj)| > 2.4$ for the two jets with largest p_{T}.

The two jets with largest p_{T} are referred to as "tagging jets", since they allow for the tagging of the VBS process by means of the cut on their invariant mass and (pseudo)rapidity difference.

Figure 5.2a illustrates the selection on the invariant mass of the tagging jets, applied after all cuts of the Inclusive selection except the M_{jj} requirement. The cut on $M_{jj} > 500\,\mathrm{GeV}$ is chosen in order to suppress a large amount of background while enhancing the signal contribution. The absolute difference of rapidities of the tagging jets is shown in Figure 5.2b.

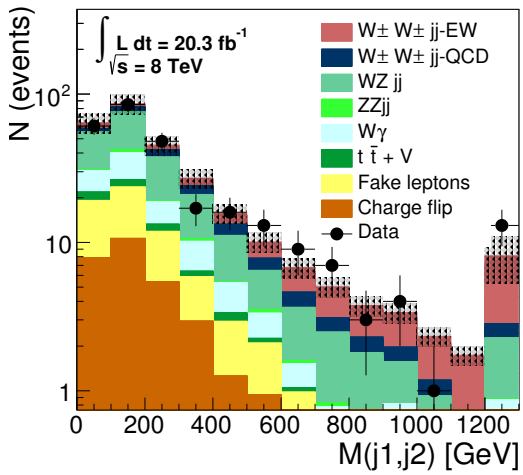

(a) Invariant mass of the tagging jets in the Inclusive signal region without application of the M_{jj} cut.

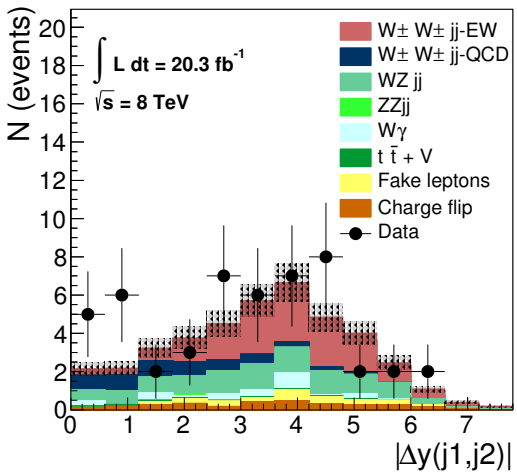

(b) Absolute difference of rapidities of the tagging jets in the Inclusive analysis region

Figure 5.2: Distributions of M_{jj} and $|\Delta\eta(jj)|$ before the selection on the respective observable is applied. The hatched area represents the systematic error on the total prediction.

5.2 Background estimates

Background events mimicking the final state of two same-charge leptons, missing transverse momentum, and two jets, although not containing electroweak or QCD-mediated $W^{\pm}W^{\pm}jj$ production as defined in Section 3.2.1 arise for various reasons:

- Background with additional prompt leptons: Two same-charge leptons are produced in the hard scattering process in addition to one or more leptons which are not detected. Leptons from the hard scattering are referred to as "prompt leptons". This background is dominated by the

final states from processes containing the production of two electroweak gauge bosons, called "diboson" processes.

- Charge mis-identification (or charge flip) background: Two opposite-charge prompt leptons are produced, but for one of them the charge is incorrectly reconstructed.
- Background with mis-identified (or fake) leptons: One or both of the selected leptons are not originating in the hard scattering, but in the decay or mis-identification of jets or photons.
- Double parton interaction background: The final state leptons and jets are produced in different hard scattering vertices through multiple parton interactions.

The physical processes leading to these backgrounds as well as the estimate of background contributions in the signal region is described in this section.

5.2.1 Background with additional prompt leptons

Background contributions due to additional prompt leptons not passing the selection criteria arise from production of two electroweak gauge bosons such as WZ/γ^*+jets and ZZ/γ^*+jets production, referred to as "diboson" production. In addition to leptonic decays of W or Z bosons in diboson production yielding events with more than two prompt leptons, semi-leptonically decaying $t\bar{t}$ pairs with an associated vector boson which decays into leptons contribute events with additional leptons. Contributions in the signal region from WZ/γ^*jj, ZZ/γ^*jj, and $t\bar{t}+V$ are estimated using MC simulation.

Background from diboson production is the largest contributing process in the signal regions (see Table 5.10). The largest contribution is from WZ/γ^*+jets production. In the following, the production of WZ/γ^*jj is referred to as $W^{\pm}Zjj$ production, where the γ^* contribution is implied as it is experimentally not separable from the Z boson.

In the signal selection, events from processes with one ore more additional prompt leptons are suppressed by selecting exactly two leptons and by vetoing events which contain additional leptons selected with looser quality and isolation requirements than the nominal leptons. Selection criteria for the additional leptons deviating from those criteria for nominal leptons are given in Table 5.3.

The contribution of this background to the signal region is estimated from MC and cross-checked in a control region selected by requiring a third lepton which passes the selection of additional leptons. All other cuts are applied as in the nominal event selection (Table 5.4), omitting the requirement on M_{jj} and $|\Delta y(j,j)|$ to retain statistics and to probe a more inclusive phase space. In Figure 5.3, the distributions of M_{jj} and $|\Delta y(j,j)|$ in this control region with an additional lepton are shown. Good agreement between data and the MC prediction dominated by $W^{\pm}Zjj$ production is observed.

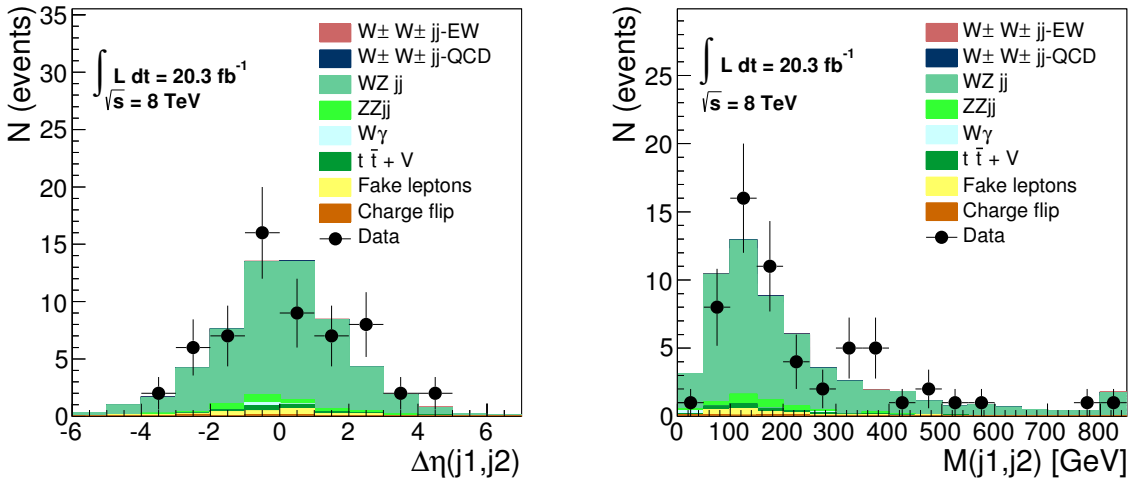

(a) Pseudorapidity difference of tagging jets

(b) Invariant mass of tagging jets

Figure 5.3: Kinematic distributions of the tagging jets in a control region requiring at least one additional veto lepton selected according to Table 5.3. In the M_{jj} distribution, the last bin contains the overflow.

Rejection of additional leptons

Background from diboson processes and $t\bar{t} + V$ production can be rejected by removing events containing additional prompt leptons. In the first step, selecting exactly two nominal leptons passing the nominal lepton requirements (Table 5.1) rejects a large part of the contribution from backgrounds with additional leptons. To further improve the background rejection, events with one or more additional leptons passing lower kinematic thresholds and looser quality requirements are rejected. The loosened criteria for selecting the additional leptons ("veto leptons") are summarized in Table 5.3. Looser criteria are applied on the quality algorithm used for the electron selection. Muons used for the additional lepton selection can be combined muons or segment tagged muons, i.e. an inner detector track with only one associated segment in the muon spectrometer is sufficient, while nominal muon selection only uses combined muons with a full track in the muon spectrometer. Kinematically, the acceptance is increased by lowering the requirement on the transverse momentum. This aims at vetoing leptons produced in WZ/γ^* with $p_{\mathrm{T}} < 15\,\mathrm{GeV}$, as additional leptons with $p_{\mathrm{T}} > 15\,\mathrm{GeV}$ are rejected by the nominal requirement of exactly two leptons. In addition, the requirement on the track isolation of electrons and muons, defined as the sum of the energy of other tracks surrounding the lepton's track within a distance of $\Delta R < 0.3$ ("pTcone30") is loosened. The calorimeter isolation, i.e. the energy sum of calorimeter cells in a cone of $\Delta R < 0.3$ around the reconstructed lepton ("ETcone30"), is not restricted for additional leptons.

The selection of additional leptons is illustrated in Figures 5.4a to 5.6b. The shown distributions contain any additional leptons selected according to the veto criteria (Table 5.3) but with looser cuts on the transverse momenta of electrons and muons, $p_{\mathrm{T}} > 1$ GeV and the track isolation pTcone30/$p_{\mathrm{T}} < 3$. These leptons are selected separately from the nominal leptons, which are not included. All event selection cuts according to the VBS phase space except for the veto on additional leptons are applied. Figures 5.4a and 5.4b show the p_{T} distributions of thus selected muons and electrons, respectively. Since soft muons and electrons are present also in the signal process, the p_{T} threshold of the veto lepton is set to $7(6)$ GeV for electrons (muons).

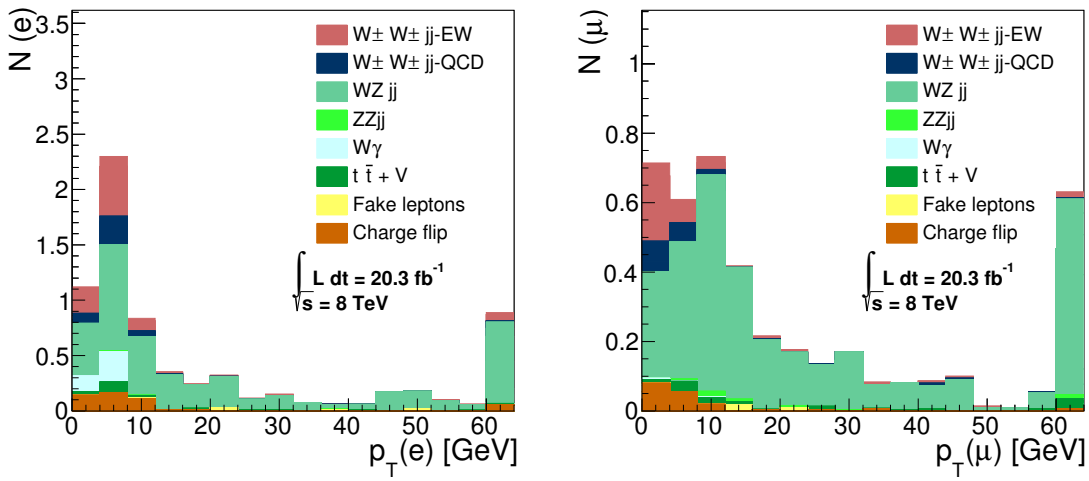

(a) Transverse momentum of additional electrons. Optimized cut for veto electrons: $p_{\mathrm{T}} > 7$ GeV.

(b) Transverse momentum of additional muons. Optimized cut for veto muons: $p_{\mathrm{T}} > 6$ GeV.

Figure 5.4: Distribution of the transverse momenta of additional, loosely selected leptons in the Inclusive analysis region without a third lepton veto. Leptons are required to have a transverse momentum $p_{\mathrm{T}} > 1$ GeV and the track isolation pTcone30/$p_{\mathrm{T}} < 3$. The last bin contains the overflow.

The distributions of the track isolation of additional electrons and muons are depicted in Figures 5.5a and 5.5b, respectively. In order to reject additional leptons in backgrounds with more than two prompt leptons, the track isolation of veto leptons is set to $13\,\%$ of the transverse momentum for electrons, and $15\,\%$ of the transverse momentum for muons.

Figures 5.6a and 5.6b show the relative calorimeter isolation of additional electrons and muons, respectively. No calorimeter isolation is required for additional leptons.

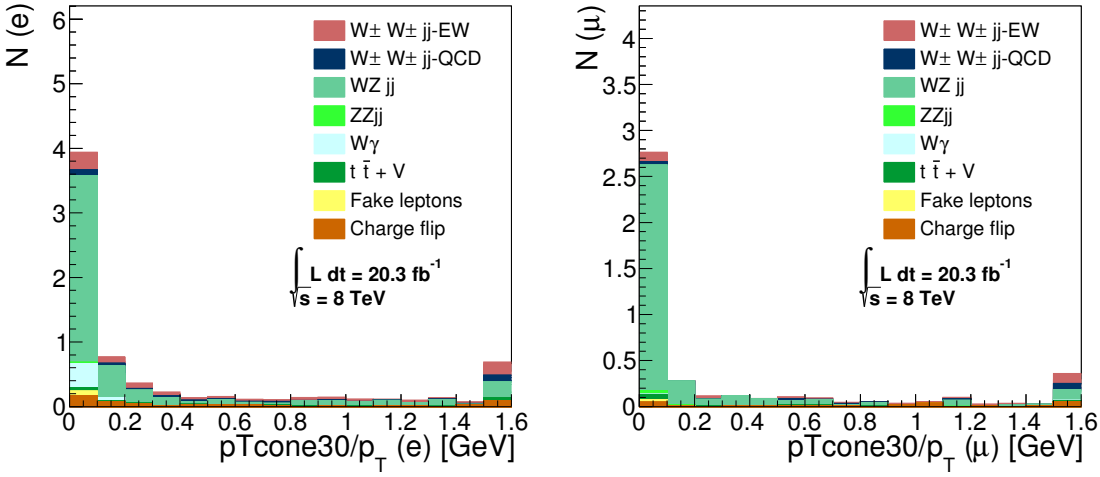

(a) Relative track isolation of additional electrons. Optimized cut for veto electrons: ptcone30/$p_{\mathrm{T}} < 0.13$

(b) Relative track isolation of additional muons. Optimized cut for veto muons: ptcone30 / $p_{\mathrm{T}} < 0.15$.

Figure 5.5: Distributions of the relative track isolation of additional, loosely selected leptons in the Inclusive analysis region without a third lepton veto. Leptons are required to have a transverse momentum $p_{\mathrm{T}} > 1$ GeV and the track isolation pTcone30 / $p_{\mathrm{T}} < 3$. The last bin contains the overflow.

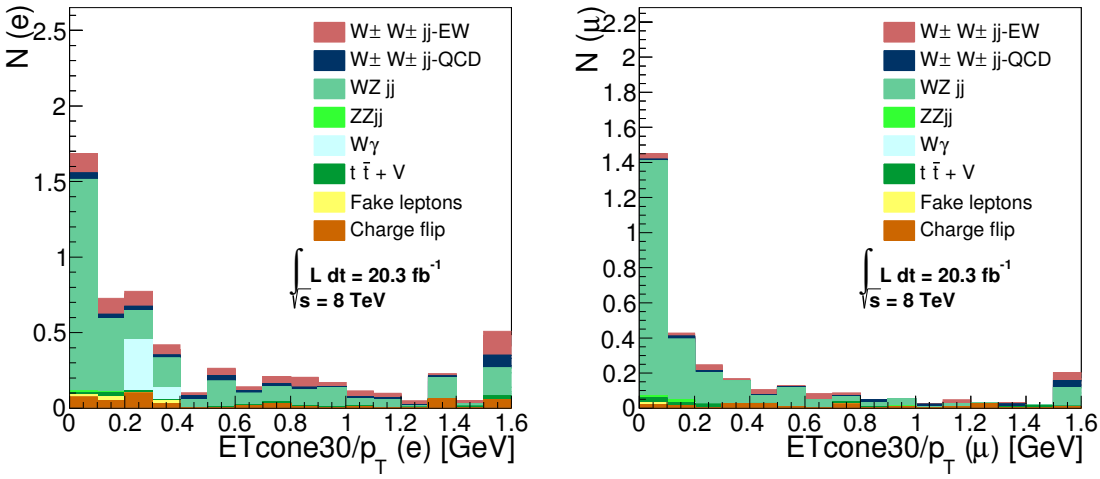

(a) Relative calorimeter isolation of additional electrons. Optimized cut for veto electrons: topoEtcone30 (corrected) / $p_{\mathrm{T}} < \infty$.

(b) Relative calorimeter isolation of additional muons. Optimized cut for veto muons: topoEtcone30 (corrected) / $p_{\mathrm{T}} < \infty$.

Figure 5.6: Distributions of the relative calorimeter isolation of additional leptons in the Inclusive analysis region without a third lepton veto. Leptons are required to have a transverse momentum $p_{\mathrm{T}} > 1$ GeV and the track isolation pTcone30/$p_{\mathrm{T}} < 3$. The last bin contains the overflow.

While the signal process $W^{\pm}W^{\pm}jj$-EW as well as the $W^{\pm}W^{\pm}jj$-QCD background are not significantly reduced by the stricter selection, the $W^{\pm}Zjj$ background is reduced by $28\,\%$ in the VBS analysis region summed over all channels, resulting in a larger significance of the measurement. In the Inclusive analysis region, the veto leads to a decrease of the $W^{\pm}Zjj$ contribution by $32\,\%$.

The comparison of event yields in the VBS signal region with and without the strict veto is given in Table 5.5.

Process	without strict veto	with strict veto
$W^{\pm}W^{\pm}jj$-EW	13.87 ± 0.25	13.80 ± 0.25
$W^{\pm}W^{\pm}jj$-QCD	1.35 ± 0.06	1.34 ± 0.06
$W^{\pm}Zjj$	10.87 ± 0.44	7.85 ± 0.38
$ZZjj$	0.15 ± 0.04	0.11 ± 0.04
$W\gamma$	1.94 ± 0.4	1.94 ± 0.4
$t\bar{t}+V$	0.21 ± 0.03	0.17 ± 0.03
Data	38.0	34.0

Table 5.5: Comparison of event yields of diboson and $t\bar{t}+V$ processes in the VBS region summed over the three final states for the selection without applying a veto on additional leptons and the selection with such a veto. In the case without strict veto, exactly two nominal leptons according to Table 5.1 are required.

Composition of the $W^{\pm}Zjj$ background

The $W^{\pm}Zjj$ final state can be produced via electroweak vertices only ($W^{\pm}Zjj$-EW) or with QCD vertices included ($W^{\pm}Zjj$-QCD). The $W^{\pm}Zjj$-EW contribution, which also contains vector boson scattering, accounts for $(17 \pm 1)\,\%$ of the combined $W^{\pm}Zjj$-EW and $W^{\pm}Zjj$-QCD event yields in the Inclusive region, and $(19 \pm 2)\,\%$ in the VBS region. Event yields split by the electroweak and QCD-mediated production of $W^{\pm}Zjj$ are listed in Table 5.6. Interference between $W^{\pm}Zjj$-EW and $W^{\pm}Zjj$-QCD (cf. Section 3.2.3) is neglected.

	ee	$e\mu$	$\mu\mu$
Inclusive region			
$W^{\pm}Zjj$-EW	0.46 ± 0.04	0.92 ± 0.05	0.42 ± 0.03
$W^{\pm}Zjj$-QCD	2.29 ± 0.22	4.64 ± 0.31	1.95 ± 0.21
VBS region			
$W^{\pm}Zjj$-EW	0.37 ± 0.03	0.8 ± 0.05	0.35 ± 0.03
$W^{\pm}Zjj$-QCD	1.69 ± 0.19	3.19 ± 0.26	1.46 ± 0.19

Table 5.6: Contributions from $W^{\pm}Zjj$-EW and $W^{\pm}Zjj$-QCD in the signal regions of the $W^{\pm}W^{\pm}jj$ selection.

The $WZjj$ background contains diagrams with b quarks in the initial and final state, for instance as illustrated in Figures 5.7a and 5.7b.

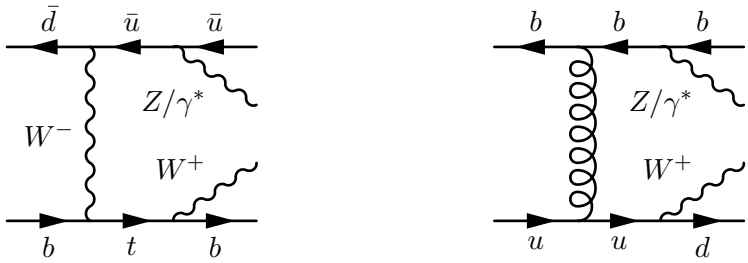

(a) $W^{\pm}Zjj$-EW (b) $W^{\pm}Zjj$-QCD

Figure 5.7: Feynman diagram of contributions from b quarks to the final state of $WZjj$, included in the definition of $W^{\pm}Zjj$ production.

Their contribution to the signal region is suppressed by the application of a b tagging algorithm and the rejection of events containing at least one jet tagged as a b jet. Nevertheless, a contribution of events with b quarks in the matrix element remains in the signal regions. According to the MC truth record, $15 \pm 2\,\%$ of $W^{\pm}Zjj$-EW events in the Inclusive region contain b quarks, and $16 \pm 2\,\%$ of $W^{\pm}Zjj$-EW events in the VBS region. In the $W^{\pm}Zjj$-QCD contribution, events containing b quarks (cf. Fig. 5.7b) account for $5 \pm 2\,\%$ of events in the Inclusive region and $5 \pm 1\,\%$ in the VBS region.

5.2.2 Charge mis-identified background

Another background to $W^{\pm}W^{\pm}jj$ events is caused by events with a hard-scattering final state containing two opposite-sign leptons, when the charge of one lepton is mis-identified such that the event passes the same-sign requirement, as a so-called charge-flip event. Even though charge mis-identification rates are low, processes like Z+jets or $t\bar{t}$ production have large cross sections compared to $W^{\pm}W^{\pm}jj$ production and can thus enter the signal region in a sizable amount. Apart from the same-charge requirement, a high cut on $E_{\mathrm{T}}^{\mathrm{miss}}$ also reduces the background due to charge mis-identification in Z+jets production.

Charge mis-identification of combined muons is highly unlikely and is therefore neglected in this study [192]. Two reasons exist for the charge of an electron to be incorrectly measured: In the inner detector, an electron can emit highly energetic bremsstrahlung which can produce an electron-positron-pair in the detector material. If the particle with higher momentum is the one with charge opposite to the original electron, the reconstructed lepton is measured with opposite charge to the prompt lepton from the scattering. Furthermore, the charge of an electron can be mis-measured due to incorrect association of tracks to clusters or a mis-reconstructed track in the inner detector. In both cases, the energy of the measured electron differs from the momentum of the prompt electron from the hard scattering.

The charge-flip rate has been measured in data by selecting events with ee pairs with an invariant mass close to the Z boson mass ($70\,\mathrm{GeV} < M_{ee} < 100\,\mathrm{GeV}$) [191]. This sample is dominated by $Z \to ee$ events, with small contributions from WZ production which are removed by subtracting the MC based estimate of these contributions. The remaining sample is assumed to contain only $Z \to ee$ events, such that any event with a same charge lepton pair must have had one lepton's charge mis-

identified. Double charge mis-identification are neglected, as the charge-flip rates are very low. A likelihood with Poissonian probability is used to extract the charge-flip rates from the number of opposite-sign and same-sign events in the $Z \to ee$ sample.

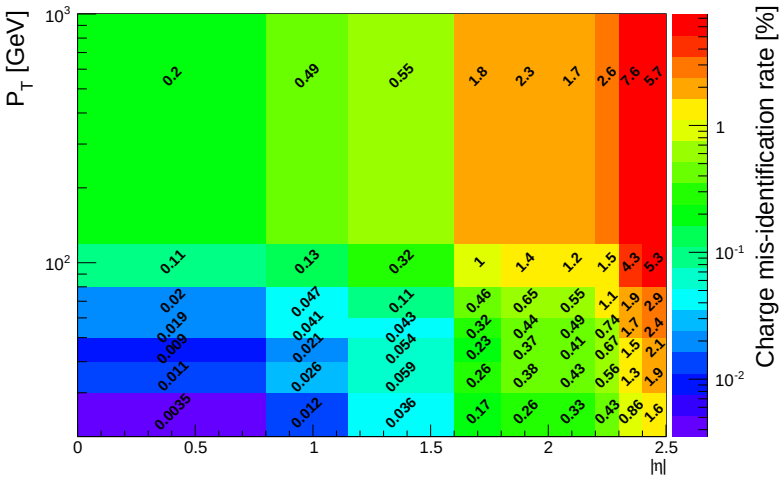

Figure 5.8: Charge mis-identification rate measured in a $Z \to ee$ data sample with electrons selected according to nominal selection criteria. Rates are given in bins of $|\eta|$ and p_{T}. From [191, 193].

Due to the mis-measurement, the p_{T} of the measured object generally deviates from the p_{T} of the original lepton. An energy correction, both by shifting and by smearing the electron's energy, is applied to the charge-flipped electrons.

To determine the contribution of background due to charge-flip in the signal region, a data sample is selected with the same criteria as the signal baseline selection. In these events, the charge of each electron is conjugated and the event weight is scaled by the electron's charge-flip rate according to its η and p_{T} coordinates. This is done separately for each electron in an event. The contribution from events with charge mis-identification is cross checked in several orthogonal control regions [191].

The main uncertainties of the estimate of background due to charge mis-identification arise from the uncertainty of the energy shift due to mis-measurement of the track and from the statistical uncertainty of the charge mis-identification rate. Both are varied within their uncertainties and the effect of the variation is propagated to the signal regions. Final systematic uncertainties of the background estimate are summarized in Section 5.3.3.

5.2.3 Background with mis-identified leptons

Events with one prompt lepton and one or more jets contribute as background to $W^{\pm}W^{\pm}jj$ production when an additional lepton is reconstructed from a jet as a so-called "fake lepton". Events from processes such as W+jets, $t\bar{t}$ with one hadronically decaying W boson, and single top production are caused to enter the signal region if one of the associated jets is reconstructed as a lepton by the reconstruction algorithm, or if a lepton from a hadronic decay within a jet passes the selection criteria. This

background contribution is suppressed by requiring strict isolation of leptons and large $E_{\mathrm{T}}^{\mathrm{miss}}$.

The probability for a jet to be mis-identified as a lepton has been measured in a data sample with two jets in the final state, called "dijet sample", selected with one tagging jet passing nominal jet selection criteria (Table 5.1) and one reconstructed lepton with $\Delta\phi(\ell, j) > 2.8$. By requiring the lepton to be back-to-back with the jet, and the transverse mass of the lepton and the missing transverse momentum to be $M_{\mathrm{T}}(\ell, E_{\mathrm{T}}^{\mathrm{miss}}) < 40\,\mathrm{GeV}$, it is ensured that this sample contains only dijet events [191].

The fake rate is then defined as the ratio of the number of events in which the lepton passes the tight nominal selection criteria (Table 5.1) to the number of events in which it passes the orthogonally defined selection criteria for "loose leptons" (Table 5.7),

$$\mathrm{f_{lepton}} = \frac{\mathrm{N_{tight}}}{\mathrm{N_{loose}}}. \tag{5.1}$$

Object selection criteria for loose leptons		
Electrons	**accept if**	comment
	`author: 1 or 3`	Cluster based reconstruction
	quality flag `OQ==0`, `bitmask 1446==0`	No problematic LAr cell found
	$p_{\mathrm{T}} > 15\,\mathrm{GeV}$	Transverse momentum
	$\lvert\eta\rvert < 2.47$ and not $1.37 \leq \lvert\eta\rvert \leq 1.52$	η as measured by the calorimeter
	quality: `loose++`	Low quality requirements
	$\lvert z0 \cdot \sin(\theta)\rvert < 5\,\mathrm{mm}$	Longitudinal impact parameter
	$\frac{d_0}{\sigma(d_0)} < 10$	Transverse impact parameter scaled by its significance
	$0.14 <$ topoEtcone30 (corrected) / $p_{\mathrm{T}} < 2.0$	Calorimeter isolation
	$0.06 <$ ptcone30 / $p_{\mathrm{T}} < 2.0$	Relative track isolation
Muons	**accept if**	comment
	isCombined and tight	Muon quality [177]
	$\lvert\eta\rvert < 2.5$	Pseudorapidity
	$p_{\mathrm{T}} > 15\,\mathrm{GeV}$	Transverse momentum
	Certain number of hits in PIXEL, SCT, and TRT	Track requirements on hits in the ID
	$\lvert z0 \cdot \sin(\theta)\rvert < 5\,\mathrm{mm}$	Longitudinal impact parameter
	$\frac{d_0}{\sigma(d_0)} < 10$	Transverse impact parameter scaled by its significance
	$0.07 <$topoEtcone30 (corrected) / $p_{\mathrm{T}} < 2.0$	Calorimeter isolation
	$0.07 <$ ptcone30 / $p_{\mathrm{T}} < 2.0$	Relative track isolation

Table 5.7: Selection of leptons with lower quality, loose leptons, for the estimation of background contribution due to mis-identified jets.

The fake factor $\mathrm{f_{lepton}}$ is measured in bins of $|\eta|$ and p_{T}. Figures 5.9a and 5.9b shows the fake factors determined by the above described method in dependence of the transverse momentum for electrons and muons, respectively.

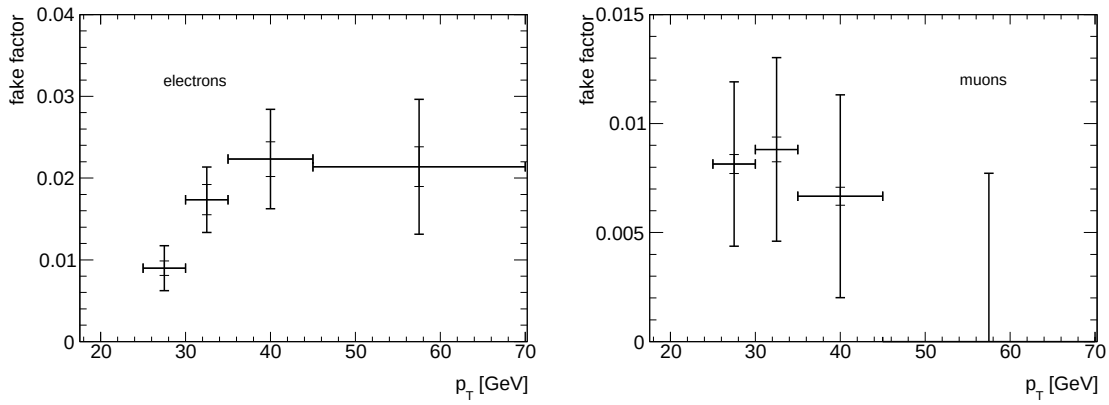

(a) Electron fake factors

(b) Muon fake factors

Figure 5.9: Fake factors determined with the dijet method [191]. The total uncertainty is given by the error bars, where the inner section shows the statistical uncertainty only.

The contribution of fake leptons in the signal region is estimated by applying these fake factors on a sample of $\mathrm{N_{tight+loose}}$ events in which one lepton passes the nominal lepton selection, and another lepton is selected according to loose lepton selection criteria listed in Table 5.7. Contribution from processes with prompt leptons in the dijet sample, namely W+jets and Z+jets processes, are subtracted based on MC. Each event is then scaled by $\mathrm{f_{lepton}}(p_{\mathrm{T,loose}}, \eta_{\mathrm{loose}})$ according to the kinematic properties of the loosely selected lepton as

$$\mathrm{N_{fake\ bg}} = \mathrm{f_{lepton}} \times \mathrm{N_{tight+loose}}. \tag{5.2}$$

The contribution from fake leptons is cross checked in several control regions. Final yields are given in Table 5.10.

The main systematic uncertainties on this background estimate are evaluated as follows: An uncertainty of the fake factors is introduced by the selection of the loose leptons in the dijet sample. By varying the cut on $M_{\mathrm{T}}(\ell, E_{\mathrm{T}}^{\mathrm{miss}})$ by 5 GeV and the $\Delta\phi(\ell, j)$ criterion by 0.1, the uncertainty of the fake factors is estimated and propagated to the signal region. The normalization of the subtraction samples with prompt leptons is varied within its uncertainty, determined from a control region. This variation is propagated to the final signal regions. The arising systematic uncertainties are summarized in Section 5.3.3.

5.2.4 Double parton scattering background

Hadronic collision events containing two or more hard interactions with momentum transfer of the same order of magnitude constitute the double-parton scattering (DPS) processes. The simulation and measurement of double- and multi-parton interaction processes are subject to large uncertainties. The first measurement of W+dijets production via DPS has been performed with ATLAS [101]. In general, for the simulation, the correlation between the two parton interactions is neglected, and instead the product of the cross-sections of the two processes is scaled by an effective area parameter related to the inelastic proton-proton scattering cross-section $\sigma_{\text{eff}} \approx 15\,\text{mb}$ [194]. For the final state of $W^{\pm}W^{\pm}jj$, events from DPS processes can enter the signal region if one gauge boson is produced at each of the vertices, or if a gauge boson pair is produced at one vertex and two jets at the other vertex. The latter contribution is included in the modelling of underlying event in the `Sherpa` samples used for the diboson processes.

To estimate the contributions from DPS processes in the $W^{\pm}W^{\pm}jj$ signal regions MC samples of DPS processes are generated with `Pythia8`. The main DPS processes with two vertices of hard interaction, and the corresponding event yields in the VBS region (Table 5.4) are shown in Table 5.8.

vertex 1	vertex 2	Events in Inclusive region	Events in VBS region
W	W	0.031 ± 0.008	0.028 ± 0.008
W	Z/γ^*	0.0056 ± 0.003	0.0056 ± 0.003
Z/γ^*	Z/γ^*	0.001 ± 0.0009	0.001 ± 0.0009
WZ	dijet	1.6 ± 0.2	1.6 ± 0.2
ZZ	dijet	0.060 ± 0.060	0.060 ± 0.060

Table 5.8: Signal yields of DPS processes for the combined ee, $e\mu$, and $\mu\mu$ final states in the VBS region with MC statistic uncertainties.

Within statistic uncertainties, the event yields are the same in the Inclusive and the VBS region. Among the processes with single boson production at two vertices, $W + W$ is the dominating process. Generally, these processes yield negligible event numbers in the signal regions. Therefore, these processes are not included in the measurement. A non-negligible contribution arises from WZ + dijet production. However, the contribution of WZ production with an additional dijet vertex is contained in the underlying event of the WZ-QCD sample used for modelling diboson background [102], so it is not included to avoid double-counting. The event yields in Table 5.8 provide an estimate for the contribution of DPS processes to the $WZjj$ background.

5.2.5 Background from a W boson in association with a converted photon

Final states with more than one lepton can also be produced by $W\gamma$+jets final states if the photon is converted into an electron-positron pair. In the case of an asymmetric conversion, where one lepton carries away the largest fraction of the initial energy of the photon, events with one leptonically

decaying W boson and one converted photon can enter the signal region [191]. Such effects are estimated using simulation of the $W + \gamma$ production as well as the conversion in the detector. Event yields estimated from MC simulation are given in Tables 5.9 and 5.10 for the inclusive and the VBS analysis regions, respectively.

5.2.6 Expected event yields

The background estimates as described above are used to determine the expected event yields in the Inclusive and VBS signal regions, respectively. Statistical errors arise from the limited MC statistics, in the case of background estimated based on simulation, and from the limited size of data samples used for the data-based background estimates. Table 5.9 presents the expected event yields in the Inclusive analysis region for all background processes discussed above.

	ee	$e\mu$	$\mu\mu$
$W^{\pm}W^{\pm}jj$-EW	3.07 ± 0.12	8.93 ± 0.2	4.9 ± 0.15
$W^{\pm}W^{\pm}jj$-QCD	0.89 ± 0.05	2.49 ± 0.09	1.43 ± 0.07
$W^{\pm}Zjj$	2.75 ± 0.22	5.56 ± 0.32	2.37 ± 0.21
$ZZjj$	0.1 ± 0.05	0.16 ± 0.1	0.07 ± 0.04
$W\gamma$	1.1 ± 0.32	1.55 ± 0.36	0.0 ± 0.0
$t\bar{t} + V$	0.15 ± 0.03	0.26 ± 0.03	0.11 ± 0.02
Fake leptons	0.73 ± 0.11	1.53 ± 0.13	0.34 ± 0.04
Charge-flip	2.05 ± 0.07	0.82 ± 0.05	0.0 ± 0.0
Data	12.0	26.0	12.0

Table 5.9: Event yields in the Inclusive analysis regions with statistical errors

Expected event yields of the signal and all background processes in the VBS analysis region are given in Table 5.10.

	ee	$e\mu$	$\mu\mu$
$W^{\pm}W^{\pm}jj$-EW	2.54 ± 0.11	7.21 ± 0.18	4.04 ± 0.13
$W^{\pm}W^{\pm}jj$-QCD	0.25 ± 0.03	0.71 ± 0.04	0.38 ± 0.03
$W^{\pm}Zjj$	2.06 ± 0.19	3.99 ± 0.26	1.81 ± 0.19
$ZZjj$	0.05 ± 0.03	0.05 ± 0.03	0.01 ± 0.00
$W\gamma$	0.7 ± 0.2	1.24 ± 0.33	0.0 ± 0.0
$t\bar{t} + V$	0.05 ± 0.02	0.1 ± 0.0	0.02 ± 0.01
Fake leptons	0.61 ± 0.1	1.27 ± 0.12	0.28 ± 0.04
Charge-flip	1.38 ± 0.06	0.66 ± 0.04	0.0 ± 0.0
Data	6.0	18.0	10.0

Table 5.10: Event yields in the VBS analysis regions with statistical errors

5.3 Systematic uncertainties

5.3.1 Theoretical predictions for diboson processes

The MC samples used for diboson background estimates are listed in Appendix D. These samples are scaled to a cross section determined at NLO-QCD. The cross section of the corresponding process at matrix-element level is calculated using VBFNLO [111] or PowhegBox [135] as described later. The uncertainties on these cross sections are evaluated as described in Section 5.3.2. Results are validated against Whizard [107] and MadGraph [106] at leading order.

Process	$\sigma_{\text{fid,incl}}$ [fb]	$\sigma_{\text{fid,VBS}}$ [fb]	$\sigma_{\text{sample(incl)}}$ [fb]	$\sigma_{\text{sample(VBS)}}$ [fb]
$W^{\pm}W^{\pm}jj$-EW	1.003 ± 0.060	0.881 ± 0.053	19.9 ± 1.2	20.8 ± 1.3
$W^{\pm}W^{\pm}jj$-QCD	0.352 ± 0.049	0.098 ± 0.018	16.7 ± 2.3	13.5 ± 2.5
$W^{\pm}Zjj$-EW	0.395 ± 0.091	0.336 ± 0.089	73.4 ± 17	75.3 ± 20
$W^{\pm}Zjj$-QCD	1.039 ± 0.21	0.640 ± 0.013	12.4 ± 2.0	12.8 ± 1.5

Table 5.11: Calculation of cross sections of diboson plus dijets processes at NLO-QCD in the inclusive ($\sigma_{\text{fid,incl}}$) and VBS fiducial ($\sigma_{\text{fid,VBS}}$) phase space volumes, respectively. The extrapolation to the full sample phase space of the corresponding sample generated with Sherpa is given based on the calculations in the inclusive ($\sigma_{\text{sample(incl)}}$) and the VBS ($\sigma_{\text{sample(VBS)}}$) regions, respectively [191].

The interference between the $W^{\pm}W^{\pm}jj$-EW and the $W^{\pm}W^{\pm}jj$-QCD processes is counted towards the $W^{\pm}W^{\pm}jj$-EW sample. The size of the interference has been determined [191] to be $16.7\,\%$ of the $W^{\pm}W^{\pm}jj$-EW cross section in the Inclusive region and $7.8\,\%$ of the $W^{\pm}W^{\pm}jj$-EW cross section in the VBS region. It can also be parametrized as [191]

$$\sigma^{\text{INT}}_{\text{VBS, fid}} = k_{\text{INT}} \times \sqrt{\sigma^{\text{EW}}_{\text{fid,VBS}} \times \sigma^{\text{QCD}}_{\text{fid,VBS}}} \text{ with } k_{\text{INT}} = 0.231. \tag{5.3}$$

5.3.2 Theory uncertainties

Uncertainties of the signal and background predictions have been determined for the Monte Carlo samples used in this analysis, mainly $W^{\pm}W^{\pm}jj$ and $W^{\pm}Zjj$. The fiducial cross sections in the inclusive and VBS phase spaces and their uncertainties have been evaluated separately for the electroweak and QCD-mediated production.

These processes are modeled with LO MC produced with Sherpa, using Matrix-Element and Parton shower matching in the CKKW scheme. The fiducial cross sections are calculated with the most accurate tools available using either PowhegBox or VBFNLO, and listed in Table 5.11. The cross sections include the full process with electrons and muons in the final state, excluding τ contributions. For the evaluation of the uncertainty, model uncertainties, scale and pdf uncertainties, as well as parton shower effects are taken into account.

$W^{\pm}W^{\pm}jj$-EW signal

The fiducial cross section for $W^{\pm}W^{\pm}jj$-EW is calculated using PowhegBox and cross-checked with VBFNLO, both at NLO-QCD. In the PowhegBox calculation, a dynamic scale of

$$\mu_{R,F} = \sum_{i=1,2} \left(p_{\mathrm{T}}(j_i) + \sqrt{M_W^2 + p_{\mathrm{T}}(W_i)^2} \right)$$

is used, while in VBFNLO, the scale is set to the momentum transfer of the exchanged W/Z boson [111]. Furthermore, the PowhegBox calculation is performed using on-shell W bosons in the final state [191]. These differences result in a modelling uncertainty of 5 % in the Inclusive region and 3 % in the VBS region, which is included in the total uncertainty.

Due to strict cuts on jet momenta and dijet mass, the parton shower has a large effect (cf. [195]). The effect of the parton shower on the NLO cross sections has been estimated to be ~ 2 % by applying different parton shower algorithms to the PowhegBox NLO events: the Pythia8 [103] parton shower with AU2 tune for the underlying event, and the Herwig++ [105] parton shower with Jimmy [196] for the underlying event [191]. In order to cover the relative change in acceptance in the Sherpa sample due to the parton shower, the uncertainty in the VBS region is increased to 4 %.

Scale and PDF uncertainties have been evaluated with VBFNLO at NLO in QCD. Varying the factorization and renormalization scales separately by factors of 2 and 0.5, the largest difference excluding extreme combinations of scale variations is taken as uncertainty, which yields an uncertainty of ± 1.5 % in both regions. The PDF uncertainty is determined from the CT10 [197] Eigenvector variations combined with the difference of central values with respect to MSTW2008 [198], and results in an uncertainty of ± 2 % in the Inclusive region and ± 3 % in the VBS region. The PowhegBox + Pythia8 calculation is used as the central value for the signal prediction. Uncertainties of the $W^{\pm}W^{\pm}jj$-EW production cross section are summarized in Table 5.12.

$W^{\pm}W^{\pm}jj$ EW		
Source of uncertainty	Uncertainty (%)	
	Inclusive region	VBS region
MC statistics	1	2
Generator	5	3
Showering model	2	4
Scale	2	2
PDF	2	3
Total	6	6

Table 5.12: Summary of theoretical uncertainties of the $W^{\pm}W^{\pm}jj$-EW process prediction [191].

The largest contribution to the total uncertainty originates in the modelling by the matrix-element generators as well as the parton showers.

$W^{\pm}W^{\pm}jj$-QCD

The fiducial cross sections for $W^{\pm}W^{\pm}jj$-QCD are calculated using the PowhegBox generator. As no alternative NLO calculation exists, the 5 % maximum difference from the $W^{\pm}W^{\pm}jj$-EW case is assumed to be valid for this process as well.

Parton shower effects are evaluated by applying two different such algorithms to the NLO events generated using PowhegBox. A cross-check with the Sherpa fiducial acceptance is carried out [191]. The differences yield uncertainties of 3 % and 7 % in the Inclusive and VBS regions, respectively.

For the scale uncertainties, a variation by a factor of 2 and 0.5 in the renormalization and factorization scales in the PowhegBox calculation yields a total uncertainty of 12 % in the Inclusive and 13 % in the VBS region. The PDF uncertainty is evaluated from CT10 Eigenvector variations as well as the difference to the central value from MSTW2008, resulting in a total PDF uncertainty of 2 % in both fiducial regions [191].

$W^{\pm}W^{\pm}jj$ QCD		
Source of uncertainty	Uncertainty (%)	
	Inclusive region	VBS region
MC statistics	4	8
Generator	5	
Showering model	3	7
Scale	12	13
PDF	2	2
Total	14	18

Table 5.13: Summary of theoretical uncertainties of the $W^{\pm}W^{\pm}jj$-QCD process prediction [191].

$W^{\pm}Zjj$-EW

For the calculation of $W^{\pm}Zjj$-EW cross sections and uncertainties, the full $\ell\ell\ell\nu jj$ final state is split in the contribution with a b-quark in the final state and the contribution without. Systematic uncertainties are determined for the contribution without b-quarks and propagated to the contribution containing b-quarks.

The total cross section at NLO QCD is calculated with VBFNLO. The parton shower effects are determined by applying different parton showering algorithms to the LO events generated using VBFNLO [191], since no NLO events can be generated with VBFNLO. As seen for the $W^{\pm}W^{\pm}jj$-EW process, the parton shower effects for NLO are smaller than for LO events, so the resulting uncertainty covers the uncertainty for NLO cross sections. Between the Pythia8 and the Herwig++

algorithm, a difference of 9 % and 10 % is obtained in the Inclusive and VBS regions, respectively.

Scale uncertainties are evaluated by varying the renormalization and factorization scales by a factor of 0.5 and 2 separately [191]. This yields an overall scale uncertainty of 2 % in the Inclusive and 5 % in the VBS region. PDF uncertainties, determined with the same procedure as for the $W^{\pm}W^{\pm}jj$-EW sample, amount to 6 % and 12 %, respectively.

All uncertainties are summarized in Table 5.14.

$W^{\pm}Zjj$-EW		
Source of uncertainty	Uncertainty (%)	
	Inclusive region	VBS region
MC statistics	1	2
Showering model	9	10
Scale	2	5
PDF	6	12
Total	12	17

Table 5.14: Summary of theoretical uncertainties of the $W^{\pm}Zjj$-EW process prediction [191].

The ratio of the contribution without b-quarks in the final state to one with b-quarks is calculated using `Sherpa`. All uncertainties are propagated from the contribution without b-quarks.

$W^{\pm}Zjj$-QCD

VBFNLO is used to determine the $W^{\pm}Zjj$-QCD fiducial cross sections [191]. For parton shower effects, LO events from `VBFNLO` are provided with a parton shower from `Herwig++` or `Pythia8`, taking the difference as the uncertainty.

For the scale and PDF uncertainties, the same procedures are applied as in the $W^{\pm}Zjj$-EW process.

Contrary to the $W^{\pm}W^{\pm}jj$ and $W^{\pm}Zjj$-EW processes, the $W^{\pm}Zjj$-QCD final state also occurs through diagrams with zero or one parton in the matrix element, which finally have two jets after parton showering. This contribution is included in the Sherpa sample and has a large parton shower uncertainty. The effect is determined using a dedicated MadGraph sample with two different parton shower models (`Pythia8` and `Herwig++`) [191]. An uncertainty of 52 % is obtained from this comparison, which results in 6 % uncertainty in the total $W^{\pm}Zjj$-QCD contribution.

All uncertainties for $W^{\pm}Zjj$-QCD are summarized in Table 5.15.

5.3.3 Experimental uncertainties

Systematic uncertainties are estimated for all background processes. For each of the backgrounds estimated from data, the uncertainty of the method was evaluated separately (cf. Sections 5.2.2 and 5.2.3). Backgrounds based on the MC prediction are subject to uncertainties on object reconstruction, which

$W^{\pm}Zjj$-QCD		
Source of uncertainty	Uncertainty (%)	
	Inclusive region	VBS region
MC statistics	2	2
Showering model	12	7
Scale	6	6
WZ +0,1 partons	6	6
PDF	5	5
Total	16	12

Table 5.15: Summary of theoretical uncertainties of the $W^{\pm}Zjj$-QCD process prediction [191].

are applied on the analysis to determine their effect on final event yields. The systematic uncertainties are estimated by varying the following properties:

- Energy resolution of electrons, muons (ID and MS), jets (JER), $E_{\mathrm{T}}^{\mathrm{miss}}$, b-tagged jets,
- Energy scale of electrons, muons, jets (JES), $E_{\mathrm{T}}^{\mathrm{miss}}$,
- Identification efficiency of electrons, muons,
- Trigger efficiency of electrons, muons,
- Efficiency of JVF cut, b-tagging,
- Contributions from heavy flavors and pile-up jets,
- Luminosity measurement, and
- Photon conversion rate.

Uncertainties of the identification and trigger efficiencies of electrons and muons are obtained by varying the corresponding scale factors within 1σ of their uncertainty. Systematic uncertainties of the MC samples for background and signal are summarized in Table 5.16 for the Inclusive region and in Table 5.17 for the VBS analysis region. The dominant contribution to the total uncertainty arises from uncertainties on jet reconstruction in the $W^{\pm}Zjj$ background.

Source	$W^{\pm}W^{\pm}jj$ EWQCD	$W^{\pm}Zjj$ EWQCD	$t\bar{t}$+V	ZZ EWQCD	$W\gamma$
b-tag scale factor (SF)	0.6	0.7	11	2.9	2.9
e energy/identification		1.9			
μ p_T/identification		0.8			
Veto-e identification SF	–	1.6-2.7	0.6-0.8	1.6-2.7	–
Veto-μ identification SF	–	0.5-1.3	0.2-0.3	0.5-1.3	–
Trigger SF		0.1-0.6			
$E_{\mathrm{T}}^{\mathrm{miss}}$	1.1	1.5	0.9	22.7	8.0
JER/JES/JVF	$\pm^{5.7}_{5.0}$	$\pm^{13}_{14}$	19	$\pm^{13}_{14}$	30
Theory	8.0	14.0	30.0	19.0	17.0
Conversions	–	–	–	–	$\pm^{22}_{13}$
Pileup	0.8	8.0	1.5	8.0	8.0
Luminosity		2.8			

Table 5.16: Systematic uncertainties of MC background and signal samples in the inclusive signal region [191] in %, summarized for all final states.

Source	$W^{\pm}W^{\pm}jj$- EWQCD	EW	QCD	$W^{\pm}Zjj$ -EWQCD	$t\bar{t}$+V	ZZ -EWQCD	$W\gamma$
b-tag scale factor (SF)	0.6			0.7	7	2.9	2.4
e energy/identification				1.9			
μ p_T/identification				0.8			
Veto-e identification SF	–			1.6-2.7	0.6-0.8	1.6-2.7	–
Veto-μ identification SF	–			0.5-1.3	0.2-0.3	0.5-1.3	–
Trigger SF				0.1-0.6			
$E_{\mathrm{T}}^{\mathrm{miss}}$	1.1			1.5	0.9	27	14.0
JER/JES/JVF	$\pm^{5.1}_{4.6}$			18	23	18	30
Theory	7.0	7.0	17.0	11.0	30.0	19.0	17.0
Conversions	–	–	–	–	–	–	$\pm^{22}_{13}$
Pileup	0.8	0.5	1.5	8.0	1.5	8.0	8.0
Luminosity				2.8			

Table 5.17: Systematic uncertainties of MC background and signal samples in the VBS signal region [191] in %, summarized for all final states.

For the data driven backgrounds, systematic uncertainties are summarized in Tables 5.18 and 5.19 for the Inclusive and VBS signal regions, respectively. In background due to fake leptons, the variation of the fake factors as well as the variation of the normalization of the samples with prompt leptons which are subtracted are propagated to the signal regions to obtain the final systematic uncertainty. The systematic uncertainty of background due to charge mis-measurement is estimated by varying the charge-flip rate and the energy correction within their uncertainties and propagating the effect to the signal regions.

Source	Fakes	Charge-Flips
Charge-Flip Rate/Energy correction	–	15-32
Fake Rate	36-51	–
Prompt Subtraction	0.6-8.0	–

Table 5.18: Systematic uncertainties of data driven background estimates in the inclusive signal region [191] in %, summarized for all final states.

Source	Fakes	Charge-Flips
Charge-Flip Rate/Energy correction	–	16-35
Fake Rate	36-51	–
Prompt Subtraction	0.6-7.0	–

Table 5.19: Systematic uncertainties of data driven background estimates in the VBS signal region [191] in %, summarized for all final states.

5.4 Measurement of the fiducial cross section

Finally, based on event counts and their uncertainties in the two fiducial regions, cross sections can be extracted and upper limits on these cross sections can be evaluated. A profile likelihood method is used where the expected number of events in channel i calculated as the sum of the expected signal events and of all background events in this channel [191],

$$N_{i,tot}^{\text{exp}}(\sigma_{W^\pm W^\pm jj}, \mathcal{L}, \theta_j) = \mathcal{L} \times \sigma_{W^\pm W^\pm jj} \times A_i \times \varepsilon_i(\theta_j) + \sum_b N_{i,b}(\theta_j). \tag{5.4}$$

Here, $\mathcal{L}$ is the integrated luminosity, A_i is the fiducial acceptance, and ε_i is the signal efficiency in this channel. The nuisance parameters (θ_j) parametrize the effects from systematic uncertainties for each source j of uncertainty. The likelihood function is defined as a product of Gaussian functions for the luminosity given its systematic uncertainty and the background uncertainties, as well as a product of Poissonian functions for the counting experiment in each channel for the number of observed events N_i^{obs} as

$$L(\sigma_{W^\pm W^\pm jj}, \mathcal{L}, \theta_j) = \text{Gauss}(\mathcal{L}_0|\mathcal{L}, \sigma_{\mathcal{L}}) \times \prod_i \text{Poisson}(N_i^{\text{obs}}|N_{i,tot}^{\text{exp}}) \times \prod_j \text{Gauss}(\theta_j^0|\theta_j, 1). \tag{5.5}$$

The fiducial cross section is now extracted by fitting this likelihood to the observed data. The uncertainties on this measurement are determined using the profile likelihood ratio

$$\lambda(\sigma_{W^\pm W^\pm jj}) = \frac{L(\sigma_{W^\pm W^\pm jj}, \hat{\hat{\mathcal{L}}}, \hat{\hat{\theta}}_j)}{L(\hat{\sigma}_{W^\pm W^\pm jj}, \hat{\mathcal{L}}, \hat{\theta}_j)}, \tag{5.6}$$

with the unconditional maximum likelihood estimates $\hat{\sigma}_{W^{\pm}W^{\pm}jj}, \hat{\mathcal{L}}, \hat{\theta}_j$ and the conditional maximum likelihood estimates $\hat{\hat{\mathcal{L}}}, \hat{\hat{\theta}}_j$ for a given value of $\sigma_{W^{\pm}W^{\pm}jj}$. According to Wilks' theorem [199], the logarithm of the likelihood ratio, usually formulated as $-2\log\lambda$, is asymptotically distributed as a χ^2 function. This allows to derive the confidence intervals from the logarithm of the likelihood ratio: The 68 % confidence level (C.L.) interval corresponds to the interval between the points of $-2\log\lambda(\sigma_{W^{\pm}W^{\pm}jj}) = 1$ [200].
The extracted cross section and its uncertainties in the inclusive analysis region are [191]

$$\sigma^{\mathrm{EWQCD}}_{W^{\pm}W^{\pm}jj} = 2.1 \pm^{0.5}_{0.5}\,(\mathrm{stat.}) \pm^{0.3}_{0.3}\,(\mathrm{syst.})\,\mathrm{fb} \tag{5.7}$$

and in the VBS analysis region, they are [191]

$$\sigma^{\mathrm{EW+INT}}_{W^{\pm}W^{\pm}jj} = 1.3 \pm^{0.4}_{0.4}\,(\mathrm{stat.}) \pm^{0.2}_{0.2}\,(\mathrm{syst.})\,\mathrm{fb}. \tag{5.8}$$

The theoretical predictions from Section 5.3.1 in the Inclusive region

$$\sigma^{\mathrm{EWQCD}}_{W^{\pm}W^{\pm}jj} = 1.52 \pm 0.12\,\mathrm{fb} \tag{5.9}$$

and in the VBS region

$$\sigma^{\mathrm{EW+INT}}_{W^{\pm}W^{\pm}jj} = 0.949 \pm 0.071\,\mathrm{fb} \tag{5.10}$$

are compared graphically to the experimental measurement in Figures 5.10a and 5.10b.

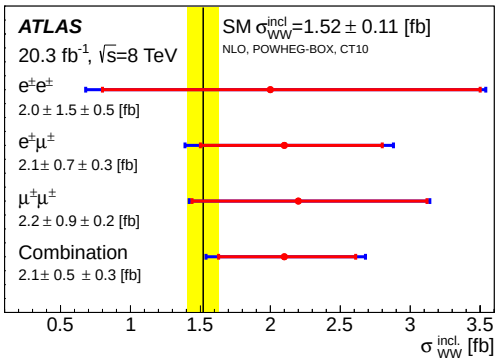

(a) Comparison of measured cross section to theoretical prediction in the inclusive analysis region. From [56].

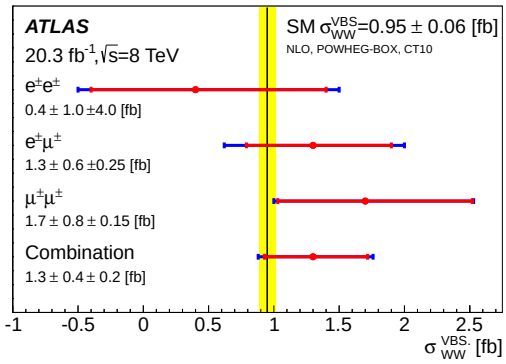

(b) Comparison of measured cross section to theoretical prediction in the VBS analysis region. From [56].

Figure 5.10: Comparison of the measured cross sections in all three final states and the combination to the theoretically predicted cross section at NLO in perturbative QCD obtained using PowhegBox. The red error bars represent the statistical error, blue error bars the systematic errors. The yellow band gives the uncertainty on the theoretical prediction.

The measured cross sections agree with the theoretical calculation obtained at NLO in perturbative QCD within the experimental uncertainties. The excess of events over the background-only prediction in the Inclusive phase space is interpreted as $W^{\pm}W^{\pm}jj$ production, observed with a significance of 4.5 standard deviations. In the VBS phase space, where $W^{\pm}W^{\pm}jj$-QCD is included in the background, the excess of events with respect to the background-only hypothesis is interpreted as $W^{\pm}W^{\pm}jj$-EW production observed with a significance of 3.6 standard deviations.

5.4.1 Kinematics of the signal

The following distributions illustrate the kinematic properties of the selected events in the VBS region. Tagging jet kinematics are used to tag the VBS process. The properties of the leptons are connected to the W boson kinematics, showing their correlation after the scattering.

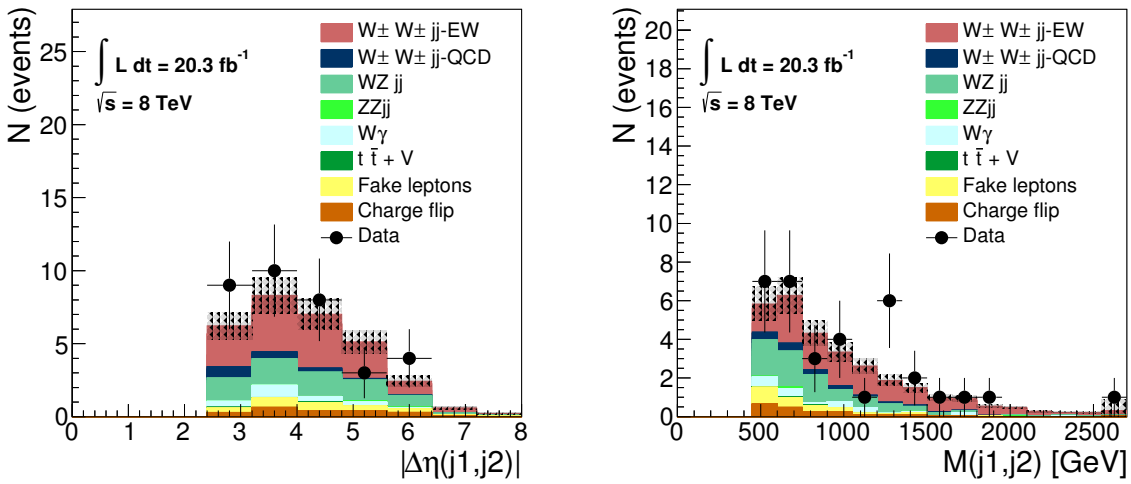

(a) Absolute pseudorapidity of tagging jets

(b) Invariant mass of tagging jets

Figure 5.11: Dijet kinematics of tagging jets in the VBS signal region. The hatched area represents the systematic uncertainty of the total prediction.

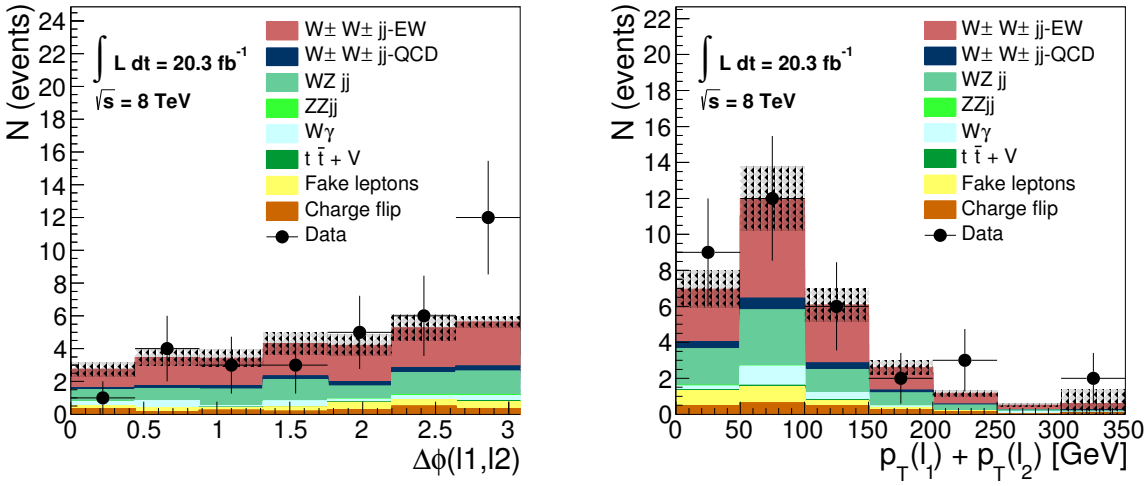

(a) Difference in azimuthal angle of the two leptons (b) Sum of the leptons' absolute transverse momenta

Figure 5.12: Kinematics of leptons in the VBS signal region. The hatched area represents the systematic uncertainty of the total prediction.

Additional kinematical distributions in the VBS signal region can be found in Appendix B.

5.5 Anomalous quartic gauge couplings in $W^{\pm}W^{\pm}jj$-EW

In addition to the measurement of the production cross section of purely electroweak $W^{\pm}W^{\pm}jj$, the analysis of $W^{\pm}W^{\pm}jj$ events provides the possibility to set limits on anomalous quartic gauge couplings. As described in Section 2.3.1, the effective field theory parametrization is well suited to describe the effects of potential new physics in the VBS channel.

Anomalous quartic gauge couplings (aQGC) are measured in a counting experiment using the VBS phase space of this analysis. In order to assess the effects of aQGC on reconstruction level in the analysis, the process is simulated with several values of aQGC and passed through the full detector simulation. Two parameters determine the deviation of an aQGC sample to the SM: The acceptance $A(\alpha_4, \alpha_5)$ of events in the VBS fiducial volume on truth level is defined as

$$A(\alpha_4, \alpha_5) = \frac{\mathrm{N}_{\mathrm{VBS,\ fid}}(\alpha_4,\ \alpha_5)}{\mathrm{N}_{\mathrm{sample}}(\alpha_4,\ \alpha_5)}. \tag{5.11}$$

The efficiency due to detector response is defined as the probability for an event in the fiducial VBS region defined at truth level to enter the signal region at reconstruction level,

$$\varepsilon(\alpha_4, \alpha_5) = \frac{\mathrm{N}_{\mathrm{VBS,\ reco}}(\alpha_4,\ \alpha_5)}{\mathrm{N}_{\mathrm{VBS,\ fid}}(\alpha_4,\ \alpha_5)}. \tag{5.12}$$

As these parameters are used for the limit setting on aQGC parameters, they are determined in dependence of $\alpha_4,\ \alpha_5$.

5.5.1 Cross sections and acceptance in the $\alpha_4,\ \alpha_5$-plane

Cross sections of electroweak production of $W^{\pm}W^{\pm}jj$ with non-zero values of $\alpha_4,\ \alpha_5$ have been calculated for a roughly elliptic region in the $\alpha_4,\ \alpha_5$-plane in which the measurement is sensitive to aQGC. The full samples are defined by the phase space cuts

$$\begin{aligned} &\text{Outgoing partons}: p_{\mathrm{T}} > 15\,\mathrm{GeV},\ |\eta| < 5,\ \Delta R(jj) > 0.4; \\ &\text{Leptons}:\ p_{\mathrm{T}} > 8\,\mathrm{GeV},\ |\eta| < 5; \end{aligned} \tag{5.13}$$

and the factorization and renormalization scales are set to the invariant mass of outgoing leptons and neutrinos,

$$\mu_F = \mu_r = M(\ell_1, \ell_2, \nu_1, \nu_2). \tag{5.14}$$

A SM Higgs boson with mass $m_H = 126\,\mathrm{GeV}$ and width $\Gamma_H = 4.18\,\mathrm{MeV}$ is included, and the PDF set `cteq6ll` [137] is used. The corresponding partonic cross sections have been determined in the scope of this work with `Whizard` on a grid of $\Delta\alpha_4 \times \Delta\alpha_5 = 0.01 \times 0.01$ and are shown in Figure 5.13a.

The parton shower algorithm of `Pythia8` is applied on a subset of these samples with $\Delta\alpha_i = 0.05$, and the acceptance to the fiducial VBS phase space (Section 5.1.4) is determined. Figure 5.13b shows

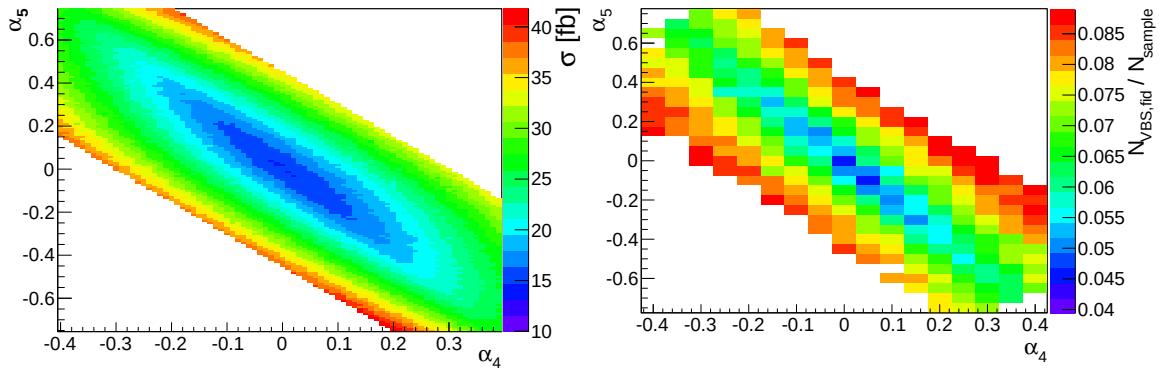

(a) Parton level cross sections in the full sample phase space (C.1) generated with Whizard for aQGC parameters with a distance $\Delta\alpha_i = 0.01$ in $\alpha_4,\ \alpha_5$

(b) Acceptance of events in the fiducial VBS volume obtained by applying the Pythia8 parton shower on events generated with Whizard for points with a distance $\Delta\alpha_i = 0.05$ in $\alpha_4,\ \alpha_5$

Figure 5.13: Dependence of the $W^{\pm}W^{\pm}jj$-EW cross section (left) and acceptance to the fiducial VBS volume (right) on the aQGC parameters $\alpha_4,\ \alpha_5$.

the points in the $\alpha_4,\ \alpha_5$-plane for which the acceptance $A(\alpha_4,\ \alpha_5)$ of the parton-showered samples has been determined. Since the selection requirements of the VBS phase space enhance the aQGC contribution, the acceptance increases with higher absolute values of $\alpha_4,\ \alpha_5$. The narrow elliptic shape of the cross section contours in the $\alpha_4,\ \alpha_5$-plane is specific to the $W^{\pm}W^{\pm}jj$ process, as the operators introducing the anomalous couplings act differently on the amplitudes of the various combinations of W and Z bosons. A comparison to the contour of $W^{\pm}Zjj$-EW cross sections in the $\alpha_4,\ \alpha_5$-plane is given in Appendix C.

5.5.2 Fiducial cross sections of anomalous couplings samples

The calculation of the cross section is based on the product of sample cross section and acceptance,

$$\sigma_{\text{VBS, fid}}^{(\alpha_4,\ \alpha_5)} \sim \sigma_{\text{sample}}(\alpha_4,\ \alpha_5) \times A(\alpha_4,\ \alpha_5),$$

which is shown in Figure 5.14a. In order to correct the sample cross section to the NLO calculation of PowhegBox (cf. sec. 5.3.1), a factor k_{aQGC} is applied, derived from the fiducial cross section of $W^{\pm}W^{\pm}jj$-EW calculated with Whizard and the parton shower of Pythia8 in the VBS phase space at LO in the SM,

$$\sigma_{\text{VBS, fid}}^{W^{\pm}W^{\pm}jj-EW}(\texttt{Whizard}) = \sigma_{\text{sample}}^{W^{\pm}W^{\pm}jj-EW} \times A(\alpha_4 = 0, \alpha_5 = 0) = 0.678\,\text{fb},$$

and the fiducial cross section calculated with PowhegBox at NLO as

$$k_{\mathrm{aQGC}} = \frac{\sigma_{\mathrm{VBS,\ fid}}^{W^{\pm}W^{\pm}jj-EW}(\texttt{PowhegBox})}{\sigma_{\mathrm{VBS,\ fid}}^{W^{\pm}W^{\pm}jj-EW}(\texttt{Whizard})} = 1.3. \tag{5.15}$$

The application of the factor k_{aQGC} to the fiducial cross sections of the aQGC samples for all values of $\alpha_4,\ \alpha_5$ is based on the assumption that the scale dependence of the $W^{\pm}W^{\pm}jj$-EW cross section is independent of the particular value of aQGC at LO, and that the scale dependence is small at NLO. The scale dependence of $W^{\pm}W^{\pm}jj$-EW production with non-zero aQGC is analyzed on Page 121 and is found to be sufficiently compliant with these assumptions. Thus, the fiducial cross section of the $W^{\pm}W^{\pm}jj$-EW process with aQGC $\alpha_4,\ \alpha_5$ is corrected by multiplying with the coefficient k_{aQGC},

$$\sigma_{\mathrm{VBS,\ fid}}^{(\alpha_4,\ \alpha_5),\ \mathrm{EW}} = k_{\mathrm{aQGC}} \times \sigma_{\mathrm{sample}}(\alpha_4,\ \alpha_5) \times A(\alpha_4,\ \alpha_5). \tag{5.16}$$

Furthermore, the interference between the purely electroweak and QCD-mediated production mechanisms of $W^{\pm}W^{\pm}jj$ is taken into account as described by Equation (5.3). The full cross section at a point $(\alpha_4,\ \alpha_5)$ is then obtained by

$$\sigma_{\mathrm{VBS,\ fid}}^{(\alpha_4,\alpha_5)} = \sigma_{\mathrm{VBS,\ fid}}^{(\alpha_4,\alpha_5),\ \mathrm{EW}} + \sigma_{\mathrm{VBS,\ fid}}^{(\alpha_4,\alpha_5),\ \mathrm{INT}} \tag{5.17}$$

$$= k_{\mathrm{aQGC}} \times \sigma_{\mathrm{sample}}(\alpha_4,\ \alpha_5) \times A(\alpha_4,\ \alpha_5) + k_{\mathrm{INT}} \cdot \sqrt{\sigma_{\mathrm{VBS,\ fid}}^{(\alpha_4,\alpha_5),\ \mathrm{EW}} \cdot \sigma_{\mathrm{VBS,\ fid}}^{\mathrm{QCD}}} \tag{5.18}$$

with $k_{\mathrm{INT}} = 0.231$. Cross sections corrected according to Equation (5.18) are depicted in Figure 5.14b.

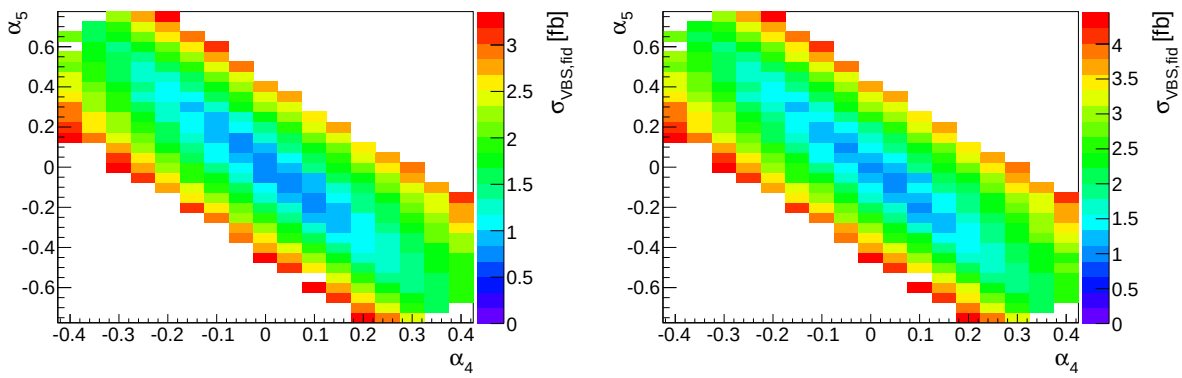

(a) Fiducial cross section at LO without interference: $\sigma_{\mathrm{sample}}(\alpha_4,\ \alpha_5) \times A(\alpha_4,\ \alpha_5)$

(b) Corrected fiducial cross section, obtained according to Equation (5.18) including interference

Figure 5.14: Cross sections of $W^{\pm}W^{\pm}jj$-EW in the fiducial VBS volume in dependence of $\alpha_4,\ \alpha_5$.

5.5.3 Efficiency in the α_4, α_5-plane

A subset of samples in the above α_4, α_5-region was run through a full ATLAS simulation in order to determine the efficiency. Table C.1 in Appendix C lists all of these samples with the corresponding cross sections. The efficiency dependence of the samples can be described with a linear dependence on the fiducial cross section, $\varepsilon = \varepsilon\left(\sigma_{\text{VBS, fid}}^{(\alpha_4,\,\alpha_5),\text{EW}}\right)$ for each of the three channels ee, $e\mu$, and $\mu\mu$ separately as [191]

$$\varepsilon(ee) = 0.5222 + \frac{0.0565}{\text{fb}}\sigma_{\text{VBS, fid}}^{(\alpha_4,\,\alpha_5),\text{EW}}, \tag{5.19}$$

$$\varepsilon(e\mu) = 0.7004 + \frac{0.0301}{\text{fb}}\sigma_{\text{VBS, fid}}^{(\alpha_4,\,\alpha_5),\text{EW}}, \tag{5.20}$$

$$\varepsilon(\mu\mu) = 0.8144 + \frac{0.0143}{\text{fb}}\sigma_{\text{VBS, fid}}^{(\alpha_4,\,\alpha_5),\text{EW}}. \tag{5.21}$$

5.5.4 Systematic uncertainties of aQGC samples

Systematic uncertainties of the generator and parton shower model as well as renormalization and factorization scale variations are evaluated for the samples generated with Whizard used for the aQGC measurement.

Model uncertainty

The samples of $W^{\pm}W^{\pm}jj$-EW production with anomalous couplings have been produced using the implementation of the effective field theory with non-linear EWSB in Whizard (SM_km.mdl) [73] adding a SM Higgs boson with mass $m_H = 126$ GeV to the effective field theory with K-matrix unitarization. In order to estimate the modelling uncertainty due to unitarization, the cross section with these settings and the aQGC parameters set to the SM values $\alpha_4 = \alpha_5 = 0$ are compared to the cross section generated with the Standard Model implementation of Whizard (SM.mdl). The results are given in Table 5.20, which shows the cross section in the sample phase space as well as in the fiducial volume after application of the Pythia8 parton shower. Differences between the two models are within the statistical uncertainties.

model	σ (sample PS) [fb]	σ (VBS PS) [fb]
SM_km.mdl ($\alpha_4 = \alpha_5 = 0$)	15.53 $\pm$ 0.08	1.45
SM.mdl	15.66 $\pm$ 0.06	1.47

Table 5.20: Comparison of two different implementations of the SM in Whizard for the $W^{\pm}W^{\pm}jj$-EW cross section, in the phase space of the sample and in the VBS fiducial volume after application of the Pythia8 parton shower, respectively. Both are generated with the factorization and renormalization scales set to $\mu_F = \mu_R = 2m_W$.

Parton shower uncertainties

The uncertainty from parton shower modelling is determined for the SM sample (α_4 = α_5 = 0), applying two different parton shower programs, Pythia8 and Herwig++, to the matrix-element level events generated with Whizard. The resulting fiductial cross sections in the VBS phase space are listed in Table 5.21. The difference amounts to 11 % between the two parton showers.

	Herwig++ showered	Pythia8 showered
$\sigma_{\text{VBS, fid}}$ [fb]	0.629 ± 0.010	0.567 ± 0.009

Table 5.21: Comparison of two parton shower programs, Pythia8 and Herwig++ applied on the Whizard sample which was generated with the factorization and renormalization scales set to $\mu_F = \mu_R = \sqrt{s_{parton}}$, the partonic center-of-mass energy.

For comparison: In the calculation of the fiducial cross section of $W^{\pm}W^{\pm}jj$-EW using PowhegBox at NLO, the application of two different parton shower models results in a difference of 4 % (cf. sec. 5.3.2). Owing to the higher accuracy of the modeling of additional emissions in the case of the NLO calculation compared to the LO calculation, it is expected that the uncertainty due to parton shower is larger in the LO case. Both results are therefore compatible.

Factorization and renormalization scale uncertainties

Renormalization and factorization scale variations are performed for the SM sample as well as for two aQGC points. The fiducial cross sections of $W^{\pm}W^{\pm}jj$-EW for the SM and the points (α_4 = 0.1, α_5 = 0) and (α_4 = 0.2, α_5 = 0) are shown in Figure 5.15a for several different values of the factorization and renormalization scales $\mu = \mu_F = \mu_R$ varied simultaneously. Figure 5.15b shows the ratio of these cross sections to the SM cross section. As the non-zero aQGC cross sections normalized to the SM feature a flat dependence, the scale dependence of the aQGC samples corresponds in good approximation to the scale dependence of the SM sample. As a consequence, the same scale factor is applied to the aQGC cross sections to scale to the NLO cross section determined with PowhegBox (cf. Section 5.3.1).

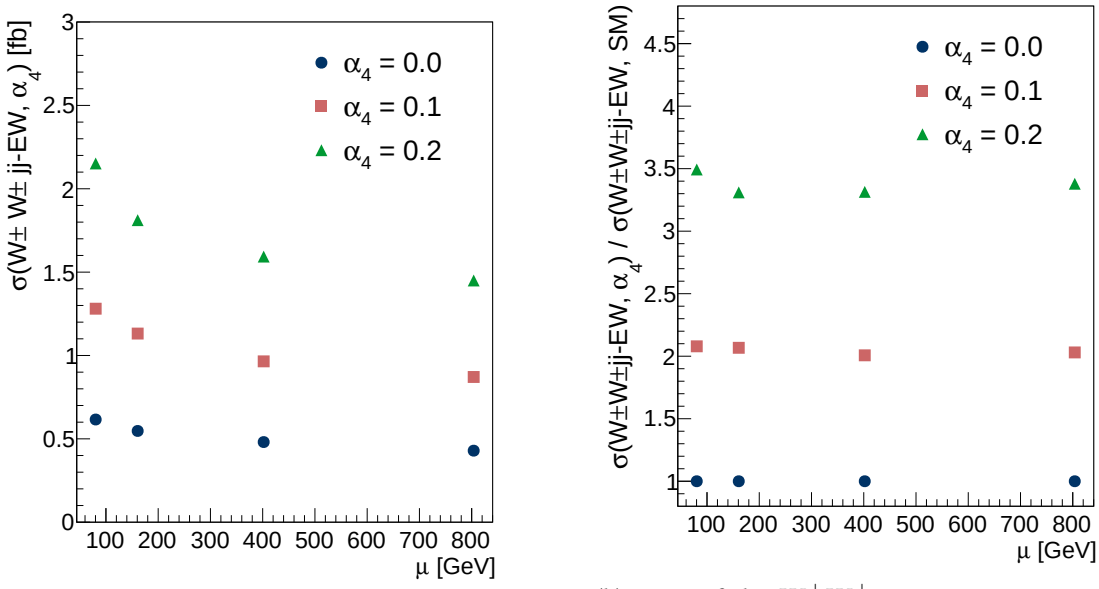

(a) Dependence of the $W^{\pm}W^{\pm}jj$-EW cross section on the factorization and renormalization scale $\mu = \mu_F = \mu_R$ for different values of α_4, while $\alpha_5 = 0$ in all cases.

(b) Ratio of the $W^{\pm}W^{\pm}jj$-EW cross section with varying aQGC parameter α_4 to the SM cross section of $W^{\pm}W^{\pm}jj$-EW in dependence on the factorization and renormalization scale varied simultaneously ($\mu = \mu_f = \mu_R$).

Figure 5.15: Scale dependence of aQGC samples.

Influence of anomalous couplings on kinematics of the final state particles

The contribution of non-zero anomalous couplings to the final state of $W^{\pm}W^{\pm}jj$ mimics the effect of new physics in the self-interaction of W bosons. Hence, the contribution of W boson scattering to the full process of $W^{\pm}W^{\pm}jj$ production is enhanced, leading to an increased correlation of the W boson decay products [201]. This effect can be seen in the following distributions showing the predictions on backgrounds and SM $W^{\pm}W^{\pm}jj$-EW production compared to the prediction with all SM backgrounds and the additional contribution from anomalous quartic gauge couplings. The histogram with filled areas represents the SM prediction. The three additional lines represent the SM prediction plus the contribution from non-zero anomalous couplings, where the SM $W^{\pm}W^{\pm}jj$-EW contribution is subtracted. Three values of α_4 and α_5 are chosen: (α_4 = 0.1, α_5 = 0), (α_4 = 0.1, α_5 = 0.1), and (α_4 = 0.1, α_5 = -0.4).

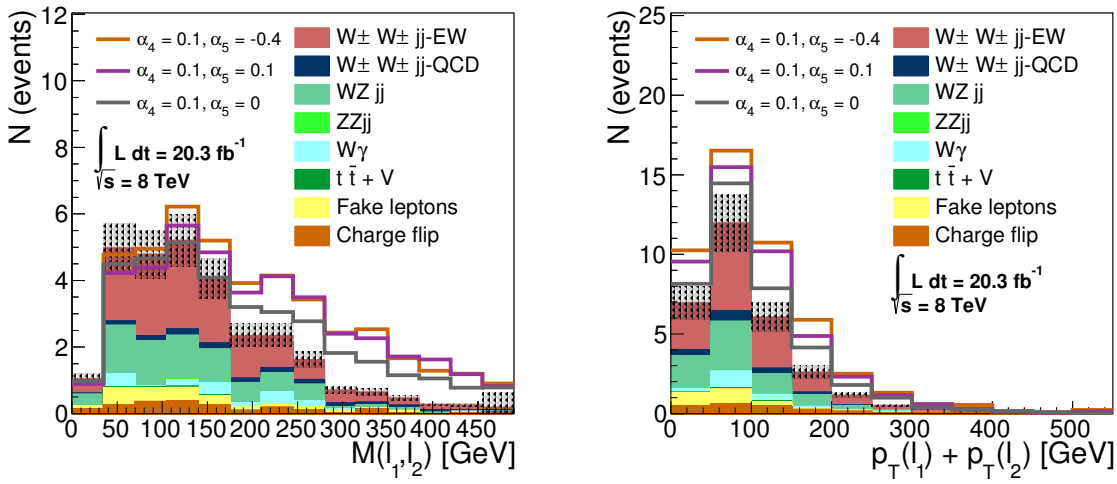

(a) Invariant mass of the charged leptons

(b) Sum of absolute values of transverse momenta of the leptons

Figure 5.16: Comparison of the kinematics of the two leptons in the VBS region for the SM and for three points in the α_4, α_5-plane close to the sensitivity of the measurement. The filled histogram shows the SM prediction, and the three additional lines the total prediction including contributions from non-zero anomalous couplings. The hatched area represents the systematic uncertainty on the total prediction.

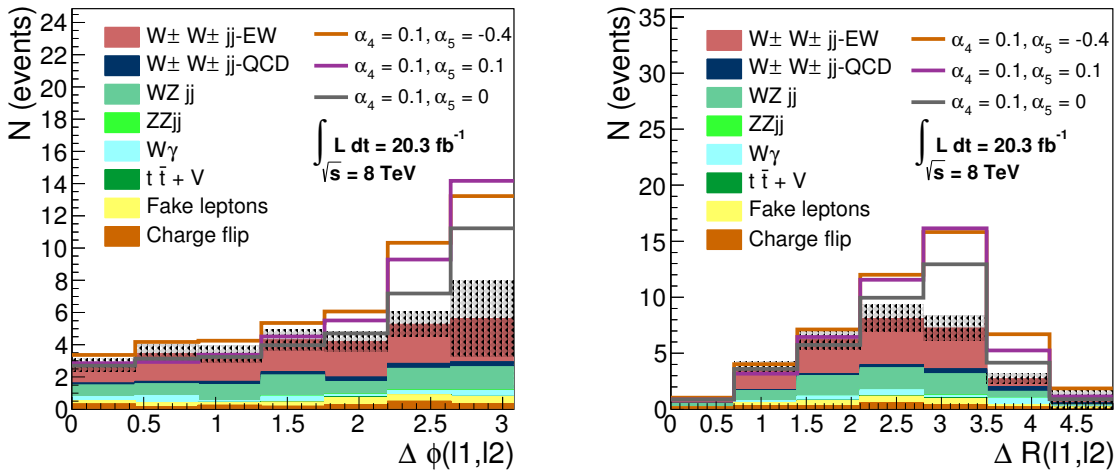

(a) Azimuth distance between the two leptons

(b) Distance between the two leptons in the pseudorapidity-azimuth-plane

Figure 5.17: Comparison of the kinematics of the two leptons in the VBS region for the SM and for three points in the α_4, α_5-plane close to the sensitivity of the measurement. The filled histogram shows the SM prediction, and the three additional lines the total prediction including contributions from non-zero anomalous couplings. The hatched area represents the systematic uncertainty on the total prediction.

Based on these observables, it is possible to optimize a phase space further suppressing the SM $W^{\pm}W^{\pm}jj$-EW component while retaining the contribution from anomalous couplings [202, 203].

More kinematic distributions can be found in Appendix C.3.

5.5.5 Measurement of anomalous couplings

Based on the aQGC predictions described above, the measurement is used to derive confidence intervals on the values of $\alpha_4,\ \alpha_5$ in $W^{\pm}W^{\pm}jj$-EW. The confidence intervals are derived based on the profile likelihood method using the number of observed events in the VBS analysis region.

The number of expected signal events is determined according to the integrated luminosity $\mathcal{L}$, the fiducial acceptance in each channel A_i, the fiducial cross section $\sigma_{\text{VBS, fid}}^{(\alpha_4,\alpha_5)}$ (5.18), and the detector efficiency $\varepsilon\left(\sigma_{\text{VBS, fid}}^{(\alpha_4,\ \alpha_5),\text{EW}}\right)$, as

$$s_i = \mathcal{L} \times A_i \times \sigma_{\text{VBS, fid}}^{(\alpha_4,\alpha_5)} \times \varepsilon\left(\sigma_{\text{VBS, fid}}^{(\hat{\alpha_4}\hat{\alpha_5}),\text{EW}}\right) \tag{5.22}$$

in each channel $i \in \{ee, e\mu, \mu\mu\}$. The anomalous couplings are extracted with a fit of the likelihood (5.5) to the observed data. The confidence intervals are obtained via the negative logarithm of the likelihood ratio for $\alpha_4,\ \alpha_5$ defined as

$$\lambda(\alpha_4,\ \alpha_5) = \frac{L(\alpha_4,\ \alpha_5, \hat{\hat{\theta}}_j)}{L(\alpha_4,\ \alpha_5, \hat{\theta}_j)}. \tag{5.23}$$

The 95 % (68.3 %) C.L. corresponds to the contour of $\lambda(\alpha_4,\ \alpha_5) > 1.92(0.5)$, shown in Figure 5.18.

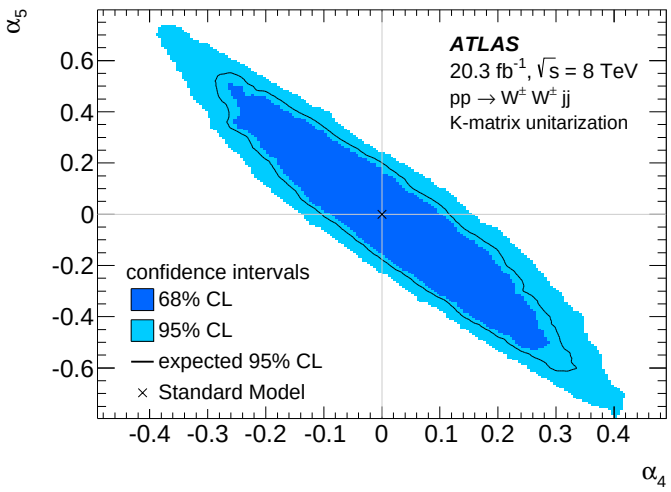

Figure 5.18: Measurement of the anomalous quartic gauge couplings $\alpha_4,\ \alpha_5$. Points outside the light blue area are excluded at 95 % confidence level (C.L.) by the measurement. The solid line marks the expected exclusion limit at 95 % C.L. Points outside the dark blue area are excluded at 68 % C.L. From [56].

The one-dimensional limits for α_4 and α_5 are

$$\alpha_4 \in [-0.139, 0.157]$$
$$\alpha_5 \in [-0.229, 0.244]. \tag{5.24}$$

5.5.6 Interpretation of aQGC in light of new resonances

The measurement of the anomalous quartic gauge coupling parameters α_4 and α_5 can be interpreted with respect to new resonances coupling to the electroweak gauge bosons as described in Section 2.3.4. Figure 5.19 illustrates the relation between aQGC contributions and resonances in the α_4, α_5-plane used for the aQGC measurement. The conversion between the contribution from resonances to anomalous couplings can be found in Table 2.4. This allows to deduce information on resonances from the aQGC measurement.

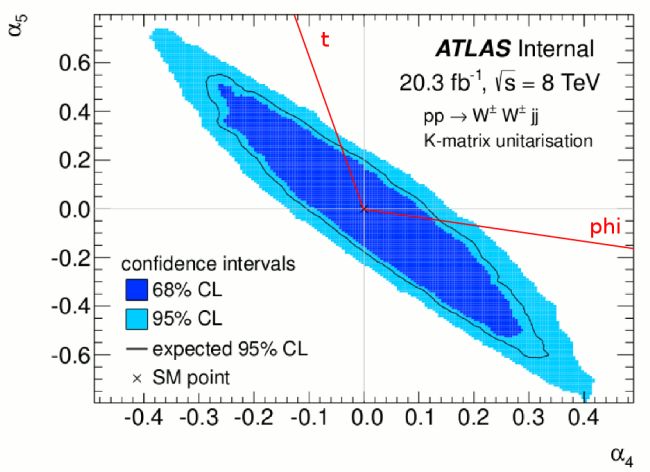

Figure 5.19: Contributions to resonances by the measurement of the anomalous quartic gauge couplings α_4, α_5.

Based on the limits derived above, the following values of the mass to coupling ratio M/g of two types of resonances are excluded at 95 % confidence level:

- For a ϕ resonance (spin = 0, isospin = 2): $\frac{M}{g} < 134$ GeV is excluded.
- For a t resonance (spin = isospin = 2): $\frac{M}{g} < 88$ GeV is excluded.

These values are to be taken with a grain of salt: The conversion is only valid as long as the approximations for the EFT are valid, i.e. a coupling larger than $g > 2.5$ is not allowed. In addition, the conversion fails above $M_{WW} > 1/2\, m_{\text{res}}$ [75, 124].

Yet, the conversion of anomalous couplings limits in terms of resonance masses and couplings allows to deduce which physical models are excluded by this measurement. In particular, possible mass ranges of new resonances in $W^{\pm}W^{\pm}$ scattering can be inferred. Future measurements in this channel will further address the question whether vector boson scattering is fully described by the SM or whether additional models come into play.

CHAPTER 6

Towards higher energy: $W^{\pm}W^{\pm}$ scattering after the LHC and ATLAS upgrades

6.1 $W^{\pm}W^{\pm}$ scattering at a higher energy Large Hadron Collider

While the LHC and ATLAS are being upgraded to higher proton-proton collision energies at the time of writing, it is worth while to investigate the prospects of measuring $W^{\pm}W^{\pm}$ scattering at an upgraded LHC. As the center-of-mass energy of the collision as well as the instantaneous luminosity increase, new opportunities and challenges arise. This chapter investigates prospects for the VBS measurement after a collider and detector upgrade, considering the effects of the following aspects of changed collider conditions.

Increase of the center-of-mass energy The facility of extracting electroweak $VVjj$ production is governed by the ratio of $VVjj$-EW and $VVjj$-QCD production cross sections, which depends on the center-of-mass energy of the proton-proton collisions. The cross sections of the $pp \to W^{\pm}W^{\pm}jj$ process in dependence of the collision energy for the electroweak and strong component are shown in Figure 6.1. The ratio of electroweak and strong $W^{\pm}W^{\pm}jj$ production in a VBS-like phase space with $M_{qq} > 500\,\text{GeV}$ increases from ~ 1.2 at 8 TeV to ~ 1.5 at $\sqrt{s} = 14\,\text{TeV}$, which will simplify the extraction of the electroweak-only component, while diminishing the $W^{\pm}W^{\pm}jj$-QCD background.

Increase of the instantaneous luminosity In addition to increased $\sqrt{s}$, the upgraded LHC will provide a larger instantaneous luminosity through reduction of the bunch spacing from 50 to 25 ns. This will lead to increased levels of pile-up interactions in the event, demanding new techniques for pile-up robust particle reconstruction and identification. For $W^{\pm}W^{\pm}$ scattering, this will be particularly challenging with respect to forward tagging jets. Within the ATLAS collaboration, the idea of extending the tracking detector to larger $|\eta|_{\text{tracker}}$ of 4.0 is currently being investigated [204]. This extension can help to eliminate pile-up jets also in forward regions.

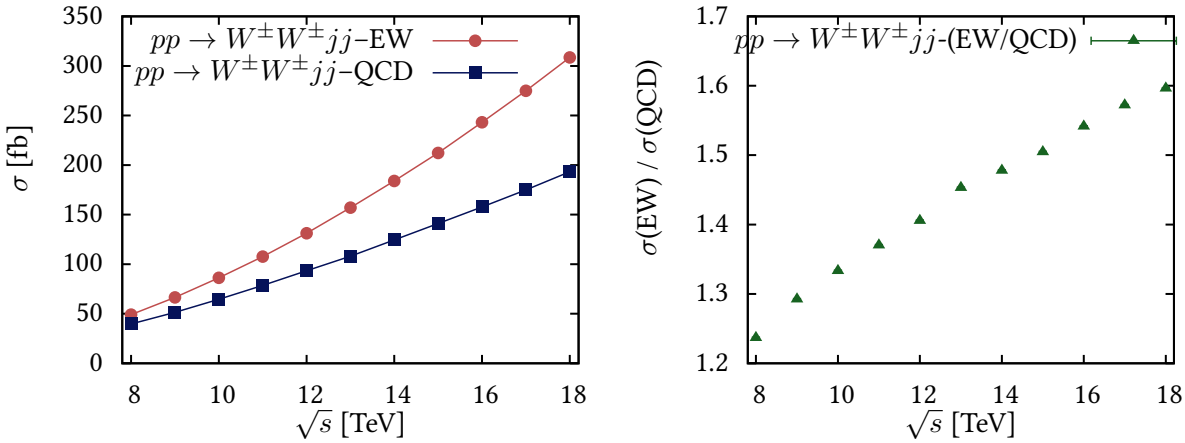

Figure 6.1: Cross section of $pp \to W^{\pm}W^{\pm}jj$ production with non-decayed final state W bosons with respect to the center-of-mass energy of the proton-proton collision. An invariant mass cut of $M_{qq} > 500$ GeV is applied. Left: Purely electroweak ("EW") production cross sections (red circles) compared to the difference between inclusive and electroweak production cross sections ("QCD", blue squares) for different proton-proton center-of-mass energies. Right: Ratio of the two cross sections plotted on the left. Note that in deviation from the standard nomenclature described in Section 3.2.1, the VVjj-QCD process includes interference here.

Furthermore, the study of the potential to extract electroweak $VVjj$ production at an upgraded LHC requires solid estimates for the **contributions from other backgrounds**. The differing dependencies of the background processes' cross-sections on the collision energy might lead to a different background composition at higher energies. At 8 TeV, the dominating background to the $W^{\pm}W^{\pm}jj$ final state arises from $W^{\pm}Zjj$ production. The effect of a tracker extension on the $W^{\pm}Zjj$ background suppression at 14 TeV is studied in the scope of this work.

After the discovery of the Higgs-like boson in Run-1, data from Run-2 will also be scrutinized with regard to possible new physics. Various models predict the existence of high-mass resonances in the electroweak sector. Resonances decaying into $W^{\pm}W^{\pm}$ pairs would enhance the $W^{\pm}W^{\pm}jj$-EW cross section and could be discovered in this channel. One type of such resonances is investigated in this chapter.

6.2 The upgraded LHC and ATLAS detector

6.2.1 Plans for the LHC

At the time of writing, the LHC is undergoing a hardware upgrade in order to reach a center-of-mass energy of the proton-proton collisions closer to its design value of 14 TeV, starting at 13 TeV in 2015 [205].

In 2015 and the following years, the LHC is scheduled to be running at 13-14 TeV center-of-mass energy, with an instantaneous luminosity of up to 10^{34} cm^{-2} s^{-1}, providing an integrated luminosity of 50-100 fb^{-1} to the experiments. After a long shutdown in 2018, upgrades in the pre-accelerator chain

and the collider collimation system will allow for an instantaneous luminosity of up to 2-3$\times 10^{34}$ cm^{-2} s^{-1}. According to the plan for the Phase-I run, this will allow the experiments to collect up to 300 fb^{-1}of proton-proton collisions. Upgrade plans for the ATLAS detector in this phase are established and collected in a Letter of Intent [206].

After 2022, a further upgrade is proposed, resulting in the High-Luminosity LHC (HL-LHC) with a planned instantaneous luminosity of $5 - 7 \times 10^{34}$ cm^{-2} s^{-1}. This leads to pile-up contributions corresponding to an average number of interactions per bunch-crossing of $\langle\mu\rangle = 140$, and it will allow the experiments to collect a total integrated luminosity of 3000 fb^{-1}.

Performance assumptions of the upgraded ATLAS detector under future collider conditions have been obtained previously by the ATLAS collaboration in [207] and [208]. They are described in Section 6.2.3.

6.2.2 Extension of the Inner Detector

In order to make best use of the increased amount of collisions while handling the challenging pile-up conditions, the experiments have to be adapted accordingly. Plans for the upgraded ATLAS detector for Phase-II include an all-silicon inner tracker (ITK) which is planned to cover the range up to $|\eta|_{\text{tracker}} = 2.5$ [209]. An effort is being made to investigate the hardware demands and the physics case of an extended tracker up to $|\eta| \leq 4.0$ [204]. This work studies the effect of an extension of the tracker up to $|\eta| \leq$4.0 on the sensitivity to scattering of $W^{\pm}W^{\pm}$ within and beyond the SM.

6.2.3 Performance assumptions for the ATLAS detector at 14 TeV

The performance of the upgraded detector based on fully simulated MC samples taking into account the properties of the upgraded detector components has been studied in [207] and [208]. As a result, parametrizations of the performance of objetcs' resolutions and efficiencies have been established and provided as a RootCore [210] package in [211]. These parametrizations can be used to modify the kinematics of particle level MC samples to match detector level kinematics. In order to study VBS at the HL-LHC, these presciptions are applied on particle level MC samples for the signal and most important background processes (see Section 6.3.2). They have been used for studies contributing to the European Strategy for Particle Physics 2012 [212], as well as the European Committee for Future Accelerators 2013 [213] and the Snowmass Energy Frontier Workshop 2013 [214].

The performance assumptions include detector momentum and energy resolution, object reconstruction efficiencies, as well as trigger efficiencies of the various objects. Where it is relevant, the dependence of resolutions and efficiencies on pile-up conditions has been investigated and is taken into account in the prescriptions. Also, when applicable, the future ITK is assumed instead of the current tracking detector. For the case of the extended tracker, no performance assumptions exist at the time of this study. Therefore, the parametrization from the largest $|\eta|$ bin in which a parametrization is available, is used in this case. The performance projections and their application in this analysis are described in Section 6.3.2.

6.3 Analysis of $W^{\pm}W^{\pm}jj$-EW at 14 TeV

Previous studies have investigated the prospects for Vector Boson Scattering in various final states at a High-Luminosity LHC with an upgraded ATLAS detector [215–217]. The potential to constrain anomalous quartic gauge couplings in $W^{\pm}W^{\pm}jj$ production in the form of dimension-8 operators (cf. Section 2.3) in an effective field theory has been studied in [217].

In the thesis at hand, the sensitivity to the SM $W^{\pm}W^{\pm}jj$-EW production as well as to additional resonances is studied. A High-Luminosity LHC is assumed with a center-of-mass energy of $\sqrt{s} = 14\,\text{TeV}$ of the proton-proton collisions. Results are scaled to a total collected luminosity of $3000\,\text{fb}^{-1}$. The nominal detector setup with the current $|\eta|$ extension of the tracking detector is compared to an extended tracking detector up to $|\eta|_{\text{tracker}} \leq 4.0$.

6.3.1 Generation of signal and background processes

The distinction of signal and background processes, especially the distinction of the purely electroweak signal process from the so-called $VVjj$-QCD background process is described in detail in Section 3.2.1. The same nomenclature is followed here.

Standard Model signal Event generation for the SM signal process, electroweak production of $W^{\pm}W^{\pm}jj$, is carried out by selecting diagrams with the final state of $\ell^{\pm}\ell^{\pm}\nu\nu jj$ with electroweak interactions only, using `Whizard` [107, 108]. The separation of purely electroweak production is realized by setting the strong coupling constant $\alpha_s = 0$. The same setting is used to generate additional resonance signal samples (see sec. 6.6).

Diboson backgrounds The background process with the same final state, $W^{\pm}W^{\pm}jj$-QCD, contains diagrams with both strong and electroweak vertices and is generated using `MadGraph` [106].

The dominant background to the $\ell^{\pm}\ell^{\pm}$ + $E_{\text{T}}^{\text{miss}}$ final state, as shown in [106], is diboson WZ/γ^*-production in the $\ell\ell\ell\nu jj$ final state. Like the $W^{\pm}W^{\pm}$ process, $W^{\pm}Zjj$ production is split into electroweak $W^{\pm}Zjj$ production and strong $W^{\pm}Zjj$ production, both generated with `MadGraph` [106].

Monte Carlo settings, sample phase spaces, and cross sections For signal and backgrounds, only final states with electrons and muons are considered ($\ell = e, \mu$), neglecting leptonically decaying τ leptons. The G_F scheme is used for the electroweak parameters (cf. Section 3.2.2). The factorization and renormalization scales are set to M_{WW} for the signal, while the `MadGraph` default scale, based on k_T event clustering [218], is used for the samples generated with `MadGraph`. On generator level, the production phase spaces are defined as described in Table 6.1.

The resulting cross sections for the generated processes in the respective phase spaces are listed in Table 6.2. The cross sections and events generated with `Whizard` and `MadGraph` have leading-order (LO) accuracy. A parton shower algorithm is applied on these events using Pythia8 [103, 104].

	$W^{\pm}W^{\pm}jj$	$W^{\pm}Z/\gamma^{*}jj$
Pseudorapidity of jets j and leptons ℓ	$\lvert\eta(j)\rvert < 5$, $\lvert\eta(\ell)\rvert < 5$	$\lvert\eta(j)\rvert < 5$, $\lvert\eta(\ell)\rvert < 5$
Transverse momenta p_{T} of jets j and leptons ℓ	$p_{\mathrm{T}}(j) > 10$ GeV, $p_{\mathrm{T}}(\ell) > 8$ GeV	$p_{\mathrm{T}}(j) > 15$ GeV, $p_{\mathrm{T}}(\ell_2) > 5$ GeV, ℓ_2: 2nd lepton ordered by p_{T}, No cut on softest lepton p_{T}
Separation and invariant mass of leptons ℓ		$\Delta R(\ell\ell) > 0.1$, $M(\ell^{+}\ell^{-}) > 0.1$ GeV
Separation and invariant mass of jets j	$\Delta R(jj) > 0.4$	$\Delta R(jj) > 0.4$, $M(jj) > 50$ GeV

Table 6.1: Generator phase space settings and cuts for the production of $pp \to \ell^{\pm}\ell^{\pm}\nu\nu jj$ and $pp \to \ell^{\pm}\ell^{\mp}\ell^{\pm}\nu jj$.

Process	σ [fb]	MC generator
$W^{\pm}W^{\pm}jj$-EW	15.95	Whizard
$W^{\pm}W^{\pm}jj$-QCD	16.03	MadGraph
$W^{\pm}Zjj$-EW	49.1	MadGraph
$W^{\pm}Zjj$-QCD	1050.0	MadGraph

Table 6.2: Cross sections of the SM signal and diboson background processes at $\sqrt{s} = 14$ TeV generated with Whizard or MadGraph. Generator uncertainties are below 1 %.

Background from detector effects Additional backgrounds to the $\ell^{\pm}\ell^{\pm}$ + $E_{\mathrm{T}}^{\mathrm{miss}}$final state arise due to mis-identification of jets as leptons, or due to the mismeasurement of a lepton's charge after conversion of bremsstrahlung. These backgrounds occur predominantly in final states with at least one electron. Estimating their contribution from MC generation would require extensive amounts of simulated events which can not be provided in the scope of this study.

Therefore, their contribution is estimated by scaling the diboson background event yields in the signal region according to the same ratio as observed in the 8 TeV analysis. The $\mu\mu$ channel is exempt from this, as it is the channel with the least detector background.

To this effect, the detector-effect background in the signal region at 14 TeV, $N_{\mathrm{detector-effect}}(14\,\mathrm{TeV})$, is obtained using the diboson event yields at 14 TeV, $N_{\mathrm{diboson},\ ee+e\mu}(14\,\mathrm{TeV})$, and a scale factor obtained from the 8 TeV analysis [56], according to:

$$N_{\mathrm{detector-effect}}(14\,\mathrm{TeV}) = N_{\mathrm{diboson},\ ee+e\mu}(14\,\mathrm{TeV})\frac{N_{\mathrm{detector-effect}}(8\,\mathrm{TeV})}{N_{\mathrm{diboson},\ ee+e\mu}(8\,\mathrm{TeV})}$$

In agreement with the results of [56], the background event yields containing electrons are therefore scaled by

$$\frac{N_{\mathrm{detector-effect}}(8\,\mathrm{TeV})}{N_{\mathrm{diboson},\ ee+e\mu}(8\,\mathrm{TeV})} = 0.94$$

in the signal region in order to account for additional background. The factor 0.94 is assumed to be independent of the phase space. This introduces a large uncertainty on the background estimate, as the actual ratio of diboson to other backgrounds' event yields at 14 TeV has to be estimated from collision data and is therefore yet unknown.

6.3.2 Application of the performance assumptions

The particle kinematics in the events are modified according to the performance projections obtained by previous studies, as described above (see Section 6.2.3). Efficiencies are applied using random numbers drawn from to the provided probability distributions.

The resulting events are subjected to object and event selection criteria closely matching those used in the 8 TeV analysis of $W^{\pm}W^{\pm}jj$ [56].

Detector resolution In the first step, the energy and momentum resolution of the detector is taken into account for the kinematics of electrons, muons, and jets. A random number is generated from a Gaussian distribution with mean 1.0 and a width according to the given parametrizations, cf. Table 6.3. The resulting factor is applied to the energy and momentum of the particle.

- For final state electrons, both the energy and the transverse momentum are smeared by the same, $|\eta|$ dependent, fraction (see Table 6.3). This fraction is obtained as a random number from a Gaussian distribution taking into account an electronic noise term, a stochastic term due to statistical fluctuations of the shower in the calorimeter, and a constant term accounting for detector non-uniformity and calibration uncertainty.

- For final state muons, the energy and the transverse momentum are smeared by the same fraction which is obtained from a Gaussian with a width combining Inner Detector (σ_{ID}) and Muon Spectrometer (σ_{MS}) properties. The Inner Detector resolution is obtained from full simulation of the all-silicon ITK tracking detector.

- The Gaussian width of the jet energy resolution contains terms for the noise, stochastic fluctuations, and constant uncertainties, with parameters N, S, and C, respectively. Of these, only the noise term is pile-up dependent. It can be expressed as a function of the number of pile-up interactions μ drawn from a Poissonian distribution with mean $\langle\mu\rangle = 140$ for each event. The associated parameters are determined for the case that an event-by-event pile-up subtraction method is utilized which employs the jets' areas [208].

Reconstruction efficiencies In the next step, the objects' reconstruction efficiencies are applied. To estimate the fraction of particles which are correctly reconstructed and identified as the correct type of object, reconstruction efficiency estimates are provided from the full-simulation studies mentioned above. For each particle, a random number n uniformly distributed in [0,1) is drawn and if $n > \epsilon_{\mathrm{reco}}$, the particle is removed from the event record.

Object	Width of Gaussian	Parameters
Electrons	$\sigma = \sqrt{0.3^2 + S^2E + C^2E^2}$	for $\lvert\eta\rvert < 1.4$: $S = 0.1$, $C = 0.01$ for $1.4 < \lvert\eta\rvert < 2.47$: $S = 0.15$, $C = 0.015$ [208]
Muons	$\sigma_{\mathrm{ID}} = p_{\mathrm{T}}\sqrt{a_1^2 + (a_2 p_{\mathrm{T}})^2}$ $\sigma_{\mathrm{MS}} = p_{\mathrm{T}}\sqrt{\frac{b_o}{p_{\mathrm{T}}}^2 + b_1^2 + (b_2 p_{\mathrm{T}})^2}$ combined: $\Rightarrow \sigma_{\mathrm{CB}} = \frac{\sigma_{\mathrm{ID}}^2\sigma_{\mathrm{MS}}^2}{\sqrt{\sigma_{\mathrm{ID}}^2+\sigma_{\mathrm{MS}}^2}}$	2 parameters for the Inner Detector (ITK) $\rightarrow$ given in 15 $\lvert\eta\rvert$ regions [207] 3 parameters for the Muon Spectrometer $\rightarrow$ given in 2 $\lvert\eta\rvert$ regions (barrel, endcap) [207]
Jets	$\frac{\sigma_{p_{\mathrm{T}}}}{p_{\mathrm{T}}} = \sqrt{\frac{N^2}{p_{\mathrm{T}}^2} + \frac{S^2}{p_{\mathrm{T}}} + C^2}$ with $N = a(\lvert\eta\rvert) + b(\lvert\eta\rvert)\mu$	a, b, S, C given in four $\lvert\eta\rvert$ bins: barrel, extended barrel, endcaps, and forward $\lvert\eta\rvert$ [208]

Table 6.3: Widths of the Gaussian distribution used for energy and momentum smearing of the various particles. Binning in $|\eta|$ of the associated parameters is given.

A transverse momentum dependent reconstruction efficiency is applied for electrons. The muon reconstruction efficiency is given in two $|\eta|$ bins. The reconstruction efficiencies for electrons and muons are listed in Table 6.4.

Object	Absolute pseudorapidity bin	Reconstruction efficiency
Electrons	$\lvert\eta\rvert < 2.47$	$0.85 - 0.191 \times \exp\left(1 - \frac{p_{\mathrm{T}}}{20\ \mathrm{GeV}}\right)$ [208]
Muons	$\lvert\eta\rvert < 0.1$ $0.1 < \lvert\eta\rvert < 2.5$	0.54 0.97 [207]

Table 6.4: Efficiency to reconstruct a generated particle in the detector and assign the correct particle type, estimated from full detector simulation.

Trigger efficiency For each of the selected leptons, the analysis determines if it has activated the trigger, causing the event to be written to storage. Trigger efficiency estimates for single electron and muon triggers are listed in Table 6.5. In the event selection, at least one of the selected leptons is required to activate the trigger system.

Object	Absolute pseudorapidity bin	Trigger efficiency
Electrons	$\lvert\eta\rvert < 2.5$	0.88 [208]
Muons	$\lvert\eta\rvert < 1.05$ $1.05 < \lvert\eta\rvert < 2.4$	0.7 0.86 [207]

Table 6.5: Trigger efficiencies for single lepton triggers, provided by the given references.

b-tagging efficiency Each jet containing a b quark or antiquark is tagged as a b-jet with a certain efficiency evaluated from MC events with full detector simulation. This efficiency takes into account a pile-up contribution with an average number of interactions per bunch crossing of $\langle\mu\rangle = 140$. It is parametrized as a function of p_{T} and $|\eta|$ with nine parameters [207, ch. 5]. The working point chosen corresponds to an average efficiency of 70 % for b-tagging.

$E_{\mathrm{T}}^{\mathrm{miss}}$ smearing The $E_{\mathrm{T}}^{\mathrm{miss}}$ observable is calculated as the negative of the vectorial sum of transverse momenta of all objects in the event. In case the objects p_{T} is modified according to detector resolution assumptions as described above, this new p_{T} is entered in the $E_{\mathrm{T}}^{\mathrm{miss}}$ calculation. In order to account for additional uncertainties in the $E_{\mathrm{T}}^{\mathrm{miss}}$ measurement of a real detector, such as pile-up effects, a smearing prescription is applied as described in [207, 219].

6.3.3 Event selection criteria

Events modified according to the performance projections are subject to object and event selection criteria which enhance the signal and suppress the background contribution. Selection criteria for the $W^{\pm}W^{\pm}jj$ final state with a VBS topology are closely adapted from the 8-TeV-analysis [56]. Events are required to fulfill the following conditions:

- Exactly two leptons are required with the same electric charge, transverse momenta $p_{\mathrm{T}} > 25$ GeV, pseudorapidity $|\eta| < |\eta|_{\mathrm{tracker}}$ (the $|\eta|$ extension of the tracker), distance $\Delta R(\ell\ell) > 0.3$, and invariant mass $M(\ell\ell) > 20$ GeV. In the ee channel, $|M(ee) - M_Z| > 10$ GeV. At least one of the leptons has to trigger the trigger system.
- Missing transverse momentum is required to be $E_{\mathrm{T}}^{\mathrm{miss}} > 40$ GeV.
- At least two jets are reconstructed with the anti-k_T algorithm with a cone parameter of 0.4, and with transverse momentum $p_{\mathrm{T}} > 30$ GeV and $|\eta| < 4.5$. The two leading jets in p_{T} are called *tagging jets* as they are indicators of the VBS process. They are required to have an absolute pseudorapidity difference of $|\Delta\eta| > 2.8$, which is increased with respect to the 8 TeV analysis.
- Events containing jets originating from b quarks are rejected with an efficiency as determined by the performance assumption study [207].
- Jets overlapping with electrons within a cone of $\Delta R = 0.2$ are removed. Events containing a pair of a selected lepton and a selected jet with $\Delta R(\ell j) < 0.3$ are rejected.
- Events containing additional electrons with $p_{\mathrm{T}} > 7$ GeV or muons with $p_{\mathrm{T}} > 6$ GeV are rejected.

In a VBS event, the decay products of the vector bosons are expected to be found central with respect to the tagging jets (cf. [52]). For the $W^{\pm}W^{\pm}jj$ final state, this implies that the two leptons should be

at smaller pseudorapidity than the two tagging jets. The centrality can be quantified in a variable such as the *lepton centrality* ζ:

$$\zeta = \min\left[\min\left(\eta_{\ell 1}, \eta_{\ell 2}\right) - \min(\eta_{j1}, \eta_{j2}), \max(\eta_{j1}, \eta_{j2}) - \max(\eta_{\ell 1}, \eta_{\ell 2})\right]$$

Thus, in addition to above-mentioned selection criteria, events are further selected according to the invariant mass of the tagging jets M_{jj} and the lepton centrality ζ. Both selection criteria are optimized separately for the nominal and the extended tracking detector.

6.3.4 Statistical analysis of the expected discovery significance

Goal of this study is to estimate the sensitivity of a realistically projected future ATLAS detector to SM and BSM signals. The sensitivity of the experiment is assessed by calculating the discovery significance of the respective signal hypothesis.

To establish the discovery of a signal, the p-value of the background-only hypothesis is determined using a profile likelihood test statistic. The p-value is defined as the probability for the test statistic to be found at values indicating equal or lower compatibility with the background-only hypothesis than the observed data. The expected significance of a measurement is calculated assuming the observation of the expected signal (Asimov dataset).

It is common to convert the p-value to the Gaussian significance Z, defined as

$$Z = \Phi^{-1}(1 - p), \tag{6.1}$$

where Φ^{-1} is the inverse cumulative probability densitiy function of the standard Gaussian. A significance of $Z = 5$, corresponding to a p-value of 2.87×10^{-7}, is widely accepted to establish a discovery.

The **profile likelihood ratio** $\lambda\left(S = 0\right)$ is defined as

$$\lambda\left(0\right) = \frac{\mathcal{L}(N|0, \hat{\hat{B}})}{\mathcal{L}(N|\hat{S}, \hat{B})} \tag{6.2}$$

where $\hat{\hat{B}}$ is the conditional maximum likelihood estimator for B in the case $S = 0$, and $\hat{S}, \hat{B}$ are the unconditional maximum likelihood estimators which are determined from the maximization of the likelihood function $\mathcal{L}$. From this, the test statistic is derived as

$$q_0 = \begin{cases} -2\log\lambda\left(0\right) & : N \geq M \\ 0 & : N < M \end{cases} \tag{6.3}$$

According to Wilks' theorem [199], for large data samples $-2\log\lambda\left(0\right)$ follows a χ^2 distribution. Using this, it can be shown (e.g. in [220]) that the median significance can be calculated as

$$Z = \sqrt{q_0}. \tag{6.4}$$

In general, the probability density function of the test statistic can be generated using toy MC experiments. In this study, an analytic form of the test statistic is formulated, assuming a Poissonian likelihood for the measurement of N events with mean $S + B$, convoluted with a Gaussian distribution describing the uncertainty of the background, which is measured to be M events. This yields the likelihood function

$$\mathcal{L}(N|S, B, M) = \frac{(S+B)^N}{N!} e^{-(S+B)} \frac{1}{2\sigma_B^2} e^{-(M-B)^2/(2\sigma_B^2)} \tag{6.5}$$

with the number of expected signal events S, which is known without uncertainty. B is the expected number of background events, which is Gaussian distributed with a standard deviation of σ_B and mean B.

In this study, the relative background uncertainty is estimated as 15 %, which roughly corresponds to the uncertainty in [56]. At 14 TeV with an integrated luminosity of 3000 fb^{-1}, event yields will be large enough such that the measurement uncertainty will be dominated by systematics and the systematic uncertainty of the background cannot be neglected.

Calculating the estimators from the minimization of $-\log \mathcal{L}$ and requiring only non-negative values for the estimators yields

$$\frac{\partial}{\partial B}(-\log \mathcal{L}(S=0)) \stackrel{!}{=} 0 \quad \Rightarrow \hat{\hat{B}} = \frac{1}{2}\left(M - \sigma_B^2 + \sqrt{(M-\sigma_B^2)^2 + 4N\sigma_B^2}\right) \tag{6.6}$$

$$\frac{\partial}{\partial S}(-\log \mathcal{L}) \stackrel{!}{=} 0 \quad \Rightarrow \hat{S} = N - B \tag{6.7}$$

$$\frac{\partial}{\partial B}(-\log \mathcal{L}) \stackrel{!}{=} 0 \quad \Rightarrow \hat{B} = M \tag{6.8}$$

Finally, the significance can be estimated as

$$Z = \sqrt{2\left[(S+B)\log\left(\frac{S+B}{B_0}\right) + B_0 - S - B\right] + \frac{(B-B_0)^2}{\sigma_B^2}} \tag{6.9}$$

with

$$B_0 = \frac{1}{2}(B - \sigma_B^2) + \sqrt{(B-\sigma_B^2)^2 + 4(S+B)\sigma_B^2}. \tag{6.10}$$

(cf. [221–223]).

6.4 Significance of SM signal measurement with the nominal ATLAS detector

Optimization of selection according to the tagging jets invariant mass M_{jj} and the lepton centrality ζ Applying all cuts listed above (Section 6.3.3), the combination of tagging jets invariant mass M_{jj} and lepton centrality ζ cuts is optimized by maximizing the significance calculated from the

resulting signal and background event yields. The optimization is performed iteratively varying both cuts simultaneously in order to take into account correlations between the observables.

The significance is estimated assuming a Poissonian likelihood with a systematic background uncertainty that is Gaussian distributed, as described above. Final significances are also calculated according to equation 6.9, assuming a systematic uncertainty of 15 %. For the nominal tracking detector up to $|\eta|$ = 2.5, the optimum values of the tagging jets invariant mass M_{jj} and lepton centrality ζ selection criteria are indicated in Table 6.6.

Cut	$M_{jj} >$	$\zeta >$
Optimal value	1400 GeV	1.6

Table 6.6: Optimized selection criteria in case of the nominal inner detector up to $|\eta|_{\text{tracker}} \leq 2.5$.

Figure 6.2 shows the distributions of these variables after application of all selection criteria but the one on the shown variable, and the respective optimization curves. For the optimization, the simulated diboson background is scaled up to account for additional backgrounds. This way, it is assumed that the other background has the same shape as the diboson background, which is conservative in this region.

Results The resulting significance for the SM $W^{\pm}W^{\pm}jj$-EW signal with these cuts applied and assuming a systematic uncertainty of 15 % on the background, also accounting for detector-effect background by scaling the ee and $e\mu$ channel, with an integrated luminosity of 3000 fb^{-1}is **Z = 18.7**.

6.5 Effect of the extension of the tracking detector on the SM signal measurement

For this study, in each case the performance of the highest $|\eta|$ bin already available from the above-mentioned studies (see Section 6.3.2) is taken for the extended region. The ATLAS inner detector, which acts as tracking device for charged particles in ATLAS, is extended from currently $|\eta| \lesssim 2.5$ ("nominal tracker") to $|\eta|_{\text{tracker}} \leq 4.0$ ("extended tracker").

6.5.1 Re-optimization of cuts

The selection applied using the tagging jets invariant mass M_{jj} and lepton centrality ζ is optimized separately for the extended tracking detector with $|\eta| < 4.0$. The optimization is performed in the same way as for the nominal tracker (see Section 6.4). The optimal values for these cuts are shown in Table 6.7, and the corresponding kinematic distributions and opimization curves for the extended tracker are shown in Figure 6.3. The resulting significance for the SM signal, assuming a background uncertainty of 15 % is **Z = 24.2**.

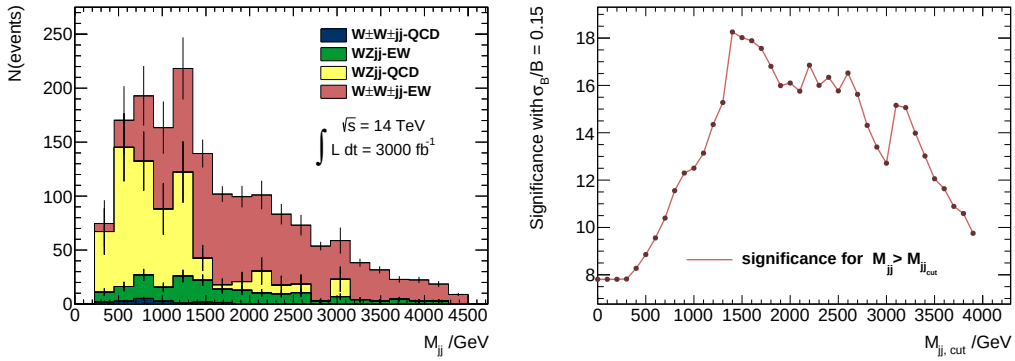

(a) Optimization of M_{jj} in the case of the nominal tracker. The optimized ζ cut is applied.

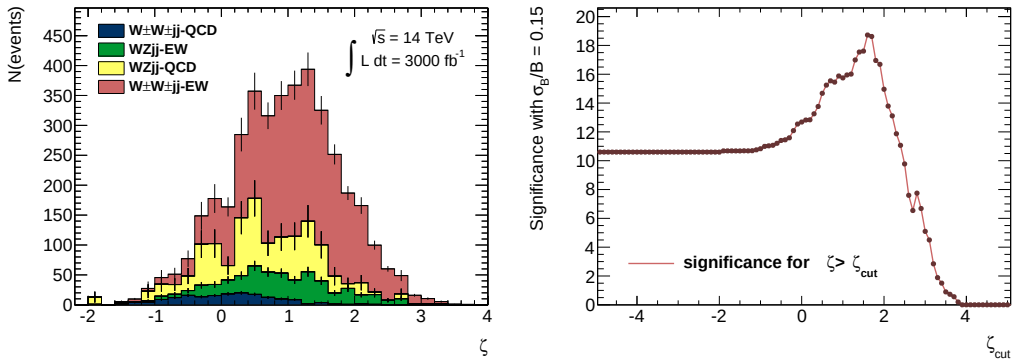

(b) Optimization of ζ in the case of the nominal tracker. The optimized M_{jj} cut is applied.

Figure 6.2: Kinematic selection optimization in the nominal tracker. The diboson background ee and $e\mu$ channel is scaled in order to account for additional background arising from detector effects.

Cut	$M_{jj} >$	$\zeta >$
Optimal value	1500 GeV	1.3

Table 6.7: Optimized cuts for the extended inner detector up to $|\eta|_{\text{tracker}} \leq 4.0$.

6.5.2 Event yields and cut efficiencies with an extended tracker

Event yields in the respective optimal phase spaces are presented in Table 6.8.

In the signal region optimized for the extended tracker, the event yields of each of the processes, signal and backgrounds, are higher than in the optimal signal region for the nominal tracker, since the selection criteria are looser. Comparing the event yields in one signal region shows that extending the tracker leads to a significant suppression of $W^{\pm}Zjj$-EW and $W^{\pm}Zjj$-QCD background, while the $W^{\pm}W^{\pm}jj$-EW signal does not change significantly. The $W^{\pm}W^{\pm}jj$-QCD background remains constant and is small compared to the $W^{\pm}Zjj$ background.

In order to study the effects of the extended tracker independently of different optimal cut values, the same criteria (see tables 6.6 and 6.7) are applied using either a tracking detector up to $|\eta|_{\text{tracker}} \leq 2.5$ (nominal tracker) or up to $|\eta|_{\text{tracker}} \leq 4.0$ (extended tracker). Events are selected as described in

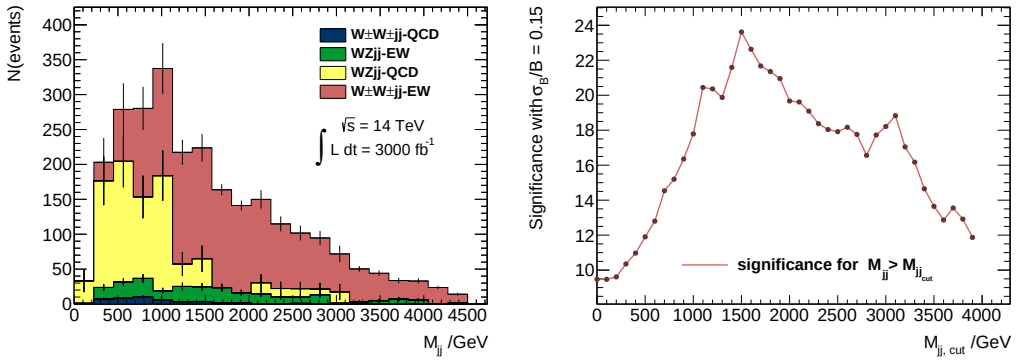

(a) Optimization of M_{jj} in the case of the extended tracker. The optimized ζ cut is applied.

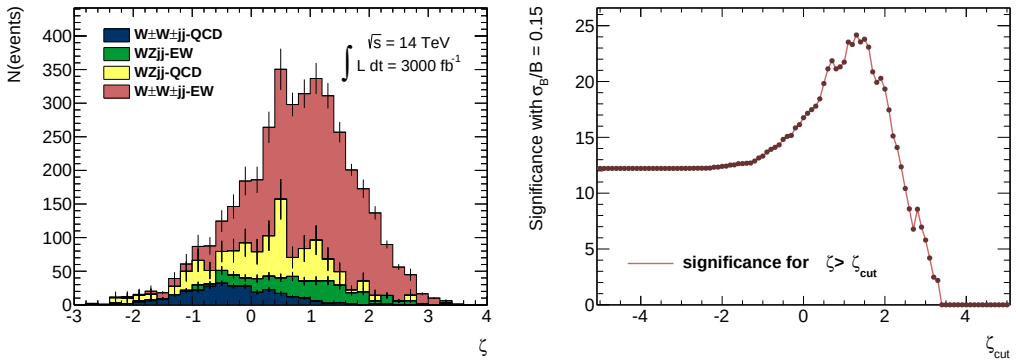

(b) Optimization of ζ in the case of the extended tracker. The optimized M_{jj} cut is applied.

Figure 6.3: Phase space optimization for the extended tracker.

Section 6.3.3. Finally, the remaining selection criteria are applied: Cuts on the invariant mass M_{jj} and the pseudorapidity difference $|\Delta\eta_{jj}|$ of the tagging jets, the veto on additional, lower-p_{T} leptons, and the cut on lepton centrality ζ in this order. The event yields and efficiencies of these consecutively applied selection criteria are listed in Table 6.9.

While the signal selection is hardly affected by the extension of the tracker, the background selection is influenced in various ways. The $W^{\pm}W^{\pm}jj$-QCD background actually increases, but its total number is very small. For the $W^{\pm}Zjj$ background, the extended tracker does not change the M_{jj} and $|\Delta\eta\,(jj)\,|$ efficiencies. However, the veto on additional leptons leads to a stronger suppression of $W^{\pm}Zjj$ background if the tracker is extended and more of the additional leptons pass the lepton acceptance. Finally, also the lepton centrality cut profits from the extended tracker and leads to rejection of more background events.

	Signal region **optimized** for the **nominal tracker** ($M_{jj} > 1400\,\text{GeV}$, $\zeta > 1.6$)		Signal region **optimized** for the **extended tracker** ($M_{jj} > 1500\,\text{GeV}$, $\zeta > 1.3$)	
Process	nominal $\lvert\eta\rvert_{\text{tracker}}$	extended $\lvert\eta\rvert_{\text{tracker}}$	nominal $\lvert\eta\rvert_{\text{tracker}}$	extended $\lvert\eta\rvert_{\text{tracker}}$
$W^{\pm}W^{\pm}jj$-EW (Signal)	676 ± 13	669 ± 13	948 ± 15	957 ± 15
$W^{\pm}W^{\pm}jj$-QCD	3 ± 1	3 ± 1	5 ± 1	5 ± 1
$W^{\pm}Zjj$-EW	60 ± 6	46 ± 6	88 ± 8	64 ± 7
$W^{\pm}Zjj$-QCD	41 ± 13	25 ± 10	83 ± 19	37 ± 12
Detector background	69 ± 26	56 ± 25	119 ± 31	78 ± 29
Significance	18.7	22.1	17.4	24.2

Table 6.8: Event yields in the respective optimized phase spaces for the nominal ($|\eta|_{\text{tracker}} \leq 2.5$) and the extended ($|\eta|_{\text{tracker}} \leq 4.0$) tracker with an integrated luminosity of $\mathcal{L} = 3000\,\text{fb}^{-1}$. Monte Carlo statistical errors are given. Signal and diboson backgrounds are determined from MC simulated events with detector performance projections applied. The detector-effect background is obtained by scaling the diboson event yields with electrons in the final state by 0.94.

Using the phase space optimized for nominal tracker extension (Table 6.6)

Nominal tracker $|\eta|_{\text{tracker}} \leq 2.5$

	$W^\pm W^\pm jj$-EW		$W^\pm W^\pm jj$-QCD		$W^\pm Zjj$-EW		$W^\pm Zjj$-QCD	
Cut	N (events)	ϵ [%]	N (events)	ϵ [%]	N (events)	ϵ [%]	N (events)	ϵ [%]
$M_{jj} > 1400\,\text{GeV}$	2662 ± 25	25	269 ± 8	3	461 ± 18	12	914 ± 62	1
$\lvert\Delta\eta_{jj}\rvert > 2.8$	2508 ± 25	94	106 ± 5	40	434 ± 18	94	790 ± 57	86
Veto add. leptons	2467 ± 24	98	104 ± 5	98	272 ± 14	63	501 ± 46	63
$\zeta > 1.6$	676 ± 13	27	2.9 ± 0.8	3	60 ± 7	22	41 ± 13	8

Extended tracker $|\eta|_{\text{tracker}} \leq 4.0$

	$W^\pm W^\pm jj$-EW		$W^\pm W^\pm jj$-QCD		$W^\pm Zjj$-EW		$W^\pm Zjj$-QCD	
Cut	N (events)	ϵ [%]	N (events)	ϵ [%]	N (events)	ϵ [%]	N (events)	ϵ [%]
$M_{jj} > 1400\,\text{GeV}$	3047 ± 27	23	425 ± 10	4	484 ± 18	11	1109 ± 68	1
$\lvert\Delta\eta_{jj}\rvert > 2.8$	2872 ± 26	94	211 ± 7	50	456 ± 18	94	960 ± 63	87
Veto add. leptons	2813 ± 25	98	207 ± 7	98	226 ± 13	50	497 ± 45	52
$\zeta > 1.6$	669 ± 13	24	2.6 ± 0.8	1	46 ± 6	20	25 ± 10	5

Using the phase space optimized for extended tracker extension (Table 6.7)

Nominal tracker $|\eta|_{\text{tracker}} \leq 2.5$

	$W^\pm W^\pm jj$-EW		$W^\pm W^\pm jj$-QCD		$W^\pm Zjj$-EW		$W^\pm Zjj$-QCD	
Cut	N (events)	ϵ [%]	N (events)	ϵ [%]	N (events)	ϵ [%]	N (events)	ϵ [%]
$M_{jj} > 1500\,\text{GeV}$	2386 ± 24	22	217 ± 7	3	405 ± 17	10	732 ± 55	1
$\lvert\Delta\eta_{jj}\rvert > 2.8$	2257 ± 23	95	89 ± 5	41	381 ± 16	94	637 ± 51	87
Veto add. leptons	2221 ± 23	98	88 ± 5	98	237 ± 13	62	389 ± 40	61
$\zeta > 1.3$	948 ± 15	43	5.0 ± 1.1	6	88 ± 8	37	83 ± 19	21

Extended tracker $|\eta|_{\text{tracker}} \leq 4.0$

	$W^\pm W^\pm jj$-EW		$W^\pm W^\pm jj$-QCD		$W^\pm Zjj$-EW		$W^\pm Zjj$-QCD	
Cut	N (events)	ϵ [%]	N (events)	ϵ [%]	N (events)	ϵ [%]	N (events)	ϵ [%]
$M_{jj} > 1500\,\text{GeV}$	2737 ± 26	21	348 ± 9	3	429 ± 17	10	910 ± 61	1
$\lvert\Delta\eta_{jj}\rvert > 2.8$	2592 ± 25	95	179 ± 7	51	402 ± 17	94	782 ± 57	86
Veto add. leptons	2539 ± 25	98	175 ± 7	98	194 ± 12	48	397 ± 41	51
$\zeta > 1.3$	958 ± 15	38	4.8 ± 1.1	3	64 ± 7	33	37 ± 12	9

Table 6.9: Event yields remaining after successive application of kinematic selection criteria, in the given order. Cut values from previous optimization are used. Event numbers are given for the signal as well as the main diboson background processes, and event numbers are scaled to $\mathcal{L} = 3000\,\text{fb}^{-1}$.

6.5.3 Effect of the extended tracker on the additional lepton veto

Since the dominant background to the $\ell^{\pm}\ell^{\pm} + E_{\mathrm{T}}^{\mathrm{miss}}$ final state arises from 3-lepton final states where one lepton is not reconstructed, requiring exactly two leptons in the final state suppresses a large amount of $W^{\pm}Zjj$ background (*loose additional lepton veto*). The background suppression is improved if also leptons outside of the nominal acceptance are counted: Events with additional leptons having lower transverse momenta ($p_{\mathrm{T}} > 7$ GeV for electrons, $p_{\mathrm{T}} > 6$ GeV for muons) are rejected (*strict additional lepton veto*).

Figure 6.4 shows the number of additional leptons with $p_{\mathrm{T}} > 7$ (6) GeV for electrons (muons) before the strict additional lepton veto and the lepton centrality cut is applied. All other cuts are applied, including the selection of exactly two leptons passing nominal selection criteria ($p_{\mathrm{T}} > 25$ GeV).

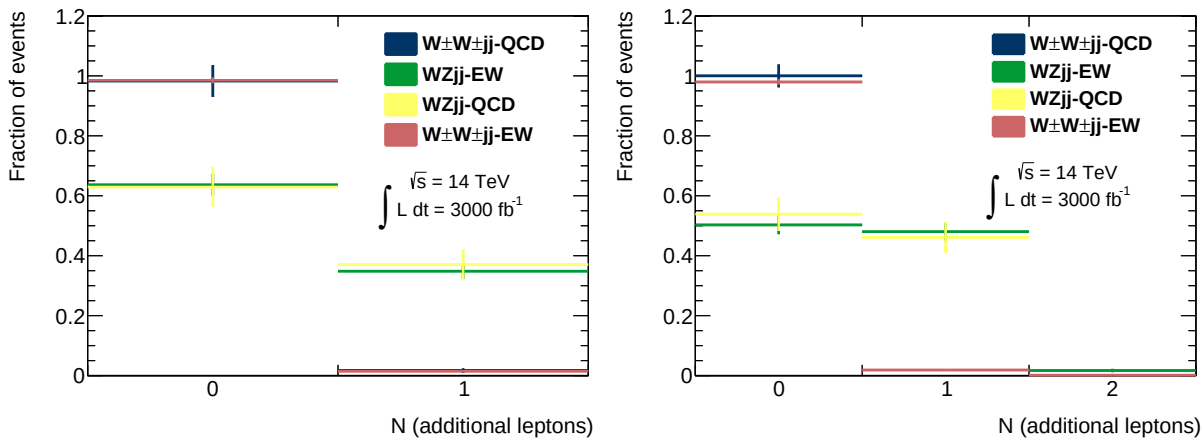

(a) Nominal tracker ($|\eta|_{\mathrm{tracker}} \leq 2.5$)

(b) Extended tracker ($|\eta|_{\mathrm{tracker}} \leq 4.0$)

Figure 6.4: Additional lepton multiplicity for nominal and extended tracker with $p_{\mathrm{T}} > 7$ (6) GeV. In both cases, the same $M_{jj} > 1500$ GeV and $|\Delta\eta_{jj}| > 2.8$ cut is applied. Each histogram is scaled to the same area in order to show which fraction of events contributes to which multiplicity, regardless of the total numbers.

As expected, more $W^{\pm}Zjj$ events contribute to the one-lepton bin when the tracking detector is extended.

Using the strict additional leptons veto instead of the loose veto, the significance increases from 11.7 to 17.4 using the nominal tracker ($|\eta|_{\mathrm{tracker}} \leq 2.5$), and from 12.4 to 24.2 using the extended tracker ($|\eta|_{\mathrm{tracker}} \leq 4.0$). The significances with loose and strict veto are summarized in Table 6.10.

	tracking $\lvert\eta\rvert_{\mathrm{tracker}} \leq 2.5$		tracking $\lvert\eta\rvert_{\mathrm{tracker}} \leq 4.0$	
	loose veto	strict veto	loose veto	strict veto
Significance	11.7	17.4	12.4	24.2

Table 6.10: Significances with and without additional lepton veto.

6.5.4 Significance as a function of $|\eta|_{\text{tracker}}$ extension

Using the optimized cuts for the extended tracker (Table 6.7) the analysis is repeated for several different $|\eta|_{\text{tracker}}$ values. Table 6.11 shows the dependence of the overall significance on the $|\eta|_{\text{tracker}}$. With increasing extension of the tracker, the significance of the $W^{\pm}W^{\pm}jj$-EW signal increases, as the background rejection profits from the extended tracker.

$\|\eta\|_{\text{tracker}}$	2.5	2.8	3.1	3.4	3.7	4.0
Significance	17.4	19.6	20.5	21.5	21.0	24.2

Table 6.11: Significance in dependence of the tracker extension.

6.6 Resonances in $W^{\pm}W^{\pm}jj$-EW: Prospects at 14 TeV

6.6.1 Resonance model

Additional resonances in VBS are introduced via an effective electroweak chiral Lagrangian [224] containing model-independent resonances with different spin-isospin configurations. The amplitudes containing resonances are unitarized with the K-matrix method. This model is implemented in the generator `Whizard` as described in [44].

In the $W^{\pm}W^{\pm}$ channel, the resonance of choice in this study is the Φ resonance with spin $J = 0$ and isospin $I = 2$, and electric charge ± 2.

To assess the sensitivity of the $W^{\pm}W^{\pm}$-VBS channel to this type of resonance, samples with two different mass values of the Φ resonance ($m_{\Phi} = 500, 1000\,\text{GeV}$) each with three different couplings ($g = 1.0, 1.75, 2.5$) have been generated. The resonance's width is calculated according to $\Gamma_{\Phi} = (g^2)/(64\pi) \times (m_{\Phi}^3)/(v^2)$ with the vaccuum expectation value of the Higgs field v. A SM Higgs boson with mass $m_H = 125\,\text{GeV}$ is included in the model.

6.6.2 Selection and kinematics of resonances

The optimization performed above enhances the SM $W^{\pm}W^{\pm}jj$-EW signal with respect to the SM diboson backgrounds. However, for the extraction of BSM resonances in this final state, the SM $W^{\pm}W^{\pm}jj$-EW component should be suppressed. Therefore, the optimal cuts for SM extraction in general are not the optimal cuts for the discovery of a new resonance.

As Figure 6.5 shows, the SM background can be further suppressed for instance by applying a cut on the azimuthal separation of the leptons, $\Delta\phi\,(\ell\ell)$.

The resonances have large contributions at invariant masses of the tagging jets lower than the SM signal selection criteria ($M_{jj} > 1400\,\text{GeV}$ or $M_{jj} > 1500\,\text{GeV}$). This is shown in Figure 6.6. Therefore, this cut should be lowered in order to gain signal events contributed from the resonance.

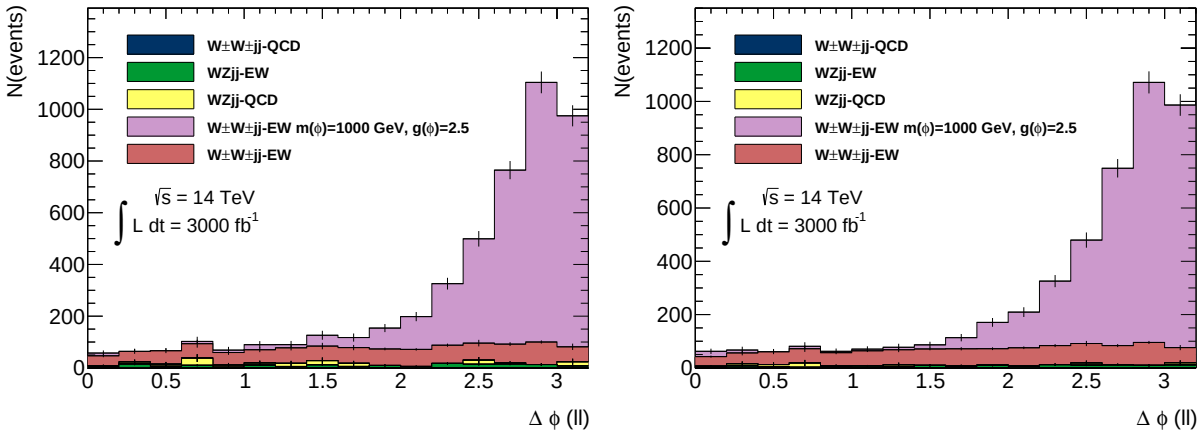

(a) Nominal tracker (b) Extended tracker

Figure 6.5: Distribution of $\Delta\phi\,(\ell\ell)$ for the Φ resonance with a mass $m_{\Phi} = 1000\,\text{GeV}$ and coupling $g = 2.5$, shown for the nominal (left) and the extended tracker (right). In both cases, the cuts optimized for the respective tracker extensions for the SM signal extraction are applied on the lepton centrality and the invariant mass of the tagging jets (tables 6.6 and 6.7).

As a consequence, three different signal regions based on the previous optimization results were compared in order to find an optimized selection: All cuts as defined in Section 6.3.3 are applied. Additionally, the cuts found to be optimal for the nominal or the extended tracker are applied (tables 6.6 and 6.7) and compared to the case when $M_{jj} > 1000\,\text{GeV}$ and $\zeta > 1.6$ are required instead. In each of these signal regions the optimal $\Delta\phi\,(\ell\ell)$ selection is applied. The latter cut set proves to yield the highest discovery significances for resonances in both the nominal and the extended tracker, combined with

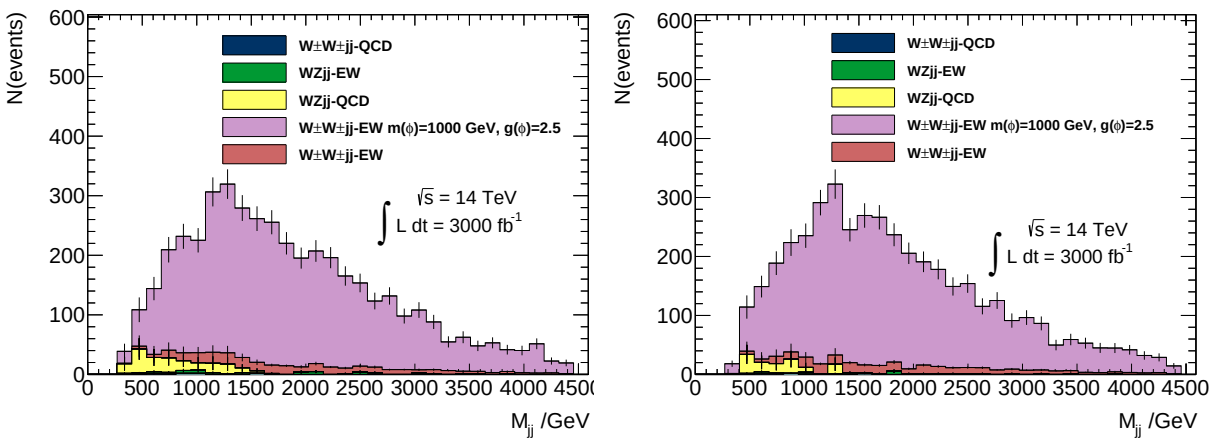

(a) Nominal tracker (b) Extended tracker

Figure 6.6: Distribution of the tagging jets' invariant mass M_{jj} for the Φ resonance with a mass $m_{\Phi} = 1000\,\text{GeV}$ and coupling $g = 2.5$. Both tracking detector setups are shown, the nominal extension up to $|\eta|_{\text{tracker}} \leq 2.5$ (left) and the extended tracker up to $|\eta|_{\text{tracker}} \leq 4.0$ (right). In both cases, a lepton centrality cut $\zeta > 1.6$ and a $\Delta\phi\,(\ell\ell) > 2.5$ cut is applied.

a $\Delta\phi(\ell\ell)$ cut. This is demonstrated exemplarily in Table 6.12 comparing the significances in different signal regions for one specific resonance ($m_\Phi = 500\,\text{GeV}$ and coupling $g = 1.75$).

Cuts	$M_{jj} > 1400\,\text{GeV}$ $\zeta > 1.6$		$M_{jj} > 1500\,\text{GeV}$ $\zeta > 1.3$		$M_{jj} > 1000\,\text{GeV}$ $\zeta > 1.6$	
	$\Delta\phi(\ell\ell)$ cut	Z	$\Delta\phi(\ell\ell)$ cut	Z	$\Delta\phi(\ell\ell)$ cut	Z
Nominal tracker	2.5	42.3	2.5	34.5	2.5	42.3
Extended tracker	2.5	42.3	2.6	35.4	2.5	44.9

Table 6.12: Discovery significances for a Φ resonance with mass $m_\Phi = 500\,\text{GeV}$ and coupling $g = 1.75$.

Similar behavior was found for other resonance configurations: also for other values of the coupling or mass, the cut set with $M_{jj} > 1000\,\text{GeV}$ yields the highest significance of the three cut sets. As a result of this optimization, the invariant mass and lepton centrality are required to be

$$M_{jj} > 1000\ \text{GeV and}\ \zeta > 1.6 \tag{6.11}$$

for the extraction of resonance signals in the following. This selection is optimal for both the nominal tracker as well as the tracking detector extended to $|\eta|_{\text{tracker}} \leq 4.0$. For the resonance signal extraction, the optimal $\Delta\phi(\ell\ell)$ cut is determined in addition (see sec. 6.6.3), and varies for each resonance type, mass, and coupling, and the extension of the tracker.

Kinematic distributions after these selections are shown in Appendix E.

6.6.3 Nominal tracker vs. extended tracker

For each resonance the optimal cut on $\Delta\phi(\ell\ell)$ as well as the corresponding discovery significance is determined and shown in tables 6.13 and 6.14.

$m_\Phi = 500\,\text{GeV}$	nominal tracker		extended tracker	
coupling g	$\Delta\phi(\ell\ell) >$	Z	$\Delta\phi(\ell\ell) >$	Z
1	2.9	20.6	2.6	21.6
1.75	2.5	42.3	2.5	44.9
2.5	2.5	67.2	2.6	71.4

Table 6.13: Discovery significances for Φ resonance with $m_\Phi = 500\,\text{GeV}$ using the nominal or the extended tracking detector and scaled to a luminosity of $\mathcal{L} = 3000\,\text{fb}^{-1}$ at $\sqrt{s} = 14\,\text{TeV}$.

In conclusion, the discovery significances for such a BSM resonance increase slightly by up to 6 % with the tracker extension. As the main benefit of the extended tracker is the suppression of $W^{\pm}Zjj$ background, while the influence on $W^{\pm}W^{\pm}$ resonances is rather small. The selection criteria under investigation in this study (M_{jj}, ζ, $\Delta\phi(\ell\ell)$) profit slightly from the tracker extension.

$m_\Phi = 1000\,\text{GeV}$	nominal tracker		extended tracker	
coupling g	$\Delta\phi\,(\ell\ell) >$	Z	$\Delta\phi\,(\ell\ell) >$	Z
1	2.9	19.6	2.9	20.0
1.75	2.9	32.5	2.9	33.7
2.5	2.9	42.9	2.7	44.8

Table 6.14: Discovery significances for Φ resonance with $m_\Phi = 1000\,\text{GeV}$ using the nominal or the extended tracking detector and scaled to a luminosity of $\mathcal{L} = 3000\,\text{fb}^{-1}$ at $\sqrt{s} = 14\,\text{TeV}$.

6.6.4 Luminosity and coupling dependent discovery significance

The possible discovery significance of Φ-type resonances increases with the collected luminosity, and differs according to the resonance mass and couplings. This dependence is investigated using the optimal kinematic selection for resonances (Equation 6.11) as well as application of the respective optimum cut in $\Delta\phi\,(\ell\ell)$.

The discovery significance of these resonances in dependence of the integrated luminosity is shown in Figure 6.7. In this case, only the nominal tracker extension up to $|\eta|_{\text{tracker}} \leq 2.5$ is considered.

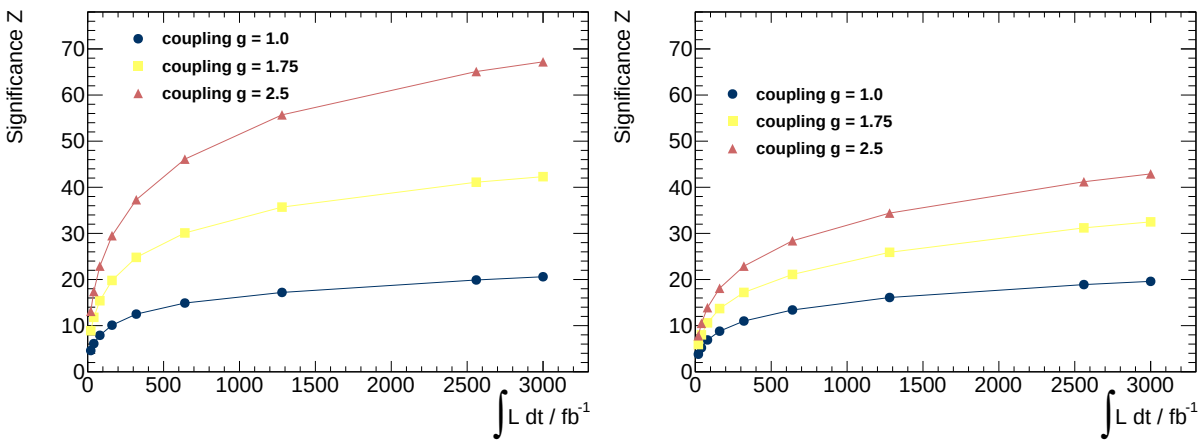

(a) $m_\Phi = 500\,\text{GeV}$ (b) $m_\Phi = 1000\,\text{GeV}$

Figure 6.7: Discovery significance of the Φ resonance with the ATLAS detector with nominal tracking detector extension, in dependence of the collected integrated luminosity of the LHC, for two different masses of the Φ resonance and three different values of the coupling.

At a given luminosity, the signal of a higher coupling resonance is observed with a higher significance. As Figure 6.7 shows, the investigated combinations of resonance masses and couplings could be discovered relatively early in the next LHC run, if they exist: The last one crosses the 5σ threshold at an integrated luminosity of $\mathcal{L} = 40\,\text{fb}^{-1}$. Thus, it will be possible to search for Φ-type resonances with masses higher than $m_\Phi = 1000\,\text{GeV}$, which were not investigated in this study.

On the other hand, it will also be possible to search for resonances with lower values of the coupling constant g. With a larger integrated luminosity, resonances with smaller couplings can be discovered, if they exist. This is illustrated in Figure 6.8.

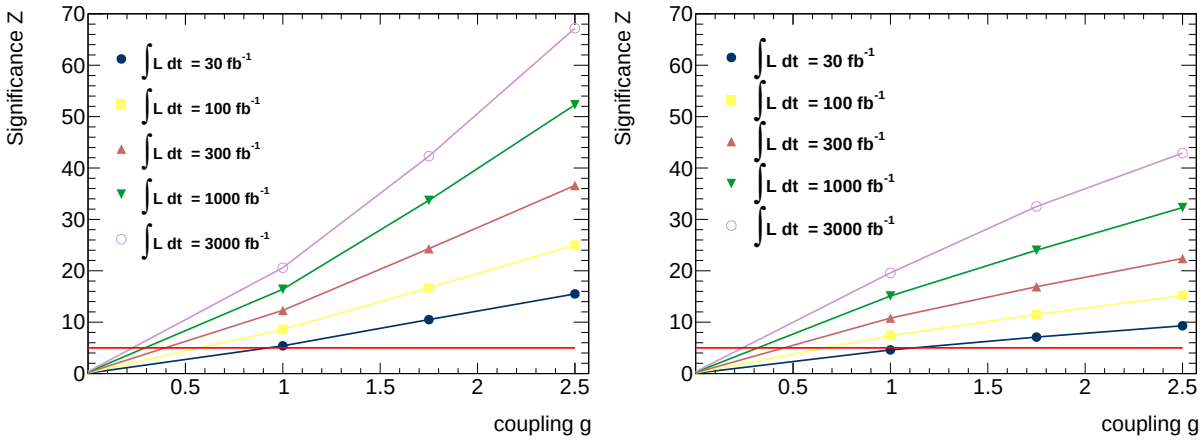

(a) $m_\Phi = 500\,\text{GeV}$ (b) $m_\Phi = 1000\,\text{GeV}$

Figure 6.8: Discovery significance of the Φ resonance in dependence of the coupling constant g of the resonance for several different amounts of integrated luminosity for two different masses. The red line indicates the significance of 5σ, which is the threshold for discovery.

6.7 Outlook

After the discovery of the Higgs-like boson, the scattering of electroweak bosons remains an insightful process at the current and upgraded LHC. It will continue to provide information on the nature of the EWSB mechanism through the measurement of the $VVjj$-EW cross sections in various channels and the possibility to discover or exclude additional resonances in the diboson channels.

The $W^\pm W^\pm jj$-EW process can be rediscovered with high significance at the upgraded LHC. If the tracking detector of ATLAS is extended to the forward region up to $|\eta| = 4.0$, the significance will increase by $\sim$30 % as the $W^\pm Zjj$ background suppression will be improved. The full background composition at higher energies will have to be studied using measured data.

A generic spin $J = 0$ and isospin $I = 2$ resonance with mass up to 1000 GeV and coupling up to 2.5 could be discovered with a luminosity of $\mathcal{L} = 40\,\text{fb}^{-1}$at the 14 TeV LHC. We can therefore conclude that it will be possible to find or exclude resonances with higher masses at the HL-LHC, which have not been studied in the scope of this work. The extension of the tracker has a small effect on the resonance search as well. In the signal region found to be optimal among the given choices, the effect is up to 6 % increase in significance with an extended tracker.

6.7.1 Vector boson scattering in other diboson channels

At the 8 TeV LHC, the only VBS channel for which the $VVjj$-EW process was significantly measured is the scattering of two W bosons with the same electric charge. In other final states, the $VVjj$-EW process has not been observed at the 8 TeV LHC as these are predominated by background processes.

BSM resonances in VBS in other final states have been studied in previous studies [215–217] of which the MC production was also partially performed in the scope of this work. In these studies, the prospects of excluding effective anomalous quartic gauge couplings or model-independent additional resonances with the ATLAS detector at the HL-LHC have been studied in the channels $ZZ \to \ell\ell\ell\ell$, $WZ \to \ell\nu\ell\ell$, $W^{\pm}W^{\pm} \to \ell^{\pm}\nu\ell^{\pm}\nu$, $WW \to \ell\nu jj$, and $W^{\pm}W^{\mp} \to \ell^{\pm}\nu\ell^{\mp}\nu$.

The goal for the next run of the LHC is the measurement of $VVjj$ final states in a VBS-like phase space in the channels $WZjj$, $ZZjj$, and $W^{\pm}W^{\mp}jj$ in order to discover the SM $VVjj$-EW production including VBS or to find new physics in this channel. A challenge will be the attempt of extracting the scattering of two longitudinally polarized weak bosons.

6.7.2 VBS at future accelerators

Apart from the HL-LHC, other accelerators with potential to study VBS are currently in different phases of development:

First of all, a linear electron-positron collider with a center-of-mass energy of 500 GeV to 1 TeV is being planned by the ILC collaboration (International Linear Collider). It provides the opportunity to measure VBS more precisely in an environment with lower hadronic activity than the LHC [225]. In case of new physics in this sector, studying VBS at the ILC will provide a complementary measurement to the LHC, which is sensitive to resonances with masses above the ILC's energy range.

In a more remote future experiment, a muon collider would be suitable to study VBS as well. A phenomenological study [226] has investigated the prospects for VBS measurement at a muon-muon collider with $\sqrt{s} = 4$ TeV. With a collision energy well above ILC range and the advantage of the jet-free environment of the lepton collider, it would provide the opportunity to investigate the shapes of diboson distributions in $VVjj$ final states and make it possible to distinguish the scattering of longitudinal bosons only with respect to transversely polarized bosons.

CHAPTER 7

Summary and conclusions

The study of the scattering of massive electroweak vector bosons at the LHC addresses two insufficiently explored aspects of the Standard Model of particle physics: The nature of the electroweak symmetry breaking mechanism and the self-interactions of the electroweak bosons. With proton-proton collision data from the ATLAS detector at the LHC, the work at hand has started the effort of the clarification of both of these aspects through the first measurement of electroweak production of two like-charge W bosons and two jets. This is also the first measurement of any process dominated by the scattering of two massive electroweak gauge bosons and therefore the first observation of a process containing the contribution from the quartic gauge interaction of massive electroweak gauge bosons at tree-level.

To prepare the analysis, Monte Carlo methods are utilized to generate the appropriate theoretical predictions for signal and background processes. Available Monte Carlo tools have been validated in this work. The signal process is defined as the electroweak production of two massive electroweak gauge bosons, which subsequently decay, and two jets. It contains the scattering of electroweak vector bosons as well as all processes not separable in a gauge invariant way, including non-resonant contributions producing the same final state. Crucial settings for the generation of this process include the right choice of electroweak scheme and the setup of the phase space and the phase space sampling.

Additionally, the important background of QCD-mediated production of the same final state has been investigated. In the case of $W^{\pm}W^{\pm}$ scattering, the ratio of QCD-mediated to electroweak production is small compared to the scattering of other combinations of electroweak gauge bosons $W^{\pm}W^{\mp}$, WZ, and ZZ, making this channel the suitable candidate for the first measurement of a process containing electroweak gauge boson scattering. Suppressing QCD-mediated production of two electroweak gauge bosons and two jets, the phase space region dominated by vector boson scattering is selected by requiring two highly energetic forward jets.

Other background contributions to the electroweak production of two like-charge W bosons and two jets include contributions from charge mis-identification of leptons, jets mis-measured as leptons, and secondary leptons from hadron decays which have been estimated with data driven techniques.

The dominant background contribution arises from events with three or four leptons due to the production of WZ or ZZ and two jets where the W and Z bosons decay leptonically. This background is suppressed by a veto on events with additional leptons selected with loose quality requirements. Monte Carlo simulations are used to estimate the contribution from $WZjj$ and $ZZjj$ processes.

The production cross section for two like-charge W bosons and two jets via electroweak interactions only has been extracted in a fiducial phase space dominated by $W^{\pm}W^{\pm}$ scattering. The measured fiducial cross section $\sigma^{\text{fiducial}}_{W^{\pm}W^{\pm}jj-\text{EW}} = 1.3 \pm 0.4(\text{stat.}) \pm 0.2(\text{syst.})\,\text{fb}$ is in good agreement with the Standard Model prediction of $\sigma^{\text{fiducial}}_{W^{\pm}W^{\pm}jj-\text{EW}} = 0.95 \pm 0.06\,\text{fb}$, which has been determined at next-to-leading order in perturbative QCD. Comparing the theoretical prediction to the measurement, it can be concluded that the next-to-leading order QCD calculation provides sufficient accuracy to model current data. In future, when statistical uncertainties decrease and if systematic uncertainties are reduced due to better understanding of their sources, next-to-leading order electroweak or higher order QCD corrections might become important.

In order to scrutinize possible effects of new physics, anomalous quartic gauge couplings have been studied in the context of $W^{\pm}W^{\pm}$ scattering. The anomalous quartic gauge coupling parameters α_4 and α_5 are introduced as coefficients to higher-order terms in an effective field theory, the Electroweak Chiral Lagrangian. As the introduction of these anomalous couplings leads to violation of the unitarity of the scattering amplitude, the K-matrix unitarization scheme has been applied. It acts like an infinitely heavy resonance and suppresses the cross section as little as possible. Non-zero anomalous quartic gauge couplings have an influence on the total cross section of the scattering process as well as the kinematics of the final state particles. Based on the simulation of these effects, the first limits on the parameters α_4 and α_5 have been derived from the measurement. Values of the anomalous couplings outside the ranges $-0.14 < \alpha_4 < 0.16$ and $-0.23 < \alpha_5 < 0.24$ are excluded at $95\,\%$ confidence level.

While quartic electroweak gauge interactions have been unconstrained by previous data, the discovery of a Higgs boson compatible with the Standard Model has provided some previous insight into the nature of the electroweak symmetry breaking mechanism. No signs of physics beyond the Standard Model have been found in the measurement of electroweak production of two like-charge W bosons and two jets. The Standard Model thus continues to prove its success at describing nature at the currently accessible experimental energies. Its prescription of both the quartic electroweak gauge interactions and the unitarization of the vector boson scattering amplitude provided by the Higgs mechanism has been probed and found to be valid for the measurement.

Higher collision energies will shed more light at the nature of the electroweak symmetry breaking mechanism and the self-interaction of the electroweak gauge bosons. With increasing center-of-mass energy and luminosity, the LHC will provide sufficient data to further explore the process of vector boson scattering in the $W^{\pm}W^{\pm}$ channel. Prospects for this measurement have been studied in this thesis. As the ratio of electroweak to QCD-mediated production of $W^{\pm}W^{\pm}jj$ increases, the extraction of the electroweak production will be facilitated. Extending the tracker of the ATLAS detector to a pseudorapidity of $|\eta| = 4.0$ will increase the significance of the measurement by $30\,\%$.

To advance the knowledge about scattering dynamics of massive electroweak gauge bosons, other channels should be measured at the LHC and future colliders. Theoretical tools for the fast and accurate simulation of these processes could be advanced, for instance by providing electroweak higher-order corrections. To complete the investigation of electroweak gauge boson scattering, extraction of the scattering component of longitudinally polarized W and Z bosons would be useful.

Appendix

APPENDIX A

Steering files for MC simulation of vector boson scattering processes

Two example minimal steering files for electroweak production of $VVjj$ events are included in this appendix. Important settings are explained in the following, both for the $W^{\pm}W^{\pm}jj$-EW and the $W^{\pm}Zjj$-EW case. The steering files are written in the native `Whizard` language Sindarin and work with `Whizard` version 2.1.1. A complete documentation for `Whizard` can be found in the manual [227].

- The utilized physical model can be chosen by the `model` specifier. Available models include the Standard Model (`SM`), as well as several effective field theory models with possibility to unitarize with the k-matrix method (e.g. `SM_km`).
- `alphas = 0` sets the strong coupling constant to zero in order to include only purely-electroweak diagrams.
- Several containers of particles concatenated by colon (:) are built and assigned to variables with the `alias` command. This allows for easier book-keeping and faster implementation, as flavors are summed automatically.
- The mass of the light leptons (e, μ) and light quarks (u, d, s, c) are set to zero in order to make automatic flavor summation possible.
- The mass of τ leptons cannot be set to zero as non-zero mass is required for the external decay algorithm. Therefore, processes involving τ leptons in the final state of the matrix element are specified separately.
- Phase space commands can be given, such as `?phs_keep_nonresonant = true` which takes care that regions of off-shell resonances are not neglected in the phase space.

- The scale command allows to set the factorization and renormalization scales simultaneously. scale = eval M [collect [allleptons]] determines the invariant mass of the leptonic decay products of the bosons for each event.
- Model specific parameters, such as the anomalous quartic gauge couplings α_4 and α_5, denoted in Whizard by a4 and a5 can be given.
- Phase space cuts are set according to the Whizard syntax.
- The compile command issues the compilation of matrix-element code.
- The collision energy and PDF information is provided.
- For the integration, the number of calls per iteration is provided in order to ensure sufficient sampling density. An accuracy goal can be set, at which the integration will be stopped.
- Events are generated according to the defined number and provided in the defined format. The ?keep_beams = false is needed for the interface to the external Pythia8 parton shower.

A.1 $W^{\pm}W^{\pm}jj$-EW generation input

```
##################################################
# Electroweak production of l+/-l+/- nu nu jj with Whizard
# anomalous couplings a4, a5 in SM_km.mdl
##################################################
model = SM_km
alphas = 0

# Set particle containers and process ============================
alias nu = n1:n2
alias NU = N1:N2
alias neutrino = n1:n2:n3:N1:N2:N3
alias lep = e1:e2
alias LEP = E1:E2
alias lepton = e1:E1:e2:E2:e3:E3
alias j = u:d:s:c:U:D:S:C:g
alias allleptons = lepton:neutrino

process vbslplp = j, j => j, j, LEP, LEP, nu, nu
process vbslmlm = j, j => j, j, lep, lep, NU, NU
process vbstplp = j, j => j, j, E3, LEP, n3, nu
```

```
process vbstmlm = j, j => j, j, e3, lep, N3, NU
process vbstauptaup = j, j => j, j, E3, E3, n3, n3
process vbstaumtaum = j, j => j, j, e3, e3, N3, N3

# Set parameters ==========================================
scale = eval M [collect [allleptons]]

mtau = 1.77705
mH = 126 GeV
wH = 0.00418 GeV
me = 0  mmu = 0
ms = 0  mc = 0
?phs_keep_nonresonant = true
a4 = 0
a5 = 0

cuts = all Dist > 0.4 [j,j] and all -5.0 < Eta < 5.0 [j] and all Pt > 15 GeV [j]
 and all -5.0 < Eta < 5.0 [lepton] and all Pt > 8 GeV [lepton]

# Compile matrix-element calculation ==============================
compile

# Set up integration ======================================
sqrts = 8 TeV
$lhapdf_file = "cteq6ll.LHpdf"
beams = p, p => lhapdf

integrate (vbslplp,vbslmlm,vbstplp,vbstmlm,vbstauptaup,vbstaumtaum)
 {iterations= 14:200000, 14:100000}

# Set up event generation =====================================
n_events = 50000
sample_format = lhef
simulate (vbslplp,vbslmlm,vbstplp,vbstmlm,vbstauptaup,vbstaumtaum)
 {checkpoint = 500 ?keep_beams = false}
```

A.2 $W^{\pm}Zjj$-EW generation input

```
##################################################
# Electroweak production of lll nu jj with Whizard
# anomalous couplings a4, a5 in SM_km.mdl
##################################################
model = SM_km
alphas = 0

# Set particle containers and process ============================
alias j = u:d:s:c:b:U:D:S:C:B:g
alias lepton = e1:E1:e2:E2:e3:E3
alias charlep = e1:E1:e2:E2
alias neu = n1:N1:n2:N2
alias taulep = e3:E3
alias taulepnu = n3:N3
alias allleptons = charlep:taulep:neu:taulepnu

process wz1 = j, j => j, j, charlep, charlep, charlep, neu
process wz2 = j, j => j, j, taulep, taulep, taulep, taulepnu
process wz3 = j, j => j, j, taulep, taulep, charlep, neu
process wz4 = j, j => j, j, charlep, charlep, taulep, taulepnu

# Set parameters ========================================
scale = eval M [collect[allleptons]]

mtau = 1.77705
mH = 126 GeV
wH = 0.00418 GeV
me  = 0  mmu = 0
ms = 0   mc = 0
mb = 0
?phs_keep_nonresonant = true
a4 = -0.4
a5 = 0

cuts = all Dist > 0.4 [j,j] and all Pt > 15 GeV [j] and all -5.0 < Eta < 5.0
[j] and all Pt > 5 GeV [extract index 2 [sort by -Pt [lepton]]] and all -5.0
< Eta < 5.0 [lepton] and all Dist > 0.3 [lepton,lepton]
```

```
# Compile matrix-element calculation ==============================
compile

# Set up integration ==========================================
sqrts = 8 TeV
$lhapdf_file = "CT10.LHgrid"
beams = p, p => lhapdf

accuracy_goal = 10
integrate (wz1,wz2,wz3,wz4) {iterations = 15:400000, 10:200000 }

n_events = 5000
sample_format = hepmc
simulate (wz1,wz2,wz3,wz4) { checkpoint = 500 ?keep_beams = false}
```

APPENDIX B

Kinematics in the VBS signal region

The following figures illustrate kinematics of the leptons and tagging jets in the VBS signal region.

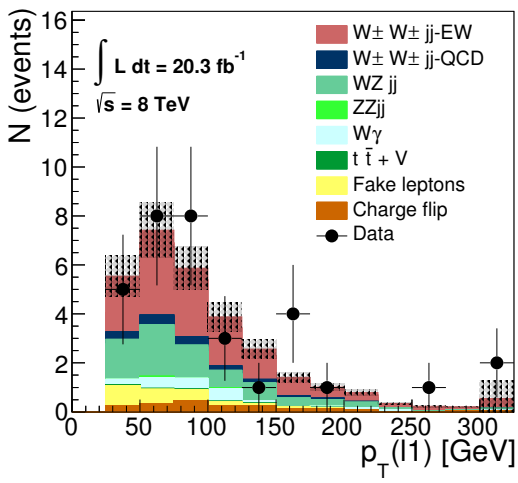

(a) Transverse momentum of lepton with largest p_{T}

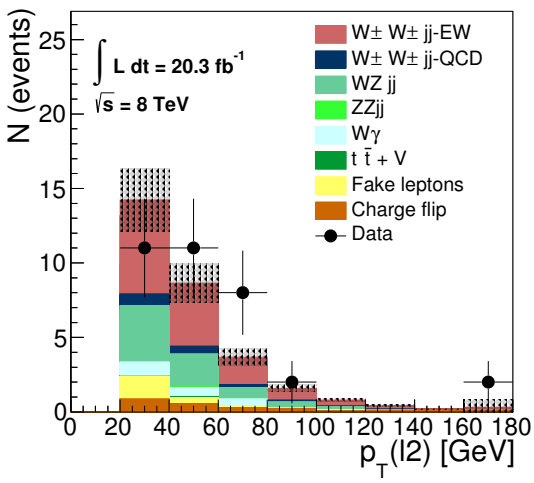

(b) Transverse momentum of lepton with second largest p_{T}

Figure B.1: Transverse momenta of leptons in the VBS signal region. The hatched area represents the systematic uncertainty on the total prediction.

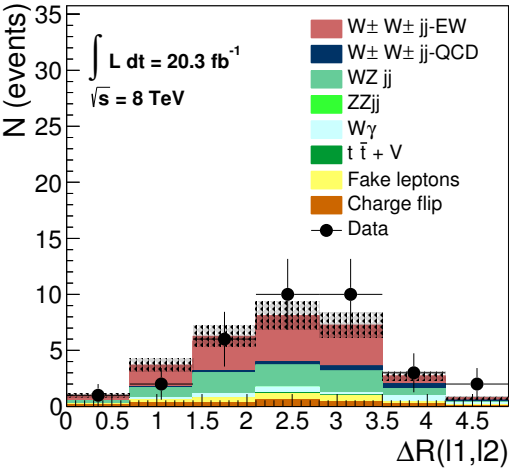

(a) Distance of leptons in the pseudorapidity-azimuth plane

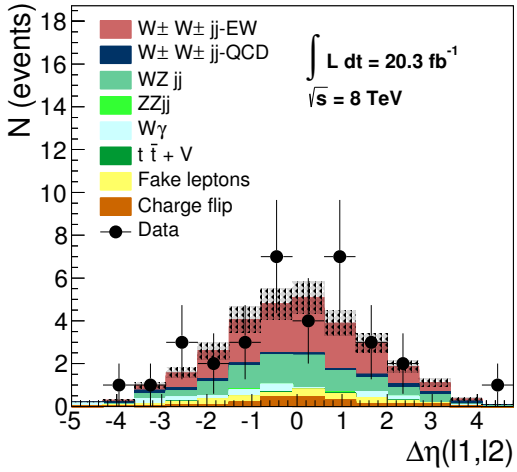

(b) Pseudorapidity difference of leptons

Figure B.2: Dilepton kinematics in the VBS signal regions. The hatched area represents the systematic uncertainty on the total prediction.

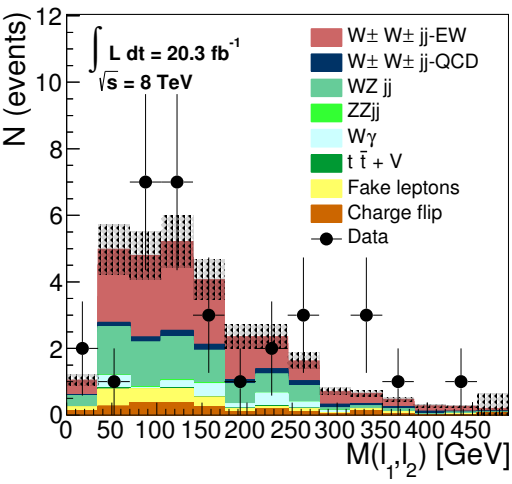

(a) Invariant mass of the two leptons

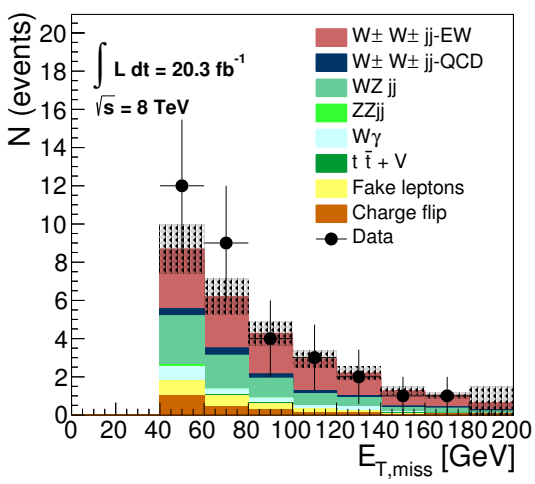

(b) Missing transverse momentum

Figure B.3: Kinematics in the VBS signal region. The hatched area represents the systematic uncertainty on the total prediction.

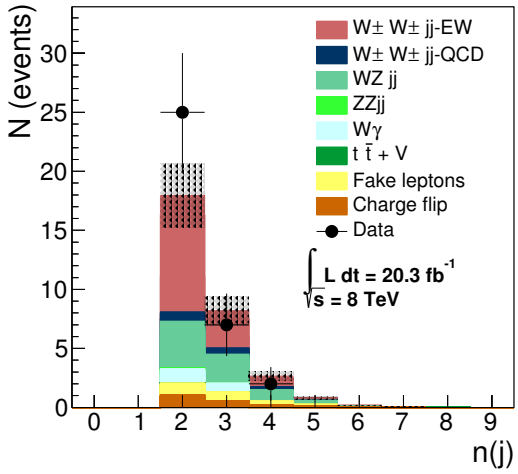

(a) Number of jets

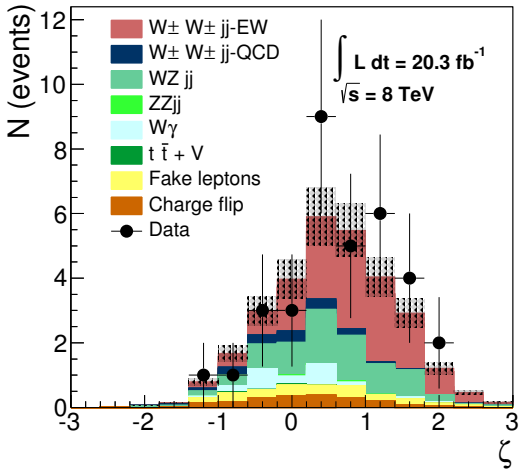

(b) Lepton centrality in the VBS region

Figure B.4: Number of jets (left) and lepton centrality (right), defined as
$\zeta = \min\left[\min\left(\eta_{\ell 1}, \eta_{\ell 2}\right) - \min(\eta_{j1}, \eta_{j2}), \max(\eta_{j1}, \eta_{j2}) - \max(\eta_{\ell 1}, \eta_{\ell 2})\right]$,
in the VBS signal region. The hatched area represents the systematic uncertainty on the total prediction.

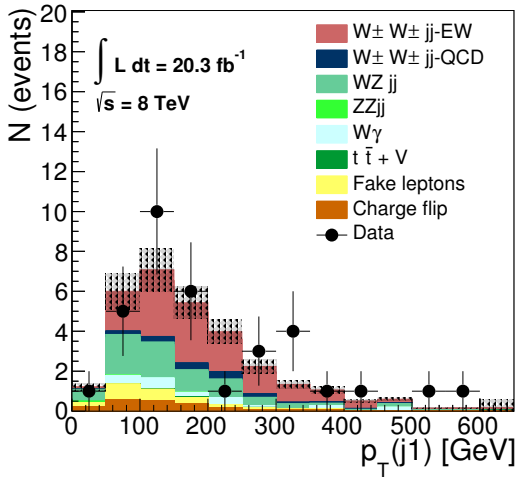

(a) Transverse momentum of the leading tagging jet

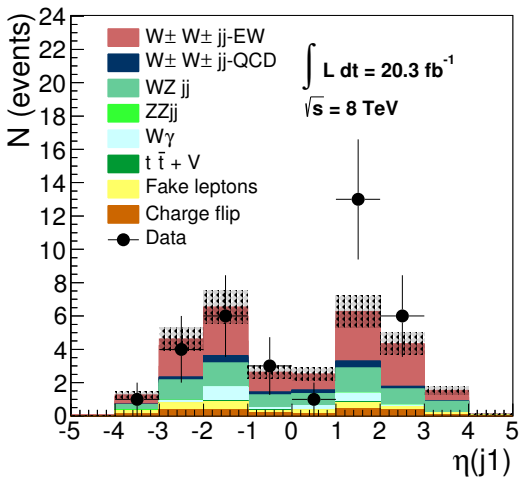

(b) Pseudorapidity of the leading tagging jet

Figure B.5: Kinematic properties of the leading tagging jet, i.e. the jet with the largest p_{T} in the event. The hatched area represents the systematic uncertainty on the total prediction.

APPENDIX C

Anomalous quartic gauge couplings in vector boson scattering

C.1 Comparison of anomalous couplings in WZ and $W^{\pm}W^{\pm}$ scattering

Scattering of WZ bosons is sensitive to anomalous quartic gauge couplings. Comparing the contour lines of cross sections in the $\alpha_4,\ \alpha_5$-plane between the $W^{\pm}W^{\pm}jj$-EW and the $W^{\pm}Zjj$-EW process in figure C.1 illustrates that both processes highest sensitivity to aQGC lies in different areas of the $\alpha_4,\ \alpha_5$-plane.

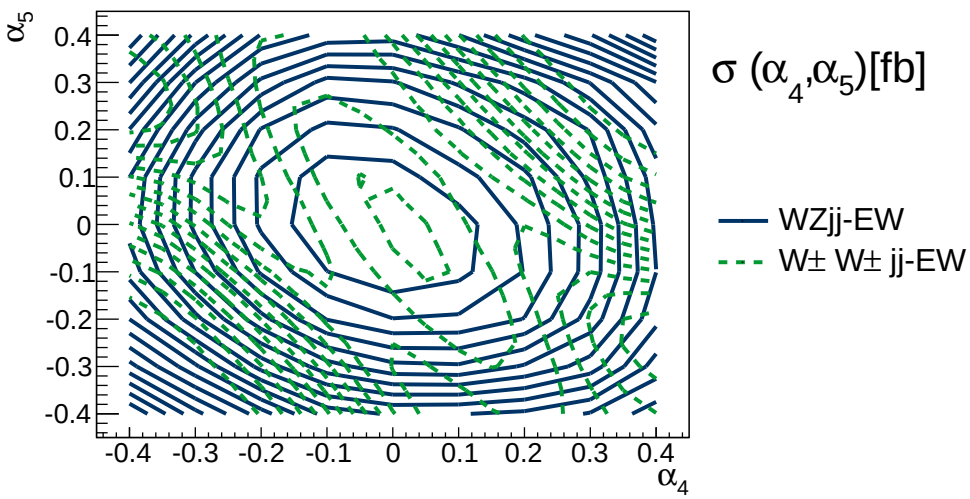

Figure C.1: Contour lines in the $\alpha_4,\ \alpha_5$-plane for $WZjj$-EW (solid blue line) and $W^{\pm}W^{\pm}jj$-EW (dashed green line), generated with Whizard in an inclusive sample phase space, (C.1) (with an additional cut of $\Delta R(\ell,\ell)$ for the $W^{\pm}Zjj$-EW process. Distances between contour lines are arbitrary.

C.2 Anomalous couplings samples used in $W^{\pm}W^{\pm}jj$-EW

The following samples have been produced in the scope of this work for the measurement of anomalous couplings in $W^{\pm}W^{\pm}$ scattering at ATLAS. The sample phase space is constrained as follows:

$$\begin{aligned} &\text{Outgoing partons}: p_{\mathrm{T}} > 15\,\mathrm{GeV},\ |\eta| < 5,\ \Delta R(jj) > 0.4; \\ &\text{Leptons}:\ p_{\mathrm{T}} > 8\,\mathrm{GeV},\ |\eta| < 5; \end{aligned} \tag{C.1}$$

and the factorization and renormalization scales are set to the invariant mass of outgoing leptons and neutrinos,

$$\mu_F = \mu_r = M(\ell_1, \ell_2, \nu_1, \nu_2). \tag{C.2}$$

A SM Higgs boson with mass $m_H = 126\,\mathrm{GeV}$ and width $\Gamma_H = 4.18\,\mathrm{MeV}$ is included, and the PDF set `cteq6ll` is used.

α_4	α_5	dataset ID	$\sigma_{\text{sample PS}}$ [fb]	A [%]	ε_{ee} [%]	$\varepsilon_{e\mu}$ [%]	$\varepsilon_{\mu\mu}$ [%]
0.00	0.00	185310	14.72 ± 0.02	4.61 ± 0.06	49.2 ± 2.3	62.5 ± 1.5	68.0 ± 2.1
0.00	0.10	185313	16.93 ± 0.02	5.66 ± 0.06	55.1 ± 2.0	61.3 ± 1.4	71.9 ± 1.8
0.00	0.20	185318	21.16 ± 0.02	6.63 ± 0.07	55.4 ± 1.8	70.2 ± 1.2	67.7 ± 1.7
0.00	-0.10	185314	17.98 ± 0.02	5.61 ± 0.06	59.7 ± 1.9	66.7 ± 1.3	74.1 ± 1.8
0.00	-0.20	185317	22.88 ± 0.02	7.09 ± 0.07	55.7 ± 1.7	66.5 ± 1.2	74.2 ± 1.6
0.10	0.00	185311	19.13 ± 0.02	6.92 ± 0.07	54.8 ± 1.8	69.7 ± 1.2	69.6 ± 1.7
0.10	0.10	185321	23.00 ± 0.02	7.32 ± 0.07	61.8 ± 1.6	65.9 ± 1.2	73.2 ± 1.6
0.10	-0.20	185327	15.90 ± 0.02	4.75 ± 0.06	49.7 ± 2.2	66.0 ± 1.4	70.7 ± 2.1
0.10	-0.40	185324	26.26 ± 0.02	7.04 ± 0.07	60.4 ± 1.7	68.8 ± 1.2	79.4 ± 1.5
0.20	-0.30	185326	18.40 ± 0.02	5.76 ± 0.06	56.4 ± 1.9	66.8 ± 1.3	70.2 ± 1.8
0.30	-0.20	185320	25.47 ± 0.03	7.78 ± 0.07	62.9 ± 1.6	71.0 ± 1.1	71.4 ± 1.5
0.30	-0.60	185316	23.15 ± 0.02	5.86 ± 0.06	53.3 ± 1.9	62.0 ± 1.4	67.0 ± 1.9
-0.10	0.00	185312	20.88 ± 0.02	6.64 ± 0.07	56.4 ± 1.8	66.3 ± 1.2	72.2 ± 1.7
-0.10	0.20	185328	16.00 ± 0.02	5.15 ± 0.06	48.3 ± 2.0	62.1 ± 1.5	67.2 ± 2.0
-0.10	0.40	185323	24.62 ± 0.02	6.83 ± 0.07	59.2 ± 1.7	69.2 ± 1.2	71.4 ± 1.7
-0.10	-0.10	185322	25.62 ± 0.03	7.71 ± 0.07	61.6 ± 1.6	65.5 ± 1.2	69.1 ± 1.6
-0.20	0.30	185325	19.28 ± 0.02	6.33 ± 0.07	54.1 ± 1.8	67.7 ± 1.3	68.4 ± 1.7
-0.30	0.20	185319	28.60 ± 0.03	7.56 ± 0.07	58.8 ± 1.7	70.2 ± 1.1	68.1 ± 1.6
-0.30	0.60	185315	23.13 ± 0.02	6.09 ± 0.07	55.1 ± 1.9	67.9 ± 1.2	72.4 ± 1.8

Table C.1: List of fully simulated WHIZARD aQGC signal samples with their corresponding dataset IDs. Additionally, the total sample cross section $\sigma_{\text{sample PS}}$, the acceptance for the fiducial VBS region A and the signal efficiencies ε in the three final states are given. The quoted uncertainties represent statistical uncertainties only. [191]

C.3 Kinematics of $W^{\pm}W^{\pm}jj$-EW events with anomalous couplings

Additional kinematic distributions for three points in the α_4, α_5-plane are shown in this appendix. All observables are depicted in the VBS analysis region. Three different points in α_4, α_5 are chosen to illustrate the effect of varying the anomalous couplings.

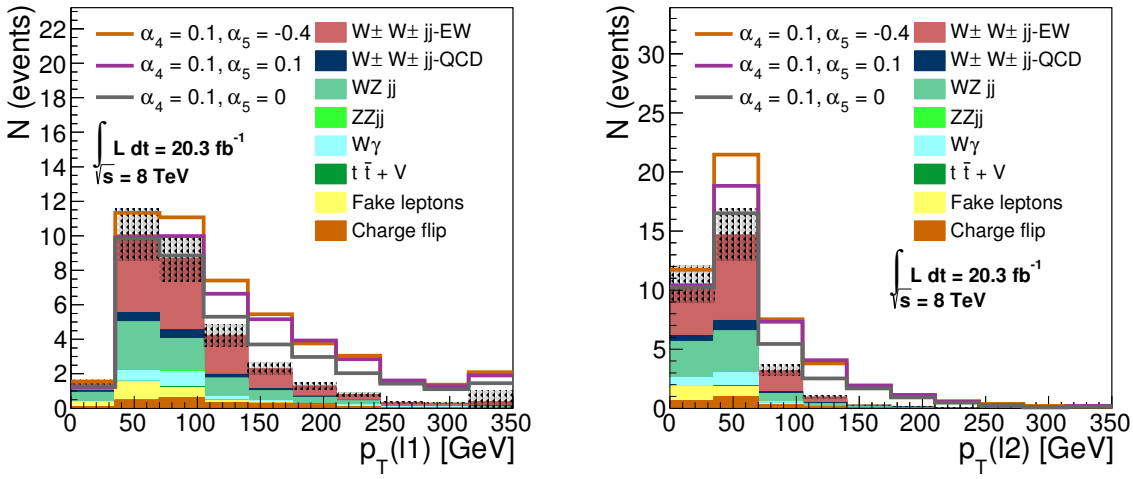

(a) Transverse momentum of the leading lepton

(b) Transverse momentum of the subleading lepton

Figure C.2: Comparison of lepton kinematics in the VBS region in the SM and three points in the α_4, α_5-plane close to the sensitivity of the measurement. The filled histogram shows the SM prediction, and the three additional lines the total prediction including contributions from non-zero anomalous couplings. The hatched area represents the systematic uncertainty on the total prediction.

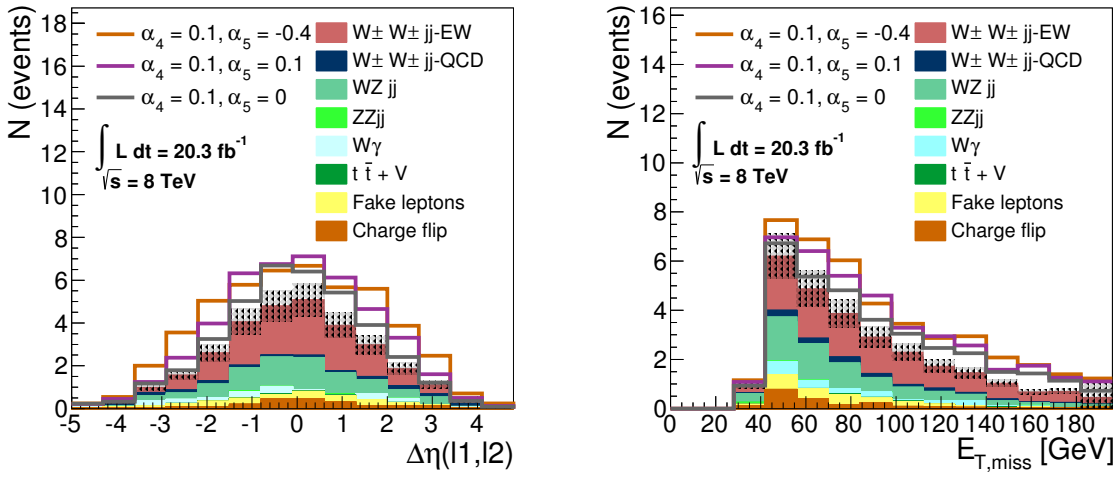

(a) Pseudorapidity difference of the two leptons

(b) Missing transverse momentum

Figure C.3: Comparison of dilepton kinematics and missing transverse momentum in the VBS region in the SM and three points in the α_4, α_5-plane close to the sensitivity of the measurement. The filled histogram shows the SM prediction, and the three additional lines the total prediction including contributions from non-zero anomalous couplings. The hatched area represents the systematic uncertainty on the total prediction.

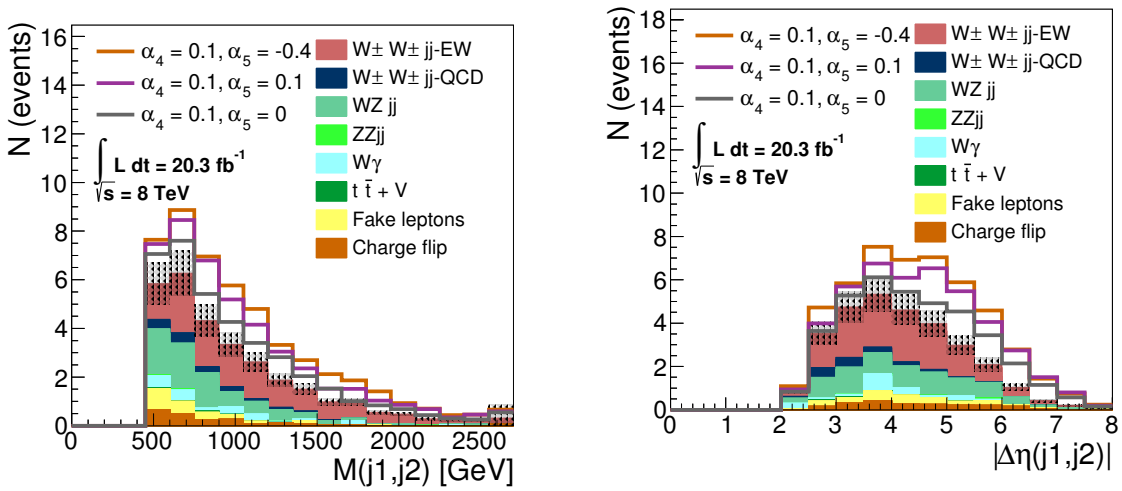

(a) Invariant mass of tagging jets

(b) Absolute difference in pseudorapidity of tagging jets

Figure C.4: Comparison of dijet kinematics in the VBS region in the SM and three points in the α_4, α_5-plane close to the sensitivity of the measurement. The filled histogram shows the SM prediction, and the three additional lines the total prediction including contributions from non-zero anomalous couplings. The hatched area represents the systematic uncertainty on the total prediction.

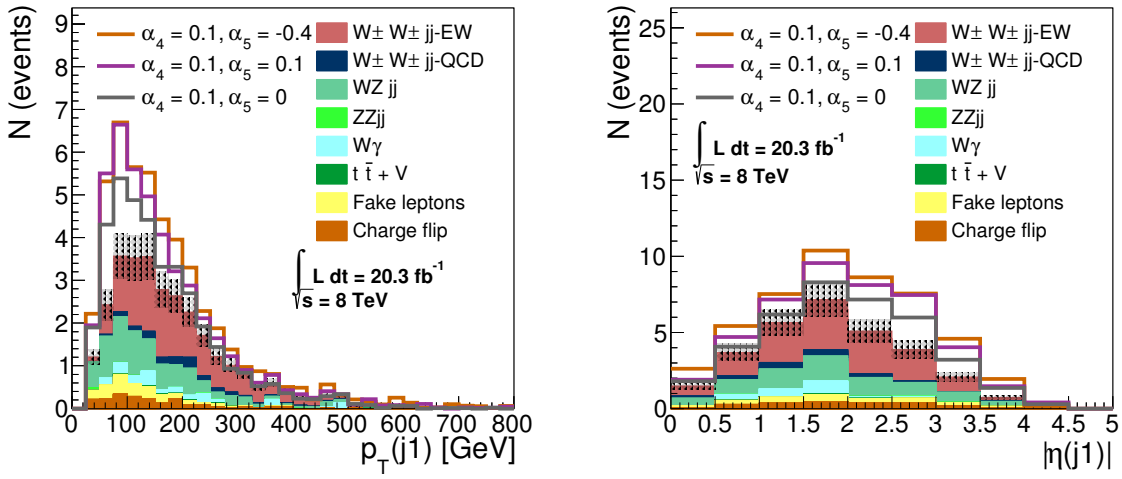

(a) Transverse momentum of leading jet

(b) Absolute pseudorapidity of leading jet

Figure C.5: Comparison of the kinematics of the leading jet in the VBS region for the SM and for three points in the α_4, α_5-plane close to the sensitivity of the measurement. The filled histogram shows the SM prediction, and the three additional lines the total prediction including contributions from non-zero anomalous couplings. The hatched area represents the systematic uncertainty on the total prediction.

APPENDIX D

Monte Carlo samples used for the analysis of $W^{\pm}W^{\pm}jj$ at 8 TeV

Monte Carlo samples of the relevant processes simulated within the ATLAS simulation framework are listed in Tables D.1 and D.2.

Sample name	ATLAS reconstruction tag	cross section [pb]	k-factor	filter efficiency
Diboson processes				
mc12_8TeV.185393.Sherpa_CT10_lnln_ls_EWK_MassiveCB.merge	e2504_s1773_s1776_r4485_r4540_p1328/	0.02762	0.8356	1.0
mc12_8TeV.147193.Sherpa_CT10_lnlnjj_WWjj_EW6.merge	e1613_s1499_s1504_r3658_r3549_p1328/	0.09588	1.0	1.0
mc12_8TeV.185396.Sherpa_CT10_lllnu_WZ_EWK_MassiveCB.merge	e2486_s1773_s1776_r4485_r4540_p1328/	0.082102	0.8944	1.0
mc12_8TeV.161982.Sherpa_CT10_llnunu_ZZ_EW6.merge	e1434_s1499_s1504_r3658_r3549_p1328/	0.0041	1.0	1.0
mc12_8TeV.147196.Sherpa_CT10_llllj_ZZjj_EW6	e1613_s1499_s1504_r3658_r3549_p1328/	0.00691	1.0	1.0
mc12_8TeV.185394.Sherpa_CT10_lnln_ls_QCD_MassiveCB.merge	e2494_s1773_s1776_r4485_r4540_p1328/	0.01608	1.0354	1.0
mc12_8TeV.126892.Sherpa_CT10_llnunu_WW	e1434_s1499_s1504_r3658_r3549_p1328/	5.4982	1.06	1.0
mc12_8TeV.179974.Sherpa_CT10_lllnu_WZ_MassiveCB.merge	e2203_s1581_s1586_r4485_r4540_p1328/	9.7446	1.2704	1.0
mc12_8TeV.185397.Sherpa_CT10_lllnu_WZ_l10_MassiveCB.merge	e2486_s1773_s1776_r4485_r4540_p1328/	9.7446	1.2704	0.24041
mc12_8TeV.126895.Sherpa_CT10_llnunu_ZZ	e1434_s1499_s1504_r3658_r3549_p1328/	0.4962	1.05	1.0
mc12_8TeV.126894.Sherpa_CT10_llll_ZZ	e1434_s1499_s1504_r3658_r3549_p1328/	8.7345	1.0	1.0
$t\bar{t}$ processes				
mc12_8TeV.110001.McAtNloJimmy_CT10_ttbar_dilepton	e1576_s1499_s1504_r3658_r3549_p1328/	253.0	1.0	0.105
mc12_8TeV.105200.McAtNloJimmy_CT10_ttbar_LeptonFilter	e1513_s1499_s1504_r3945_r3549_p1328/	253.0	1.0	0.5427
mc12_8TeV.119353.MadGraphPythia_AUET2BCTEQ6L1_ttbarW	e1352_s1499_s1504_r3658_r3549_p1328/	0.1041	1.18	1.0
mc12_8TeV.174830.MadGraphPythia_AUET2BCTEQ6L1_ttbarWjExcl	e1672_s1499_s1504_r3658_r3549_p1328/	0.05337	1.18	1.0
mc12_8TeV.174831.MadGraphPythia_AUET2BCTEQ6L1_ttbarWjjIncl	e1672_s1499_s1504_r3658_r3549_p1328/	0.041482	1.18	1.0
mc12_8TeV.119355.MadGraphPythia_AUET2BCTEQ6L1_ttbarZ	e1352_s1499_s1504_r3658_r3549_p1328/	0.06769	1.34	1.0
mc12_8TeV.174832.MadGraphPythia_AUET2BCTEQ6L1_ttbarZjExcl	e1672_s1499_s1504_r3658_r3549_p1328/	0.045357	1.34	1.0
mc12_8TeV.174833.MadGraphPythia_AUET2BCTEQ6L1_ttbarZjjIncl	e1672_s1499_s1504_r3658_r3549_p1328/	0.039772	1.34	1.0

Table D.1: Monte Carlo samples used for the 8 TeV analysis: Diboson and $t\bar{t}$ production.

Sample name	ATLAS reconstruction tag	cross section [pb]	k-factor	filter efficiency
W + γ production				
mc12_8TeV.146436.AlpgenJimmy_AUET2CTEQ6L1_WgammaNp0	e1260_s1469_s1470_r3542_r3549_p1328/	230.	1.15	0.314
mc12_8TeV.146437.AlpgenJimmy_AUET2CTEQ6L1_WgammaNp1	e1260_s1469_s1470_r3542_r3549_p1328/	59.5	1.15	0.449
mc12_8TeV.146438.AlpgenJimmy_AUET2CTEQ6L1_WgammaNp2	e1260_s1469_s1470_r3542_r3549_p1328/	21.4	1.15	0.545
mc12_8TeV.146439.AlpgenJimmy_AUET2CTEQ6L1_WgammaNp3	e1293_s1469_s1470_r3542_r3549_p1328/	7.12	1.15	0.630
(WgammaNp0 to WgammaNp3 with _LeptonPhotonFilter)				
mc12_8TeV.146434.AlpgenJimmy_AUET2CTEQ6L1_WgammaNp4	e1293_s1469_s1470_r3542_r3549_p1328/	2.12	1.15	1.0
mc12_8TeV.146435.AlpgenJimmy_AUET2CTEQ6L1_WgammaNp5	e1293_s1469_s1470_r3542_r3549_p1328/	0.467	1.15	1.0
mc12_8TeV.185304.Sherpa_CT10_Wenugamma2jetVBS.merge	e2366_s1581_s1586_r4485_r4540_p1328/	0.4496	1.0	1.0
mc12_8TeV.185305.Sherpa_CT10_Wmunugamma2jetVBS.merge	e2366_s1581_s1586_r4485_r4540_p1328/	0.4496	1.0	1.0
mc12_8TeV.185306.Sherpa_CT10_Wtaunugamma2jetVBS.merge	e2366_s1581_s1586_r4485_r4540_p1328/	0.4496	1.0	1.0
DPI Samples				
mc12_8TeV.147281.Pythia8_AU2CTEQ6L1_DPI_W_W_2l2j	e1720_s1581_s1586_r3658_r3549_p1328/	0.0258	1.0	0.0752
mc12_8TeV.147283.Pythia8_AU2CTEQ6L1_DPI_W_Z_2l2j	e1720_s1581_s1586_r3658_r3549_p1328/	0.139	1.0	0.00873
mc12_8TeV.147286.Pythia8_AU2CTEQ6L1_DPI_Z_Z_2l2j	e1720_s1581_s1586_r3658_r3549_p1328/	0.213	1.0	0.00457
mc12_8TeV.147288.Pythia8_AU2CTEQ6L1_DPI_WZ_dijet_2l2j	e1720_s1581_s1586_r3658_r3549_p1328/	1.43	1.0	0.102
mc12_8TeV.147289.Pythia8_AU2CTEQ6L1_DPI_ZZ_dijet_2l2j	e1720_s1581_s1586_r3658_r3549_p1328/	1.86	1.0	0.0422

Table D.2: Monte Carlo samples used for the 8 TeV analysis: $W\gamma$ and DPI processes.

APPENDIX E

Kinematic distributions of resonances at 14 TeV

Kinematic distributions of a Φ resonance in the $\ell^{\pm}\nu\ell^{\pm}\nu jj$ final state are shown below, using the nominal tracker setup of ATLAS ($|\eta|_{\text{tracker}} < 2.5$). They are selected according to the criteria described in section 6.3.3 and equation 6.11. No requirement on the azimuthal distance of leptons, $\Delta\phi\,(\ell\ell)$, is applied.

This appendix shows kinematic distribution sensitive to these resonances. For searches, a mass reconstruction technique [141] can be used to enhance the resonance signal.

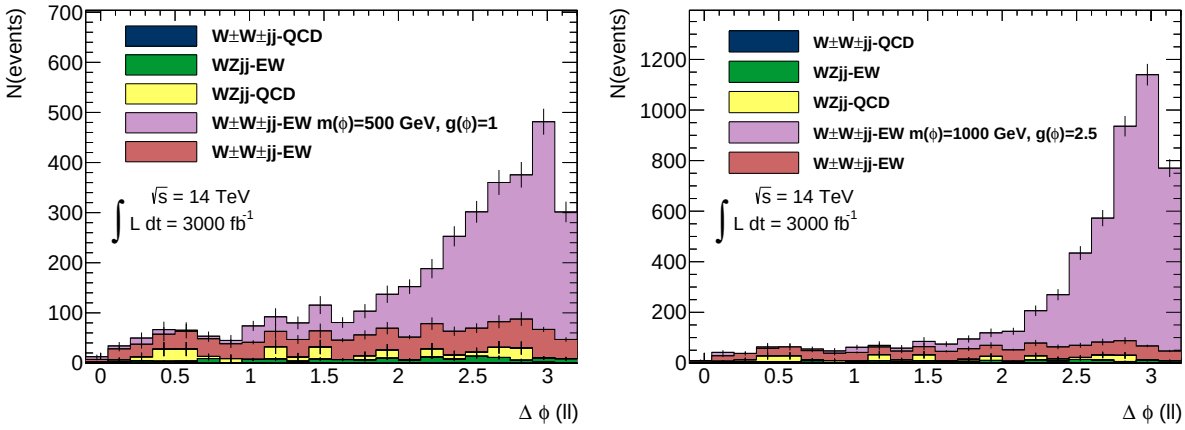

(a) $m_{\Phi} = 500\,\text{GeV}$, $g = 1.0$

(b) $m_{\Phi} = 1000\,\text{GeV}$, $g = 2.5$

Figure E.1: Distribution of azimuthal distance of the charged leptons, $\Delta\phi\,(\ell\ell)$, in the $\ell^{\pm}\nu\ell^{\pm}\nu jj$ final state with the ATLAS detector with nominal tracking detector extension. A Φ resonance with two different mass and coupling configurations is shown as signal.

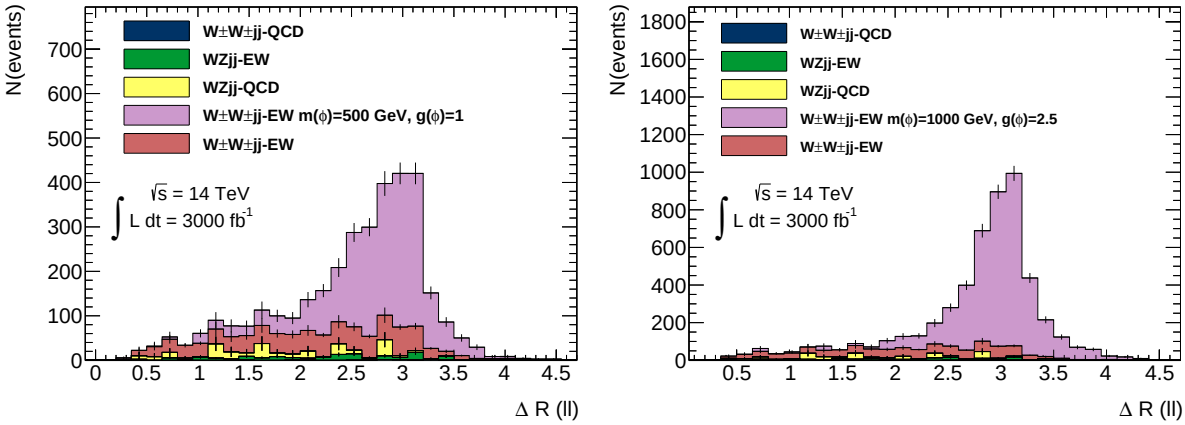

(a) $m_\Phi = 500\,\text{GeV}$, $g = 1.0$ (b) $m_\Phi = 1000\,\text{GeV}$, $g = 2.5$

Figure E.2: Distribution of distance $\Delta R(\ell\ell)$ between the charged leptons in the $\ell^\pm\nu\ell^\pm\nu jj$ final state with the ATLAS detector with nominal tracking detector extension. A Φ resonance with two different mass and coupling configurations is shown as signal.

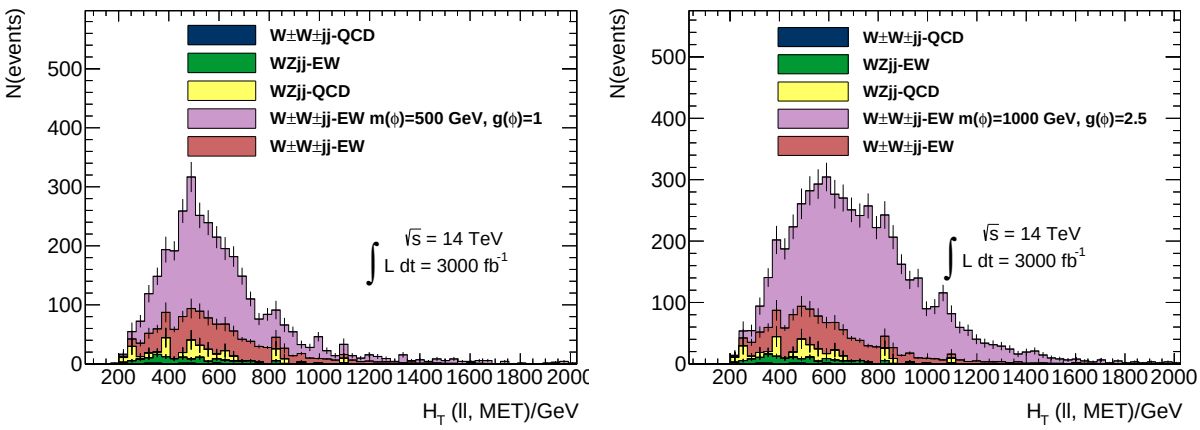

(a) $m_\Phi = 500\,\text{GeV}$, $g = 1.0$ (b) $m_\Phi = 1000\,\text{GeV}$, $g = 2.5$

Figure E.3: Distribution of $H_T(\ell\ell, E_\text{T}^\text{miss})$ in the $\ell^\pm\nu\ell^\pm\nu jj$ final state with the ATLAS detector with nominal tracking detector extension. A Φ resonance with two different mass and coupling configurations is shown as signal.

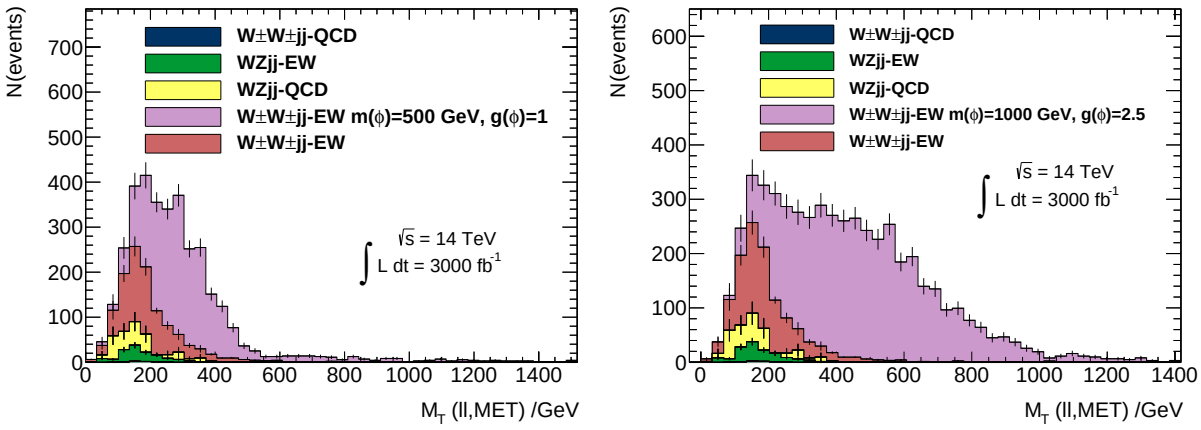

(a) $m_\Phi = 500\,\text{GeV}$, $g = 1.0$ (b) $m_\Phi = 1000\,\text{GeV}$, $g = 2.5$

Figure E.4: Distribution of $M_T(\ell\ell, E_{\text{T}}^{\text{miss}})$ in the $\ell^\pm\nu\ell^\pm\nu jj$ final state with the ATLAS detector with nominal tracking detector extension. A Φ resonance with two different mass and coupling configurations is shown as signal.

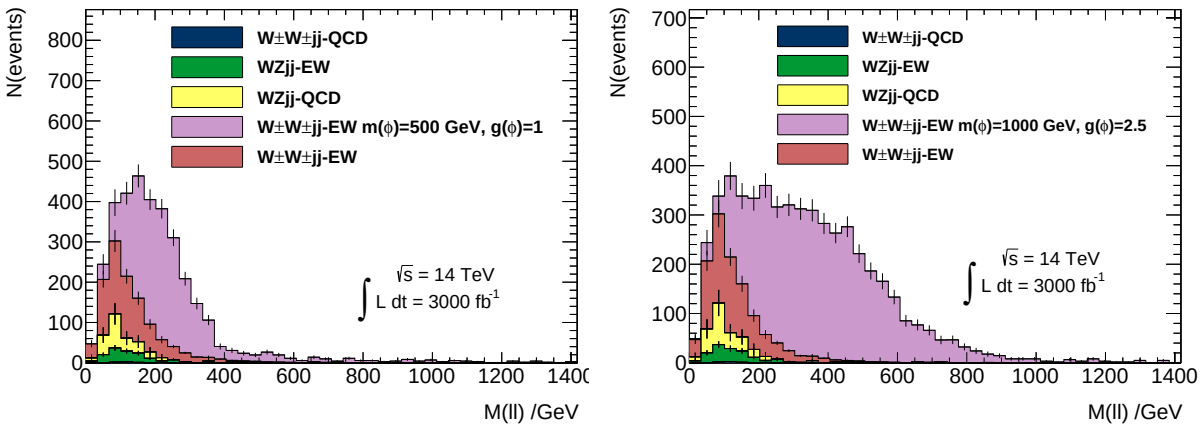

(a) $m_\Phi = 500\,\text{GeV}$, $g = 1.0$ (b) $m_\Phi = 1000\,\text{GeV}$, $g = 2.5$

Figure E.5: Distribution of $M(\ell\ell)$ in the $\ell^\pm\nu\ell^\pm\nu jj$ final state with the ATLAS detector with nominal tracking detector extension. A Φ resonance with two different mass and coupling configurations is shown as signal.

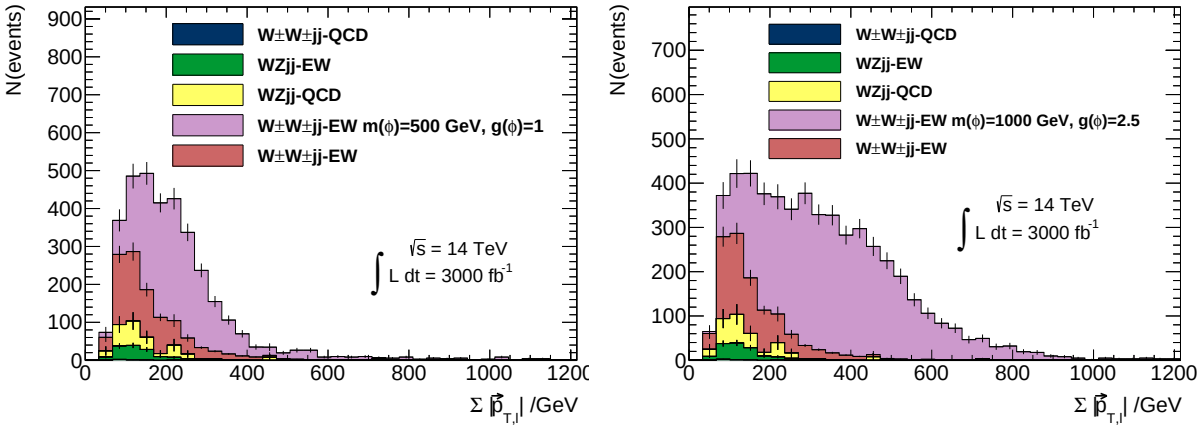

(a) $m_\Phi = 500\,\text{GeV}$, $g = 1.0$ (b) $m_\Phi = 1000\,\text{GeV}$, $g = 2.5$

Figure E.6: Distribution of the sum of the absolute values of lepton transverse momenta, $\Sigma|\vec{p}_{T,\ell}|$, in the $\ell^\pm\nu\ell^\pm\nu jj$ final state with the ATLAS detector with nominal tracking detector extension. A Φ resonance with two different mass and coupling configurations is shown as signal.

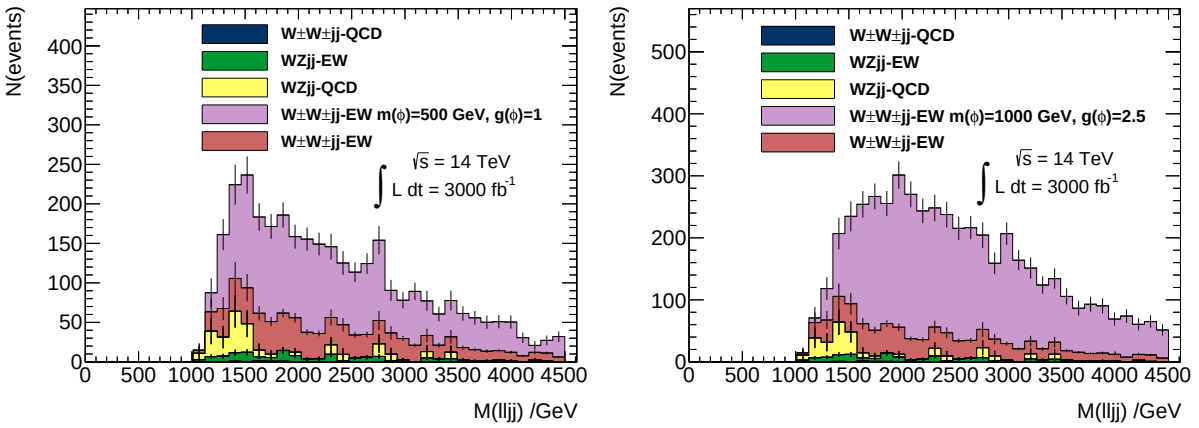

(a) $m_\Phi = 500\,\text{GeV}$, $g = 1.0$ (b) $m_\Phi = 1000\,\text{GeV}$, $g = 2.5$

Figure E.7: Distribution of the invariant mass of jets and leptons, $M(\ell\ell jj)$, in the $\ell^\pm\nu\ell^\pm\nu jj$ final state with the ATLAS detector with nominal tracking detector extension. A Φ resonance with two different mass and coupling configurations is shown as signal.

Bibliography

[1] *ROOT*, URL: root.cern.ch.

[2] *RIVET*, URL: http://rivet.hepforge.org.

[3] *SFRAME*, URL: http://sourceforge.net/projects/sframe/.

[4] *GNUPLOT*, URL: http://gnuplot.info.

[5] *LATEX*, URL: latex-project.org.

[6] *EMACS*, URL: www.gnu.org/software/emacs/.

[7] ATLAS Collaboration, "Observation of a new particle in the search for the Standard Model Higgs boson with the ATLAS detector at the LHC", *Phys.Lett.* B716 (2012) pp. 1–29, DOI: 10.1016/j.physletb.2012.08.020, arXiv: 1207.7214 [hep-ex], URL: http://www.sciencedirect.com/science/article/pii/S037026931200857X.

[8] S. Chatrchyan et al., "Observation of a new boson at a mass of 125 GeV with the CMS experiment at the LHC", *Phys.Lett.* B716 (2012) pp. 30–61, DOI: 10.1016/j.physletb.2012.08.021, arXiv: 1207.7235 [hep-ex].

[9] P. W. Higgs, "Broken symmetries, massless particles and gauge fields", *Phys.Lett.* 12 (1964) pp. 132–133, DOI: 10.1016/0031-9163(64)91136-9.

[10] F. Englert and R. Brout, "Broken Symmetry and the Mass of Gauge Vector Mesons", *Phys.Rev.Lett.* 13 (1964) pp. 321–323, DOI: 10.1103/PhysRevLett.13.321.

[11] S. Glashow, "Partial Symmetries of Weak Interactions", *Nucl.Phys.* 22 (1961) pp. 579–588, DOI: 10.1016/0029-5582(61)90469-2.

[12] LEP TGC Working Group (ALEPH, DELPHI, L3, OPAL), *A Combination of Preliminary Results on Gauge Boson Couplings Measured by the LEP Experiments*, LEPEWWG/TGC/2003-01(2003), 2004, URL: http://lepewwg.web.cern.ch/LEPEWWG/lepww/tgc.

[13] P. Achard et al., "Study of the $e^+e^- \to Z\gamma$ process at LEP and limits on triple neutral-gauge-boson couplings", *Phys.Lett.* B597 (2004) pp. 119–130, DOI: 10.1016/j.physletb.2004.07.002, arXiv: hep-ex/0407012 [hep-ex].

[14] P. Achard et al., "Measurement of triple gauge boson couplings of the W boson at LEP", *Phys.Lett.* B586 (2004) pp. 151–166, DOI: 10.1016/j.physletb.2004.02.045, arXiv: hep-ex/0402036 [hep-ex].

[15] P. Achard et al., "Study of the $W^+W^-\gamma$ process and limits on anomalous quartic gauge boson couplings at LEP", *Phys.Lett.* B527 (2002) pp. 29–38, DOI: 10.1016/S0370-2693(02)01167-X, arXiv: hep-ex/0111029 [hep-ex].

[16] G. Abbiendi et al., "Constraints on anomalous quartic gauge boson couplings from nu anti-nu gamma gamma and q anti-q gamma gamma events at LEP-2", *Phys.Rev.* D70 (2004) p. 032005, DOI: 10.1103/PhysRevD.70.032005, arXiv: hep-ex/0402021 [hep-ex].

[17] M. Veltman, "Second Threshold in Weak Interactions", *Acta Phys.Polon.* B8 (1977) p. 475.

[18] B. W. Lee, C. Quigg, and H. Thacker, "Weak Interactions at Very High-Energies: The Role of the Higgs Boson Mass", *Phys.Rev.* D16 (1977) p. 1519, DOI: 10.1103/PhysRevD.16.1519.

[19] J. Butterworth, B. Cox, and J. R. Forshaw, "WW scattering at the CERN LHC", *Phys.Rev.* D65 (2002) p. 096014, DOI: 10.1103/PhysRevD.65.096014, arXiv: hep-ph/0201098 [hep-ph].

[20] J. Schumacher, M. Kobel, and N. Wermes, "Sensitivity of ATLAS to Alternative Mechanisms of Electroweak Symmetry Breaking in Vector Boson Scattering $qq \to qql\nu l\nu$", Presented on 27 Sep 2010, PhD thesis: Bonn U., 2010.

[21] F. Halzen and A. Martin, *Quarks & Leptons: An introductory course in modern particle physics*, New York, USA: John Wiley & Sons, 1984.

[22] D. Griffiths, *Introduction to Elementary Particles*, New York, USA: John Wiley & Sons, 1987.

[23] M. E. Peskin and D. V. Schroeder, *An Introduction to Quantum Field Theory (Frontiers in Physics)*, Perseus Books, 2008, ISBN: 0201503972.

[24] E. Noether, "Invariant Variation Problems", *Gott.Nachr.* 1918 (1918) pp. 235–257, DOI: 10.1080/00411457108231446, arXiv: physics/0503066 [physics].

[25] J. Schwinger, "Quantum Electrodynamics. I. A Covariant Formulation", *Phys. Rev.* 74 (10 Nov. 1948) pp. 1439–1461, DOI: 10.1103/PhysRev.74.1439, URL: http://link.aps.org/doi/10.1103/PhysRev.74.1439.

[26] R. P. Feynman, "Space-Time Approach to Non-Relativistic Quantum Mechanics", *Rev. Mod. Phys.* 20 (2 Apr. 1948) pp. 367–387, DOI: 10.1103/RevModPhys.20.367, URL: http://link.aps.org/doi/10.1103/RevModPhys.20.367.

[27] J. Schwinger, "Quantum Electrodynamics. III. The Electromagnetic Properties of the Electron: Radiative Corrections to Scattering", *Phys. Rev.* 76 (6 Sept. 1949) pp. 790–817, DOI: 10.1103/PhysRev.76.790, URL: http://link.aps.org/doi/10.1103/PhysRev.76.790.

[28] R. P. Feynman, "A Relativistic Cut-Off for Classical Electrodynamics", *Phys. Rev.* 74 (8 Oct. 1948) pp. 939–946, DOI: 10.1103/PhysRev.74.939, URL: http://link.aps.org/doi/10.1103/PhysRev.74.939.

[29] E. Fermi, "An attempt of a theory of beta radiation. 1.", *Z.Phys.* 88 (1934) pp. 161–177, DOI: 10.1007/BF01351864.

[30] G. Münster and G. Bergner, *Gauge Theories of the Strong and Electroweak Interactions*, URL: http://pauli.uni-muenster.de/tp/fileadmin/lehre/skripte/muenster/Gauge-theories.pdf (visited on 10/26/2014).

[31] S. Weinberg, "A Model of Leptons", *Phys. Rev. Lett.* 19 (21 Nov. 1967) pp. 1264–1266, DOI: 10.1103/PhysRevLett.19.1264, URL: http://link.aps.org/doi/10.1103/PhysRevLett.19.1264.

[32] A. Salam, "Weak and Electromagnetic Interactions", *Conf.Proc.* C680519 (1968) pp. 367–377.

[33] D. J. Gross and F. Wilczek, "Ultraviolet Behavior of Nonabelian Gauge Theories", *Phys.Rev.Lett.* 30 (1973) pp. 1343–1346, DOI: 10.1103/PhysRevLett.30.1343.

[34] H. D. Politzer, "Reliable Perturbative Results for Strong Interactions?", *Phys.Rev.Lett.* 30 (1973) pp. 1346–1349, DOI: 10.1103/PhysRevLett.30.1346.

[35] A. Hebecker, Lecture at the Autumn Blockkurs 2013, Graduiertenkolleg Masse-Spektrum-Symmetry, URL: https://indico.desy.de/getFile.py/access?contribId=2&resId=0&materialId=slides&confId=8574.

[36] J. Wess and B. Zumino, "Supergauge transformations in four dimensions", *Nuclear Physics B* 70.1 (1974) pp. 39–50, ISSN: 0550-3213, DOI: http://dx.doi.org/10.1016/0550-3213(74)90355-1, URL: http://www.sciencedirect.com/science/article/pii/0550321374903551.

[37] R. Peccei and H. R. Quinn, "Constraints Imposed by CP Conservation in the Presence of Instantons", *Phys.Rev.* D16 (1977) pp. 1791–1797, DOI: 10.1103/PhysRevD.16.1791.

[38] L. Susskind, "Dynamics of Spontaneous Symmetry Breaking in the Weinberg-Salam Theory", *Phys.Rev.* D20 (1979) pp. 2619–2625, DOI: 10.1103/PhysRevD.20.2619.

[39] S. Weinberg, "Implications of Dynamical Symmetry Breaking", *Phys.Rev.* D13 (1976) pp. 974–996, DOI: 10.1103/PhysRevD.13.974.

[40] L. Randall and R. Sundrum, "A Large mass hierarchy from a small extra dimension", *Phys.Rev.Lett.* 83 (1999) pp. 3370–3373, DOI: 10.1103/PhysRevLett.83.3370, arXiv: hep-ph/9905221 [hep-ph].

[41] N. Arkani-Hamed, A. G. Cohen, and H. Georgi,
"Electroweak symmetry breaking from dimensional deconstruction",
Phys.Lett. B513 (2001) pp. 232–240, DOI: 10.1016/S0370-2693(01)00741-9,
arXiv: hep-ph/0105239 [hep-ph].

[42] *ATLAS Supersymmetry public results*, URL:
https://twiki.cern.ch/twiki/bin/view/AtlasPublic/SupersymmetryPublicResults.

[43] S. Dawson and S. Willenbrock,
"Radiative corrections to longitudinal vector boson scattering", *Phys.Rev.* D40 (1989) p. 2880,
DOI: 10.1103/PhysRevD.40.2880.

[44] J. Reuter, W. Kilian, and M. Sekulla,
"Simplified Models for New Physics in Vector Boson Scattering - Input for Snowmass 2013"
(2013), arXiv: 1307.8170 [hep-ph].

[45] D. A. Dicus and V. S. Mathur,
"Upper Bounds on the Values of Masses in Unified Gauge Theories",
Phys. Rev. D 7 (10 May 1973) pp. 3111–3114, DOI: 10.1103/PhysRevD.7.3111,
URL: http://link.aps.org/doi/10.1103/PhysRevD.7.3111.

[46] M. Lemoine and M. Veltman,
"Radiative corrections to $e^+e^- \to W^+W^-$ in the Weinberg model",
Nuclear Physics B 164 (1980) pp. 445–483, ISSN: 0550-3213,
DOI: http://dx.doi.org/10.1016/0550-3213(80)90521-0,
URL: http://www.sciencedirect.com/science/article/pii/0550321380905210.

[47] M. S. Chanowitz and M. K. Gaillard, "The TeV Physics of Strongly Interacting W's and Z's",
Nucl.Phys. B261 (1985) p. 379, DOI: 10.1016/0550-3213(85)90580-2.

[48] M. S. Chanowitz and M. Golden,
"Like-Charged Gauge-Boson Pairs as a Probe of Electroweak Symmetry Breaking",
Phys. Rev. Lett. 61 (9 Aug. 1988) pp. 1053–1056, DOI: 10.1103/PhysRevLett.61.1053,
URL: http://link.aps.org/doi/10.1103/PhysRevLett.61.1053.

[49] G. L. Kane and C.-P. Yuan, "How to study longitudinal W's in the TeV region",
Phys. Rev. D 40 (7 Oct. 1989) pp. 2231–2244, DOI: 10.1103/PhysRevD.40.2231,
URL: http://link.aps.org/doi/10.1103/PhysRevD.40.2231.

[50] V. D. Barger et al., "Strong W^+W^+ scattering signals at pp supercolliders",
Phys.Rev. D42 (1990) pp. 3052–3077, DOI: 10.1103/PhysRevD.42.3052.

[51] R. N. Cahn et al., "Transverse Momentum Signatures for Heavy Higgs Bosons",
Phys.Rev. D35 (1987) p. 1626, DOI: 10.1103/PhysRevD.35.1626.

[52] D. L. Rainwater and D. Zeppenfeld, "Observing $H \to W^{(*)}W^{(*)} \to e^{\pm}mu^{\mp}p_T$ in weak boson fusion with dual forward jet tagging at the LHC", *Phys. Rev. D* 60.hep-ph/9906218. MAD-PH-1112. 11 (June 1999) 113004/1–10. 12 p.

[53] G. L. Kane, W. Repko, and W. Rolnick, "The Effective W+-, Z0 Approximation for High-Energy Collisions", *Phys.Lett.* B148 (1984) pp. 367–372, DOI: 10.1016/0370-2693(84)90105-9.

[54] S. Dawson, "The Effective W Approximation", *Nucl.Phys.* B249 (1985) pp. 42–60, DOI: 10.1016/0550-3213(85)90038-0.

[55] C. Englert et al., "Observing Strongly Interacting Vector Boson Systems at the CERN Large Hadron Collider", *Phys.Rev.* D80 (2009) p. 035027, DOI: 10.1103/PhysRevD.80.035027, arXiv: 0810.4861 [hep-ph].

[56] ATLAS Collaboration, "Evidence for Electroweak Production of $W^{\pm}W^{\pm}jj$ in pp Collisions at $\sqrt{s} = 8$ TeV with the ATLAS Detector", *Phys. Rev. Lett.* 113 (14 Oct. 2014) p. 141803, DOI: 10.1103/PhysRevLett.113.141803, arXiv: 1405.6241 [hep-ex], URL: http://link.aps.org/doi/10.1103/PhysRevLett.113.141803.

[57] ATLAS Collaboration, "Measurement of the $WW + WZ$ cross section and limits on anomalous triple gauge couplings using final states with one lepton, missing transverse momentum, and two jets with the ATLAS detector at $\sqrt{s} = 7$ TeV" (2014), arXiv: 1410.7238 [hep-ex].

[58] "Measurement of the electroweak production of dijets in association with a Z-boson and distributions sensitive to vector boson fusion in proton-proton collisions at $\sqrt{s}$ = 8 TeV using the ATLAS detector", *J. High Energy Phys.* 04.arXiv:1401.7610. CERN-PH-EP-2013-227 (Jan. 2014), https://atlas.web.cern.ch/Atlas/GROUPS/PHYSICS/PAPERS/STDM-2013-02/ 031. 42 p.

[59] S. D. Rindani, "Strong gauge boson scattering at the LHC" (2009), arXiv: 0910.5068 [hep-ph].

[60] G. van den Oord, "Recursion, Monte Carlo and Vector Boson Scattering at Hadron Colliders", PhD thesis: Radboud Universiteit Nijmegen, 2012.

[61] B. Holdom, "The accidental Higgs", *Phys.Rev.* D90 (2014) p. 015004, DOI: 10.1103/PhysRevD.90.015004, arXiv: 1404.6229 [hep-ph].

[62] A. Belyaev et al., "The Technicolor Higgs in the Light of LHC Data" (2013), arXiv: 1309.2097 [hep-ph].

[63] T. Alanne, S. Di Chiara, and K. Tuominen, "LHC Data and Aspects of New Physics", *JHEP* 1401 (2014) p. 041, DOI: 10.1007/JHEP01(2014)041, arXiv: 1303.3615 [hep-ph].

[64] M. Carena, L. Da Rold, and E. Pontón, "Minimal Composite Higgs Models at the LHC", *JHEP* 1406 (2014) p. 159, DOI: 10.1007/JHEP06(2014)159, arXiv: 1402.2987 [hep-ph].

[65] D. Lopez-Val and T. Robens,
"Delta r and the W-boson mass in the Singlet Extension of the Standard Model" (2014),
arXiv: 1406.1043 [hep-ph].

[66] A. Broggio et al., "Limiting two-Higgs-doublet models" (2014), arXiv: 1409.3199 [hep-ph].

[67] C. Degrande et al., "Monte Carlo tools for studies of non-standard electroweak gauge boson interactions in multi-boson processes: A Snowmass White Paper" (2013),
arXiv: 1309.7890 [hep-ph].

[68] V. Koch, "Aspects of chiral symmetry", *Int.J.Mod.Phys.* E6 (1997) pp. 203–250,
DOI: 10.1142/S0218301397000147, arXiv: nucl-th/9706075 [nucl-th].

[69] J. Gasser and H. Leutwyler, "Chiral perturbation theory to one loop",
Annals of Physics 158.1 (1984) pp. 142–210.

[70] A. PICH ZARDOYA, *Effective field theory*,
Lecture at the Autumn Blockkurs 2014, Graduiertenkolleg Masse-Spektrum-Symmetry,
URL: https://indico.desy.de/contributionDisplay.py?contribId=0&confId=10715.

[71] T. Appelquist and C. W. Bernard, "Strongly Interacting Higgs Bosons",
Phys.Rev. D22 (1980) p. 200, DOI: 10.1103/PhysRevD.22.200.

[72] A. C. Longhitano, "Heavy Higgs Bosons in the Weinberg-Salam Model",
Phys.Rev. D22 (1980) p. 1166, DOI: 10.1103/PhysRevD.22.1166.

[73] A. Alboteanu, W. Kilian, and J. Reuter,
"Resonances and Unitarity in Weak Boson Scattering at the LHC", *JHEP* 0811 (2008) p. 010,
DOI: 10.1088/1126-6708/2008/11/010, arXiv: 0806.4145 [hep-ph].

[74] W. Kilian, *Electroweak Symmetry Breaking, The bottom-Up Approach*,
Springer Tracts in Modern Physics, Volume 198, 2003, ISBN: 0-387-40097-4.

[75] D. Reichelt, *Studien zur Überprüfung der vorhergesagten Beziehung zwischen effektiven aQGC Parametern und expliziten Resonanzen*, 2014,
URL: http://iktp.tu-dresden.de/IKTP/pub/14/BA_main_german.pdf.

[76] O. Eboli, M. Gonzalez-Garcia, and J. Mizukoshi, "$pp \to jje^{\pm}\mu^{\pm}\nu\nu$ and $jje^{\pm}\mu^{\mp}\nu\nu$ at $\mathcal{O}(\alpha_{\rm em}^6)$ and $\mathcal{O}(\alpha_{\rm em}^4\alpha_s^2)$ for the study of the quartic electroweak gauge boson vertex at LHC",
Phys.Rev. D74 (2006) p. 073005, DOI: 10.1103/PhysRevD.74.073005,
arXiv: hep-ph/0606118 [hep-ph].

[77] U. Schnoor and A. Vest, *Generator level studies on anomalous quartic gauge couplings*,
Working Group on Electroweak Precision Measurements at the LHC, Apr. 16, 2013,
URL: http://indico.cern.ch/event/245037/session/1/material/slides/0?contribId=23.

[78] E. P. Wigner, "Resonance Reactions and Anomalous Scattering",
Phys.Rev. 70 (1946) pp. 15–33, DOI: 10.1103/PhysRev.70.15.

[79] O. Schlimpert, "Anomale Kopplungen bei der Streuung schwacher Eichbosonen", MA thesis: Karlsruher Institut für Technologie, 2013, URL: http://www.itp.kit.edu/prep/diploma/PSFiles/Diplom_Schlimpert.pdf.

[80] G. Bélanger and F. Boudjema, "Probing quartic couplings of weak bosons through three vector production at a 500 GeV NLC", *Physics Letters B* 288.1–2 (1992) pp. 201–209, ISSN: 0370-2693, DOI: http://dx.doi.org/10.1016/0370-2693(92)91978-I, URL: http://www.sciencedirect.com/science/article/pii/037026939291978I.

[81] V. M. Abazov et al., "Search for anomalous quartic $WW\gamma\gamma$ couplings in dielectron and missing energy final states in $p\bar{p}$ collisions at $\sqrt{s}$ = 1.96 TeV", *Phys.Rev.* D88 (2013) p. 012005, DOI: 10.1103/PhysRevD.88.012005, arXiv: 1305.1258 [hep-ex].

[82] S. Chatrchyan et al., "Study of exclusive two-photon production of W^+W^- in pp collisions at $\sqrt{s} = 7$ TeV and constraints on anomalous quartic gauge couplings", *JHEP* 1307 (2013) p. 116, DOI: 10.1007/JHEP07(2013)116, arXiv: 1305.5596 [hep-ex].

[83] CMS Collaboration, "A search for WWγ and WZγ production and constraints on anomalous quartic gauge couplings in pp collisions at $\sqrt{s}$ = 8 TeV", *Phys. Rev. D* 90.arXiv:1404.4619. CMS-SMP-13-009. CERN-PH-EP-2014-046 (Apr. 2014), Comments: Submitted to Phys. Rev. D 032008. 33 p.

[84] P. Anger, M. Kobel, and S. Lammers, "Probing Electroweak Gauge Boson Scattering with the ATLAS Detector at the Large Hadron Collider", Presented 01 Sep 2014, PhD thesis: Dresden, Tech. U., June 2014.

[85] T. Sandmann, *Constraints on Anomalous Quartic Gauge Couplings in the Electroweak Gauge Boson Scattering WZjj Final State with the ATLAS Detector*, 2012, URL: http://iktp.tu-dresden.de/IKTP/pub/14/Diplomarbeit_TSandmann.pdf.

[86] J. Beringer et al., *Review of Particle Physics (RPP)*, 2012, DOI: 10.1103/PhysRevD.86.010001, Chapter 37. Monte Carlo techniques.

[87] J. Beringer et al., *Review of Particle Physics (RPP)*, 2012, DOI: 10.1103/PhysRevD.86.010001, Chapter 38. Monte Carlo Event generators.

[88] M. Dobbs et al., "Les Houches guidebook to Monte Carlo generators for hadron collider physics" (2004) pp. 411–459, arXiv: hep-ph/0403045 [hep-ph].

[89] A. Buckley et al., "General-purpose event generators for LHC physics", *arXiv:1101.2599 [hep-ex, physics:hep-ph]* (Jan. 2011), URL: http://arxiv.org/abs/1101.2599 (visited on 01/23/2014).

[90] R. Brock et al., "Handbook of perturbative QCD; Version 1.1: September 1994", *Rev. Mod. Phys.* (1994).

[91] J. Beringer et al., *Review of Particle Physics (RPP)*, 2012, DOI: 10.1103/PhysRevD.86.010001, Chapter 9. Quantum Chromodynamics.

[92] J. C. Collins, D. E. Soper, and G. F. Sterman, "Factorization of Hard Processes in QCD", *Adv.Ser.Direct.High Energy Phys.* 5 (1988) pp. 1–91, arXiv: hep-ph/0409313 [hep-ph].

[93] G. Altarelli and G. Parisi, "Asymptotic freedom in parton language", *Nuclear Physics B* 126.2 (1977) pp. 298–318, ISSN: 0550-3213, DOI: http://dx.doi.org/10.1016/0550-3213(77)90384-4, URL: http://www.sciencedirect.com/science/article/pii/0550321377903844.

[94] V. Gribov and L. Lipatov, "Deep inelastic e p scattering in perturbation theory", *Sov.J.Nucl.Phys.* 15 (1972) pp. 438–450.

[95] Y. L. Dokshitzer, "Calculation of the Structure Functions for Deep Inelastic Scattering and e+ e- Annihilation by Perturbation Theory in Quantum Chromodynamics.", *Sov.Phys.JETP* 46 (1977) pp. 641–653.

[96] J. Winter et al., URL: http://www.isgtw.org/feature/sherpa-and-open-science-grid-predicting-emergence-jets (visited on 09/23/2014).

[97] V. Sudakov, "Vertex parts at very high-energies in quantum electrodynamics", *Sov.Phys.JETP* 3 (1956) pp. 65–71.

[98] B. Webber, *Parton shower Monte Carlo event generators*, URL: http://www.scholarpedia.org/article/Parton_shower_Monte_Carlo_event_generators (visited on 09/10/2014).

[99] S. Catani et al., "QCD matrix elements + parton showers", *JHEP* 0111 (2001) p. 063, DOI: 10.1088/1126-6708/2001/11/063, arXiv: hep-ph/0109231 [hep-ph].

[100] D. Yennie, S. C. Frautschi, and H. Suura, "The infrared divergence phenomena and high-energy processes", *Annals Phys.* 13 (1961) pp. 379–452, DOI: 10.1016/0003-4916(61)90151-8.

[101] ATLAS Collaboration, "Measurement of hard double-parton interactions in $W(\to l\nu)$+ 2 jet events at $\sqrt{s}$=7 TeV with the ATLAS detector", *New J.Phys.* 15 (2013) p. 033038, DOI: 10.1088/1367-2630/15/3/033038, arXiv: 1301.6872 [hep-ex].

[102] T. Gleisberg et al., "Event generation with SHERPA 1.1", *JHEP* 0902 (2009) p. 007, DOI: 10.1088/1126-6708/2009/02/007, arXiv: 0811.4622 [hep-ph].

[103] T. Sjostrand, S. Mrenna, and P. Z. Skands, "A Brief Introduction to PYTHIA 8.1", *Comput.Phys.Commun.* 178 (2008) pp. 852–867, DOI: 10.1016/j.cpc.2008.01.036, arXiv: 0710.3820 [hep-ph].

[104] T. Sjostrand, S. Mrenna, and P. Z. Skands, "PYTHIA 6.4 Physics and Manual", *JHEP* 0605 (2006) p. 026, DOI: 10.1088/1126-6708/2006/05/026, arXiv: hep-ph/0603175 [hep-ph].

[105] S. Gieseke, P. Stephens, and B. Webber, "New formalism for QCD parton showers", *JHEP* 0312 (2003) p. 045, DOI: 10.1088/1126-6708/2003/12/045, arXiv: hep-ph/0310083 [hep-ph].

[106] J. Alwall et al., "The automated computation of tree-level and next-to-leading order differential cross sections, and their matching to parton shower simulations" (2014), arXiv: 1405.0301 [hep-ph].

[107] W. Kilian, T. Ohl, and J. Reuter, "WHIZARD: Simulating Multi-Particle Processes at LHC and ILC", *Eur.Phys.J.* C71 (2011) p. 1742, DOI: 10.1140/epjc/s10052-011-1742-y, arXiv: 0708.4233 [hep-ph].

[108] M. Moretti, T. Ohl, and J. Reuter, "O'Mega: An Optimizing matrix element generator" (2001), arXiv: hep-ph/0102195 [hep-ph].

[109] *Tauola*, URL: http://tauolapp.web.cern.ch/tauolapp/ (visited on 09/12/2014).

[110] E. Barberio, B. van Eijk, and Z. Was, "PHOTOS: A Universal Monte Carlo for QED radiative corrections in decays", *Comput.Phys.Commun.* 66 (1991) pp. 115–128, DOI: 10.1016/0010-4655(91)90012-A.

[111] K. Arnold et al., "VBFNLO: A Parton level Monte Carlo for processes with electroweak bosons", *Comput.Phys.Commun.* 180 (2009) pp. 1661–1670, DOI: 10.1016/j.cpc.2009.03.006, arXiv: 0811.4559 [hep-ph].

[112] S. Alioli et al., "A general framework for implementing NLO calculations in shower Monte Carlo programs: the POWHEG BOX", *JHEP* 1006 (2010) p. 043, DOI: 10.1007/JHEP06(2010)043, arXiv: 1002.2581 [hep-ph].

[113] ATLAS Collaboration, "The ATLAS Simulation Infrastructure", *Eur.Phys.J.* C70 (2010) pp. 823–874, DOI: 10.1140/epjc/s10052-010-1429-9, arXiv: 1005.4568 [physics.ins-det].

[114] M. Dobbs and J. B. Hansen, "The HepMC C++ Monte Carlo event record for High Energy Physics", *Comput.Phys.Commun.* 134 (2001) pp. 41–46, DOI: 10.1016/S0010-4655(00)00189-2.

[115] K. Hagiwara et al., "$(g-2)_\mu$ and $\alpha(M_Z^2)$ re-evaluated using new precise data", *J.Phys.* G38 (2011) p. 085003, DOI: 10.1088/0954-3899/38/8/085003, arXiv: 1105.3149 [hep-ph].

[116] J. Beringer et al., *Review of Particle Physics (RPP)*, 2012, DOI: 10.1103/PhysRevD.86.010001, Chapter 1. Physical Constants.

[117] S. Dittmaier and M. Kramer,
"Electroweak radiative corrections to W boson production at hadron colliders",
Phys.Rev. D65 (2002) p. 073007, DOI: 10.1103/PhysRevD.65.073007,
arXiv: hep-ph/0109062 [hep-ph].

[118] A. Denner et al., "Standard Model Higgs-Boson Branching Ratios with Uncertainties",
Eur.Phys.J. C71 (2011) p. 1753, DOI: 10.1140/epjc/s10052-011-1753-8,
arXiv: 1107.5909 [hep-ph].

[119] T. Melia et al., "W^+W^+ plus dijet production in the POWHEGBOX",
Eur.Phys.J. C71 (2011) p. 1670, DOI: 10.1140/epjc/s10052-011-1670-x,
arXiv: 1102.4846 [hep-ph].

[120] F. Campanario et al., "Next-to-leading order QCD corrections to W^+W^+ and W^-W^- production in association with two jets", *Phys.Rev.* D89 (2014) p. 054009,
DOI: 10.1103/PhysRevD.89.054009, arXiv: 1311.6738 [hep-ph].

[121] Z. Liang,
URL: https://indico.cern.ch/event/293542/contribution/5/material/slides/1.pdf
(visited on 09/26/2014).

[122] CMS Collaboration,
"Vector boson scattering in a final state with two jets and two same-sign leptons",
tech. rep. CMS-PAS-SMP-13-015, CERN, 2014.

[123] P. Anger et al., "A Measurement of WZ Production in Proton-Proton Collisions at $\sqrt{s} = 8$ TeV with the ATLAS Detector", tech. rep. ATL-COM-PHYS-2014-144, CERN, Feb. 2014.

[124] M. Sekulla, Private Communications, 2014.

[125] T. Melia et al.,
"Next-to-leading order QCD predictions for W^+W^+jj production at the LHC",
JHEP 1012 (2010) p. 053, DOI: 10.1007/JHEP12(2010)053, arXiv: 1007.5313 [hep-ph].

[126] B. Jager, C. Oleari, and D. Zeppenfeld, "Next-to-leading order QCD corrections to W+ W+ jj and W- W- jj production via weak-boson fusion", *Phys.Rev.* D80 (2009) p. 034022,
DOI: 10.1103/PhysRevD.80.034022, arXiv: 0907.0580 [hep-ph].

[127] A. Denner, L. Hosekova, and S. Kallweit,
"NLO QCD corrections to W+ W+ jj production in vector-boson fusion at the LHC",
Phys.Rev. D86 (2012) p. 114014, DOI: 10.1103/PhysRevD.86.114014,
arXiv: 1209.2389 [hep-ph].

[128] M. Billoni et al., "Next-to-leading order electroweak corrections to $pp \to W + W- \to 4$ leptons at the LHC in double-pole approximation", *JHEP* 1312 (2013) p. 043,
DOI: 10.1007/JHEP12(2013)043, arXiv: 1310.1564 [hep-ph].

[129] S. Gieseke, T. Kasprzik, and J. H. Kühn,
"Vector-boson pair production and electroweak corrections in HERWIG++",
Eur.Phys.J. C74.8 (2014) p. 2988, DOI: 10.1140/epjc/s10052-014-2988-y,
arXiv: 1401.3964 [hep-ph].

[130] S. Dittmaier, *Talk at IKTP Dresden*,
URL: http://iktp.tu-dresden.de/IKTP/Seminare/IS2012/dittmaier.pdf.

[131] E. Accomando, A. Denner, and S. Pozzorini,
"Logarithmic electroweak corrections to $e + e- \to \nu_e \bar{\nu}_e W + W-$", *JHEP* 0703 (2007) p. 078,
DOI: 10.1088/1126-6708/2007/03/078, arXiv: hep-ph/0611289 [hep-ph].

[132] W. Kilian, T. Ohl, and J. Reuter,
"WHIZARD: Simulating Multi-Particle Processes at LHC and ILC",
Eur.Phys.J. C71 (2011) p. 1742, DOI: 10.1140/epjc/s10052-011-1742-y,
arXiv: 0708.4233 [hep-ph].

[133] T. Ohl, "Vegas revisited: Adaptive Monte Carlo integration beyond factorization",
Comput.Phys.Commun. 120 (1999) pp. 13–19, DOI: 10.1016/S0010-4655(99)00209-X,
arXiv: hep-ph/9806432 [hep-ph].

[134] W. Kilian et al., "An Analytic Initial-State Parton Shower", *JHEP* 1204 (2012) p. 013,
DOI: 10.1007/JHEP04(2012)013, arXiv: 1112.1039 [hep-ph].

[135] S. Frixione, P. Nason, and C. Oleari,
"Matching NLO QCD computations with Parton Shower simulations: the POWHEG method",
JHEP 0711 (2007) p. 070, DOI: 10.1088/1126-6708/2007/11/070,
arXiv: 0709.2092 [hep-ph].

[136] S. Hoeche, S. Schumann, and F. Siegert,
"Hard photon production and matrix-element parton-shower merging",
Phys.Rev. D81 (2010) p. 034026, DOI: 10.1103/PhysRevD.81.034026,
arXiv: 0912.3501 [hep-ph].

[137] J. Pumplin et al.,
"New generation of parton distributions with uncertainties from global QCD analysis",
JHEP 0207 (2002) p. 012, DOI: 10.1088/1126-6708/2002/07/012,
arXiv: hep-ph/0201195 [hep-ph].

[138] N. Madysa, "Untersuchung differenzieller Verteilungen für die Streuung zweier Eichbosonen VV → VV am Large Hadron Collider", 2012,
URL: http://iktp.tu-dresden.de/IKTP/pub/12/madysa_bachelor_1.0.pdf.

[139] *Conventions in VBFNLO for Anomalous Quartic Gauge Boson Couplings*, URL:
http://www.itp.kit.edu/~vbfnloweb/wiki/doku.php?id=documentation:details:aqgc
(visited on 10/22/2014).

[140] *FeynRules: Anomalous quartic electroweak gauge-boson interactions*, URL: http://feynrules.irmp.ucl.ac.be/wiki/AnomalousGaugeCoupling (visited on 10/22/2014).

[141] Stefanie Todt, "Mass reconstruction for the search of new resonances in like-sign WW scattering", To be published.

[142] A. Badalian et al., "Resonances in Coupled Channels in Nuclear and Particle Physics", *Phys.Rept.* 82 (1982) p. 31, DOI: 10.1016/0370-1573(82)90014-X.

[143] C. Degrande, *EFT for electroweak bosons*, Talk at Institut für Kern- und Teilchenphysik, TU Dresden, June 26, 2014, URL: http://iktp.tu-dresden.de/IKTP/Seminare/IS2014/2014-06-26-Degrande.pdf (visited on 10/23/2014).

[144] *Form factors and unitarity bound*, URL: http://www.itp.kit.edu/~vbfnloweb/wiki/doku.php?id=download:formfactor.

[145] C. Bittrich, *Study of the Effects of Anomalous Quartic Gauge Couplings on the Scattering of Two Gauge Bosons $VV \to VV$ at the Large Hadron Collider*, 2012, URL: http://iktp.tu-dresden.de/IKTP/pub/12/Bachelorarbeit-Carsten-Bittrich.pdf.

[146] A. Melzer, *Vergleich unterschiedlicher Parametrisierungen anomaler Vier-Eichboson-Kopplungen in der Streuung zweier Eichbosonen $WZ \to WZ$ und gleich geladener $WW \to WW$ am Large Hadron Collider*, 2013, URL: http://iktp.tu-dresden.de/IKTP/pub/13/Bachelorarbeit_Alexander_Melzer.pdf.

[147] O. S. Bruning et al., "LHC Design Report. 1. The LHC Main Ring" (2004), ed. by O. S. Bruning.

[148] "LEP Design Report: Vol. 2. The LEP Main Ring" (1984).

[149] M. Benedikt et al., "LHC Design Report. 3. The LHC injector chain" (2004), ed. by M. Benedikt.

[150] M. Lamont, "Status of the LHC", *J.Phys.Conf.Ser.* 455 (2013) p. 012001, DOI: 10.1088/1742-6596/455/1/012001.

[151] ATLAS Collaboration, "The ATLAS Experiment at the CERN Large Hadron Collider", *Journal of Instrumentation* 3.08 (2008) S08003, URL: http://stacks.iop.org/1748-0221/3/i=08/a=S08003.

[152] J. Beringer et al., *Review of Particle Physics (RPP)*, vol. D86, 2012 p. 010001, DOI: 10.1103/PhysRevD.86.010001.

[153] C. W. Fabjan and F. Gianotti, "Calorimetry for Particle Physics", *Rev. Mod. Phys.* 75.CERN-EP-2003-075 (Oct. 2003) 1243–1286. 96 p.

[154] URL: https://svnweb.cern.ch/cern/wsvn/atlasoff/MuonSpectrometer/MuonValidation/MuonDQA/MuonRawDataMonitoring/RpcRawDataMonitoring/tags/RpcRawDataMonitoring-01-01-20/ (visited on 09/17/2014).

[155] ATLAS Collaboration, *ATLAS Computing: technical design report*, Technical Design Report ATLAS, Geneva: CERN, 2005.

[156] C. Eck et al., *LHC computing Grid: Technical Design Report. Version 1.06 (20 Jun 2005)*, Technical Design Report LCG, Geneva: CERN, 2005.

[157] ATLAS Collaboration, "Properties of Jets and Inputs to Jet Reconstruction and Calibration with the ATLAS Detector Using Proton-Proton Collisions at $\sqrt{s} = 7$ TeV", tech. rep. ATLAS-CONF-2010-053, CERN, July 2010.

[158] G. P. Salam, "Towards Jetography", *Eur.Phys.J.* C67 (2010) pp. 637–686, DOI: 10.1140/epjc/s10052-010-1314-6, arXiv: 0906.1833 [hep-ph].

[159] ATLAS Collaboration, "Jet energy measurement and its systematic uncertainty in proton-proton collisions at $\sqrt{s} = 7$ TeV with the ATLAS detector" (2014), arXiv: 1406.0076 [hep-ex].

[160] ATLAS Collaboration, "Electron performance measurements with the ATLAS detector using the 2010 LHC proton-proton collision data", *The European Physical Journal C* 72.3 (2012) pp. 1–46, ISSN: 1434-6044, DOI: 10.1140/epjc/s10052-012-1909-1, URL: http://dx.doi.org/10.1140/epjc/s10052-012-1909-1.

[161] C. Anastopoulos et al., "Supporting document on electron efficiency measurements using the 2012 LHC proton-proton collision data", tech. rep. ATL-COM-PHYS-2013-1295, CERN, Sept. 2013.

[162] *Electron Reconstruction (ATLAS twiki page)*, URL: https://twiki.cern.ch/twiki/bin/viewauth/AtlasProtected/ElectronReconstruction (visited on 09/02/2014).

[163] ATLAS Collaboration, *Expected Performance of the ATLAS Experiment - Detector, Trigger and Physics*, Geneva: CERN, 2009, arXiv: 0901.0512 [hep-ex].

[164] N. van Eldik, *Muon reconstruction in ATLAS*, Talk at Institut für Kern- und Teilchenphysik, TU Dresden, June 13, 2013, URL: http://iktp.tu-dresden.de/IKTP/Seminare/IS2012/eldik.pdf (visited on 11/23/2014).

[165] S. Hassani et al., "A muon identification and combined reconstruction procedure for the ATLAS detector at the LHC using the (MUONBOY, STACO, MuTag) reconstruction packages", *Nucl.Instrum.Meth.* A572 (2007) pp. 77–79, DOI: 10.1016/j.nima.2006.10.340.

[166] P. Bagnaia et al.,
"Calibration model for the MDT chambers of the ATLAS Muon Spectrometer",
tech. rep. ATL-MUON-PUB-2008-004. ATL-COM-MUON-2008-006,
backup paper for Atlas Detector paper: CERN, Feb. 2008.

[167] "Performance of Missing Transverse Momentum Reconstruction in ATLAS studied in Proton-Proton Collisions recorded in 2012 at 8 TeV", tech. rep. ATLAS-CONF-2013-082, CERN, Aug. 2013.

[168] *ATLAS Luminosity results (ATLAS twiki page)*,
URL: http://twiki.cern.ch/twiki/bin/view/AtlasPublic/LuminosityPublicResults (visited on 09/03/2014).

[169] ATLAS Collaboration, "Improved luminosity determination in pp collisions at $\sqrt{s}$ = 7 TeV using the ATLAS detector at the LHC", *Eur.Phys.J.* C73 (2013) p. 2518,
DOI: 10.1140/epjc/s10052-013-2518-3, arXiv: 1302.4393 [hep-ex].

[170] *Luminosity for physics (ATLAS twiki page)*,
URL: https://twiki.cern.ch/twiki/bin/viewauth/Atlas/LuminosityForPhysics#2012_8_TeV_Moriond_2013 (visited on 09/03/2014).

[171] T. Luminosity Group, "Preliminary Luminosity Determination in pp Collisions at $\sqrt{s}$ = 8 TeV using the ATLAS Detector in 2012", tech. rep. ATL-COM-LUM-2012-013, CERN, Nov. 2012.

[172] J.-B. Blanchard, J.-B. de Vivie, and P. Mastrandrea,
"In situ scales and smearings from Z and J/Ψ events", tech. rep. ATL-COM-PHYS-2013-1653, CERN, Dec. 2013.

[173] *Recommendations of the EGamma Group (ATLAS twiki page)*,
URL: https://twiki.cern.ch/twiki/bin/viewauth/AtlasProtected/EGammaCalibrationGEO20#2013_Set_1_Recommendations_Septe (visited on 09/01/2014).

[174] *ATLAS Egamma Quality Definitions (ATLAS twiki page)*, URL: https://twiki.cern.ch/twiki/bin/viewauth/AtlasProtected/TechnicalitiesForMedium1.

[175] S. Laplace and J. de Vivie, "Calorimeter isolation and pile-up",
tech. rep. ATL-COM-PHYS-2012-467, CERN, May 2012.

[176] ATLAS Collaboration, "Measurement of the inclusive isolated prompt photon cross section in pp collisions at $\sqrt{s}$ = 7 TeV with the ATLAS detector", *Phys.Rev.* D83 (2011) p. 052005,
DOI: 10.1103/PhysRevD.83.052005, arXiv: 1012.4389 [hep-ex].

[177] "A Muon identification and combined reconstruction procedure for the ATLAS detector at the LHC using (Muonboy, STACO, MuTag) reconstruction packages",
Nucl. Instrum. Methods 572.1 (2007) p. 77,
URL: http://dx.doi.org/10.1016/j.nima.2006.10.340.

[178] *ATLAS Muon Quality Definitions (ATLAS twiki page)*, URL: https://twiki.cern.ch/twiki/bin/view/AtlasProtected/MCPAnalysisGuidelinesData2012.

[179] *ATLAS Muon Track Recommendations (ATLAS twiki page)*, URL: https://twiki.cern.ch/twiki/bin/viewauth/AtlasProtected/MCPAnalysisGuidelinesData2012#Criteria_for_the_associated_inne (visited on 11/03/2014).

[180] M. Cacciari, G. P. Salam, and G. Soyez, "The anti-kt jet clustering algorithm", *JHEP* 04 (2008) p. 063, DOI: 10.1088/1126-6708/2008/04/063, arXiv: 0802.1189 [hep-ph].

[181] D. W. Miller, A. Schwartzman, and D. Su, "Jet-Vertex Association Algorithm", tech. rep. ATL-COM-PHYS-2008-008, CERN, Jan. 2008.

[182] *ATLAS heavy flavor tagging with MV1 algorithm (ATLAS twiki page)*, URL: https://twiki.cern.ch/twiki/bin/view/AtlasProtected/BTaggingMV1.

[183] "b-tagging in dense environments", tech. rep. ATL-PHYS-PUB-2014-014, CERN, Aug. 2014.

[184] Package tag: GoodRunsList-00-01-04, URL: http://atlasdqm.web.cern.ch/atlasdqm/grlgen/All_Good/data12_8TeV.periodAllYear_DetStatus-v61-pro14-02_DQDefects-00-01-00_PHYS_StandardGRL_All_Good.xml (visited on 11/03/2014).

[185] Package tag: egammaAnalysisUtils-00-04-57, URL: https://svnweb.cern.ch/trac/atlasoff/browser/Reconstruction/egamma/egammaAnalysis/egammaAnalysisUtils/tags/egammaAnalysisUtils-00-04-57/egammaAnalysisUtils/VertexPositionReweightingTool.h (visited on 11/05/2014).

[186] *ATLAS data preparation (ATLAS twiki page)*, URL: https://twiki.cern.ch/twiki/bin/viewauth/Atlas/DataPreparationCheckListForPhysicsAnalysis (visited on 11/05/2014).

[187] *ATLAS MET cleaning (ATLAS twiki page)*, URL: https://twiki.cern.ch/twiki/pub/AtlasProtected/HowToCleanJets2011/IsBadLooser.C (visited on 11/05/2014).

[188] *ATLAS trigger matching recommendations (ATLAS twiki page)*, URL: https://twiki.cern.ch/twiki/bin/viewauth/Atlas/TriggerObjectsMatching#Object_Distance (visited on 11/05/2014).

[189] *ATLAS trigger scale factors)*, URL: https://svnweb.cern.ch/trac/atlasoff/browser/Trigger/TrigAnalysis/TrigMuonEfficiency/tags/TrigMuonEfficiency-00-02-42/TrigMuonEfficiency/LeptonTriggerSF.h (visited on 11/05/2014).

[190] ATLAS Collaboration, "A measurement of the ATLAS muon reconstruction and trigger efficiency using J/psi decays", tech. rep. ATLAS-CONF-2011-021, CERN, Mar. 2011.

[191] P. Anger et al.,
"Same Sign $W^{\pm}W^{\pm}$ Production and Limits on Anomalous Quartic Gauge Couplings",
tech. rep. ATL-COM-PHYS-2013-990, CERN, July 2013.

[192] URL: https://indico.cern.ch/event/205773/material/slides/0?contribId=4
(visited on 11/12/2014).

[193] URL: https://twiki.cern.ch/twiki/pub/AtlasProtected/VectorBosonScattering2012/misID_VBS_24_04_2013.root (visited on 11/12/2014).

[194] F. Abe et al., "Double parton scattering in $\bar{p}p$ collisions at $\sqrt{s} = 1.8$TeV",
Phys.Rev. D56 (1997) pp. 3811–3832, DOI: 10.1103/PhysRevD.56.3811.

[195] B. Jager and G. Zanderighi, "NLO corrections to electroweak and QCD production of W+W+ plus two jets in the POWHEGBOX", *JHEP* 1111 (2011) p. 055,
DOI: 10.1007/JHEP11(2011)055, arXiv: 1108.0864 [hep-ph].

[196] *Jimmy MC generator*, URL: http://jimmy.hepforge.org/.

[197] H.-L. Lai et al., "New parton distributions for collider physics", *Phys.Rev.* D82 (2010) p. 074024,
DOI: 10.1103/PhysRevD.82.074024, arXiv: 1007.2241 [hep-ph].

[198] A. Martin et al., "Parton distributions for the LHC", *Eur.Phys.J.* C63 (2009) pp. 189–285,
DOI: 10.1140/epjc/s10052-009-1072-5, arXiv: 0901.0002 [hep-ph].

[199] S. S. Wilks,
"The Large-Sample Distribution of the Likelihood Ratio for Testing Composite Hypotheses",
The Annals of Mathematical Statistics 9.1 (Mar. 1938) pp. 60–62,
DOI: 10.1214/aoms/1177732360, URL: http://dx.doi.org/10.1214/aoms/1177732360.

[200] O. Behnke et al., eds., *Data Analysis in High Energy Physics*, WILEY-VCH, 2013.

[201] W. Kilian, Private Communications, 2012.

[202] C. Hasterok, M. Kobel, and K. Zuber,
"Optimization of the Search for Contributions of Anomalous Quartic Gauge Couplings to Vector Boson Scattering at the Large Hadron Collider", Presented 14 Nov 2013,
Dresden, TU Dresden, Oct. 2013.

[203] C. Gumpert, "Measurement of electroweak production of two like-charge W bosons and two jets with the ATLAS detector", To be published, Dresden, TU Dresden.

[204] To be published, "Large eta task force report", tech. rep.

[205] URL: http://press.web.cern.ch/press-releases/2014/06/cern-announces-lhc-restart-schedule.

[206] "Letter of Intent for the Phase-I Upgrade of the ATLAS Experiment",
tech. rep. CERN-LHCC-2011-012. LHCC-I-020, CERN, Nov. 2011.

[207] "Performance assumptions based on full simulation for an upgraded ATLAS detector at a High-Luminosity LHC", tech. rep. ATL-PHYS-PUB-2013-009, CERN, Sept. 2013.

[208] "Performance assumptions for an upgraded ATLAS detector at a High-Luminosity LHC", tech. rep. ATL-PHYS-PUB-2013-004, CERN, Mar. 2013.

[209] "Letter of Intent for the Phase-II Upgrade of the ATLAS Experiment", tech. rep. CERN-LHCC-2012-022. LHCC-I-023, Draft version for comments: CERN, Dec. 2012.

[210] *Root Core*, URL: http://twiki.cern.ch/twiki/bin/view/AtlasComputing/RootCore (visited on 09/20/2014).

[211] *Truth to reco functions package*, URL: http://svnweb.cern.ch/trac/atlasgroups/browser/PhysicsAnalysis/EuropeanStrategy/TruthToRecoFunctions (visited on 09/20/2014).

[212] R. Aleksan et al., "Physics Briefing Book: Input for the Strategy Group to draft the update of the European Strategy for Particle Physics" (2013).

[213] "ECFA High Luminosity LHC Experiments Workshop: Physics and Technology Challenges. 94th Plenary ECFA meeting" (Nov. 2013), URL: https://cds.cern.ch/record/1631032/files/pecfa-13-284_ReportHighLuminosityNov13.pdf.

[214] "Physics at a High-Luminosity LHC with ATLAS" (2013), arXiv: 1307.7292 [hep-ex].

[215] T. ATLAS-Collaboration, "Studies of Vector Boson Scattering with an Upgraded ATLAS Detector at a High-Luminosity LHC", tech. rep. ATL-PHYS-PUB-2012-005, CERN, Nov. 2012.

[216] P. Anger et al., "Studies of Vector Boson Scattering with an Upgraded ATLAS Detector at a High-Luminosity LHC", tech. rep. ATL-UPGRADE-PUB-2012-006, CERN, Dec. 2012.

[217] "Studies of Vector Boson Scattering And Triboson Production with an Upgraded ATLAS Detector at a High-Luminosity LHC", tech. rep. ATL-PHYS-PUB-2013-006, CERN, June 2013.

[218] *Scales in MadGraph (MadGraph FAQ)*, URL: https://cp3.irmp.ucl.ac.be/projects/madgraph/wiki/FAQ-General-13.

[219] URL: http://twiki.cern.ch/twiki/bin/viewauth/AtlasProtected/EtmissHighLumi4EFCA.

[220] G. Cowan et al., "Asymptotic formulae for likelihood-based tests of new physics", *The European Physical Journal C* 71.2 (Feb. 2011), arXiv: 1007.1727 pp. 1–19, ISSN: 1434-6044, 1434-6052, DOI: 10.1140/epjc/s10052-011-1554-0, URL: http://arxiv.org/abs/1007.1727 (visited on 06/30/2014).

[221] *Statistics recommendations: Profile likelihood (ATLAS twiki page)*, URL: https://twiki.cern.ch/twiki/pub/AtlasProtected/ATLASStatisticsFAQ/PLvsInt.pdf.

[222] *Statistics recommendations (ATLAS twiki page)*, URL: https://twiki.cern.ch/twiki/pub/AtlasProtected/ATLASStatisticsFAQ/SigRec_v1.pdf.

[223] B. Kegl, *Talk at the Machine Learning Challenge*, URL: https://indico.cern.ch/event/316800/material/slides/0.pdf.

[224] M. S. Chanowitz, "Quantum corrections from nonresonant W W scattering", *Phys.Rept.* 320 (1999) pp. 139–146, DOI: 10.1016/S0370-1573(99)00077-0, arXiv: hep-ph/9903522 [hep-ph].

[225] G. Weiglein et al., "Physics interplay of the LHC and the ILC", *Phys.Rept.* 426 (2006) pp. 47–358, DOI: 10.1016/j.physrep.2005.12.003, arXiv: hep-ph/0410364 [hep-ph].

[226] V. D. Barger et al., "Studying a strongly interacting electroweak sector via longitudinal gauge boson scattering at a muon collider", *Phys.Rev.* D55 (1997) pp. 142–154, DOI: 10.1103/PhysRevD.55.142, arXiv: hep-ph/9606417 [hep-ph].

[227] *Whizard manual*, URL: http://whizard.hepforge.org/manual.pdf.

List of Figures

2.1 Feynman diagram of electroweak vector boson scattering . . . 13
2.2 $VV \to VV$ diagrams included in vector boson scattering at tree-level . . . 14
2.3 Center-of-mass energy dependence of scattering cross sections of Vector Boson Scattering processes in the various channels . . . 16

3.1 Running of the strong coupling α_s. From Particle Data Group review on QCD [91]. . . . 25
3.2 Illustration of the factorization theorem . . . 26
3.3 Monte Carlo simulated event as produced by the SHERPA generator . . . 28
3.4 Computing chain for ATLAS simulation and data taking . . . 31
3.5 Levels in a MC simulation of a high-energy collision event. . . . 32
3.6 Categorization of Feynman diagrams with $VVjj$ final state at leading-order. . . . 34
3.7 Example diagrams for non-resonant contributions to the fully fermionic final state . . . 35
3.8 Dependence of cross section on the center-of-mass energy for the $W^{\pm}W^{\pm}jj$-EW process generated at NLO . . . 37
3.9 Topology of a typical vector boson scattering event with two W bosons in the final state . . . 41
3.10 Feynman diagrams included in electroweak $\ell^+\ell^-\nu\nu jj$ production which lead to a divergence in the low dilepton mass spectrum . . . 42
3.11 Kinematic properties of the leading jet in the $W^{\pm}W^{\pm}jj$ final state comparing the electroweak and the QCD-mediated production . . . 45
3.12 Kinematic properties of the tagging jets in the $W^{\pm}W^{\pm}jj$ final state comparing the electroweak and the QCD-mediated production . . . 45
3.13 Pseudorapidity distribution of the leading and subleading jet in the $W^{\pm}W^{\pm}jj$ final state comparing the electroweak and the QCD-mediated production . . . 46
3.14 Product of pseudorapidity coordinates of the two tagging jets in the $W^{\pm}W^{\pm}jj$ final state comparing the electroweak and the QCD-mediated production . . . 47
3.15 Kinematic distributions of the leptonic decay products of the W bosons and missing transverse momentum in the $pp \to W^{\pm}W^{\pm}jj$ channel comparing the electroweak and QCD-mediated production . . . 47
3.16 Kinematic distributions of the leptonic decay products of the W bosons in the $pp \to W^{\pm}W^{\pm}jj$ channel comparing the electroweak and QCD-mediated production . . . 48
3.17 Transverse momentum distributions comparing the inclusive production of $jj\ell^{\pm}\ell^{\pm}\nu\nu$ to the resonant diboson pair production . . . 49

3.18 Invariant mass of the W boson and pseudorapidity difference of the two hardest jets comparing the inclusive production of $jj\ell^{\pm}\ell^{\pm}\nu\nu$ to the resonant diboson pair production 50
3.19 Higgs mass dependence of electroweak production of $W^{\pm}W^{\pm}jj$. 51
3.20 Comparison of different phase space settings for electroweak production of $jj\ell^{\pm}\ell^{\pm}\nu\nu$ in differential cross sections of the leptons 53
3.21 Comparison of different phase space settings for electroweak production of $jj\ell^{\pm}\ell^{\pm}\nu\nu$ in differential cross sections of the jets 53
3.22 Comparison of different phase space settings for electroweak production of $jj\ell^{\pm}\ell^{\pm}\nu\nu$ in differential cross sections of the lepton-neutrino pairs and the pseudorapidity difference of the two hardest jets 54
3.23 Comparison of the invariant mass of tagging jets at reconstruction level with and without a cut on M_{qq} on parton level 55
3.24 Comparison of kinematics of the two hardest jets in the final state of $jj\ell^{\pm}\ell^{\pm}\nu\nu$ for different generators 57
3.25 Comparison of transverse momenta in the final state of $jj\ell^{\pm}\ell^{\pm}\nu\nu$ for different generators . . . 57
3.26 Illustration of the K-Matrix unitarization method 59
3.27 Total cross section of $W^+W^+ \to W^+W^+$ with a SM Higgs with mass $m_H = 125$ GeV 60
3.28 Unitarized and non-unitarized cross sections for the process$pp \to jje^+\nu_e e^+\nu_e$ in a loose VBS-like volume in dependence of α_4 61

4.1 ATLAS detector overview 65
4.2 Plan view of the ATLAS Inner Detector 66
4.3 ATLAS calorimeter overview 69
4.4 Cumulative amount of material of the various calorimeter components 72
4.5 Cut-away view of the Muon Spectrometer 74
4.6 Muon trigger system 76
4.7 Geometric layout of the ATLAS magnets and the tile calorimeter 78
4.8 Cumulative luminosity delivered by the LHC 83

5.1 Event display of an event with two positively charged muons $\mu^+\mu^+$ in the VBS region 94
5.2 Distributions of M_{jj} and $|\Delta\eta(jj)|$ before the selection on the respective observable is applied . 95
5.3 Kinematics of tagging jets in the control region with at least one additional lepton 97
5.4 Transverse momentum distribution of additional leptons 98
5.5 Relative track isolation of additional leptons 99
5.6 Relative calorimeter isolation of additional leptons 99
5.7 Feynman diagram of contributions from b quarks to the final state of $WZjj$, included in the definition of $W^{\pm}Zjj$ production. 101
5.8 Charge mis-identification rate measured in a $Z \to ee$ data sample with electrons selected according to nominal selection criteria 102
5.9 Fake factors determined with the dijet method 104
5.10 Comparison of measured cross section to theoretical prediction 114
5.11 Dijet kinematics of tagging jets in the VBS signal region. 115
5.12 Kinematics of the leptons in the VBS signal region. 116

5.13 Dependence of the $W^{\pm}W^{\pm}jj$-EW cross section and acceptance to the fiducial VBS volume on the aQGC parameters $\alpha_4,\ \alpha_5$. 118
5.14 Cross sections of $W^{\pm}W^{\pm}jj$-EW in the fiducial VBS volume in dependence of $\alpha_4,\ \alpha_5$. 119
5.15 Scale dependence of aQGC samples. 122
5.16 Kinematics of leptonic decay products of the W bosons in the VBS region in the SM compared to three $(\alpha_4,\ \alpha_5)$ points 123
5.17 Kinematics of leptonic decay products of the W bosons in the VBS region in the SM compared to three $(\alpha_4,\ \alpha_5)$ points 123
5.18 Measurement of the anomalous quartic gauge couplings $\alpha_4,\ \alpha_5$ 124
5.19 Contributions to resonances by the measurement of the anomalous quartic gauge couplings $\alpha_4,\ \alpha_5$. 125

6.1 Cross sections of purely electroweak and QCD-mediated $pp \to W^{\pm}W^{\pm}jj$ production verses center-of-mass energy of the proton-proton collision 128
6.2 Kinematic selection optimization in the nominal tracker 138
6.3 Phase space optimization for the extended tracker. 139
6.4 Additional lepton multiplicity for nominal and extended tracker 142
6.5 Distribution of $\Delta\phi\,(\ell\ell)$ for the Φ resonance with a mass $m_{\Phi} = 1000\,\text{GeV}$ and coupling $g = 2.5$ for the nominal and the extended tracker 144
6.6 Distribution of the invariant mass of the tagging jets for the Φ resonance with a mass $m_{\Phi} = 1000\,\text{GeV}$ and coupling $g = 2.5$ for the nominal and the extended tracker 144
6.7 Discovery significance of the Φ resonance with nominal tracker extension in dependence of the integrated luminosity of the LHC 146
6.8 Discovery significance of the Φ resonance in dependence of the coupling 147

B.1 Transverse momenta of leptons in the VBS signal region 161
B.2 Dilepton kinematics in the VBS signal regions: ΔR and $|\Delta\eta|$ 162
B.3 Kinematics in the VBS signal region: $M_{\ell\ell}$ and $E_{\text{T}}^{\text{miss}}$ 162
B.4 Number of jets and lepton centrality in the VBS signal region 163
B.5 Kinematic properties of the leading tagging jet 163

C.1 Comparison of contour lines in the $\alpha_4,\ \alpha_5$-plane for $WZjj$-EW and $W^{\pm}W^{\pm}jj$-EW 165
C.2 Comparison lepton kinematics between the SM and three $(\alpha_4,\ \alpha_5)$ points in the VBS region . . 167
C.3 Comparison of the SM to three $(\alpha_4,\ \alpha_5)$ points showing dilepton kinematics and missing transverse momentum in the VBS region 168
C.4 Dijet kinematics in the SM compared to three $(\alpha_4,\ \alpha_5)$ points in the VBS region 168
C.5 Tagging jet kinematics in the SM compared to three $(\alpha_4,\ \alpha_5)$ points in the VBS region 169

E.1 Distribution of azimuthal distance of the charged leptons, $\Delta\phi\,(\ell\ell)$, in the $\ell^{\pm}\nu\ell^{\pm}\nu jj$ final state with the ATLAS detector with nominal tracking detector extension 175
E.2 Distribution of distance $\Delta R(\ell\ell)$ between the charged leptons in the $\ell^{\pm}\nu\ell^{\pm}\nu jj$ final state with the ATLAS detector with nominal tracking detector extension 176
E.3 Distribution of $H_T(\ell\ell, E_{\text{T}}^{\text{miss}})$ in the $\ell^{\pm}\nu\ell^{\pm}\nu jj$ final state with the ATLAS detector with nominal tracking detector extension 176

E.4 Distribution of $M_T(\ell\ell, E_{\mathrm{T}}^{\mathrm{miss}})$ in the $\ell^{\pm}\nu\ell^{\pm}\nu jj$ final state with the ATLAS detector with nominal tracking detector extension . . . 177
E.5 Distribution of $M(\ell\ell)$ in the $\ell^{\pm}\nu\ell^{\pm}\nu jj$ final state with the ATLAS detector with nominal tracking detector extension . . . 177
E.6 Distribution of the sum of the absolute values of lepton transverse momenta, $\Sigma|\vec{p}_{T,\ell}|$, in the $\ell^{\pm}\nu\ell^{\pm}\nu jj$ final state with the ATLAS detector with nominal tracking detector extension . . . 178
E.7 Distribution of the invariant mass of jets and leptons, $M(\ell\ell jj)$, in the $\ell^{\pm}\nu\ell^{\pm}\nu jj$ final state with the ATLAS detector with nominal tracking detector extension . . . 178

List of Tables

2.1 Overview of leptons of the SM and corresponding values of the charges . . . 8
2.2 Overview of quarks of the SM and corresponding values of the charges . . . 9
2.3 Gauge bosons of the SM ordered by the corresponding gauge group. . . . 9
2.4 Resonances in VBS and their properties . . . 19
2.5 Experimental constraints on quartic gauge couplings involving photons . . . 22

3.1 Values of the parameters of the electroweak theory, from [116]. . . . 36
3.2 Cross sections determined with the MadGraph generator for electroweak and QCD-mediated production of $VVjj$ final states of different VV combinations at a center-of-mass energy of $\sqrt{s} = 8$ TeV generated with a $M_{jj} > 150$ GeV cut . . . 40
3.3 Comparison of inclusive and restricted cross sections . . . 49
3.4 Comparison of integrated cross sections with different phase space setup . . . 52

5.1 Summary of selection criteria for analysis objects with ATLAS specific terminology. . . . 89
5.2 Summary of baseline event selection. . . . 91
5.3 Selection of additional leptons ("veto leptons") which are vetoed in the event selection. . . . 92
5.4 Summary of signal event selection for the Inclusive and VBS phase spaces. . . . 93
5.5 Comparison of event yields of diboson and $t\bar{t} + V$ processes in the VBS region summed over the three final states for the selection without applying a veto on additional leptons and the selection with such a veto . . . 100
5.6 Contributions from $W^{\pm}Zjj$-EW and $W^{\pm}Zjj$-QCD in the signal regions of the $W^{\pm}W^{\pm}jj$ selection. . . . 100
5.7 Selection of leptons with lower quality, loose leptons, for the estimation of background contribution due to mis-identified jets. . . . 103
5.8 Signal yields of DPS processes for the combined ee, $e\mu$, and $\mu\mu$ final states in the VBS region with MC statistic uncertainties. . . . 105
5.9 Event yields in the Inclusive analysis regions with statistical errors . . . 106
5.10 Event yields in the VBS analysis regions with statistical errors . . . 106
5.11 Calculation of cross sections of diboson plus dijets processes at NLO-QCD . . . 107
5.12 Summary of theoretical uncertainties of the $W^{\pm}W^{\pm}jj$-EW process prediction [191]. . . . 108
5.13 Summary of theoretical uncertainties of the $W^{\pm}W^{\pm}jj$-QCD process prediction [191]. . . . 109
5.14 Summary of theoretical uncertainties of the $W^{\pm}Zjj$-EW process prediction [191]. . . . 110
5.15 Summary of theoretical uncertainties of the $W^{\pm}Zjj$-QCD process prediction [191]. . . . 111

5.16 Systematic uncertainties of MC background and signal samples in the inclusive signal region [191] in %, summarized for all final states. 112
5.17 Systematic uncertainties of MC background and signal samples in the VBS signal region [191] in %, summarized for all final states. 112
5.18 Systematic uncertainties of data driven background estimates in the inclusive signal region [191] in %, summarized for all final states. 113
5.19 Systematic uncertainties of data driven background estimates in the VBS signal region [191] in %, summarized for all final states. 113
5.20 Comparison of two different implementations of the SM in Whizard for the $W^{\pm}W^{\pm}jj$-EW cross section, in the phase space of the sample and in the VBS fiducial volume after application of the Pythia8 parton shower, respectively. Both are generated with the factorization and renormalization scales set to $\mu_F = \mu_R = 2m_W$. 120
5.21 Comparison of two parton shower programs, Pythia8 and Herwig++ applied on the Whizard sample which was generated with the factorization and renormalization scales set to $\mu_F = \mu_R = \sqrt{s_{parton}}$, the partonic center-of-mass energy. 121

6.1 Generator phase space settings and cuts for the production of $pp \to \ell^{\pm}\ell^{\pm}\nu\nu jj$ and $pp \to \ell^{\pm}\ell^{\mp}\ell^{\pm}\nu jj$. 131
6.2 Cross sections of the SM signal and diboson background processes at $\sqrt{s} = 14$ TeV 131
6.3 Widths of the Gaussian distribution used for energy and momentum smearing of the various particles 133
6.4 Efficiency to reconstruct a generated particle in the detector and assign the correct particle type, estimated from full detector simulation. 133
6.5 Trigger efficiencies for single lepton triggers 133
6.6 Optimized selection criteria in case of the nominal inner detector up to $|\eta|_{\text{tracker}} \leq 2.5$. 137
6.7 Optimized cuts for the extended inner detector up to $|\eta|_{\text{tracker}} \leq 4.0$. 138
6.8 Event yields in the optimized phase space regions for the nominal and the extended tracker . . 140
6.9 Event yields remaining after successive application of kinematic selection criteria, in the given order 141
6.10 Significances with and without additional lepton veto. 142
6.11 Significance in dependence of the tracker extension. 143
6.12 Discovery significances for a Φ resonance with mass $m_{\Phi} = 500$ GeV and coupling $g = 1.75$. . . 145
6.13 Discovery significances for Φ resonance with $m_{\Phi} = 500$ GeV using the nominal or the extended tracking detector and scaled to a luminosity of $\mathcal{L} = 3000\,\text{fb}^{-1}$ at $\sqrt{s} = 14$ TeV. 145
6.14 Discovery significances for Φ resonance with $m_{\Phi} = 1000$ GeV using the nominal or the extended tracking detector and scaled to a luminosity of $\mathcal{L} = 3000\,\text{fb}^{-1}$ at $\sqrt{s} = 14$ TeV. 146

C.1 List of fully simulated Whizard aQGC signal samples with their corresponding dataset IDs, cross sections and acceptances to the fiducial VBS region 166

D.1 Monte Carlo samples used for the 8 TeV analysis: Diboson and $t\bar{t}$ production. 172
D.2 Monte Carlo samples used for the 8 TeV analysis: $W\gamma$ and DPI processes. 173